



HAL
open science

Mesosopic simulation of electrolyte and polymer dynamics in a charged slit pore

Lisbeth Perez Ocampo

► **To cite this version:**

Lisbeth Perez Ocampo. Mesoscopic simulation of electrolyte and polymer dynamics in a charged slit pore. Theoretical and/or physical chemistry. Sorbonne Université, 2019. English. NNT : 2019SORUS295 . tel-03015841

HAL Id: tel-03015841

<https://theses.hal.science/tel-03015841v1>

Submitted on 20 Nov 2020

HAL is a multi-disciplinary open access archive for the deposit and dissemination of scientific research documents, whether they are published or not. The documents may come from teaching and research institutions in France or abroad, or from public or private research centers.

L'archive ouverte pluridisciplinaire **HAL**, est destinée au dépôt et à la diffusion de documents scientifiques de niveau recherche, publiés ou non, émanant des établissements d'enseignement et de recherche français ou étrangers, des laboratoires publics ou privés.



Thèse de doctorat

Pour l'obtention du grade de

Docteur de Sorbonne Université

École doctorale de Chimie Physique et Chimie Analytique de Paris Centre

Mesoscopic simulation of electrolyte and polymer dynamics in a charged slit pore

Lisbeth PEREZ OCAMPO

Soutenance prévue le 21/11/2019 devant un jury composé de :

Pr. Jean-François DUFRÊCHE (Université de Montpellier) Rapporteur
Pr. Arnaud VIDECOQ (ENSIL-ENSCI) Rapporteur
Dra. Anne BOUTIN (ENS, Paris) Examinatrice
Pr. Christos LIKOS (Université de Vienne) Examineur
Dra. Marie JARDAT (Sorbonne Université, Paris) Directrice de thèse
Dr. Vincent DAHIREL (Sorbonne Université, Paris) Co-encadrant

Contents

List of Figures	iii
List of Tables	1
Introduction	2
1 Theoretical description of an electrolyte solution in a slit pore	5
1.1 Electric Double Layer	5
1.2 ζ -potential	6
1.3 Evaluation of the ζ -potential	7
1.4 Poisson-Nernst-Planck theory	9
1.5 Ionic density profile within the PB theory	10
1.6 Electro-osmotic flow	17
1.7 Surface Conductivity	19
1.8 Limit of PNP theory	21
2 Simulation Method	22
2.1 Choice of the simulation method	23
2.2 Simulation of a pure MPCD fluid	28
2.3 Simulation of embedded solute particles in a MPCD bath	35
2.4 Computation of the transport coefficients of solute particles	39
3 Transport of an electrolyte solution under confinement	44
3.1 Introduction	45
3.2 Parameters of the simulation	46
3.3 Implementation of the MPCD code	52
3.4 Influence of the electrostatic confinement on the density profile of ions	55
3.5 Diffusion Coefficient of ions	65
3.6 Velocity field of solvent and ions	77
3.7 Poiseuille flow: study of the viscosity	83
3.8 Electric conductivity	88
3.9 Prediction of the ionic velocity profiles	94
4 Polymers in confinement	102
4.1 Brief introduction on polymers	104
4.2 Structural properties of polymers	105
4.3 Modelling of the system	108
4.4 Systems investigated in the present work	114
General conclusions	139
Appendix	142
A	143

Contents

A.1 Results found in section 3.9	143
A.2 Main findings of the previous work of L. Weiss <i>et.al.</i>	152
Bibliography	155

List of Figures

1.1	Schematic representation of the charges and potentials at a positively charged interface. The region between the surface (electric potential Ψ^0 ; charge density σ^0) and the IHP (distance β from the surface) is free of charge. The IHP (electric potential Ψ^i ; charge density σ^i) is the locus of specifically adsorbed ions. The diffuse layer starts at $x = d(OHP)$, with potential Ψ^d and charge density σ^d . The slip plane or shear plane is located at $x = d^{ek}$. The potential at the slip plane is the electrokinetic or zeta-potential, ζ ; the electrokinetic charge density is σ^{ek} [10].	6
1.2	On the left: Representation of a colloidal system. On the right: Approximation of a colloidal system, by considering that the radius of curvature tends to infinity.	8
1.3	Simple scheme that represent the range of the z direction in the slit pore, where $-L/2$ and $L/2$ correspond to the location of the charged surfaces. 0 is the middle of the slit pore.	11
1.4	Visualization of surface conduction, where the dashed line represents the slip plane [14].	20
2.1	From the microscopic model (left) to the mesoscopic model (right) where the solvent molecules are described as a dielectric and viscous continuum.	24
2.2	Schematic representation for different methods of simulation (LB,DPD,and MPCD) [64]	26
2.3	Schematic representation of the MPCD algorithm, that shows how the two steps (streaming and collision) are carried out one after the other at each time step.	28
2.4	Schematic representation of collision step on MPCD.	29
2.5	Schematic representation of the parameters that are used in a simulation.	30
2.6	Bounce back condition between fluid particles and the wall	32
2.7	Schematic representation of the simulation box and of the zone under which is imposed the uniform velocity ($x < d$)	34
2.8	Representation of the cell-linked-list.	37
2.9	Mean square displacement (M.S.D.) as a function of the time obtained to carry out the study of the diffusion coefficient by layers. This particular case correspond to the M.S.D. of the system $\sigma_{wall} = -1 e/nm^2$ and $c_{add} = 0.5 mol/L$ for the layer close to the wall.	41
2.10	$Sc(t)$ as a function of the time obtained to carry out the study of the diffusion coefficient by layers. This particular case correspond to the M.S.D. of the system $\sigma_{wall} = -1 e/nm^2$ and $c_{add} = 0.5 mol/L$ for the layer close to the wall.	42
3.1	Systematic study carried out with the modified MPCD code for three different cases: In (a) a bulk solution was simulated; in (b) the case of neutral confining was obtained confining the bulk solution with infinite neutral walls in the z -direction and finally in (c) the electrostatic confinement case was simulated adding negative charges at the walls.	45

List of Figures

3.2	In order to choose the correct value of a_0 (the simulation cell size), the electro-osmotic (a) and Poiseuille (b) flow profile were obtained as a function of the distance to the wall for different values of a_0 by using the MPCD code.	49
3.3	System simulated with Multi-particle Collision Dynamics. Two parallel, infinite charged walls are separated by the ions in a solvent. An electric field E is applied along the surfaces. The solvent can explore the whole space between the walls, separated by a distance L_{hyd} , while an effective ion-wall diameter σ_w restricts the ion to a space of width $L_{el} = L_{hyd} - \sigma_w$. The average surface charge density σ_{wall} is distributed over discrete size of charge $-e/d$ located at a depth w within the solid wall.	51
3.4	Schematic representation of the system seen in Figure 5.3 when artificial periodic condition in the z direction is applied by adding a slab of vacuum that prevents long-range interactions.	53
3.5	In order to choose the correct value of the k -vectors, the Coulombic potential $U_{Coulomb}$ is obtained for different values of the k as a function of α . This is an example of the method carried out for a system with $\sigma_{wall} = -0.5 e/nm^2$ and $c_{add} = 0.5 mol/L$	54
3.6	Density profiles of counterions as function of the distance to the wall for $\sigma_{wall} = -0.5 e/nm^{-2}$. Vertical blue dashed lines represent the positions of the walls. . .	56
3.7	Density profiles of counterions as a function of the distance to the wall for $\sigma_{wall} = -1 e/nm^{-2}$. Vertical blue dashed lines represent the position of the walls. . . .	57
3.8	Density profiles of co-ions as a function of the distance to the wall for $\sigma_{wall} = -0.5 e/nm^{-2}$. Vertical blue dashed lines represent the positions of the walls.	59
3.9	Density profiles of co-ions as a function of the distance to the wall for $\sigma_{wall} = -1 e/nm^{-2}$. Vertical blue dashed lines represent the positions of the walls.	60
3.10	Comparison between ion density profiles obtained through PB (green dashed line) and MPCD (blue line) as a function of the distance to the wall. The case shown here corresponds to $\sigma_{wall} = -0.5$ (Figure (b)), -1 and $-2 e/nm^{-2}$ (Figure (a)) and no added salt. Black dashed vertical lines indicate the positions of the walls. For PB calculations we took $L_z = L_{el}$ (see Fig. 3.3).	62
3.11	Comparison between ion density profiles obtained through PB and MPCD as a function of the distance to the wall. Counterions density profiles correspond to blue lines (MPCD) and dashed lines (PB) and co-ions density profiles correspond to green lines (MPCD) and dashed lines (PB) for the case of $\sigma_{wall} = -0.5 e/nm^{-2}$. Black dashed vertical lines indicate the positions of the walls.	63
3.12	Comparison between ion density profiles obtained through PB and MPCD as a function of the distance to the wall. Counterions density profiles correspond to blue lines (MPCD) and dashed lines (PB) and co-ions density profiles correspond to green lines (MPCD) and dashed lines (PB) for the case of $\sigma_{wall} = -2 e/nm^{-2}$. Black dashed vertical lines indicate the positions of the walls.	64
3.13	Comparison of the ionic diffusion coefficient in bulk solutions between MPCD and experimental results. This as a function of the ion concentration and divided by the diffusion coefficient of an ion at infinite dilution. Experiments correspond to an aqueous solution of potassium chloride at 198 K.	66

List of Figures

3.14	Comparison of the diffusion coefficient parallel to the wall (in the whole space between the slit pore) between a bulk ionic solution and an ionic solution confined between neutral walls, as a function of the ion concentration. In the latter case, different confinements are considered, <i>i.e.</i> different distances between walls in the slit pore (values of the distances are designated by the different color crosses).	67
3.15	Self diffusion coefficient of ions with direction parallel to the walls in a slit pore of charged walls as a function of the concentration and of the charge of the walls (different colors) for different confinements (different symbols). Figure a) counterions and b) co-ions. In each case a comparison with the bulk case is carried out.	68
3.16	N_{layer1}/N_{layer2} is presented as a function of the concentration of added salt varying the charge on the wall. Where the number of ions that is considered here is of both ions (counterions and co-ions). This analysis is made for the confinement $Lz = 4.5 \text{ nm}$	70
3.17	(a) Self diffusion coefficient of co-ions computed by layers in the direction parallel to the wall as a function of the concentration and of the charge of the walls for the low confinement <i>i.e.</i> $Lz = 4.5 \text{ nm}$. (b) Concentration of co-ions as a function of the concentration of added salt varying the charge on the wall computed by layer for the low confinement <i>i.e.</i> $Lz = 4.5 \text{ nm}$	71
3.18	(a) Self diffusion coefficient of counterions computed by layers in the direction parallel to the wall as a function of the concentration and of the charge of the walls for the low confinement <i>i.e.</i> $Lz = 4.5 \text{ nm}$. (b) Concentration of counterions as a function of the concentration of added salt varying the charge on the wall computed by layer for the low confinement <i>i.e.</i> $Lz = 4.5 \text{ nm}$	72
3.19	N_{layer1}/N_{layer2} is presented as a function of the concentration of added salt varying the charge on the wall. The number of ions that is considered here is for both ions (counterions and co-ions). This analysis is made for the confinement $Lz = 3.0 \text{ nm}$	74
3.20	(a) Self diffusion coefficient of co-ions computed by layers in the direction parallel to the wall as a function of the concentration and of the charge of the walls for the low confinement <i>i.e.</i> $Lz = 3.0 \text{ nm}$. (b) Concentration of co-ions as a function of the concentration of added salt varying the charge on the wall computed by layer for the low confinement <i>i.e.</i> $Lz = 3.0 \text{ nm}$	75
3.21	(a) Self diffusion coefficient of counterions computed by layers in the direction parallel to the wall as a function of the concentration and of the charge of the walls for the low confinement <i>i.e.</i> $Lz = 3.0 \text{ nm}$. (b) Concentration of counterions as a function of the concentration of added salt varying the charge on the wall computed by layer for the low confinement <i>i.e.</i> $Lz = 3.0 \text{ nm}$	76

List of Figures

3.22	Velocity profile of the solvent (electro-osmotic velocity) as a function of the distance to the wall, varying σ_{wall} and c_{add} . Each plot corresponds to a different confinement. The different values of the concentration of added salt are represented by the different line styles, <i>i.e.</i> continuous thin lines are $c_{add} = 0 \text{ mol/L}$, dotted lines correspond to $c_{add} = 0.5 \text{ mol/L}$, continuous thick lines belong to the case $c_{add} = 1 \text{ mol/L}$ and finally dashed lines refers to $c_{add} = 2 \text{ mol/L}$. Whereas, the different σ_{wall} are given by different colors, being red lines -0.5 e/nm^2 , green -1 e/nm^2 and blue -2 e/nm^2	78
3.23	Comparison of solvent velocity profiles as a function of the distance to the wall obtained from a) full PNP, b) MPCD and c) applying Eq. 3.13 to the density profiles obtained through MPCD. This was done for the low confinement <i>i.e.</i> when $Lz = 4.5 \text{ nm}$ when no added salt is considered.	80
3.24	Comparison of solvent velocity profile as a function of the distance to the wall obtained from a) full PNP, b) MPCD and c) applying Eq. 3.13 to the density profiles obtained through MPCD. This was done for the low confinement <i>i.e.</i> when $Lz = 4.5 \text{ nm}$. The corresponding values for the concentration of added salt and the charge surface are shown in the sub-caption of each figure.	82
3.25	Poiseuille velocity profiles obtained from MPCD simulations compared to the analytic result of Eq. 3.14 with a value of η fitted so that the agreement with MPCD is the best. A comparison of the MPCD curves (orange lines) and the fitting curves (blue lines) is shown for the case where ions (a) and no ions (a) are taken into account by using $g = 3 \times 10^{-5} a_0/t_0^2$,	84
3.26	Fitting of the Poiseuille profiles obtained through MPCD done by using Eq. 3.15 keeping the viscosity fixed at the expected value with L_z new as fitting parameters. Comparison of the MPCD curves (orange lines) and the fitting curves (blue lines) for the case where ions (a) and no ions (a) are taken into account by using $g = 3 \times 10^{-5} a_0/t_0^2$	85
3.27	Ion velocity profile as a function of the distance to the walls for several concentrations of added salt and surface charge on the walls. The different values of the concentration of added salt are represented by the different line styles, <i>i.e.</i> dotted lines correspond to $c_{add} = 0.5 \text{ mol/L}$, continuous thick lines belong to the case $c_{add} = 1 \text{ mol/L}$ and finally dashed lines refers to $c_{add} = 2 \text{ mol/L}$. Whereas, the different σ_{wall} are given by different colors, being red lines -0.5 e/nm^2 , green -1 e/nm^2 and blue -2 e/nm^2 . This case correspond to $Lz = 4.5 \text{ nm}$	87
3.28	Ion velocity profile as a function of the distance to the walls for several concentrations of added salt and surface charge on the walls. The different values of the concentration of added salt are represented by the different line styles, <i>i.e.</i> dotted lines correspond to $c_{add} = 0.5 \text{ mol/L}$, continuous thick lines belong to the case $c_{add} = 1 \text{ mol/L}$ and finally dashed lines refers to $c_{add} = 2 \text{ mol/L}$. Whereas, the different σ_{wall} are given by different colors, being red lines -0.5 e/nm^2 , green -1 e/nm^2 and blue -2 e/nm^2 . This case correspond to $Lz = 3.0 \text{ nm}$	87

List of Figures

3.29	Ion velocity profile as a function of the distance to the walls for several concentrations of added salt and surface charge on the walls. The different values of the concentration of added salt are represented by the different line styles, <i>i.e.</i> continuous thin lines are $c_{add} = 0.2 \text{ mol/L}$, dotted lines correspond to $c_{add} = 0.5 \text{ mol/L}$, continuous thick lines belong to the case $c_{add} = 1 \text{ mol/L}$ and finally dashed lines refers to $c_{add} = 2 \text{ mol/L}$. Whereas, the different σ_{wall} are given by different colors, being red lines -0.5 e/nm^2 , green -1 e/nm^2 and blue -2 e/nm^2 . This case correspond to $Lz = 1.5 \text{ nm}$	88
3.30	Comparison of the conductivity in bulk solutions of a 1-1 electrolyte in water between MPCD and experimental results as a function of the ion concentration, and divided by the ideal conductivity σ^0).	89
3.31	Comparison of the conductivity (in the whole space between the silt pore) between a bulk solution and an ionic solution confined between neutral walls, as a function of the ion concentration. For the latter case, different confinements are taken into account, <i>i.e.</i> different distances between walls in the slit pore (values of the distance are designated by the different coloured circles).	90
3.32	Electric conductivity in the middle of the pore as a function of the concentration of added salt and varying the charge on the wall. The electro-osmotic contribution is removed for each case and the conductivity is divided by the ideal conductivity value. This is the case $Lz = 4.5 \text{ nm}$	91
3.33	Electric conductivity in the region close to the walls as a function of the concentration of added salt and varying the charge on the wall. The electro-osmotic contribution is removed for each case and the conductivity is divided by the ideal conductivity value. This is the case $Lz = 4.5 \text{ nm}$	92
3.34	Electric conductivity in the middle of the pore as a function of the concentration of added salt and varying the charge on the wall. The electro-osmotic contribution is removed for each case and the conductivity is divided by the ideal conductivity value. This is the case $Lz = 3.0 \text{ nm}$	93
3.35	Electric conductivity in surface layer as a function of the concentration of added salt and varying the charge on the wall. The electro-osmotic contribution is remove for each case and divided by the ideal conductivity value. This is the case $Lz = 3.0 \text{ nm}$	93
3.36	Velocity parallel to the wall of a solute of radius $a = 2.25 \text{ \AA}$ in a slit pore of size $Lz = 4.5 \text{ nm}$ with $\delta = 0 \text{ \AA}$ (blue) and with $\delta = 0.23 \text{ \AA}$ (orange) computed by equation 3.20.	96
3.37	Comparison of the mobility as a function to the distance to the wall predicted by equation 3.21 (black line), the ions velocity profiles for the systems $\sigma_{wall} = -0.5, -1$ and -2 e/nm^2 for a fixed $c_{add} = 2 \text{ mol/L}$	97
3.38	Comparison of the mobility as a function to the distance to the wall predicted by equation 3.21 (black line), the ions velocity profiles for the systems $\sigma_{wall} = -0.5, -1$ and -2 e/nm^2 for a fixed $c_{add} = 2 \text{ mol/L}$ (red and green dashed lines respectively) and the curve corresponding to μ_{HM} multiplied by $\langle V_{bulk} \rangle / V^0$ (orange line). Case of and $Lz = 4.5 \text{ nm}$	98

List of Figures

3.39	Comparison between: a) Counterions velocity profile as function of the distance to the wall b) Hydrodynamic approach multiplied by the value of the velocity at bulk for the case of $c_{add} = 0.5 \text{ mol/L}$ and $Lz = 4.5 \text{ nm}$	99
3.40	Comparison between: a) Counterions velocity profile as function of the distance to the wall b) Hydrodynamic approach multiplied by the value of the velocity at bulk for the case of $c_{add} = 1 \text{ mol/L}$ and $Lz = 4.5 \text{ nm}$	100
4.1	Systems under study. On the left part: A Poiseuille flow is applied into a slit pore that contains a linear polymer. On the right part: An electro-osmotic flow is applied into a slit pore that contains a linear polymer.	103
4.2	Architecture of polymer chain: a linear chain (a), a branched chain (b), and a cross-linked polymer (c) , where a bead represents a monomer here.	104
4.3	Various models for a linear chain polymer in a continuous space: a bead-stick model (a), a bead-spring model (b), and a pearl-necklace model (c).	105
4.4	End-to-end vector \mathbf{R} is defined by $\mathbf{R} = \mathbf{r}_N - \mathbf{r}_0$	105
4.5	Center of mass \mathbf{r}_G and the radius of gyration \mathbf{R}_g in the bead-stick model	107
4.6	Conformation of a chain with the arbitrary distribution of torsion angles ϕ_i and bending angles θ_i	109
4.7	Comparison of the profiles applied on the study: red curves correspond to the Poiseuille flow, whereas black and green curves correspond to the electro-osmotic flow for no salt and salt respectively. All the curves are taking considering the same v_{max}	116
4.8	Comparison of the monomer probability distribution obtained by the MPCD simulation and the theory (Eq. 4.53) as a function of the distance to the center channel when no flow is induced for the $L_z = 17 a_0 \approx 4 R_g$ case.	117
4.9	Monomer probability distribution as a function of the distance to the center channel when applying an electro-osmotic flow for the no added salt case for the case $L_z = 17 a_0 \approx 4 R_g$	119
4.10	Monomer probability distribution as a function of the distance to the center channel when applying an electro-osmotic flow for the case with 2 mol/L of added salt for the case $L_z = 17 a_0 \approx 4 R_g$	119
4.11	Comparison of the monomer probability distribution for an induced Poiseuille and electro-osmotic flows for both concentrations of added salt as a function of the distance to the center channel when high forces are taken into account. Case of $L_z = 17 a_0 \approx 4 R_g$	120
4.12	Comparison of the monomer probability distribution for an induced Poiseuille and electro-osmotic flows for both concentrations of added salt as a function of the distance to the center channel when small forces are taken into account. Case of $L_z = 17 a_0 \approx 4 R_g$	121
4.13	Monomer probability distribution as a function of the distance to the center channel when no induced flow is consider for the case of $L_z = 34 a_0 \approx 8.15 R_g$	122
4.14	Asphericity divided by R_g^2 as a function of the distance to the center channel when no induced flow is consider for the case of $L_z = 34 a_0 \approx 8.15 R_g$	122

List of Figures

4.15	Monomer probability distribution as a function of the distance to the center channel when applying an electro-osmotic flow for the no added salt case when $L_z = 34 a_0 \approx 8.15 R_g$	123
4.16	Monomer probability distribution as a function of the distance to the center channel when applying an electro-osmotic flow for the added salt case (2mol/L) when $L_z = 34 a_0 \approx 8.15 R_g$	124
4.17	Comparison of the monomer probability distribution as a function of the distance to the center of the channel for the induced Poiseuille and electro-osmotic flow (for $c_{add} = 0$ and 2 mol/L cases), when considering only high forces. Case of $L_z = 34 a_0 \approx 8.15 R_g$	125
4.18	Asphericity for an induced electro-osmotic flow (divided by R_g^2) as a function of the distance to the wall is shown for the case of $c_{add} = 2 \text{ mol/L}$ in (a) and for $c_{add} = 0 \text{ mol/L}$ in (b). In both graphs the case of bulk, equilibrium and induced Poiseuille flow only for high forces is also shown. Case of $L_z = 34 a_0 \approx 8.15 R_g$	126
4.19	Comparison of the monomer probability distribution at equilibrium considering an attractive and a repulsive wall, as a function of the distance to the center of the channel for the case of $L_z = 34 a_0 \approx 8.15 R_g$	127
4.20	Asphericity (divided by R_g^2) as a function of the distance to the center of the channel, at equilibrium, is shown for the case of an attractive (blue curve) a repulsive wall (black curve), for the case of $L_z = 34 a_0 \approx 8.15 R_g$, and for the bulk situation.	128
4.21	Monomer probability distribution for the cases of a repulsive and an attractive wall, when considering an induced electro-osmotic flow (no added salt case), as a function of the distance to the center of the channel. The equilibrium curves (<i>i.e.</i> without flow) for both cases, are also plotted in order to have a point of reference. Case of $L_z = 34 a_0 \approx 8.15 R_g$	129
4.22	Asphericity (divided by R_g^2) as a function of the distance to the center of the channel, when applying an electro-osmotic flow for attractive and repulsive walls, considering the $L_z = 34 a_0 \approx 8.15 R_g$ case. Here only the case of $c_{add} = 0 \text{ mol/L}$ for the electro-osmotic flow is taken into account. Bulk and equilibrium for attractive and repulsive walls are shown as references.	130
4.23	Monomer probability distribution for the cases of repulsive wall and attractive wall, when considering an induced Poiseuille flow, as a function of the distance to the center of the channel. The equilibrium curves (<i>i.e.</i> without flow) for both cases, are also plotted in order to have a point of reference. Case of $L_z = 34 a_0 \approx 8.15 R_g$	131
4.24	Comparison of the monomer probability distribution under an induced electro-osmotic flow as a function of the distance to the center channel, for the cases when a repulsive and an attractive wall are considered. Case of $L_z = 34 a_0 \approx 8.15 R_g$	132
4.25	Asphericity (divided by R_g^2) as a function of the distance to the center channel, when applying an electro-osmotic flow for attractive and repulsive walls, considering the $L_z = 34 a_0 \approx 8.15 R_g$ case. Here only the case of $c_{add} = 2 \text{ mol/L}$ for the electro-osmotic flow is taken into account. Bulk, and equilibrium for attractive and repulsive walls are also show.	132

List of Figures

4.26	Comparison between the monomer probability distribution of a flexible and stiff polymer, as a function of the distance to the center of the channel without flow for the case $L_z = 34 a_0 \approx 8.15 R_g$. In this case we considered the case with repulsive walls.	133
4.27	Comparison between the monomer probability distributions of a flexible and of a stiff polymer, as a function of the distance to the center of the channel for the $L_z = 34 a_0 \approx 8.15 R_g$ case. In this case we considered the case with attractive walls.	134
4.28	Comparison between the monomer probability distribution, for a linear flexible and stiff polymer, as a function of the distance to the center channel when inducing an electro-osmotic flow (no added salt) for the $L_z = 34 a_0 \approx 8.15 R_g$ case. In this case we considered the case with repulsive and attractive walls.	135
4.29	Comparison between the monomer probability distribution, for a flexible and stiff polymer, as a function of the distance to the center of the channel under an induced Poiseuille flow for the case $L_z = 34 a_0 \approx 8.15 R_g$. In this case we considered the case with repulsive walls.	135
4.30	Comparison between the monomer probability distribution, for a flexible and stiff polymer, as a function of the distance to the center of the channel under an induced Poiseuille flow for the case $L_z = 34 a_0 \approx 8.15 R_g$. In this case we considered the case with attractive walls.	136
4.31	Monomer probability distribution as a function of the distance to the center of the channel under an induced electro-osmotic flow for the case $L_z = 34 a_0 \approx 8.15 R_g$. A comparison between the case of repulsive and attractive walls for a flexible and stiff polymer is carried out.	137
A.1	Comparison between: a) Counterions velocity profiles as function of the distance to the wall b) Hydrodynamic approach multiplied by the value of the velocity at bulk for the case of $c_{add} = 0.5 \text{ mol/L}$ and $Lz = 4.5 \text{ nm}$	143
A.2	Comparison between: a) Counterions velocity profiles as function of the distance to the wall b) Hydrodynamic approach multiplied by the value of the velocity at bulk for the case of $c_{add} = 1 \text{ mol/L}$ and $Lz = 4.5 \text{ nm}$	144
A.3	Comparison between: a) Counterions velocity profiles as function of the distance to the wall b) Hydrodynamic approach multiplied by the value of the velocity at bulk for the case of $c_{add} = 2 \text{ mol/L}$ and $Lz = 4.5 \text{ nm}$	144
A.4	Comparison between: a) Co-ions velocity profiles as function of the distance to the wall b) Hydrodynamic approach multiplied by the value of the velocity at bulk for the case of $c_{add} = 0.5 \text{ mol/L}$ and $Lz = 4.5 \text{ nm}$	145
A.5	Comparison between: a) Co-ions velocity profiles as function of the distance to the wall b) Hydrodynamic approach multiplied by the value of the velocity at bulk for the case of $c_{add} = 1 \text{ mol/L}$ and $Lz = 4.5 \text{ nm}$	146
A.6	Comparison between: a) Co-ions velocity profiles as function of the distance to the wall b) Hydrodynamic approach multiplied by the value of the velocity at bulk for the case of $c_{add} = 2 \text{ mol/L}$ and $Lz = 4.5 \text{ nm}$	146

List of Figures

A.7	Comparison between: a) Counterions velocity profiles as function of the distance to the wall b) Hydrodynamic approach multiplied by the value of the velocity at bulk for the case of $c_{add} = 0.5 \text{ mol/L}$ and $Lz = 4.5 \text{ nm}$	147
A.8	Comparison between: a) Counterions velocity profiles as function of the distance to the wall b) Hydrodynamic approach multiplied by the value of the velocity at bulk for the case of $c_{add} = 1 \text{ mol/L}$ and $Lz = 4.5 \text{ nm}$	148
A.9	Comparison between: a) Counterions velocity profiles as function of the distance to the wall b) Hydrodynamic approach multiplied by the value of the velocity at bulk for the case of $c_{add} = 2 \text{ mol/L}$ and $Lz = 4.5 \text{ nm}$	148
A.10	Comparison between: a) Co-ions velocity profiles as function of the distance to the wall b) Hydrodynamic approach multiplied by the value of the velocity at bulk for the case of $c_{add} = 0.5 \text{ mol/L}$ and $Lz = 4.5 \text{ nm}$	149
A.11	Comparison between: a) Co-ions velocity profiles as function of the distance to the wall b) Hydrodynamic approach multiplied by the value of the velocity at bulk for the case of $c_{add} = 1 \text{ mol/L}$ and $Lz = 4.5 \text{ nm}$	149
A.12	Comparison between: a) Co-ions velocity profiles as function of the distance to the wall b) Hydrodynamic approach multiplied by the value of the velocity at bulk for the case of $c_{add} = 2 \text{ mol/L}$ and $Lz = 4.5 \text{ nm}$	150
A.13	Comparison between: a) Counterions velocity profiles as function of the distance to the wall b) Hydrodynamic approach multiplied by the value of the velocity at bulk for the case of $c_{add} = 0.5 \text{ mol/L}$ and $Lz = 1.5 \text{ nm}$	151
A.14	Comparison between: a) Counterions velocity profiles as function of the distance to the wall b) Hydrodynamic approach multiplied by the value of the velocity at bulk for the case of $c_{add} = 1 \text{ mol/L}$ and $Lz = 1.5 \text{ nm}$	151
A.15	Comparison between: a) Counterions velocity profiles as function of the distance to the wall b) Hydrodynamic approach multiplied by the value of the velocity at bulk for the case of $c_{add} = 1.5 \text{ mol/L}$ and $Lz = 1.5 \text{ nm}$	152
A.16	Monomer probability distribution $P_{mon}(z)$ for fully flexible chains as a function of the applied flow strengths. Taking into account the channel symmetry with its center at $z = 0$, only half the profile of each topology is depicted; ring polymers are in red/yellow, linear ones in green/blue. Forces f are in units of $msa_0t_0^2$ ^[133]	153
A.17	Ratio of ring polymer velocity v_R to linear polymer velocity v_L depicted as a function of the flow strength f for varying rigidity ^[133]	154
A.18	Relative increase of the transport velocity of ring polymers v_R to linear ones v_L is plotted as a function of the attraction to the spots strength ϵ . Polymers of various persistence lengths L_P are shown. Error bars are either indicated or smaller than the symbols. $\epsilon = 0k_B T$ corresponds to an undecorated channel wall. The inset depicts the enlargement for weak attraction strengths ^[133]	154

List of Tables

3.1	Lx , Ly and Lz as a function of a_0 for different values of a_0	47
3.2	Corresponding values of g for different values of a_0	48
3.3	Simulation parameters used in the study. The concentration parameter $c_{add} = 0$ mol/L denotes an ionic solution with no added salt. The cell size is $a_0 = 0.15 nm$	52
3.4	Debye length compute for different added salt concentration. Following Eq. 3.11, where ρ_s the salt concentration in the reservoirs is taken from the plateau value of the ion density profile.	58
3.5	On the left side: Schematic representation of the layer division of the system, the blue part refers to layer 2 and green parts refer to layer 1 and layer 3. On the right side: A table showing the layers ranges defined in each system, where the blue part of the table corresponds to the lowest confinement, <i>i.e.</i> $Lz = 4.5nm$. The gray part is then the confinement $Lz = 3.0nm$	58
3.6	Values of the ion density profile in the middle of the slit pore where electroneutrality exists for the system with $L_z = 4.5 nm$	61
3.7	Comparison of the values of the counterions diffusion coefficient, where D_{pore} correspond to the results obtained at subsection 3.5.3.2 and as D_{av} to the results computed using eq. 3.12 for all the systems.	73
3.8	Comparison of the values of the co-ions diffusion coefficient, where D_{pore} correspond to the results obtained at subsection 3.5.3.2 and as D_{av} to the results computed using eq. 3.12 for all the systems.	74
3.9	Values of the slip length for different systems at the larger confinement $Lz = 4.5 nm$	81
3.10	Values of the conductivity and diffusion in bulk, obtained for different ion concentrations by using MPCD simulation	98

Introduction

Since the early developments of electricity, scientists began investigating ways to store this form of energy, leading to more and more efficient electrical devices. Indeed, instruments like friction generators and Leyden jars were used to investigate electric performance. More specifically, during the performance of one experiment, an important fact occurred, the day Alessandro Volta invented a reliable and stable source of electricity. The so-called Volta pile, which consisted of zinc and silver plates, connected with paper soaked in brine, was then invented. Later, this source of power became an important tool for many electrical investigations. For example, in 1808 Ferdinand Friedrich Reuss carried out two types of simple experiments using an apparatus with a U-tube (filled with water) and two electrodes connected to a Volta pile. In his first set of experiments he inserted a plug of clay in the U-tube and discovered that when a voltage is applied, the water level rises in one part of the tube. In another experiment, he inserted quartz sand above the clay plug and found that the clay particles migrated through the sand layer^[1]. In fact, power generation and energy storage technologies, which utilize electrochemical devices, such as lithium-ion batteries or fuel cells, have since been extensively studied, leading to continuous performance improvements. At the core of these electrochemical devices we find complex electrolyte solutions and charged surfaces. The transport of the ions and the solvent through the charged solid interface affects the total performance of the devices. The study of transport phenomena is then a central area of research in the development of innovative electrochemical devices. These charged interfaces are at the origin of electrokinetic effects, which are characterized by the coupling of hydrodynamics and electric phenomena^[1]. Electrokinetic phenomena (EKP) are interfacial phenomena which can take place in colloidal systems. These have attracted more and more attention, since they can be used for biological separation, to create micro-electromechanical systems, nano-scales separation processes, and many other experimental techniques in energy storage and biomedical science.

Electrokinetic phenomena are called interfacial phenomena because they often arise in fluids in contact with particles or other surfaces. Generally, they are characterized by the tangential motion of the fluid, at the surface, due to an external force. Such forces may consist in an electric field, a pressure gradient, a concentration gradient, or simply gravity^[2]. Due to their importance in a variety of context, from environment to biology or from micro-fluid to electroacoustic exploration, various simulation strategies have been developed to address the challenge of the multiple lengths and time scales involved in such phenomena. A common example of EKP is electrophoresis, which describes the movement of ions, charged colloidal particles or polyelectrolytes, immersed in a liquid, under the influence of an external electric field. Similarly, there is the so called electro-osmosis phenomenon, which induces the motion of a liquid through an immobilized set of charged particles, a porous plug, a capillary, or a membrane, in response to an applied electric field. On the other hand, if a pressure gradient is applied on the same system, a streaming potential is recovered. Streaming potentials are then created by charge accumulations caused by the flow of counter-charges inside capillaries or pores^[2].

The discovery of the electrokinetic phenomena such as electrophoresis, electro-osmosis or

Introduction

streaming potentials, gave rise to the concept of the electrical double layer (EDL), that characterizes the structural organization of ions in the vicinity of a charged surface. Indeed, this concept was introduced by Helmholtz and its study became important for the understanding of any EKP. The Poisson-Nernst-Planck (PNP) theory is a good candidate when studying them at the mesoscale. At equilibrium, PNP is equivalent to the Poisson-Boltzmann (PB) theory. In both PNP and PB theories, the Poisson equation relates the local electrostatic potential to the ionic concentration. Whenever an external force (*e.g.* an electric field) is applied, the Navier-Stokes (NS) equation is used for momentum conservation along with other assumptions such as the incompressibility condition. The PNP thus assumes that ions are point-like particles, and excluded volume effects between ions, as well as hydrodynamic couplings between moving ions are not taken in account. As a consequence, the ionic mobility is equivalent to the one obtained in the case of a bulk solution at infinite dilution. Therefore, if one considers the case of an ionic solution in a charged slit pore, some properties such as the ionic velocity and *a fortiori* the electrical conductivity of the system cannot be accounted for in a reliable way. Also, the structural and dynamic properties of complex molecules in such a slit pore will not be well described if hydrodynamic interactions are neglected. In this context, our aim is to investigate the influence of non ideal effects on the dynamics of ions and of complex molecules in a slit pore from a theoretical point of view.

The ions mobility in bulk and under confinement has been studied at different scales in the MEM team of PHENIX laboratory. In particular, Pierre Turq and coworkers Olivier Bernard, Jean-François Dufrêche and Serge Durand-Vidal have developed an analytical theory of the transport properties of electrolyte solutions, in order to compute the velocity of ions under an electric field, and thus to predict the electrical conductivity. The treatment of non ideal effects in the theory is remarkably valid for bulk electrolytes up to molar concentrations^[3-5], but it can hardly be adapted to confined electrolytes. In particular, the treatment of hydrodynamic interactions between ions is much more complex in the presence of walls. Member of the teams, in particular Marie Jardat, used mesoscopic simulations techniques to complement analytical theories^[6]. A Brownian Dynamics (BD) simulation method was developed, but it is again not adapted to the treatment of hydrodynamics under confinement. Only at a finer scale, atomistic models of confined electrolytes were studied thanks to Molecular Dynamics (MD) simulations, under the supervision of Virginie Marry and Benjamin Rotenberg, which led to the conclusion that macroscopic treatments of the solvent are surprisingly working well at the nanometric scale^[7]. In the case of clay surfaces, only in the very first water layer close to the surface the electroosmotic flow was significantly different from PNP predictions. Nevertheless, MD simulations remain reduced to study extensively the effect of confinement on ion mobility, and therefore to get quantitative predictions of the electrical conductivity inside a charged pore.

The current work aims at extending these previous efforts from the MEM team. Actually, before the present work, there was no attempt to check with numerical simulations how the confinement quantitatively affects the transport of charge carriers compared to the predictions of bulk theories. Numerous numerical simulations at the mesoscopic level have been developed which could in principle be used to study the EKP, and in particular the individual motion of ions in a confined environment. Each one of them presents advantages and disadvantages depending of what feature of the system we are interested in. In the present work, we need a simulation method that allows us to account for hydrodynamic effects and other non-ideal

Introduction

contributions to the transport of ions or complex molecules in confined media, over relatively long time scales. We have chosen to use the MultiParticle Collision Dynamics (MPCD) simulation method. In MPCD, an explicit but highly simplified description of the solvent is used, where ballistic motions and local momentum exchanges between solvent particles are tuned to reproduce the properties of a fluid at the Navier-Stokes level. It is a discrete solvent with the hydrodynamic properties of a continuous solvent, whose hydrodynamic regime can be chosen thanks to a relatively small number of parameters. Solute particles can be embedded in the MPCD solvent bath, and evolve through a classical molecular dynamics algorithm. Explicit direct interactions between solutes and with the walls of a slit pore can thus be taken into account, and hydrodynamic interactions between solutes emerge.

In this thesis, we have used MPCD to focus on three issues. First, we have computed the dynamic properties of ions in charged slit pores, at equilibrium and under an external electric field, in order to investigate properties that are not well predicted by the Poisson-Nernst-Planck equation. We have in particular determined the velocities of ions as a function of their distance to the walls in the presence of an electro-osmotic flow. Strong departures from the ideal behaviour have been observed. Second, we have tested whether the values of these quantities could be predicted by existing theories, *i.e.* using calculations that would be much faster to run than numerical simulations. Finally, we have focused on the dynamics of polymers under an electro-osmotic flow. Indeed, the structure of polymers under a Poiseuille flow in a slit pore is known to differ from its structure at equilibrium. Electro-osmotic flows induce in some cases a shear rate larger than the Poiseuille flow, so that the structure of polymers under these flows is expected to be affected in another way.

More specifically, the present work is articulated in four chapters. Since the electric double layer (EDL) plays an important role in the understanding of EKP, Chapter 1 theoretically defines the EDL, at equilibrium and under an external field. In order to understand the choice of our method of simulation, a review of the advantages and disadvantages of existing methods to study electrokinetic phenomena is presented in Chapter 2. Then, a detailed explanation of the chosen algorithm is carried out. The third chapter is dedicated to the results we have obtained for the properties of ionic solutions in a charged slit pore. The end of this chapter concerns the possible description of the ions velocity profiles from analytic theories. Finally, Chapter 4 presents the method we have used to study the dynamics of polymers under an electro-osmotic flow in a slit pore and the results we have obtained. The manuscript ends with a general conclusion.

Theoretical description of an electrolyte solution in a slit pore

Contents

1.1	Electric Double Layer	5
1.2	ζ -potential	6
1.3	Evaluation of the ζ -potential	7
1.4	Poisson-Nernst-Planck theory	9
1.5	Ionic density profile within the PB theory	10
1.5.1	Poisson-Boltzmann equation	10
1.5.2	Case without added salt	12
1.5.3	Case with added salt	14
1.6	Electro-osmotic flow	17
1.7	Surface Conductivity	19
1.8	Limit of PNP theory	21

1.1 Electric Double Layer

Under certain conditions, surfaces in contact with ionic aqueous solutions have a tendency to gain surface charges. This phenomenon mainly arises from adsorption or dissociation of chemical groups. As a result, because of electrostatic forces, the charged surface attracts the counterions (particles with opposite charges to the surface) present in the solution and repels the co-ions (particles with the same charges as the surface)^[8].

Thus, a model that represents the electrical state of a charged surface is the so-called Electric Double Layer (EDL), whose simplest picture consists in one layer made of immobile charges, the surface or titratable charges, firmly bound to the particle or solid surface, while the other layer is distributed more or less diffusely within the solution in contact with the surface. This layer contains an excess of counterions (ions opposite in sign to the fixed charges), and has a deficit of co-ions (ions of the same sign as the fixed charges).

There exist as well more elaborate models for the uncharged region between the surface and the locus of hydrated counterions, often called the Stern layer. On the contrary, ions beyond it form the diffuse layer or Gouy layer (also denoted as Gouy-Chapman layer). In some cases, the separation of the EDL into a charge-free Stern layer and a diffuse layer is not sufficient to interpret experiments. Then, the Stern layer is subdivided into an inner Helmholtz layer (IHL), bounded by the surface and the inner Helmholtz plane (IHP) and an outer Helmholtz layer (OHL), located between the IHP and the outer Helmholtz plane (OHP). This is shown in Fig. 1.1 for a simple case^[9].

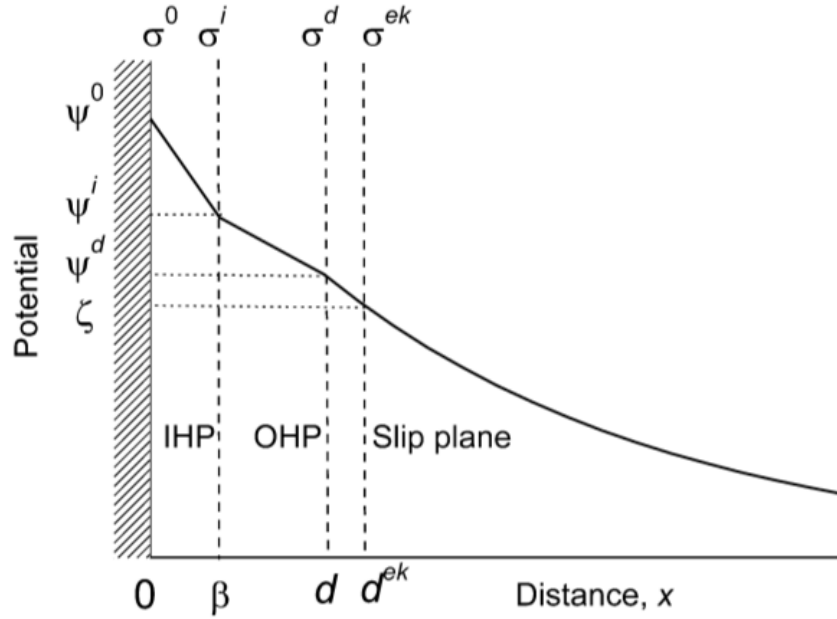


Figure 1.1 – Schematic representation of the charges and potentials at a positively charged interface. The region between the surface (electric potential Ψ^0 ; charge density σ^0) and the IHP (distance β from the surface) is free of charge. The IHP (electric potential Ψ^i ; charge density σ^i) is the locus of specifically adsorbed ions. The diffuse layer starts at $x = d(OHP)$, with potential Ψ^d and charge density σ^d . The slip plane or shear plane is located at $x = d^{ek}$. The potential at the slip plane is the electrokinetic or zeta-potential, ζ ; the electrokinetic charge density is σ^{ek} [10].

The necessity of this subdivision occurs when some ion types (possessing a chemical affinity to the surface in addition to purely Coulombic interactions), are specifically adsorbed at the surface, whereas other ion types interact with the charged surface only through electrostatic forces [11]. The IHP is the locus of the former ions, and the OHP determines the beginning of the diffuse layer, which is the generic part of the EDL (*i.e.*, the part governed by purely electrostatic forces). The fixed surface-charge density is denoted σ^0 , the charge density at the IHP σ^i , and that in the diffuse layer σ^d . As the system is electroneutral, then $\sigma^0 + \sigma^i + \sigma^d = 0$.

1.2 ζ -potential

As commented previously, a tangential liquid flow along a charged solid surface can be caused by an external electric field (electrophoresis, electro-osmosis) or by an applied mechanical force (pressure gradient, gravity). Thus, experiments and recent molecular dynamic simulations [12] have shown that in such tangential motion a very thin layer of fluid adheres to the surface: it is called the hydrodynamically stagnant layer, which extends from the surface to some specified distance, d^{ek} , where a so-called hydrodynamic slip plane is assumed to exist. For distances to the wall, $x < d^{ek}$, one has the stagnant layer in which no hydrodynamic flows can develop. Thus, some authors speak of a distance-dependent viscosity with roughly a step-function dependence [13]. The space charge for $x > d^{ek}$ is hydrodynamically mobile and electrokinetically active, and a particle (if spherical) behaves hydrodynamically as if it had a

radius $a + d^{ek}$.

The space charge for $x < d^{ek}$ is hydrodynamically immobile, but can still be electrically conducting. The electrostatic potential at the plane, where the division between the hydrodynamically mobile and immobile is located, is identified as the electrokinetic or zeta-potential, ζ .

General experience indicates that the plane of shear is located very close to the OHP. Both planes are abstractions of reality. The OHP is interpreted as a sharp boundary between the diffuse and the non-diffuse parts of the EDL, but it is very difficult to locate it exactly. Similarly, the slip plane is interpreted as a sharp boundary between the hydrodynamically mobile and immobile fluid. In reality, none of these transitions are sharp. However, liquid motion may be hindered in the region where ions experience strong interactions with the surface. Therefore, it is possible that the immobilization of the fluid extends further out of the surface than the beginning of the diffuse part of the EDL. This means that, in practice, the ζ -potential is equal to or lower in magnitude than the diffuse-layer potential, Ψ^d . In the latter case, the difference between Ψ^d and ζ is a function of the ionic strength: at low ionic strength, the decay of the potential as a function of distance is small and $\zeta \cong \Psi^d$; at high ionic strength, the decay is steeper and $|\zeta| \leq |\Psi^d|$.

1.3 Evaluation of the ζ -potential

Although the notion of slip plane is generally accepted, its specific location is usually not well known. In fact, ζ is fully defined by the nature of the surface, its charge (often determined by pH), the electrolyte concentration in the solution, and the nature of the electrolyte and of the solvent.

Experiments demonstrate that different researchers often find different ζ -potentials for supposedly identical interfaces. Sometimes, the surfaces are not in fact identical: the high specific surface area and surface reactivity of colloidal systems make ζ very sensitive to even minor amounts of impurities in solution. This can partly explain variations in electrokinetic determinations from one laboratory to another.

Alternatively, since ζ is not a directly measurable property, it may be that an inappropriate model has been used to convert the electrokinetic signal into a ζ -potential. The level of sophistication required (for the model) depends on the situation and on the particular phenomena investigated. The choice of measuring technique and of the theory used depends to a large extent on the purpose of the electrokinetic investigation^[10].

There are instances in which the use of simple models can be justified, even if they do not yield the correct ζ -potential. For example, if electrokinetic measurements are used as a sort of quality control tool, one is interested in rapidly (online) detecting modifications in the electrical state of the interface rather than in obtaining accurate ζ -potentials. However, when the purpose is to compare the calculated values of ζ of a system under given conditions using different electrokinetic techniques, it may be essential to find a true ζ -potential. The same applies to those cases in which ζ is used to perform calculations for other physical quantities.

Furthermore, there may be situations in which the use of simple theories may be misleading even for simple quality control. For example, there are ranges of ζ -potential and double layer thickness for which the electrophoretic mobility does not depend linearly on ζ , as assumed in simple models^[10]. Two samples might have the same true ζ -potential and quite different

mobilities because of their different sizes. The simple theory would make us believe that their electrical surface characteristics are different when they are not.

An important factor in the reliable estimation of ζ is the possibility that charges behind the shear plane may contribute to the excess conductivity of the double layer (stagnant layer or inner layer conductivity.) If it is assumed that charges located between the surface and the plane of shear are electrokinetically inactive, then the ζ -potential will be the only interfacial quantity explaining the observed electrokinetic signal. Otherwise, a correct quantitative explanation of electrokinetic phenomena will require the additional estimation of surface conduction.

Thus, in order to obtain similar values of the ζ -potential independently of the given experiment, it is necessary to introduce the concept of surface conduction as described by Delgado *et al.* in Ref. 10. Surface conduction refers to the excess electric conduction that takes place in dispersed systems due to the presence of electric double layers. Then, excess charges in them may move under the influence of electric fields applied tangentially to the surface^[14].

One of the main goals of this thesis is to obtain an analytical prediction of the surface conductivity in order to give experimentalists a tool that allows them to estimate the ζ -potential in a more accurate way. To do so, first we carry out the surface conductivity via simulation in order to be able to validate our analytical prediction.

In what follows we consider a slit geometry as an approximate colloidal system, given that the radius of curvature of a large colloidal particle may be assumed to tend to infinity (leading to a planar geometry). We have thus a charged surface in contact with an electrolyte solution. Finally as surface conductivity is the consequence of an applied external force to ions, we apply an electric field, which moves the ions, allowing us to get their velocity near the surface (see Fig. 1.2).

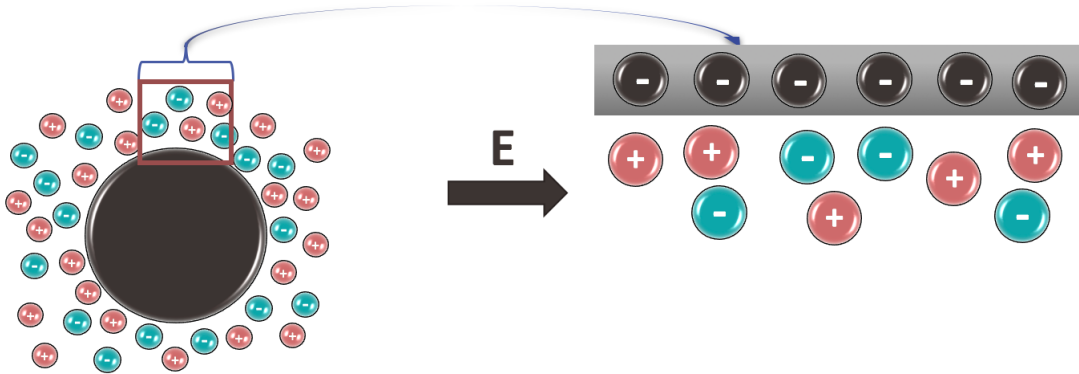


Figure 1.2 – On the left: Representation of a colloidal system. On the right: Approximation of a colloidal system, by considering that the radius of curvature tends to infinity.

As mentioned in the Introduction, EKP is often tackled at the mesoscale using PNP theory, which is made of two contributions, one due to equilibrium interactions (no external electric-field), which assumes that electrostatic interactions at equilibrium are described by the Poisson-Boltzmann (PB) equation, and the second referring to non-equilibrium interactions (due to an applied electric field), which deals with the dynamics of the fluid described by the Nernst-Planck equation. In the following sections we present the Poisson-Nernst-Planck theory.

1.4 Poisson-Nernst-Planck theory

The Nernst-Planck equation is a conservation of mass equation that describes the influence of an ionic concentration gradient and that of an electric field on the flux of chemical species, specifically ions. Thus, starting from the conservation of mass equation and considering an incompressible fluid, *i.e.* $\nabla \cdot \mathbf{u} = 0$, where \mathbf{u} is the fluid velocity, we have for each specie i ,

$$\frac{Dn_i}{Dt} + \nabla \cdot \mathbf{j}_i = 0 \quad (1.1)$$

where $\frac{D(\cdot)}{Dt} = \frac{\partial(\cdot)}{\partial t} + \mathbf{u} \cdot \nabla(\cdot)$ is the material derivative, n_i and \mathbf{j}_i are the ionic concentration and the flux respectively. Thus, the equation becomes:

$$\frac{\partial n_i}{\partial t} + \mathbf{u} \cdot \nabla n_i + \nabla \cdot \mathbf{j}_i = 0 \quad (1.2)$$

where the convection term is represented by $\mathbf{u} \cdot \nabla n_i$. The flux density for the Nernst-Planck equation is usually expressed as,

$$\mathbf{j}_i = -M_i n_i \nabla \mu_i \quad (1.3)$$

with M_i the mobility and where the local electrochemical potential μ_i , is the sum of an ideal and an excess term, given by:

$$\mu_i = k_B T \ln(n_i/n_i^0) + \mu_i^{ex} \quad (1.4)$$

where n_i^0 is the concentration of reference and k_B and T denote the Boltzmann constant and the temperature respectively. The excess part is written as an electrostatic term:

$$\mu_i^{ex} = z_i e \Psi \quad (1.5)$$

where e is the elementary charge and Ψ the electrostatic potential. The electrochemical potential gradient is given by:

$$\nabla \mu_i = \frac{k_B T}{n_i} \nabla n_i + z_i e \nabla \Psi \quad (1.6)$$

The mobility is given by the Einstein's relation

$$M_i = \frac{D_i^0}{k_B T} \quad (1.7)$$

where D_i denotes the diffusion coefficient of the i -th ionic species in at infinite dilution. The flux can therefore be expressed as:

$$\mathbf{j}_i = -D_i^0 \left(\nabla n_i + \frac{z_i e n_i}{k_B T} \nabla \Psi \right) \quad (1.8)$$

The first term on the right hand side of the Eq 1.8 is the flux due to diffusion (Fick's law), whilst the second term is the flux due to electro migration, which is highly non-linear. Plugging this expression in Eq. 1.1 we obtain the Nernst-Planck Equation for a dilute solution, *i.e.*

$$\frac{\partial n_i}{\partial t} + \mathbf{u} \cdot \nabla n_i + \nabla \cdot \left[-D_i^0 \left(\nabla n_i + \frac{z_i e n_i}{k_B T} \nabla \Psi \right) \right] = 0 \quad (1.9)$$

It is important to notice that Nernst-Planck equation gives N equations with $N + 1$ unknowns. In order to solve the system of equations one more equation is needed. This can be achieved describing the electrostatic potential via the Poisson equation leading to a mean field approach, i.e.

$$\rho_f = \nabla \cdot \mathbf{D} \quad (1.10)$$

ρ_f is the free charge density and \mathbf{D} is the electric displacement vector. For any given linear dielectric material we can express \mathbf{D} as

$$\mathbf{D} = \epsilon \mathbf{E} \quad (1.11)$$

where $\epsilon = \epsilon_r \epsilon_0$ is the permittivity of the material, in this case the solvent. \mathbf{E} is the electric field generated by the charges present within the system and since $\nabla \times \mathbf{E} = 0$ we may write $\mathbf{E} = -\nabla \Psi$. Thus,

$$\mathbf{D} = -\epsilon \nabla \Psi \quad (1.12)$$

Plugging this expression in Poisson equation yields,

$$\rho_f = -\nabla \cdot (\epsilon \nabla \Psi) \quad (1.13)$$

Using a mean field approximation, the free charge density can be defined in terms of the mean (volume averaged) ion concentrations n_i

$$\rho_f = \sum_{i=1}^N z_i e n_i \quad (1.14)$$

Therefore, the Poisson-Nernst-Planck equations is written

$$\begin{cases} \frac{\partial n_i}{\partial t} + \mathbf{u} \cdot \nabla n_i - \nabla \cdot \left[D_i^0 \left(\nabla n_i + \frac{z_i e n_i}{k_B T} \nabla \Psi \right) \right] = 0 \\ \rho_f = \sum_{i=1}^N z_i e n_i \end{cases} \quad (1.15)$$

the system has identical number of equations and unknowns.

1.5 Ionic density profile within the PB theory

1.5.1 Poisson-Boltzmann equation

The Poisson equation describes the potential field caused by a given distribution of charges immersed in a dielectric medium:

$$\epsilon \nabla^2 \Psi = -\rho_f \quad (1.16)$$

where $\epsilon = \epsilon_r \epsilon_0$ is the permittivity, Ψ the electric potential and ρ_f the free charge density given by the mobile ions see Eq 1.14. If we consider an electrolyte solution where ion species

are supposed to behave according to Boltzmann statistics, thus, ionic concentration can be expressed as,

$$n_i = n_{i\infty} \exp\left(-\frac{z_i e \Psi}{k_B T}\right) \quad (1.17)$$

where $n_{i\infty}$ is the ionic concentration at the neutral state where $\Psi = 0$. And then plugging Eq. 1.17 in Eq. 1.16 for one-dimension yields,

$$\epsilon \frac{\partial^2 \Psi}{\partial z^2} = - \sum_{i=1}^N z_i e n_{i\infty} \exp\left(-\frac{z_i e \Psi}{k_B T}\right) \quad (1.18)$$

where z is the direction perpendicular to the plans of the slit pore (see Figure 1.3).



Figure 1.3 – Simple scheme that represent the range of the z direction in the slit pore, where $-L/2$ and $L/2$ correspond to the location of the charged surfaces. 0 is the middle of the slit pore.

This is the so-called Poisson-Boltzmann (PB) equation, which gives the configuration of the physical system at equilibrium. If we take the particular case of $N = 1$ (only cations) then the equation becomes,

$$\epsilon \frac{\partial^2 \Psi}{\partial z^2} = -z_+ e n_{+\infty} \exp\left(-\frac{z_+ e \Psi}{k_B T}\right) \quad (1.19)$$

In this case $n_{+\infty}$ will correspond to the concentration of counterions that are inside of the slit pore. Whereas, if we take the case where cations and anions are considered, *i.e.* $N = 2$ then the equation becomes,

$$\epsilon \frac{\partial^2 \Psi}{\partial z^2} = -z_+ e n_{+\infty} \exp\left(-\frac{z_+ e \Psi}{k_B T}\right) - z_- e n_{-\infty} \exp\left(-\frac{z_- e \Psi}{k_B T}\right) \quad (1.20)$$

Contrary to the case with $N = 1$, $n_{+\infty}$ will not correspond to the concentration of coions inside the slit pore, since salt is added in the solvent between the charged surface of the slit pore from a fictitious reservoir. This phenomena is called Donnan effect. As a result, $n_{int} \neq n_{ext}$ where n_{int} and n_{ext} are the concentration of salt inside and outside the pore respectively. However, the relation between n_{int} and n_{ext} can be found by comparing the salt chemical potential inside and outside the pore (*i.e.* $\mu_{ext}^s = \mu_{int}^s$).

Using the expression of the chemical potential of an ion i in the interlayer spacing,

$$\mu_i = \mu_i^0 + k_B T \ln n_i(z) + z_i e \psi(z) \quad (1.21)$$

and

$$\mu_{int}^s = \mu_+^0 + \mu_-^0 + k_B T \ln n_{+\infty} n_{-\infty}. \quad (1.22)$$

In the aqueous solution

$$\mu_{ext}^s = \mu_+^0 + \mu_-^0 + 2k_B T \ln n_{ext} \quad (1.23)$$

Thus, the chemical equilibrium implies $n_{+\infty}n_{-\infty} = n_{ext}^2$ as ψ is defined within an additive constant, we can choose^[15] $n_{+\infty} = n_{ext}$, therefore $n_{-\infty} = n_{ext}$. This choice allows then to modify the Poisson Boltzmann equation according to

$$\frac{d^2\Psi}{dz^2} = \frac{\kappa_{ext}^2}{z} \sinh(z\Psi) \quad (1.24)$$

where $\kappa_{ext}^2 = \sqrt{8\pi l_B z^2 n_{ext}}$. Solving this equation we were able to compute n_{int} as a function of n_{ext} . Hence, if the external concentration is known, the ionic distribution can be determined.

In the following, we will focus our attention in the development of two particular cases: The first is the no salt case, which means that only counterions of the charge surface are taken into account. Whereas, the second is the case with salt, which is the case where both counterions and co-ions are considered.

1.5.2 Case without added salt

First, we consider the particular case of only one specie of ions in the slit pore, the counterion, *i.e.* the case without salt. Then, PB can be read as,

$$\epsilon \frac{\partial^2\Psi}{\partial z^2} = -z_+ e n_{+\infty} \exp\left(-\frac{z_+ e\Psi}{k_B T}\right) \quad (1.25)$$

To conserve electroneutrality in this case: $\int_{-L/2}^{L/2} z_+ e n_+ dV = -2\sigma_{wall} L_x L_y$, with L_x and L_y the dimension of the charged surfaces in the x and y directions, *i.e.* it is assumed that there are only counterions to balance the surface charge σ_{wall} .

Then, substituting $\psi = -z_+ e\Psi/k_B T$ (ψ describes the strength of electrostatic energy compared to thermal energy, thus a dimensionless quantity) leads to:

$$\frac{\partial^2\psi}{\partial z^2} = \frac{z_+^2 e^2 n_{+\infty}}{\epsilon k_B T} \exp(\psi) \quad (1.26)$$

Since the Bjerrum length is defined as $l_b = \frac{e^2}{4\pi\epsilon k_B T}$, thus

$$\frac{\partial^2\psi}{\partial z^2} = 4\pi l_B z_+^2 n_{+\infty} \exp(\psi) \quad (1.27)$$

This equation can be solved analytically using the boundary conditions

$$\left. \frac{\partial\psi}{\partial z} \right|_{z=L/2} = \frac{\sigma_{wall}}{\epsilon} \frac{z_+ e}{k_B T} = 4\pi z_+ \sigma'_{wall} l_B \quad (1.28)$$

$$\left. \frac{\partial\psi}{\partial z} \right|_{z=0} = 0 \quad (1.29)$$

Eq. 1.28 is directly derived from $\left. \frac{\partial\Psi}{\partial z} \right|_{z=L/2} = -\frac{\sigma_{wall}}{\epsilon}$ using the definition of ψ . Indeed, this boundary condition considers the surface charge in the walls, *i.e.* at $z = \pm L/2$. Furthermore, in the last equality $\sigma'_{wall} e = \sigma_{wall}$, the number density of charges was introduced. Whereas

in Eq. 1.29, the boundary condition accounts for a center line which is free of any electric field, thus the force on any ion, which is located exactly at the center line is zero, as required by symmetry. That is the reason why this condition is with $z = 0$, which corresponds to the channel center. Multiplying both sides by $\partial\psi/\partial z$ results in:

$$\frac{\partial\psi}{\partial z} \frac{\partial^2\psi}{\partial z^2} = 4\pi l_B z_+^2 n_{+\infty} \frac{\partial\psi}{\partial z} \exp(\psi) \quad (1.30)$$

$$\frac{1}{2} \frac{\partial}{\partial z} \left[\left(\frac{\partial\psi}{\partial z} \right)^2 \right] = 4\pi l_B z_+^2 n_{+\infty} \frac{\partial}{\partial z} [\exp(\psi)] \quad (1.31)$$

Integrating this equation results in:

$$\frac{1}{2} \left(\frac{\partial\psi}{\partial z} \right)^2 = 4\pi l_B z_+^2 n_{+\infty} (\exp \psi - A) \quad (1.32)$$

$$\frac{\partial\psi}{\partial z} = \sqrt{8\pi l_B z_+^2 n_{+\infty} (\exp \psi - A)} \quad (1.33)$$

Here, A is an integration constant. Integrating Eq. 1.33 yields:

$$\frac{\partial\psi}{\sqrt{\exp(\psi) - A}} = \sqrt{8\pi l_B z_+^2 n_{+\infty}} \partial z \quad (1.34)$$

$$2 \frac{\tan^{-1} \sqrt{\frac{\exp(\psi)}{A} - 1}}{\sqrt{A}} = \sqrt{8\pi l_B z_+^2 n_{+\infty}} z + B \quad (1.35)$$

$$\sqrt{\frac{\exp \psi}{A} - 1} = \tan \left(\sqrt{2\pi l_B z_+^2 n_{+\infty}} Az + \frac{B\sqrt{A}}{2} \right) \quad (1.36)$$

$$\exp(\psi) = A \left(\tan^2 \left(\alpha z + \frac{C}{2} \right) + 1 \right) = A \left(\frac{\sin^2 \left(\alpha z + \frac{C}{2} \right)}{\cos^2 \left(\alpha z + \frac{C}{2} \right)} + 1 \right) = \frac{A}{\cos^2 \left(\alpha z + \frac{C}{2} \right)} \quad (1.37)$$

$$\psi = -2 \ln \left(\cos \left(\alpha z + \frac{C}{2} \right) \right) + \ln A \quad (1.38)$$

$$\psi = 2 \frac{k_B T}{q_i} \left[\ln \left(\cos \left(\alpha z + \frac{C}{2} \right) \right) + \ln A \right] \quad (1.39)$$

Here, B is another integration constant resulting from the integration of Eq. 1.33. α and C represent combination of various integration (and normalization) constants $\alpha = \sqrt{2\pi l_B z_i^2 n_{+\infty}} A$ with a dimension of 1-over-length, as $n_{+\infty}$ has a dimension of $1/\text{length}^3$ times the Bjerrum length. Furthermore, C is dimensionless as A and B are dimensionless.

Here, we have three constants, and two boundary conditions, leaving A as integration constant undetermined. A symbolizes an arbitrary, but constant shift in the potential/meanfield electrostatic energy compared to thermal energy with no influence on $\frac{\partial\psi}{\partial z}$. To determine the

integration constant C and α , one goes back to the boundary conditions in Eq. 1.28 and Eq. 1.29.

$$\frac{\partial \Psi}{\partial z} = 2\alpha \tan(\alpha z + C/2) \quad (1.40)$$

$$\left. \frac{\partial \Psi}{\partial z} \right|_{z=0} = 0 = 2\alpha \tan(0 + C/2) \rightarrow C = 0 \quad (1.41)$$

$$\left. \frac{\partial \Psi}{\partial z} \right|_{z=L/2} = 4\pi\sigma'_{wall} z_+ l_B = 2\alpha \tan(\alpha z) \quad (1.42)$$

Setting $C = 0$ satisfies the boundary condition of Eq. 1.29, leaving us with 1.28, which is solved iteratively using equation Eq. 1.42. Finally, we can derive the final expression for the electric potential is,

$$\Psi(z) = 2 \ln [\cos(\alpha z)] \quad (1.43)$$

Given that,

$$\frac{\partial^2 \Psi}{\partial z^2} = -\frac{z_+ e n_+}{\epsilon} \quad (1.44)$$

$$\frac{\partial^2 \psi}{\partial z^2} = -\frac{z_+^2 e^2 n_+}{\epsilon k_B T} \quad (1.45)$$

Then,

$$n_+ = \frac{\epsilon k_B T}{z_+^2 e^2 n_+} \frac{\partial^2 \psi}{\partial z^2} \quad (1.46)$$

$$n_+ = \frac{2\epsilon k_B T}{z_+^2 e^2 n_+} \frac{\alpha^2}{\cos^2(\alpha z)} \quad (1.47)$$

$$n_+ = \frac{\alpha^2}{2\pi l_B z_+^2} \frac{1}{\cos^2(\alpha z)}$$

1.5.3 Case with added salt

In the special case where the electrostatic potential is small, say, $\Psi \ll 0.025V$, the term $z_i e \Psi / k_B T$ is smaller than unity, and then it is possible to approximate the exponential of the Eq. 1.18 using Taylor expansion as $\exp(X) \simeq 1 + X$. Then, the linearisation of the Poisson-Boltzmann equation is given by,

$$\epsilon \frac{\partial^2 \Psi}{\partial z^2} = -\sum_{i=1}^N z_i e n_{i\infty} \left(1 - \frac{z_i e \Psi}{k_B T} \right) \quad (1.48)$$

Then, if we re-write the equation in terms of cations and anions,

$$\begin{aligned}\epsilon \frac{\partial^2 \Psi}{\partial z^2} &= -z_+ e n_{+\infty} \left(1 - \frac{z_+ e \Psi}{k_B T}\right) - z_- e n_{-\infty} \left(1 - \frac{z_- e \Psi}{k_B T}\right) \\ &= -z_+ e n_{+\infty} + \frac{z_+^2 e^2 \Psi}{k_B T} n_{+\infty} - z_- e n_{-\infty} + \frac{z_-^2 e^2 \Psi}{k_B T} n_{-\infty}\end{aligned}\quad (1.49)$$

Because of electroneutrality condition

$$z_+ n_{+\infty} = z_- n_{-\infty} \quad (1.50)$$

In what follows we will have in any case $z_+ = -z_-$ so that

$$\epsilon \frac{\partial^2 \Psi}{\partial z^2} = \frac{z_+^2 e^2 \Psi}{k_B T} (n_{+\infty} + n_{-\infty}) \quad (1.51)$$

Hence,

$$\frac{\partial^2 \Psi}{\partial z^2} = \kappa^2 \Psi \quad (1.52)$$

The solution for the Eq. 1.52 is,

$$\Psi = A \exp(\kappa z) + B \exp(-\kappa z) \quad (1.53)$$

Given the following boundary conditions,

$$\begin{aligned}\frac{\partial \Psi}{\partial z} \Big|_{z=L/2} &= - \frac{\partial \Psi}{\partial z} \Big|_{z=-L/2} = \frac{\sigma_{wall}}{\epsilon} \\ \frac{\partial \Psi}{\partial z} \Big|_{z=0} &= 0\end{aligned}\quad (1.54)$$

where σ_{wall} is the surface charge on the walls. Now, taking the first derivative of Ψ ,

$$\frac{\partial \Psi}{\partial z} = A \kappa \exp(\kappa z) - B \kappa \exp(-\kappa z) \quad (1.55)$$

and applying the second boundary condition gives,

$$A = B \quad (1.56)$$

Then, if we now apply the first boundary condition, taking into account that Bjerrum length

is defined as $l_B = e^2/(4\pi\epsilon k_B T)$,

$$\begin{aligned}
 A\kappa \exp\left(\frac{\kappa L}{2}\right) - B\kappa \exp\left(-\frac{\kappa L}{2}\right) &= \frac{4\pi l_B k_B T \sigma_{wall}}{e^2} \\
 \Leftrightarrow A &= \frac{4\pi l_B k_B T \sigma_{wall}}{e^2 \kappa \exp\left(\frac{\kappa L}{2}\right)} + B \exp\left(\frac{-2\kappa L}{2}\right) \\
 \Rightarrow A - A \exp\left(\frac{-2\kappa L}{2}\right) &= \frac{4\pi l_B k_B T \sigma_{wall}}{e^2 \kappa \exp\left(\frac{\kappa L}{2}\right)} \\
 \Leftrightarrow A &= \frac{4\pi l_B k_B T \sigma_{wall}}{e^2 \kappa \left[\exp\left(\frac{\kappa L}{2}\right) - \exp\left(\frac{-\kappa L}{2}\right)\right]} \\
 &\Leftrightarrow A = \frac{4\pi l_B k_B T \sigma_{wall}}{2e^2 \kappa \sinh\left(\frac{\kappa L}{2}\right)}
 \end{aligned} \tag{1.57}$$

Therefore, Eq. 1.53 becomes,

$$\begin{aligned}
 \Psi &= A \exp(\kappa z) + A \exp(-\kappa z) \\
 &= A[\exp(\kappa z) + \exp(-\kappa z)] \\
 &= 2A \cosh(\kappa z)
 \end{aligned} \tag{1.58}$$

Thus,

$$\Psi = \frac{4\pi l_B k_B T \sigma_{wall}}{e^2 \kappa \sinh\left(\frac{\kappa L}{2}\right)} \cosh(\kappa z) \tag{1.59}$$

Let's now compute the ionic concentration. We know,

$$n_i = n_{i\infty} \exp(-\psi) \tag{1.60}$$

given that

$$\psi = \frac{z_i e \Psi}{k_B T} \tag{1.61}$$

Rearranging Eq. ?? yields,

$$n_{+\infty} = \frac{\kappa^2 \epsilon k_B T}{2z_+^2 e^2} \tag{1.62}$$

Then, using the definition of the Bjerrum length, we may write,

$$n_{+\infty} = \frac{\kappa^2}{8\pi l_B z_+^2} \tag{1.63}$$

Thus,

$$n_+ = \frac{\kappa^2}{8\pi l_B z_+^2} \exp(-\psi) \tag{1.64}$$

Linearisation via Taylor expansion gives for cations,

$$\exp(-\psi) \simeq 1 - \psi \tag{1.65}$$

and for anions,

$$\exp(\psi) \simeq 1 + \psi \quad (1.66)$$

Therefore,

$$n_{\pm} = \frac{\kappa^2}{8\pi l_B z_{\pm}^2} \left(1 \mp \frac{4\pi l_B k_B T \sigma_{wall}}{e^2 \kappa \sinh(\frac{\kappa L}{2})} \cosh(\kappa z) \right)$$

Actually, in the general case of any value of the electrostatic potential, the PB equation can be solved numerically. As mentioned earlier the Debye length should be calculated taking into account the Donnan effect, *i.e.* the fact that the system is in equilibrium with the reservoir of salt at the concentration c_{ext} . To solve the Poisson-Boltzmann equation in a self-consistent way, we have used a code developed previously in the laboratory by Jean-François Dûfreche that allowed us to compute: first, the external concentration of the reservoir that leads to the correct internal concentration in the pore (the one computed by simulations), and second the ionic density profiles.

1.6 Electro-osmotic flow

Electro-osmotic flow (EOF) is a phenomenon induced by an external applied electric field tangential to a charged solid-fluid interface, which leads to the motion of a liquid across a porous material. It was first reported in 1809 by F.Reuss in Ref 1, who showed that water could flow through a plug of clay by applying an electric voltage. This is because clay is composed of closely packed charged aluminosilicate particles. Thus, water can then flow through the narrow spaces between these particles. More generally, any combination of an electrolyte confined by charged walls would generate electro-osmotic flows under an external electric field.

Such flow is caused by the Coulomb force induced by an electric field on net mobile electric charge in a solution. Because the chemical equilibrium between a solid surface and an electrolyte solution typically leads to the interface acquiring a net fixed electrical charge, a layer of mobile ions, known as an electrical double layer or Debye layer, forms in the region near the interface. When an electric field is applied to the fluid (usually via electrodes placed at inlets and outlets), the net charge in the electric double layer is moved by the resulting Coulomb force. The resulting flow is called electroosmotic flow.

When the fluid motion is governed by the the Navier-Stokes (NS) equation, *i.e.*

$$\rho \left(\frac{\partial \mathbf{u}}{\partial t} + \mathbf{u} \cdot \nabla \mathbf{u} \right) = -\nabla p + \eta \nabla^2 \mathbf{u} - \varepsilon_0 \varepsilon_f \nabla^2 \Psi \mathbf{E} \quad (1.67)$$

where ρ , \mathbf{u} and η denote the density, velocity and pressure of the fluid respectively. If we consider the incompressibility condition, *i.e.*,

$$\nabla \cdot \mathbf{u} = 0 \quad (1.68)$$

Assuming the external applied electric field to be much weaker than the one induced by the surface charge of the solid surface, one can consider that the ionic concentrations near the walls are not affected by the external electric field and thus the induced EOF.

When the EOF is fully developed, *i.e.* $d\mathbf{u}/dt = 0$, with no external pressure gradient across the charged surface and in the limit of low Reynolds number ($\Rightarrow (\mathbf{u} \cdot \nabla)\mathbf{u} = \mathbf{0}$) Eq. 1.67 and 1.68 may be simply written as,

$$\eta \frac{d^2 u}{dy^2} = \varepsilon_0 \varepsilon_f \frac{d^2 \Psi}{dy^2} E_x . \quad (1.69)$$

Integration yields

$$u(z) = \frac{\epsilon}{\eta} E_x \Psi(z) + Az + B \quad (1.70)$$

where A and B are constants to be determined and Ψ is given by Eq 1.59 and Eq 1.43, depending on whether salt is inserted or not.

The EDL thickness is of the order of nanometers, which is much smaller than the characteristic length of microfluidic devices. The EOF velocity profile in a microchannel is almost uniform and is referred to a “plug-like flow”. Therefore, one can use the constant velocity to describe the EOF velocity outside the EDL, which is known as the Smoluchowski slip velocity. In the presence of salt and under the low potential assumption (*i.e.* Debye-Hückel regime) the boundary conditions read:

- $u(z = \pm L/2) = 0$
- $\Psi(z = \pm L/2) = -\frac{4\pi l_B \sigma_{wall}}{\kappa} \tanh(\kappa L/2)$

and the solution for the velocity profile is given by:

$$u(z) = u_{max} [\cosh(\kappa z) - 1] \quad (1.71)$$

where

$$u_{max} = \frac{e E_x \sigma_{wall}}{\eta \kappa \sinh(\kappa L/2)} \quad (1.72)$$

On the other hand, when no salt is added the exact solution of the non-linear problem the solution reads:

$$u(z) = u_{ref} \ln \left[\cos \left(\frac{\alpha z}{\alpha L/2} \right) \right] \quad (1.73)$$

where

$$u_{ref} = \frac{e E_x}{2\pi \eta l_B} \quad (1.74)$$

Another way to express the velocity profile is to consider the particular case of the NS equation in steady state, for small Reynolds numbers. The expression then reduces to,

$$\eta \nabla^2 \mathbf{u} + \mathbf{F}_v = 0 \quad (1.75)$$

where \mathbf{u} is the fluid velocity, η its viscosity and \mathbf{F}_v the volumetric force acting on it. Then, in the electro-osmosis, the volumetric force \mathbf{F}_v enters the Stokes equation to balance the viscous stress arising from an applied electric field $\mathbf{E} = E_x \mathbf{e}_x$ along the surfaces, *i.e.*

$$\mathbf{F}_v = (n_+(z) - n_-(z)) e \mathbf{E} \quad (1.76)$$

where $n_{\pm}(z)$ is the local counterion/co-ion concentration. Thus, the solution for the velocity profile $u(z)$ in the laminar regime can also be found in terms of the local counterion concentration. To do so, we substitute Eq 1.76 into Eq 1.75 and solve the equation, which leads to

$$u(z) = u(L_{hyd}/2) - \frac{eE}{\eta} \int_{L_{hyd}/2}^z \int_0^{z'} (n_+(z) - n_-(z)) dz'' dz' \quad (1.77)$$

where $u(L_{hyd}/2)$ is determined by the boundary conditions. The ionic density profile can be determined either from a simulation or from a continuous theory such as the Poisson-Boltzmann equation.

1.7 Surface Conductivity

When an external electric field is applied on a medium containing charged particles, an electric current is created and can be described by using Ohm's law, given by:

$$\mathbf{J} = \sigma \mathbf{E} \quad (1.78)$$

where \mathbf{J} is the current density and \mathbf{E} the electric field at a given location in the medium, whereas σ is a material dependent parameter known as electric conductivity. Then, this parameter will be influenced by the movement of the charged particles, which in turn will depend on the characteristics of the medium.

When this phenomenon occurs along an interface, a phenomenon called surface conductivity arises. It consists in the excess conduction that takes place in dispersed systems due to the presence of electric double layers. This phenomenon can be visualized in Fig 1.4. In this figure, it is assumed that the double layer consists of two parts, a Stern layer or non-diffusive part, containing immobile cations (counterions in this case) and a diffuse part, containing both types of ions (*i.e.* counterions and co-ions). The border between the Stern and the diffuse part is assumed to be identical to the slip plane (dashed line), although in more general situations these assumptions are not necessarily valid. Thus, surface conduction is due to the migration of excess charges in the interface^[14]. And it can be deduced that it has three contributions:

- The electro-osmotic flow, which induces an electric flow (movement of ions)
- The counterions, in from the reference frame of the solvent move as a result of the attraction with co-ions.
- The co-ions, in from the reference frame of the solvent move as a result of the attraction with counterions.

Then, independently of the charge distribution, $\sigma_{surface}$ (surface conductivity) can always be defined through the two-dimensional Ohm's law,

$$\mathbf{J}^{\sigma} = \sigma_{surface} \mathbf{E} \quad (1.79)$$

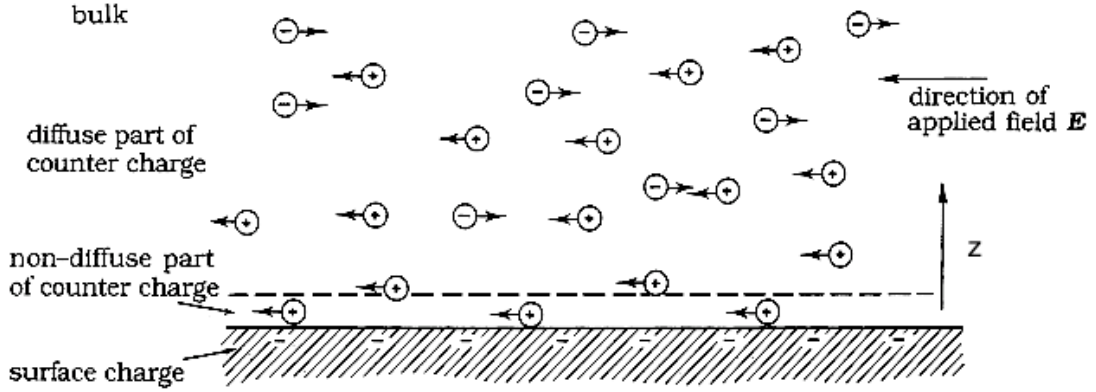


Figure 1.4 – Visualization of surface conduction, where the dashed line represents the slip plane^[14].

where \mathbf{J}^σ and \mathbf{E} are the surface current density and the applied tangential electric field, at a given location in the medium.

As $\sigma_{surface}$ reflects the distribution of charges and their mobilities in the double layer, this quantity contains relevant double layer information, particularly regarding its dynamic properties. Thus, its study is important to answer questions such as how far mobile ions are beyond or within the slip plane, or, for that matter, what the slip process really means physically.

Although phenomenologically surface conduction is treated as if taking place in a plane, in reality the conducting layer will have a certain thickness. The excess conduction depends on z (the distance away from the surface charge). At large z , it is zero, because the excess is zero, but it changes with decreasing z , depending on local concentrations $n_i(z)$ and local mobilities $M_i(z)$. General experience has suggested that in the diffuse part of the double layer $M_i(z) = M_i(\infty) = M_i(bulk)$. Regarding the situation in the inner layer, the position is less certain, but there are many indications that in several cases bound ions can move tangentially.

The computation of the surface conductivity can be partially done through some models, as for example with the Bikerman formula^[10]. In this work, the surface conductivity is obtained in the diffuse double layer outside the plane of shear. Thus, since this is not precisely $\sigma_{surface}$, we will note this quantity $\sigma_{surface}^d$. In order to compute it, it is necessary to recognize that the conductivity in this region consists of two parts: a migration contribution, caused by the movement of charges with respect to the liquid; and a convective contribution, due to the electro-osmotic liquid flow beyond the shear plane, which gives rise to an additional mobility of the charges and hence leads to an extra contribution to $\sigma_{surface}^d$. Then Bikerman equation reads^[10] :

$$\sigma_{surface}^d = \frac{2e^2 N_A z^2 n}{k_B T \kappa} \left[D_+ (\exp(-ze\zeta/2k_B T) - 1) \left(1 + \frac{3M_+}{z^2} \right) + D_- (\exp(-ze\zeta/2k_B T) - 1) \left(1 + \frac{3M_-}{z^2} \right) \right] \quad (1.80)$$

where n is the electrolyte amount concentration, N_A is the Avogadro constant, D_{pm} are the

ionic diffusion coefficients and M_{\pm} is the dimensionless mobility of the cations and anions respectively given by,

$$M_{\pm} = \frac{2}{3} \left(\frac{k_B T}{e} \right)^2 \frac{\epsilon_r \epsilon_0}{\eta D_{\pm}} \quad (1.81)$$

Bikerman equation expresses $\sigma_{surface}^d$ as a function of the electrolyte and double-layer parameters considering a symmetrical z-z electrolyte^[16]. In Eq 1.80, the first part of the equation for both species *i.e.* $D_{\pm}(\exp(-ze\zeta/2k_B T) - 1)$ corresponds to the migration term, whereas the second part for both species *i.e.* $D_{\pm}(\exp(-ze\zeta/2k_B T) - 1)(\frac{3M_{\pm}}{z^2})$ is related to the convection term. In order to get $\sigma_{surface}^d$ it is necessary to have the value of the ζ -potential, which can be problematic as explained in Sec 1.3. Thus, another method to compute surface conductivity is needed. If the velocity profiles of ions as a function of their distance to the charged surfaces is known, the surface conductivity can be predicted in principle.

1.8 Limit of PNP theory

The theory developed in this section, called Poisson-Nerst-Planck is usually adopted in the study of electrokinetic phenomena. Indeed plenty of work were carried out^[17-21], ranging from the study of ion transport in different geometries, ion permeation to transport phenomena of polarizable molecules in multi-component systems, among others. Thus, PNP theory has proven to be an efficient tool, bringing with it good approximative results. Nonetheless, it is important to recall that this theory makes some assumptions such as:

- Solvent is a structureless dielectric continuum carrying a uniform dielectric permittivity.
- Ions are point-like charges.
- Ion-ion correlations are neglected. In particular, the mobilities of ions are those of an ideal solution (see Eq. 1.15), *i.e.* at infinite dilution.
- Charges on the surface are smeared out to give a uniform surface charge density

Therefore, in the study of a specific system, it is important to keep in mind the limitation that this theory has in order to reproduce the system. In particular, we are interested in the study of dynamic properties of ions in charge slit pores in this thesis. Therefore, the use of PNP theory seems to be a good way to tackle the problem. However, since in dynamics the correlation among ions are important to characterize the system, we are wondering if Poisson-Nerst-Planck theory can predict the non ideal case of the dynamics of the ions.

Simulation Method

Contents

2.1	Choice of the simulation method	23
2.1.1	Microscopic approach	23
2.1.2	Mesoscopic approach	24
2.1.3	Multiparticle Collision Dynamics	27
2.2	Simulation of a pure MPCD fluid	28
2.2.1	Algorithm	28
2.2.2	MPCD parameters	29
2.2.3	Viscosity of the MPCD fluid	30
2.2.4	Fluid-solid boundary conditions for multiparticle collision dynamics	31
2.2.5	Simulation of the flow of a fluid in a porous medium	34
2.3	Simulation of embedded solute particles in a MPCD bath	35
2.3.1	Verlet algorithm for interacting solutes	35
2.3.2	Interactions between embedded particles	36
2.3.3	Coupling between solute and MPCD fluid	37
2.3.3.1	MPCD - Central force coupling	37
2.3.3.2	MPCD-CC	38
2.4	Computation of the transport coefficients of solute particles	39
2.4.1	Diffusion coefficient	39
2.4.2	Determination of the diffusion coefficient of a solute at infinite dilution . .	40
2.4.3	Electrical conductivity	42

The search of a deeper understanding of fluids phenomena at smaller scales led to the development of a completely new field called nanofluidics^[22], which looks at fluids confined at the nanometer scale. Since then, these phenomena were used for different technological applications, such as ion enrichment^[23], nanofluidic transistors or the recently proposed nanofluidic diodes^[24,25].

In particular, the creation of new instruments and techniques at the nanometer scale gave the possibility to manipulate confined fluids ranging from 1 – 100 *nm* and to push the experimental measurements beyond the current state of art. Among these techniques we find new electrical detection techniques, Surface Force Apparatus (SFA), Atomic Force Microscopy (AFM), Nano-particle Image Velocimetry (nano-PIV) coupling PIV to TIRF set-up (Total Internal Reflection Fluorescence)^[26]. Although experimental research has improved a lot in this area, it is still limited by the available detection tools, which cannot capture all the physical phenomena happening at this dimension^[27]. This is the reason why computational techniques are useful in order to observe and overpass the limitations of experimental apparatuses at a lower cost.

Nowadays, there exists plenty of different numerical algorithms^[28,29] which treat a variety of systems at a wide range of scales. However, a successful study on a particular system is directly related to a wise choice of the method of simulation. Thus, depending on the size of the system and on the type of phenomenon we are interested in, one would privilege a method rather than another. In this chapter, we shall describe and justify the choice of the method of simulation picked for our study. In order to do so, we present the different methods of simulation (Section 2.1), underlying the pros and cons of each one of them. Furthermore, in section 2.2 and section 2.3 we describe the theory and implementation of our method for the fluid and solute particles respectively. Finally at Section 2.4 it is illustrated how the transport coefficients were obtained through the treatment of the information got by the chosen simulation method.

In this thesis, we will focus mainly in modelling solutes, which may be confined between walls possibly charged. Taking a simplistic approach, one can visualise confined solutions as made of three distinct parts, which need to be coupled together: a solvent (*e.g.* water), a solute (*e.g.* ions or polymers) and boundaries (*e.g.* solid walls). Then, it is possible to classify the algorithms in two categories: the first takes into consideration the solvent at the granular level, meaning that each solvent particle is explicit whilst the second treats the solvent as a continuum. Depending on the choice made, the boundaries may or may not be explicit.

2.1 Choice of the simulation method

2.1.1 Microscopic approach

The study of atomistic phenomena involves simulation methods such as Monte Carlo (MC) or Molecular Dynamics^[30]. The former makes use of a series of microscopic states which are generated through stochastic laws. Because MC does not use equations of motion, it cannot include the concept of explicit time, and thus it is merely a simulation technique for phenomena in thermodynamical equilibrium. This is why, if one is interested in modelling the transient regime (*i.e.* dynamics), and thus wishes to study the physical movements of atoms and molecules, the Molecular Dynamics (MD) method can be chosen. More specifically, atoms and molecules interact for a fixed period of time, giving a view of the dynamic evolution of the system. The forces acting upon atoms are described using interatomic potentials, also called "force fields". Although a correct microscopic description is achieved by this method, some limitations are present. Indeed, the number of particles, time step, and total time duration must be carefully selected, in a way that the calculation can finish in a reasonable CPU time. Nonetheless, this time should allow the simulation to describe the relevant time scales of the process studied. Another source of problems can be found in the boundary conditions, in that sense, the box size must be large enough to avoid periodic boundary condition artefacts. Considering all the previous limitations, it can be deduced that this method is computationally expensive for the kind of systems we are interested in. If one is interested in an electrolyte solution confined between walls distant from about 10 *nm*, the number of atoms that constitute the solid, the solvent and ions is huge. Then, it should only be used if we are looking at the physics taking place at the microscopic (*i.e.* molecular) level for a short time. Nevertheless, both MC and MD methods were used to analyse electro-osmotic

effects^[31–33] at the atomic scale, for relatively small systems. One objective of these studies was to make a link with descriptions at a larger scale, or with coarse-grained descriptions of the same systems.

2.1.2 Mesoscopic approach

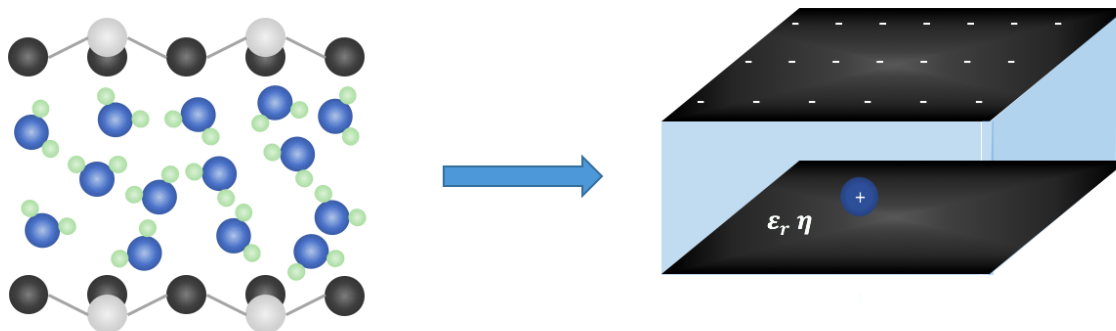


Figure 2.1 – From the microscopic model (left) to the mesoscopic model (right) where the solvent molecules are described as a dielectric and viscous continuum.

Marry *et al.*^[34] made a comparison between atomistic and mesoscopic simulations studying electro-osmotic phenomena at steady state and during the transient regime. They observed that the mesoscopic ionic concentration profiles obtained at equilibrium are in agreement with MD results, even though most mesoscopic models are unable to reproduce the oscillations arising from the molecular size of the solvent. On the other hand, the induced electro-osmotic flow (as obtained with the mesoscopic model) was found to be in good agreement with the Poisson-Nernst-Planck equation during the transient regime. They concluded that atomistic methods are not essential for this type of study and that the choice of mesoscopic methods presents a major computational cost advantage, without losing relevant physics.

Mesoscopic simulations that treat the system at a coarse-grained scale, have been developed since 1970 (see Fig. 2.1) to bridge the gap between atomistic simulations and the real macroscopic world, and to overcome the inherent difficulties faced by conventional methods when applied to complex fluid systems. Thus, the main idea consists in replacing the solvent molecules by a continuous medium or by a granular solvent in order to fasten the calculations. However, the dynamics of complex fluids such as colloidal or polymer suspensions, biological macromolecules, membranes, to mention only a few, is often governed by the hydrodynamic behaviour of the solvent. Moreover, as the dynamics of solutes in a solution drives many properties such as thermal or electrical conductivity to the rate of chemical reactions, then it is important that for the study of such systems a proper inclusion of the solvent dynamics is carried out. Then, coupling between the solvent and the solute is necessary in order to take into consideration thermal fluctuations and hydrodynamic interactions^[35] between solute particles. In other words, the motion of the solvent is directly linked to the interaction with the solute thereby influencing the dynamical properties of the system. To do so, most transport theories rely on a description of hydrodynamic interactions derived from the Stokes equation of fluid dynamics at low Reynolds numbers. For example, the Fuoss-Onsager theory

of electrolyte transport^[36,37] and the classical theories of polymer transport^[38–40] both include hydrodynamics using the Oseen tensor. Indeed, this tensor can be derived by evaluating the effect of a force applied on a fixed point of the fluid described by the Stokes equation. However, this modelling is limited since the size and shape of the particles have no explicit influence on hydrodynamic interactions. That is the reason why other numerical alternatives were created to overcome this constraints. As a result, a variety of mesoscopic methods came out, among them: lattice gas automata LGA^[41], lattice Boltzmann LB^[42], smoothed-particle hydrodynamics SPH^[43,44], dissipative particle dynamics DPD^[45], direct simulation Monte Carlo DSMC^[46], fluid particle dynamics^[47], and others^[48]. Indeed, the basic goal of all these approaches is very similar: to obtain hydrodynamic behaviour on length scales much larger than the atomic scale. Mass and momentum conservation are the essential ingredients to obtain the correct hydrodynamic behaviour, whereas the detailed interactions and dynamics of the solvent molecules are not important. Therefore, the dynamics on the microscopic scale can be strongly simplified, as long as the conservation laws are strictly satisfied. Then, in order to choose the correct method of simulations, we look at the differences between them.

For instance, Ermak and Mc Cammon created Brownian Dynamics (BD)^[49], which is an efficient method used to study the dynamics of polymers or colloidal suspensions (*e.g* see Ref. 50). In BD, particles are governed by a random motion, with hydrodynamic interactions between them. One of its advantages is that it accounts for the size effects of the solutes, such as those due to a charge distribution near the interface, which were found to play an important role in induced electro-osmotic flows^[51]. In this simulation technique hydrodynamic interactions are modelled by the Rotne-Prager tensor^[40]. Although BD has been very successful in computing transport coefficients for various systems^[52–56], it still has several major pitfalls. For example, in the case of a highly concentrated systems, the Rotne-Prager tensor can turn to be non positive, preventing the simulation to proceed. Furthermore, when strong attractive interactions between particles exist, random displacements can lead the system to be in regions that should not be realistic to explore, which leads to strong instabilities of the simulation. This kind of difficulties can be partially overcome through the use of Metropolis Adjusted Langevin Algorithm (MALA)^[57]. Moreover, it is very difficult to adapt such simulation strategies to confined solutions for which the use of the Rotne-Prager tensor is no longer valid^[58], so that, BD is restricted to simple geometries^[59,60]. More specifically, this technique faces the main problem that the computational effort scales with the cube of the particle number due to the inversion of matrices. For the purpose of our work, we are interested in both dilute and highly concentrated systems; hence BD is not a suitable choice.

On the other hand, a completely new line of approach for the simulations of fluids was triggered by the discovery of Frisch, Hasslacher and Pomeau^[41] who introduced lattice gas automata (LGA) algorithm. The probability to have a certain velocity direction is propagated from site to site on a regular lattice, while fluid-dynamical models yield the correct Navier-Stokes hydrodynamic behaviour at a coarse-grained scale^[61]. The so-called Lattice-Boltzmann algorithm holds some promise as a practical tool for modelling complex fluid flows, as it is computationally much more efficient than MD. Not only the number of elementary operations per particle and per time step are smaller for LB, but also, and more importantly, the time steps in LB are orders of magnitude larger: in a single LB time step the changes in the relative particle positions are typically comparable to the mean free path of the particles, whereas in MD corresponding changes in local particle configurations usually require hundreds of time

steps. Thanks to the increased computational efficiency, LGA and LB models are well suited to simulate complex fluid systems such as colloidal suspensions^[62] and polymer solutions^[63], electrokinetic phenomena which are characterised by a multiplicity of length scales and which are therefore too computationally intensive to be modelled by MD. The drawback of this method is that ions are not explicitly described so the finite size effects between ions cannot be taken into account.

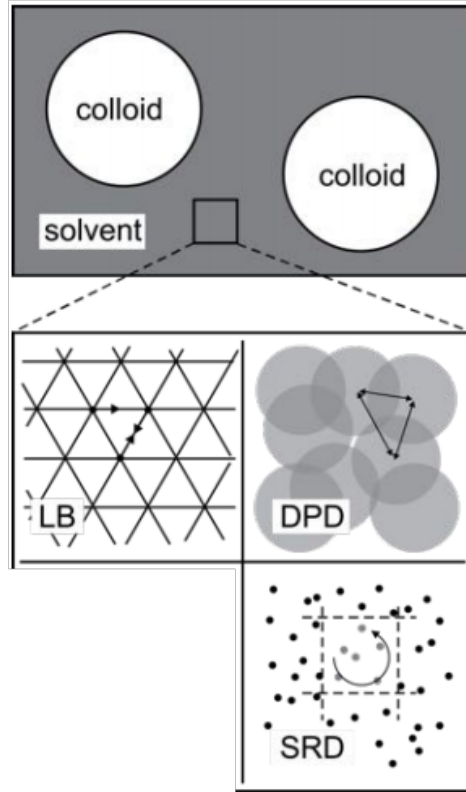


Figure 2.2 – Schematic representation for different methods of simulation (LB,DPD,and MPCD)^[64]

A popular alternative is the Dissipative Particle Dynamics (DPD) introduced by Hoogerbrugge and Koelman in 1992^[45]. DPD is an off-lattice mesoscopic simulation technique^[45] that does not suffer from some of the restrictions imposed by the lattice. This method clusters a number of molecules into a single DPD particle, then each particle interacts with each other, moving together in a Lagrangian fashion, subject to soft repulsive-only potentials^[65]. Specifically, for simple fluids, there are three types of forces acting on each dissipative particle: the first is a purely repulsive conservative force, the second is a dissipative force that reduces velocity differences between the particles, and the third is a stochastic force directed along the lines connecting the particle centers^[61]. The relation between dissipative particle dynamics and hydrodynamics was investigated by Español and by Marsh et al.^{[66],[67]} who showed that the DPD model should obey the Navier-Stokes equation, at least in the limit where the time step tends to zero. As the DPD algorithm satisfies conservation of mass and momentum, it seems likely that the finite time step version will also exhibit the correct hydrodynamic behaviour. Approximate expressions for the transport coefficients of the DPD fluid have only

been derived in the limit that the time step of the discretized equations of motion tends to zero^[67]. The fact that the DPD model reproduces Boltzmann statistics and Navier-Stokes behaviour makes it an attractive numerical tool to simulate complex fluids. Indeed, several authors^{[68], [69]} have already applied the method for this purpose. One drawback of DPD is that in any case the particles that mimic solvent particles interact with each other and with solute particle, which increases the amount of interactions to be computed at each time step.

Another mesoscopic method that relies on an explicit but highly simplified solvent is the multiparticle collision dynamics (MPCD). This is the technique we have chosen in the present work. In MPCD the solvent particles are point-like and interact only during the so-called collision steps where momentum is exchanged between them. This renders the algorithm very efficient. Thus, MPCD is a fluid algorithm which was developed with the purpose of coupling the solute with the solvent^[70], which is the reason why it captures hydrodynamic couplings (in simple and complex fluids), and the thermal fluctuations in various hydrodynamic regimes, always fulfilling a perfect conservation of mass, momentum and energy.

In this thesis, in order to underline the advantages of this method with respect to the analytic study of electro-osmosis, we shall compare the MPCD method with the Poisson Nernst Planck theory, which is often adopted when dealing with electrokinetic effects^[71]. On one hand, ions are assumed to be point-like particles in the PNP model, meaning that the excluded volume effects between ions are not taken into account, whereas MPCD describes ions as individual diffusing particles. On the other hand, PNP considers that the ions mobility is not influenced by electrostatic and hydrodynamic interactions, because the ionic mobility is assumed to be the same as in a solution at infinite dilution. That is why MPCD brings us an alternative way to study this phenomenon.

2.1.3 Multiparticle Collision Dynamics

In 1991 Malevanets and Kapral proposed a simulation method initially called Stochastic Rotation Dynamics (SRD), later renamed Multi-particle collision dynamics (MPCD), as a reference to a larger category of algorithms, resulting from the multiple changes SRD suffered through the years. MPCD proved to be a versatile tool as it is capable to capture hydrodynamic couplings in both simple and complex fluids, for various hydrodynamic regimes, and is not restricted to specific geometries. Collisions between point-like solvent particles occur at fixed discrete time intervals, and although space is discretized into cells, which define the multi-particle collision environment, spatial and velocity coordinates of the particles remain continuous variables. This ensures unconditional numerical stability and has an H-theorem^[70].

MPCD is particularly well suited for (i) studying phenomena where both thermal fluctuations and hydrodynamics are important, (ii) for systems with Reynolds and Péclet numbers of order of 0.1 to 10, (iii) if exact analytical expressions for the transport coefficients and consistent thermodynamics are needed, and (iv) for modeling complex phenomena for which the constitutive relations are not known. Common examples where MPCD was employed are for instance the prediction of the dynamics of colloidal suspensions^[70,72-74] (which includes clustering, sedimentation^[64] and shear flow^[75]) and polymers solutions^[76-79]. Although MPCD is able to address the challenge of the multiple length and time scales involved in electro-kinetic phenomena^[53,80], the method has not been used extensively by the scientific community. During this thesis we will make use of MPCD to study the electro-osmosis phenomenon and the

dynamics of polymers under an electroosmotic flow; in the subsequent sections we will explain the different details related to this method of simulation.

2.2 Simulation of a pure MPCD fluid

2.2.1 Algorithm

In this algorithm, the fluid is represented by point-like particles with $m_f = 1$ (fluid mass), whose positions and velocities evolve in two different steps: the streaming and the collision steps.

The former (*i.e.* streaming step) allows transport of the quantity of fluid material. Position and velocities are propagated integrating Newton's equations of motion, for a time window denoted as Δt_c , which corresponds to the physical time of the displacement between two collision phases. It is important to note that during this step particles do not interact with each other so that they have a ballistic motion. Hence, the position is updated using:

$$r_i(t + \delta t_c) = r_i(t) + v_i(t)\delta t_c \quad (2.1)$$

where r_i , v_i are the position and the velocity of the i -th fluid particle respectively.

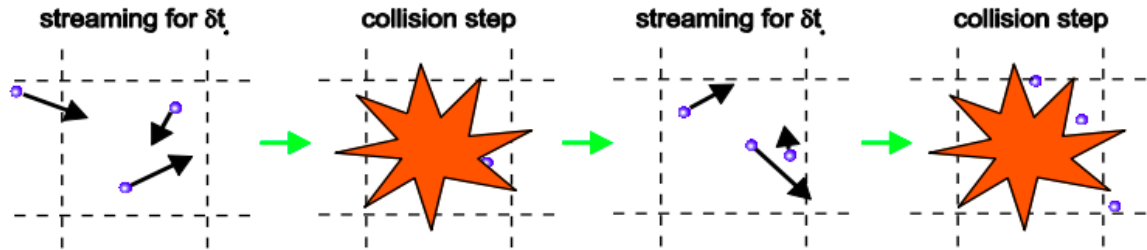


Figure 2.3 – Schematic representation of the MPCD algorithm, that shows how the two steps (streaming and collision) are carried out one after the other at each time step.

On the other hand the collision step (*i.e.* second step) allows exchange of momentum between the particles. The simulation box is divided into cubic cells of size a_0 , where momentum exchanges between the enclosed fluid particles occur. A randomly oriented axis is defined for each collision cell, and the fluid particle velocities relative to the velocity of the cell center of mass are rotated by an angle α around this axis. All particles in the cell follows the same rotation, but the rotations in different cells and at different times remain statistically independent as the axis is randomly oriented. Thus, the rotation angle α is a fixed simulation parameter, common to all rotation cells. In addition, the rotation axis is randomly chosen at each new collision phase and is different in each new cell. With this step the velocity of the cell centre of mass is conserved. Therefore, the velocity is obtained using:

$$v_i(t + \delta t_c) = v_{c.o.m}^{cell}(t) + R_\alpha[v_i(t) - v_{c.o.m}^{cell}(t)] \quad (2.2)$$

where $v_{c.o.m}^{cell}(t)$ is the velocity of the center of mass of the cell, R_α is the rotation matrix and α is the random angle that is fixed in the simulation.

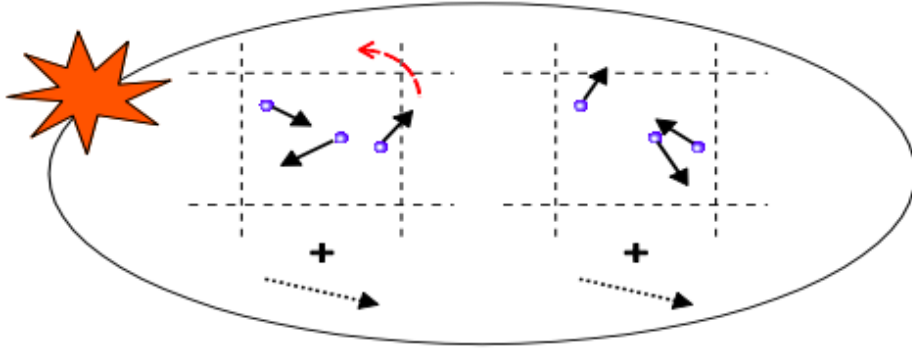


Figure 2.4 – Schematic representation of collision step on MPCD.

However MPCD, was not originally Galilean invariant^[70] meaning that translations are not conserved. This was due to the rigid grid imposed in the collision step. At low temperatures this is particularly evident, because the particles diffuse so slowly that they will be trapped in the same cell, colliding with the same set of particles during many time steps. However, this violates molecular-chaos assumptions (*i.e.*, particles become correlated and retain information of previous collisions) leading to velocity dependent transport coefficients. On the other hand, at high temperatures, this problem does not arise, since the particles diffuse fast enough between different cells and thus collide with different sets of neighbours. This can be solved by restoring Galilean invariance to the method. In order to do so, Ihle and Kroll^[81,82] proposed to perform a random translation of the collision cell at each time step to prevent particles from participating in the same momentum exchange twice. This translation is carried out considering the boundary conditions, before each collision phase, and returning the cell network to its original position after each rotation. In addition to restoring Galilean invariance, this grid-shift procedure accelerates momentum transfer between cells and leads to a collisional contribution to the transport coefficients.

2.2.2 MPCD parameters

A simulation of the MPCD fluid involves the following set of parameters:

1. The time between two collisions is defined as Δt_c and is related to the mean free path λ , which influences many hydrodynamic variables, thereby determining the dynamic regime of the fluid.
2. The angle of rotation α .
3. The numerical density γ corresponds to the number of MPCD fluid particles per cell collision, from which the density of the fluid can be computed using $\rho_f = \frac{\gamma m_f}{a_0^3}$.

Reduced units are computed using a_0 as the unit length, m_f as the unit mass and $k_B T$ is set to one. The characteristic velocity is then the thermal velocity of the fluid particles, $v_0 = \sqrt{k_B T / m_f}$, and $t_0 = a_0 / v_0$ represents the characteristic time. This defines the dimensionless

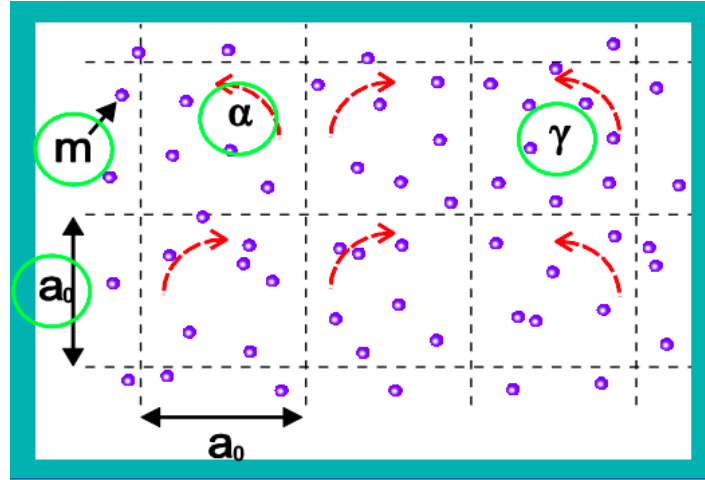


Figure 2.5 – Schematic representation of the parameters that are used in a simulation.

mean free path $\lambda = \frac{\delta t_c}{t_0}$, the characteristic viscosity $\eta_0 = \sqrt{k_B T m_f} / a_0^2$, and the acceleration $g_0 = a_0 / t_0^2$.

Finally the lengths of the box of simulation are given by L_z for the z -direction (in what follows this will be the direction perpendicular to the wall of the slit pore), L_y for the y -direction and L_x for the x -direction, where those parameters are scaled with respect to the cell size a_0 .

2.2.3 Viscosity of the MPCD fluid

The kinematic viscosity demonstrates the ease with which the amount of movement is transferred between the different fluid cells, and is given by $\nu = \eta / \rho$, where η is the dynamic viscosity or absolute viscosity and ρ is the fluid density. Indeed, this quantity has been calculated theoretically^[70,81–83] for a MPCD fluid by means of kinetic theory and its validity has been checked with simulations. As the movement of a MPCD fluid is done by two steps, namely the streaming and collisional steps, the corresponding kinematic viscosity will be formed by these two contributions, *i.e.* the total kinematic viscosity will read $\nu = \nu_{kin} + \nu_{coll}$. Thus, using the kinetic theory of fluids, Kikuchi *et al.*^[72] and Ihle *et al.*^[84] found analytic expressions for both terms.

- Streaming step: also called particle regime happens when short rotation angle and large collision times are considered. In this regime, the kinetic transport is dominant and this is due to the movement of the particles themselves, *i.e.* when a particle moves, it carries a certain amount of the relevant quantities such as momentum and energy. The kinetic contribution due to the kinematic viscosity ν_{kin} is given by particles streaming between collision steps. As the contribution of the momentum arises from particle motion, we expect that $\nu_{kin} / \nu_0 \sim \lambda$. Actually ν_{kin} reads^[70]:

$$\nu_{kin} = \lambda \left[\frac{1}{[4 - 2 \cos \alpha - 2 \cos(2\alpha)]} \frac{5\gamma}{\gamma - 1 + \exp -\gamma} - \frac{1}{2} \right] \quad (2.3)$$

In gases, where $Sc \ll 1$, this contribution dominates because the collision between particles does not happen frequently.

- Collision step: also called collective regime, happens when large rotation angles and small collision times are considered. In this regime, the collisional contribution is dominant and this is due to the transfer of energy and momentum from one particle to another during the collision step. This results in a collisional contribution on the kinematic viscosity ν_{col} . Each collision step distributes momentum among particles in a cell. Since there are $1/\lambda$ collision steps per unit time t_0 , this suggests that the collisional contribution onto the kinetic viscosity should scale as $\nu_{coll}/\nu_0 \sim 1/\lambda$, where ν_{coll} reads^[64]:

$$\nu_{coll} = \frac{1}{\lambda} \frac{(1 - \cos\alpha)}{18} \left(1 - \frac{1}{\gamma} + \frac{\exp^{-\gamma}}{\gamma} \right) \quad (2.4)$$

This contribution dominates in fluids where $Sc \approx 10^2 - 10^3$, since more collisions take place.

From the previous equations we can note that the kinematic viscosity is given in terms of MPCD parameters. The selection of numerical values used in this work will be explained in the following Chapter. Nonetheless, simulations confirm that $\nu = \nu_{kin} + \nu_{coll}$ is very well described by these two contributions over the whole parameter range^[72,81,82]. A comparison of the contributions of η_{coll} and η_{kin} to the total viscosity shows that, as expected, at large mean free paths the kinetic contribution dominates, whereas at small λ the collisional contribution is dominating. Hence, we can conclude that a collisional viscosity significantly larger than the kinetic viscosity is important for the observation of hydrodynamic effects.

2.2.4 Fluid-solid boundary conditions for multiparticle collision dynamics

Since the system that will be studied is confined special attention should be brought upon the fact that interfaces affect strongly fluid flow. Therefore, in order to study our system, it is necessary to examine various methods needed to impose macroscopic fluid-solid boundary condition in MPCD simulation. In general, fluids in contact with a solid phase have a zero normal component of the velocity at the interface, whereas the tangential velocity inherently depends on molecular interactions at the interface. Thus, two options can be considered to simulate this interaction: stick (or no slip boundary condition) and slip boundary conditions. The former implies that the tangential velocity of the fluid relative to that of the boundary vanishes at the interface. The latter means that the tangential velocity of the fluid is unaffected by the presence of the interface. Then, the question is: Which of one these is more adequate? To answer this question, we have to take a look on how real surfaces behave. It is known that most of them satisfy a partial slip condition, meaning that the relative tangential velocity of the fluid is diminished near the surface, but remains nonzero^[61,85]. It is possible then, to have an idea of the amount of slip, to define a hypothetical distance into the surface at which the relative tangential velocity would be zero. For shear flow in the x -direction relative to a

boundary at $z = 0$ we have^[86]

$$\lambda_{slip} = \frac{u_x(0)}{\partial_z u_x(0)} \quad (2.5)$$

Note that for perfect slip boundaries λ_{slip} diverges. The importance of slip in a macroscopic system can be expressed through the effective Knudsen number. The conventional Knudsen number is defined as the ratio between mean free path length and a representative physical length scale of the system, and is useful to quantify the viscous character of a flow. Here we define it as the ratio between slip length and system size

$$Kn = \frac{\lambda_{slip}}{L} \quad (2.6)$$

From this definition and considering the slip length as the distance from the surface at which stick boundary conditions apply, we see that a small Knudsen number implies that stick boundary conditions are a good approximation for the system. In physical systems, slip notably arises from hydrophobicity or surface roughness and often is not evident unless the system size is of the order of microns^[61,85].

Then, to achieve stick boundary conditions in our method, one would need a mechanism to decrease the relative fluid tangential velocity at the wall. To do this, several methods are possible. We shall make a quick review of the main ones available.

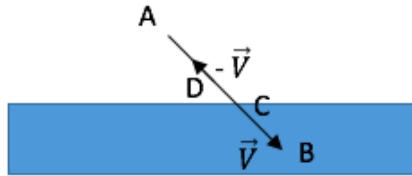


Figure 2.6 – Bounce back condition between fluid particles and the wall

Bounce-back boundary condition (BB), was first proposed for MPCD simulations by Malevanets and Kapral^[70] and functions by controlling the momentum flux at the boundary. As we can see in Fig. 2.6, whenever a fluid particle enters the wall (*i.e.* B position), it is replaced by a particle leaving the wall and entering the fluid (*i.e.* D position), with an opposite direction of the velocity. This process occurs at the end of each streaming step. As a result, the average relative velocity of the fluid near the wall is zero, since the relative velocity distribution of particles reflected from the wall mirrors the corresponding distribution of particles approaching the wall.

If we consider moving boundary conditions, it is necessary to determine a suitable location at which the boundary condition applies. For example, if we consider a colloid as the solid boundary, the contact point between the fluid particle and the colloid depends on the trajectory of both. An easy solution for this is restoring all participating particles to their positions at a one and half Verlet time step earlier, and then repeat this procedure until either no new overlaps occur or a threshold number of iterations is reached.

Stochastic Reflection Rules (SRR) is a method initially proposed by Inoue *t al.*^[87] to simulate a two dimensional suspended solid and later extended to the three-dimensional motion of spherical colloid by Padding *et al*^[88]. In SRR, the point of contact in a fluid-solid

collision is determined in the same manner as in BB, with the exception that the new relative fluid velocities obtained come from a half-space Maxwell-Boltzmann distribution rather than from direct velocity reversals. Thus energy conservation is replaced with the use of a thermostat. In simulations of colloidal diffusion employing stochastic boundary conditions it was found that the autocorrelation functions of the linear and angular velocity were well represented by theoretical predictions for colloids with stick boundary conditions.

Although the last method can be more accurate and thus improve our simulations, it is computationally less efficient. This is due to the calculation of the exact position at which the particle touches the surface. For that reason, bounce-back boundary condition was adopted in our simulations.

Nonetheless, the choice of this method introduces non-physical effects near the wall. These spurious effects can be fixed. Studying the steady Poiseuille flow profile, it was found that the bounce-back rule is not sufficient to guarantee absence of slip at the walls. This problem arises from the intersection of MPCD cells with the wall. Since the cells near the surface are partially occupied by a solid, the number of particles of the fluid in these cells is less than the average γ . It follows with a lower collisional viscosity in boundary cells. To correct this effect, virtual particles are added in these cells during the collision step. To achieve this, the following methods can be used:

- **Method of bulk filling rule (BFR)** It was introduced by Lamura *et.al.*^[89] and consists in adding $(\gamma - n_{cell})$ virtual particles to the cell with Maxwell-Boltzmann distributed velocities. This process is carried out during the collision step of each boundary cell, if and only if this cell has a number of particles n_{cell} less than γ .
- **Symmetrized Bulk Filling Rule (SBR)** As for previous the method we have the same problem due to the larger number of particles in boundary cells with respect to bulk cells. A way to solve it, is to eliminate (for cells with $N_{fluid} > \gamma$) the velocity of the center-of-mass velocity corresponding to $n_{cell} - \gamma$ particles. Meaning, that

$$v'_{cm} = \frac{1}{\gamma} [N_{fluid} v_{cm} - (N_{fluid} - \gamma) v_{MB}] \quad (2.7)$$

where v_{MB} is obtained using the Maxwell-Boltzmann distribution of a particle with mass $(N_{fluid} - \gamma)m_f$.

- **Virtual Particle Condition (VPC)** In this method particles are inserted randomly within the parts of boundary cells that overlap with the solid. The velocity of each pseudo particle is given by the Maxwell-Boltzmann distribution around the velocity of the wall at the particle position. As for other rules involving pseudo particles, their density is equal to the bulk particle density. However, rather than on a cell-wise basis, we choose the total number of pseudo particles according to the total overlap volume of boundary cell with solid regions in the system. This has the benefit that the fluctuations in the number of pseudo particles per cell approximates the cell-wise fluctuation in the bulk particle density. This collision rule allows a natural extension to angular momentum conserving implementation of the MPCD algorithm, since pseudo particles have both position and velocity, unlike pseudo particles in the BFR. A potential complication in the VPC is that it can be computationally costly to disperse pseudo particles in solid with complex geometry^[90].

In what follows, we apply a non-slip boundary condition between the solvent and the walls by using the bounce-back reflection rules and the so-called virtual particles method. Note that in order to account for the size of the counterions, we also use the bounce-back rules for the ions, but at a finite distance from the wall.

2.2.5 Simulation of the flow of a fluid in a porous medium

Once that the fluid boundary conditions were determined, the following step consists in simulate the flow of the fluid. To do so, it is important to first highlight the different kinds of flows that can be created, depending on how the flow arises. If the movement of the fluid is induced by an applied electric potential across a porous material containing ions, then this is an electro-osmotic flow. On the other hand, the Poiseuille flow is created due to a pressure-induced flow. Thus, in this section a discussion of how they are implemented in the MPCD code is carried out. To obtain a Poiseuille flow, from an experimental point of view, a pressure gradient is used. However, in the MPCD simulations it is not possible to do it in the same way. Thus, two different methods will be presented in order to create the flow.

- Flow at the entrance of the simulation box

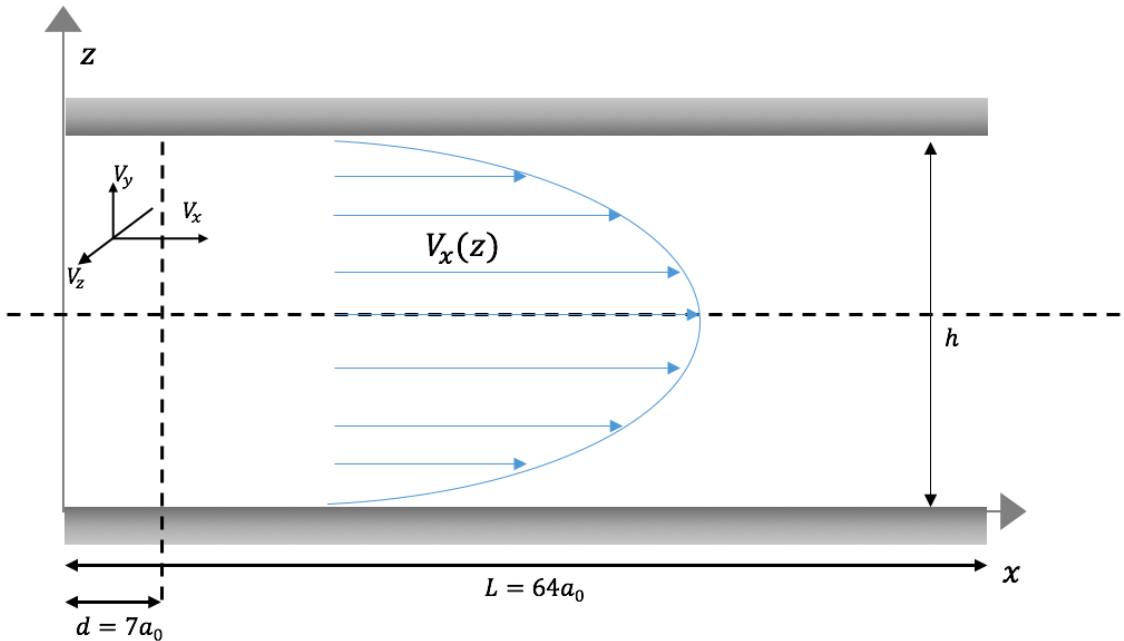


Figure 2.7 – Schematic representation of the simulation box and of the zone under which is imposed the uniform velocity ($x < d$).

In this method^[91] we impose to the fluid an uniform speed in a portion of the simulation box. As it is shown in Figure 2.7 a uniform velocity is given on all the fluid molecules located in the portion of the simulation box corresponding to an abscissa x less than $d = 7 a_0$. More precisely, when a particle of fluid is located in this "slice" of the simulation box, with $0 < x < d$, we will redistribute the velocity of this particle as

follows:

$$V_x = V_{flow} + \xi_x \quad (2.8)$$

$$V_y = \xi_y \quad (2.9)$$

$$V_z = \xi_z \quad (2.10)$$

Here V_{flow} is the speed imposed on the fluid and (ξ_x, ξ_y, ξ_z) are three random numbers distributed according to a Gaussian law which depends on the temperature. This method was not applied in our simulation method because the results can only be exploited in the middle of the simulation box along the x-direction, far from the ends, restricting the study.

- Flow induced by a constant force

The second method^[92] consists in accelerating the fluid particles by a constant force, *i.e* the particle will be governed by the following equations of movement:

$$r_i(t + \delta t) = r_i(t) + v_i(t)\delta t + \frac{\delta t^2}{2}g\hat{x} \quad (2.11)$$

$$v_i(t + \delta t) = v_i(t) + \delta tg\hat{x} \quad (2.12)$$

where \hat{x} is the unit vector in the flow direction. The external force is defined by $F = \rho g\hat{x}$ where g is a constant. However, under these conditions, as the force is applied to the fluid molecules, the energy increases in the system. Thus, this additional energy must be dissipated if we want to remain in the ensemble where (N, V, T) is conserved. Then, although the fluid-solid (wall) interactions are a kind of friction which makes possible the dissipation of this energy, still a use of a thermostat is required to keep the energy constant. Indeed, this method was used in order to induce a Poiseuille flow.

To induce an electro-osmotic flow we have applied an electric field to the charged solutes (ions). Thus the force will be defined as $F = e\rho E\hat{x}$. In this, E corresponds to the applied electric field that is in the \hat{x} direction.

2.3 Simulation of embedded solute particles in a MPCD bath

2.3.1 Verlet algorithm for interacting solutes

Solutes interact with each other, and may have a mass (M) larger than solvent particles. To compute their trajectories, we use the Verlet algorithm of standard MD simulations, with a time step Δt_{MD} . The value of Δt_{MD} depends on the nature of the interaction potential, and is often smaller than Δt_c . Then, the position and the velocity of the solute j are given by:

$$R_j(t + \delta t_{MD}) = R_j(t) + V_j(t)\Delta t_{MD} + \frac{F_j(t)}{2M}\Delta t_{MD}^2 \quad (2.13)$$

$$V_j(t + \delta t_{MD}) = V_j(t) + \frac{F_j(t) + F_j(t + \Delta t_{MD})}{2M} \Delta t_{MD} \quad (2.14)$$

where M is the solute mass and F_j is the force acting on solute j at the beginning of the step, which derives from a given interaction potential.

An important feature to consider in any method of simulation is its efficiency. Indeed one shall hope to reduce resource consumption and completion time as much as possible, maintaining a good description of the physics of the system. In MPCD, when solute particles are added, a new set of masses and lengths scales are introduced. Thus, it is important to bear in mind that the simulation cost scales with the number of solute particles N . Hence, in order to optimize the efficiency of the simulation, one should keep N as small as possible. This can be achieved by keeping σ/a_0 and the box size L small, where σ is the diameter of a particle. Unfortunately, both choices induce errors. Reducing σ/a_0 leads to a less accurate short-range hydrodynamic field, whilst decreasing the box size L breaks the long-range nature of the hydrodynamic interactions. Thus a compromise among the two has to be done, in order to have an efficient MPCD code. We come back to this issue in next section.

2.3.2 Interactions between embedded particles

The interactions between embedded solutes are taken into account in the equation of motion Eq. 2.13 and Eq. 2.14. In terms of efficiency the fact that MPCD use pair-wise interactions between solutes, leads into a computational cost of the order of the square of number of solutes particles. Accordingly, a tool named cell-linked-list^[93] consisting in finding all atom pairs within a given cut-off distance, is used. This works subdividing the simulation domain into cells with an edge length greater than or equal to the cut-off radius of the interaction to be computed. Then, the particles are sorted into these cells and the interactions are computed between particles in the same or neighbouring cells (see Fig). As a consequence, instead of having a computational waste of $O(N^2)$, now it is reduced to $O(N)$. Special adjustments are necessary to take into account boundary conditions^[94].

For example, in the case where we study an electrolyte solution, ions experience electrostatic interactions due to the charge they bear. This is written as:

$$U_{el}(r_{ij}) = k_B T \frac{l_B z_i z_j}{r_{ij}} \quad (2.15)$$

with z_i denoting the valency of charge i , r_{ij} the distance between the i and j -particle and l_B the Bjerrum length

If only one species of ion is taken into consideration *e.g.* only positive ions, then no other interactions are needed as the Coulomb interaction is purely repulsive. Otherwise, the Coulomb attraction between oppositely charged ions should be balanced by a short-range repulsion. In order to assess the influence of excluded volume effects between ions, a WCA (Weeks-Chandler-Anderson) potential is applied. Such potential reads:

$$U_{WCA}(r_{ij}) = 4\epsilon_{WCA} \left[\left(\frac{\sigma_{WCA}}{r_{ij}} \right)^{12} - \left(\frac{\sigma_{WCA}}{r_{ij}} \right)^6 \right] + \epsilon_{WCA} \quad \text{if } r_{ij} < 2^{1/6} \sigma_{WCA} \quad (2.16)$$

where $\epsilon_{WCA} = k_B T$ in our case.

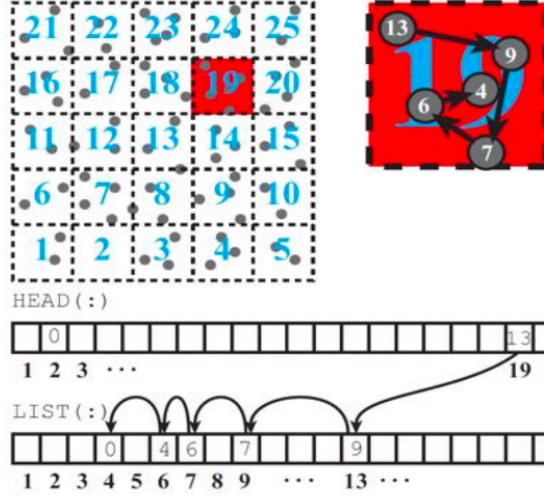


Figure 2.8 – Representation of the cell-linked-list.

2.3.3 Coupling between solute and MPCD fluid

In the Multi-particle Collision Dynamics method, solute particles are coupled with the MPCD fluid, which leads to the emergence of hydrodynamic interactions (HI) between solutes. Indeed, there are several ways to carry out the coupling. We shall now discuss those.

2.3.3.1 MPCD - Central force coupling

This coupling method was proposed by Malevanets et Kapral in 2000^[95]. The coupling between the solvent particles and MPCD fluid is carried out during the propagation phase of the solvent dynamics through a repulsive force between solute and fluid particles of short range, which creates a spherical zone around the solute depleting the solvent^[95,96]. This means that, the solvent particles close to a solute no longer have a ballistic movement; instead, a displacement under the action of the force is carried out. Such force is derived from a short-ranged repulsion potential of the WCA type^[97].

$$\psi_{cf} = \begin{cases} 4\epsilon_{cf} \left[\left(\frac{\sigma_{cf}}{r_{ij}} \right)^{12} - \left(\frac{\sigma_{cf}}{r_{ij}} \right)^6 + \frac{1}{4} \right] & \text{if } r_{ij} < 2^{1/6}\sigma_{cf} \\ 0 & \text{if } r_{ij} > 2^{1/6}\sigma_{cf} \end{cases} \quad (2.17)$$

where r_{ij} is the distance of separation between one fluid particle i and one solute j with σ_{cf} being the diameter of the solute with respect to the fluid. Indeed, this potential represents a stiff repulsive interaction.

On the other hand, solutes interact between them through an interaction potential to be defined. Usually, a repulsion short-range type WCA is used, by defining an interaction diameter between the nano-particles σ_{cc} . However, the parameter σ_{cf} is not equal to half the diameter of the nano-particles σ_{cc} and must be chosen carefully. Indeed, interactions between solutes and solvent particles can induce a depletion effect, *i.e.* an effective attraction between solutes which is not necessarily representative of the interaction that is sought in this model. Particularly, since in MPCD code the solvent particles are point-like particles,

depletion interaction only takes place when the solute particles are in contact. Then a possible solution is to choose^{[64][96]}

$$\sigma_{cc} > 2\sigma_{cf} \quad (2.18)$$

By defining this, we leave an accessible gap for the solvent particles flux. However, this method of coupling does not allow us to account for the effects of non-slip of the solvent on the surface of solutes, since only the radial component of the speed of the pair of particles considered is changed by this central force interaction. Alternative schemes can lead to an effective stick boundary condition^[96,98]. It is therefore necessary to add rules to take into account these effects. In our work, as we are interested in the dynamics of small ions or of small polymer beads, we have not used this coupling scheme. We have chosen a simpler one, that is computationally more efficient, named the collisional coupling.

2.3.3.2 MPCD-CC

In cases where the solute particles are rather small, another possibility is to couple the solute with the solvent during the collision step, when the momentum exchange occurs as discussed in^[97]. This coupling scheme is rather crude, but it is the most efficient from the computational point of view.

In this approach, every solute particle is taken to be a point-particle which participates in the MPCD collision. If the solute i has a mass M_m and velocity \mathbf{w}_i , the center of mass velocity of the particles in the collision cell is

$$\mathbf{u} = \frac{m_f \sum_{i=1}^{n_{cell}} \mathbf{v}_i + M_m \sum_{i=1}^{N_m} \mathbf{w}_i}{n_{cell}m_f + N_m M_m} \quad (2.19)$$

where N_m is the number of solute particles in the collision cell. A stochastic collision of the relative velocities of both the solvent particles and embedded solute particles is then performed in the collision step. This results in an exchange of momentum between the solvent and embedded solutes. The new solute momenta are then used as initial conditions for a molecular-dynamics Verlet update during the subsequent streaming time step, Δt . Alternatively, the momentum exchange, Δp , can be included as an additional force $\Delta p/\Delta t$ in the molecular dynamics integration. If there are no other interactions between solutes these degrees of freedom stream freely during this time interval. In the case of electro-osmosis simulations, we account for Coulomb interactions and short-ranged repulsions between ions. When using this approach, the average mass of solvent particles per cell, $m_f n_{cell}$, should be of the order of the solute mass M_m (assuming one embedded particle per cell)^[92]. This corresponds to a neutrally buoyant object which responds quickly to the fluid flow but is not kicked around too violently. It is also important to note that the average number of solutes per cell, $\langle N_m \rangle$ should be smaller than unity in order to properly resolve hydrodynamic interactions between the solvent particles^[99].

This scheme was used for instance to study the dynamics of small polymer chains^[77,80,97,100], and allowed to recover the scaling laws of Zimm theories^[79]. More recently, this method has been used for a model of solutes with several sites^[101], to mimic hydrodynamic interactions at the surface of a colloidal particle. Despite these successes, a previous work found that the diffusion coefficients of simple electrolytes predicted by MPCD-CC differed from those

obtained by Brownian dynamics with hydrodynamic interactions^[102]. Indeed, one limitation of the MPCD-CC scheme is that the solute influences the solvent at the length scale of the collision cell a_0 only, so that the hydrodynamic size of the solute is of the order of a_0 in any case. In real systems, the hydrodynamic radius of a simple ion or of a nano-particle is close to its structural radius derived from the atomic structure. It means that the structural size should also be of the order of a_0 , or in other words, that the size of the cell in MPCD should be chosen to match the structural size when the collisional coupling is used. In practice, in several papers, authors suggest to choose a value of the structural diameter of the order of a_0 ^[76,103], but it was shown in Dahirel *et.al.* 2018^[104] that choosing the solute radius equal to $a_0/1.3$ allows one to maximise hydrodynamic coupling between spherical solutes.

2.4 Computation of the transport coefficients of solute particles

2.4.1 Diffusion coefficient

Diffusion is the process which is caused by the molecular motion of the particles in the fluid due to thermal fluctuations.

The self-diffusion coefficient is given by the Einstein relation

$$\frac{\partial \langle r^2(t) \rangle}{\partial t} = 2dD \quad (2.20)$$

where d is the dimension and $\langle r^2(t) \rangle$ is the mean-square displacement. Here, it is important to realize that, whereas D is a macroscopic transport coefficient, $\langle r^2(t) \rangle$ has a microscopic interpretation: it is the mean-square distance over which the labelled molecules have moved in a time interval t . This immediately suggests how to measure D in a computer simulation: for every particle i , we measure the distance travelled in time t , $\Delta r_i(t)$, and we plot the mean square of these distances as a function of the time t :

$$\langle (\Delta r(t))^2 \rangle = \frac{1}{N} \sum_{i=1}^N (\Delta r_i(t))^2 \quad (2.21)$$

Let us specify what we mean by the displacement of a particle in a system with periodic boundary conditions. The displacement that we are interested in is simply the time-integral of the velocity of the tagged particle.

$$\Delta r(t) = \int_0^t v(t') dt' \quad (2.22)$$

Then, the diffusion coefficient can be expressed in terms of the velocity of the particles by:

$$D = \frac{1}{2d} \int_0^\infty d\tau \langle v_x(\tau) v_x(0) \rangle \quad (2.23)$$

where $\tau \equiv t - t''$. Indeed the quantity $\langle v_x(t') v_x(t'') \rangle$ is called the velocity auto-correlation function, and it measures the memory between the velocity of a particle at times t' and t'' . The velocity auto-correlation function (VACF) is an equilibrium property of the system, because it describes correlations between velocities at different times along an equilibrium trajectory. At equilibrium the VACF is invariant under a change of the time origin

and depends only on the difference of t' and t'' . Indeed, such relation between a transport coefficient and an integral over a time-correlation function is called a Green-Kubo relation. Thus, the self-diffusion coefficient of solutes D is computed using equilibrium trajectories, *i.e.* the mean-squared displacement as a function of time is computed, and the diffusion coefficient of solutes is deduced from the slope at long time^[92] or alternatively, the time correlation of the velocity is computed. To compute the diffusion coefficient from the time correlation function of the velocity one needs to sample precisely both the short times and the long time scales. This requires to store a lot of data. For this reason we have chosen to compute the self-diffusion coefficient from the m.s.d.

However, the standard method used in bulk fluids (*i.e.* Einstein relation or the Kubo relation), is not valid for systems with interfaces or for confined fluids. Particularly, in confined liquids the mean square displacement will be bounded by the size of the confined region and it will be difficult to unambiguously find the diffusion coefficient, since it will be different for different regions. The time dependence of the MSD, computed for particles initially in the region of interest, will become linear only at times long enough for the molecules to sample all regions, and then its slope will give the diffusion coefficient averaged over all regions.

Thus in order to overpass these limitation the method introduced by Liu et.al.^[105] was used. In this method the diffusion tensor is split in two components *i.e.* parallel D_{\parallel} and perpendicular D_{\perp} to the surface, due to the symmetry of the system. Moreover, because the properties of the confined fluid depend on the distance from the surface, it is possible to divide the pore into layers. Thus, it is possible to compute D_{\parallel} and D_{\perp} from the mean-square displacement of molecules in each layer, centered at a distance z_i from the surface. Hence we introduce a function S_C^i whose value is 1 if the molecule remains continuously in the i -th layer during the interval $[0, t]$ and 0 otherwise^[106]. Then, we have

$$D_{\parallel}(z_i) = \lim_{t \rightarrow \infty} \frac{\langle [\Delta x^2(t) + \Delta y^2(t)] S_C^i(t) \rangle}{4t \langle S_C^i(t) \rangle} \quad (2.24)$$

We will only make use of the parallel component of the diffusion coefficient in this study, we will not discuss the corresponding expression of the perpendicular component.

Thus the way to carry out with the study is by plotting the mean square displacement (m.s.d.) as shown in Figure 2.9 for each case. Thus from the curve the slope is obtained and then divided by the corresponding value of D^0 . The typical evolution of S_C with time is displayed on Fig 2.10. Finally, for each system the slope is computed to then be applied into Eq. 2.24.

2.4.2 Determination of the diffusion coefficient of a solute at infinite dilution

Since the calculations of the transport coefficients are not always easily comparable between them, it is important to determine the values of the diffusion coefficient at infinite dilution, *i.e.* for only one solute in a bath of solvent, where the solute is coupled collisionally with the solvent. This self-diffusion coefficient is denoted by D^0 in what follows. D^0 represents diffusion in a system when no interaction among the solutes is carried out. To do this calculation of D^0 , it is important to take into account two aspects:

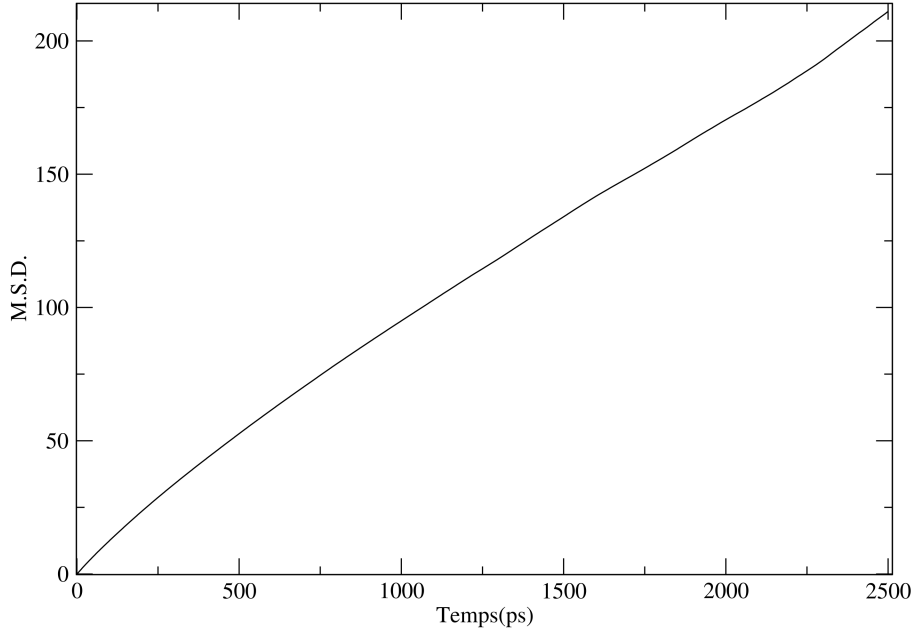


Figure 2.9 – Mean square displacement (M.S.D.) as a function of the time obtained to carry out the study of the diffusion coefficient by layers. This particular case correspond to the M.S.D. of the system $\sigma_{wall} = -1 e/nm^2$ and $c_{add} = 0.5 mol/L$ for the layer close to the wall.

- When taking into account the hydrodynamic interactions, which are long-ranged, the calculation of the diffusion coefficient will depend on the size of the simulation box L_{box} for periodic systems. Then, to avoid this problem it is possible to choose a large size of L_{box} , although this will increase the time calculation due to the large amount of solvent particles that are needed to be taken into account.
- For the calculation of D^0 , the same conditions of the infinite solution must be considered, which correspond to the case of a single solute particle in a large volume of pure solvent. A simulation with these conditions is too expensive computationally speaking, therefore, more solute particles must be considered in the simulation box with the condition of always trying to approach the system of infinite dilution. If solutes do not interact with each other, it is as if they were at infinite dilution.

Knowing that the dependence of the diffusion coefficients with the size of the simulation box is predicted theoretically by equation^[107,108]:

$$D(L_{box}) = D(\infty) - 2.837 \frac{k_B T}{6\pi\eta L_{box}}, \quad (2.25)$$

We can get the value of the diffusion coefficient at infinite dilution when using $\eta = \eta_{solvent}$. From the study done by Xudong^[109] the following conclusions were found:

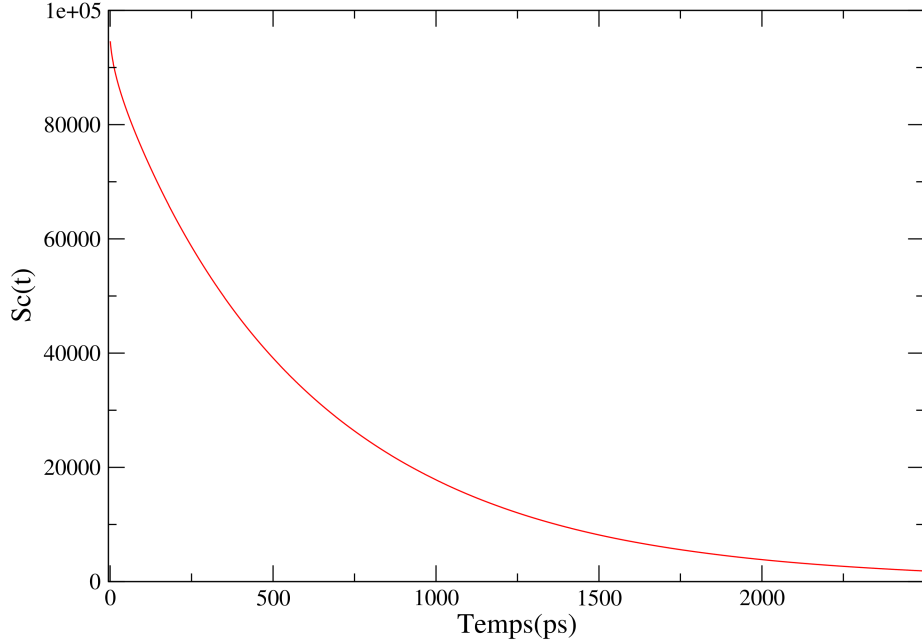


Figure 2.10 – $Sc(t)$ as a function of the time obtained to carry out the study of the diffusion coefficient by layers. This particular case correspond to the M.S.D. of the system $\sigma_{wall} = -1 e/nm^2$ and $c_{add} = 0.5 mol/L$ for the layer close to the wall.

- For an infinitely dilute system the agreement found between the equation 2.25 and the results obtained through the simulations are good. Both of them give a value of $D_{(\infty)}^0 = 0.0421a_0^2t_0^{-1}$, for a system that considers $M_m = 10m_f$, $\gamma = 5$ and $\alpha = 130$, Here we refer to infinitely dilute when there are no direct interaction between the solutes, or indirect interaction.
- When $L_{box} > 25a_0$, the influence of the finite-size effect of the simulation box becomes negligible. We can consider that $D(L_{box} > 25a_0) \simeq D(L_{box} = \infty)$. Then, for smaller sizes of the simulation box, we will have to make the respective correction.

More specifically, for further comparisons of D in the different systems the value D^0 , *i.e.*, $D_{(\infty)}^0 = 0.0421a_0^2t_0^{-1}$ will be used in this thesis.

2.4.3 Electrical conductivity

Two method were employed, in order to compute the electric conductivity of a system containing ions from MPCD. The first made use of the Kubo's formula, by using the following

equation, from trajectories computed from equilibrium simulations

$$\sigma(t) = \lim_{t \rightarrow \infty} \frac{e^2}{3Vk_B T} \int_0^t \left\langle \sum_{i=1}^N z_i v_i(t_0 + t') \sum_{i=1}^N z_i v_i(t_0) \right\rangle_{>t_0} dt' \quad (2.26)$$

where V is the volume of the simulation box, z_i is the particle valence, e is the elementary charge, N is the total number of solute particles in the simulation box and v_i is the velocity of the i -th particle. As we said before for the diffusion coefficient one needs a good sampling both of short and long times to compute this kind of correlation function.

Another method based in non-equilibrium simulations can be used to obtain the electric conductivity. It makes use of the ion velocities and density profiles obtained through MPCD simulation in the case where an external electric field is applied, *i.e.* from non equilibrium simulations. Actually, using the basic definition of the electric conductivity which is the ratio of the flux of charges to the electric field, we have:

$$\frac{\sigma(z) \vec{E}}{e} = \rho_+(z) \vec{V}_+ + \rho_-(z) \vec{V}_- \quad (2.27)$$

where $\rho_{\pm}(z)$ are the counterion and co-ion density profile, \vec{V}_{\pm} are the counterion and co-ion velocity profiles, \vec{E} the applied electric field and e the elemental charge.

We have used non-equilibrium simulations to compute the electric conductivity of bulk ionic solutions, ionic solutions between neutral walls and ionic solutions in a charged slit pore. In the last case, under the applied electric field, an electro-osmotic contribution appears that modifies the velocities of ions. As we will show in Section 3.8, we can remove this contribution to obtain the electric conductivity in the reference frame of the solvent.

Transport of an electrolyte solution under confinement

Contents

3.1	Introduction	45
3.2	Parameters of the simulation	46
3.2.1	MPCD fluid	46
3.2.2	Solute parameters	47
3.2.3	System studied	50
3.3	Implementation of the MPCD code	52
3.3.1	Validation of the Ewald summation in a slab geometry	52
3.4	Influence of the electrostatic confinement on the density profile of ions	55
3.4.1	Counterions	55
3.4.2	Coions	58
3.4.3	The ionic density profiles are those of PB	60
3.5	Diffusion Coefficient of ions	65
3.5.1	Difusion in bulk solution	65
3.5.2	Influence of a neutral confinement	66
3.5.3	Influence of an electrostatic confinement	67
3.5.3.1	Diffusion coefficient averaged over all the simulation box	67
3.5.3.2	Diffusion coefficient as a function of the distance to the walls	69
3.5.4	Summary of the main findings	77
3.6	Velocity field of solvent and ions	77
3.6.1	Electro-osmosis flow	77
3.6.2	Electro-osmotic velocity obtained through MPCD compared with the velocity obtained through Smoluchovski theory	79
3.7	Poiseuille flow: study of the viscosity	83
3.7.1	Velocity field of ions	86
3.7.1.1	Low confinement	86
3.7.1.2	Medium confinement	87
3.7.1.3	High confinement	88
3.8	Electric conductivity	88
3.8.1	Conductivity in bulk solution	89
3.8.2	Influence of a neutral confinement	90
3.8.3	Influence of an electrostatic confinement	91
3.8.3.1	Conductivity by layers	91
3.8.4	Conclusion	94
3.9	Prediction of the ionic velocity profiles	94
3.9.1	Introduction	94
3.9.2	Hydrodynamic calculation of the solute velocity between walls	94
3.9.3	Accounting for non-ideal effects	97
3.9.4	Application of the method	98
3.9.5	Conclusion	99

3.1 Introduction

The MPCD code was modified to account for electrostatic effects and the coupling with hydrodynamics in order to analyse the dynamics of the ions in confined systems. Then, in order to make a systematic study, three different systems were simulated: a) a bulk solution of a 1-1 electrolyte, b) the same system in the presence of a neutral confinement by two parallel and infinite neutral walls and c) the case where there is an electrostatic confinement between walls of same charge. In this case, the amount of ions having a charge opposite to the wall is larger than those of same charges (see Fig. 3.1). By doing so, we shall be able to see the effect of the presence of the wall on the ions dynamics.

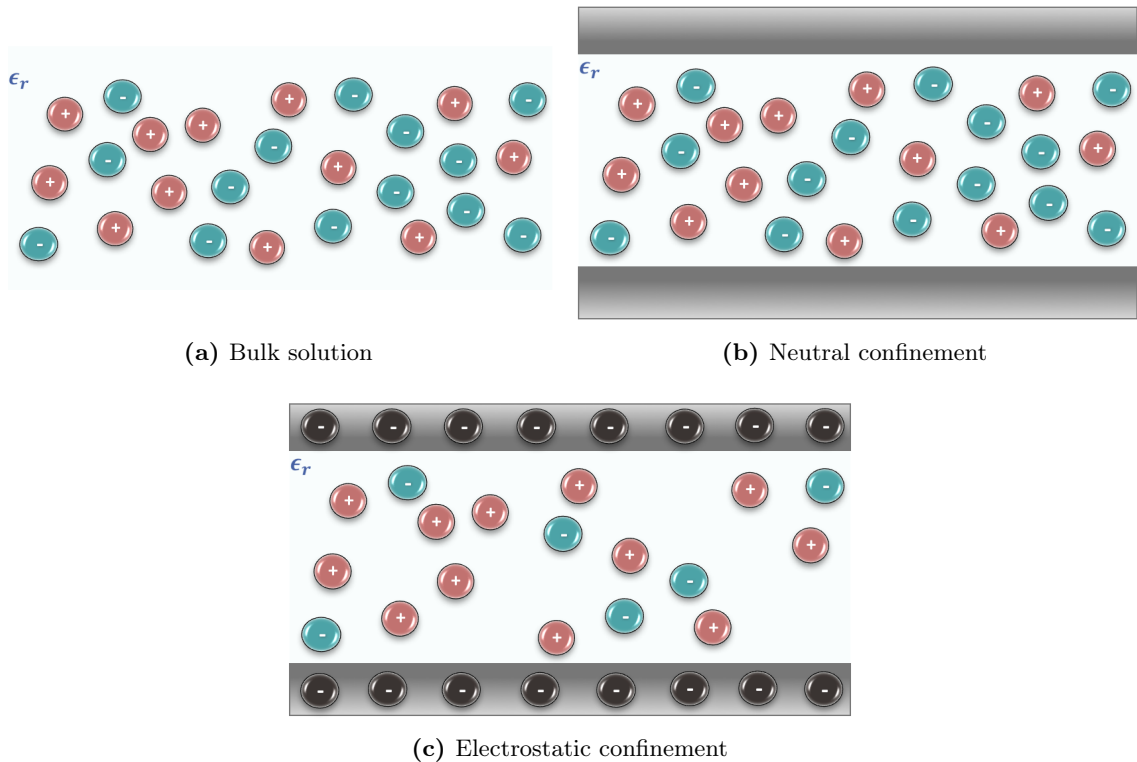


Figure 3.1 – Systematic study carried out with the modified MPCD code for three different cases: In (a) a bulk solution was simulated; in (b) the case of neutral confining was obtained confining the bulk solution with infinite neutral walls in the z -direction and finally in (c) the electrostatic confinement case was simulated adding negative charges at the walls.

For each case, we obtain the equilibrium and non-equilibrium properties with and without an external electric field respectively (*i.e.* an induced external electric field parallel to the walls $eE = 0.2 a_0^{-2} t_0^{-1}$). In the first case we compute a) the density profiles of ions in the direction

perpendicular to the walls, b) the diffusion coefficients of ions in the direction parallel to the walls and c) the electrical conductivity of the solution inside the slit pore; whereas in the latter we carry out a) the velocity profile of the solvent under an electric field, which is the so-called electro-osmotic flow, b) the velocity profiles of counterions and of co-ions under an applied electric field and c) the electrical conductivity of the solution inside the slit pore.

The system studied (slit pore under electrostatic confinement) is made of two parts. The first is a non-mobile solid phase, which could represent a porous material saturated by water. Clays are for instance common examples. Besides, when solid phases are in contact with electrolytes, electric charges appear at the surface. This electric charge is partly screened by the counterions present in the liquid phase, which adsorb at the interface, forming the so-called Stern layer (see Chapter. 1). For the time being we neglect adsorption-desorption phenomena as well as any diffusion in this layer. Thus, the solid phase possesses a surface charge density σ_{wall} , inside the solid part. We consider here that the surface does not change with time. The second part is made of liquid phase, in other words the electrolyte which is made of dissociated ionic species in a continuous solvent with permittivity $\epsilon = \epsilon_r \epsilon_0$, where ϵ_r is the relative permittivity and ϵ_0 is the permittivity in vacuum. The fluid viscosity η and temperature T are assumed to be uniform. The ionic species are particles with charge $q_i = \pm e$ and a finite size, meaning that the excluded volume effects are considered.

Now that we defined the different parts involved in our system, we need to determine the different parameters used in our simulations, which will have to be correctly picked in order to recover all physical details we are interested in. The selection of such parameters is described in the next section.

3.2 Parameters of the simulation

The MPCD code accounts for the coupling between hydrodynamic and electrostatic effects. However, a separate choice of the parameters is required for the ion dynamics (solute) and the fluid dynamics (solvent). The choice of these parameters needs to be done such that the different time scales at play are correctly considered. In other words, one should keep in mind that (i) characteristic numbers ought to be in the right regimes and (ii) all the time scales need to be sufficiently close to each other in order to gain computational efficiency. More specifically, since solute particles have a finite size, the correct radius sizes should be chosen according to the cell size. Hence, it should be large enough to contain less than two particles in each MPCD cell, but not too large so that it would maintain high computational efficiency.

3.2.1 MPCD fluid

First, we begin selecting the fluid parameters. Besides, the viscosity can inform us on the right choice for these parameters, as an accurate analytical expression for the kinematic viscosity in MPCD is known. The solution reads $\nu = \nu_{kinetic} + \nu_{collision}$ (see the derivation in Section 2.2.3) and is thus the sum of the viscosity due to kinetic effects and the viscosity due to collisions. Kinetic transport is dominant in gases, whereas in fluids momentum mostly arises from collisions. Considering that ν is a function of δt_0 and α , Ripoll *et al.* showed the influence of these two contributions on the kinematic viscosity as a function of the rotation angle and the collision time step^[92].

They found that the collisional contribution is dominant for large collision angles and small collision times, whilst the kinetic viscosity is dominant in the opposite case (*i.e.* small collision angles and large collision times). As we are interested in modelling liquids we will take the parameters such that the collisions become more important than the kinetic counterpart. Then, to quantify the values of δt_0 and α , we can look at the Schmidt number, which is defined as $Sc = \nu/D_f$ ^[102], where ν is the kinematic viscosity and D_f is the mass diffusivity. Sc then expresses the ratio of the time scale of diffusive mass transfer over the time scale of momentum transfer in the fluid. In particular, in liquids, Sc is of the order of 10^2 - 10^3 . A theoretical prediction for the Schmidt number of a MPCD fluid as a function of the collision time, for different values of the rotation angle, was carried out by Ripoll *et al.* (see the discussion in 92). Sc becomes considerably larger than unity for the same range of parameters, where the collisional viscosity is considerably larger than the kinetic viscosity. More specifically, using $\alpha = 130^\circ$, $\gamma = 5$, $\lambda = 0.1 a_0$, results in $Sc \sim 10$, which is the wished value. In fact as long as λ lies within the range of 0.002 - 0.1, the value of Sc is correct for our purposes. Hence, the viscosity value is $\eta = 3.96 a_0^{-1} t_0^{-1}$ according to this parameter selection.

3.2.2 Solute parameters

We now turn to the selection of the solute parameters, *i.e.* particle size and the mass. Concerning the former, the value needs to be chosen taking into consideration two aspects: the first is related to the amount of solute that can be found in a cell of simulation; whereas the second is related to the hydrodynamic radius, *i.e.* both values (particle and hydrodynamic radius) have to be close enough in order to consider a correct hydrodynamic contribution. Thus, a choice of the grid parameter has to be done, in order to do a correct selection of the particle size value.

Indeed, a choice of the cell size is necessary in order to avoid spurious effects in the solute dynamics. In particular such effects become more important when:

- the cell size increases and exceeds the minimal distance of approach between solutes
- the concentration of solutes increases
- attractions between solutes exist

Then, we conducted a study of the cell size to allow us to choose the correct a_0 value in the context of Poiseuille and electro-osmotic flows simulations. To do so, different values of the size cell were tested. Such parameters were selected keeping $(L_x \times L_y \times L_z) = (45 \times 36 \times 36) \text{ \AA}^3$ fixed and varying a_0 (increasing a_0 results in a decrease of the number of cells defined in the simulation box).

$a_0 (\text{\AA})$	$L_x (a_0)$	$L_y (a_0)$	$L_z (a_0)$
0.75	60	48	48
1	45	36	36
1.5	30	24	24
3	15	12	12

Table 3.1 – L_x , L_y and L_z as a function of a_0 for different values of a_0

Chapter 3. Transport of an electrolyte solution under confinement

In all the cases, a flow with $Re = 0.5$ was considered. Table 3.1 illustrates the different values used. The corresponding results are shown in Fig. 3.2 a) and 3.2 b) for the electro-osmotic and Poiseuille velocity profile respectively. In particular, in the electro-osmosis case, the profiles were obtained taking into consideration a system with $\sigma_{wall} = -2 e/nm^2$, $c_{add} = 0 \text{ mol/L}$ (*i.e.* no added salt), $\sigma_w = 1 \text{ \AA}$ (size particle) and $eE = 0.1 a_0^{-2} t_0^{-1}$ (applied electric field). Thus, all the curves were divided by the pre-factor on the following equation

$$V_x(z) = \frac{eE}{2\pi\eta l_B} \ln\left(\frac{\cos(\alpha z)}{\cos(\alpha L_z/2)}\right) \quad (3.1)$$

which was derived in Chapter 1, and corresponds to the theoretical velocity profile when no added salt is considered in the system. This division was carried out to be able to compare the profiles obtained.

In the case of the Poiseuille velocity profile, a selection of the force value was first obtained. To do so, the theoretical equation of the velocity profile was used, *i.e.*

$$V_x(z) = V_{max} \left(\frac{4z}{L_z} - \frac{4z^2}{L_z^2} \right) \quad (3.2)$$

with $V_{max} = \frac{-L_z^2}{8\eta} \frac{\partial p}{\partial x} = \frac{L_z^2}{8\eta} \gamma g$, where γ is the numerical density and g is the acceleration. Then, considering that Re is given by,

$$Re = \frac{V_{max} L_z \gamma}{\eta} \quad (3.3)$$

and the fact that we choose to keep a fix value of $Re = 0.5$, the value of g for each case were obtained and are presented in Table 3.2.

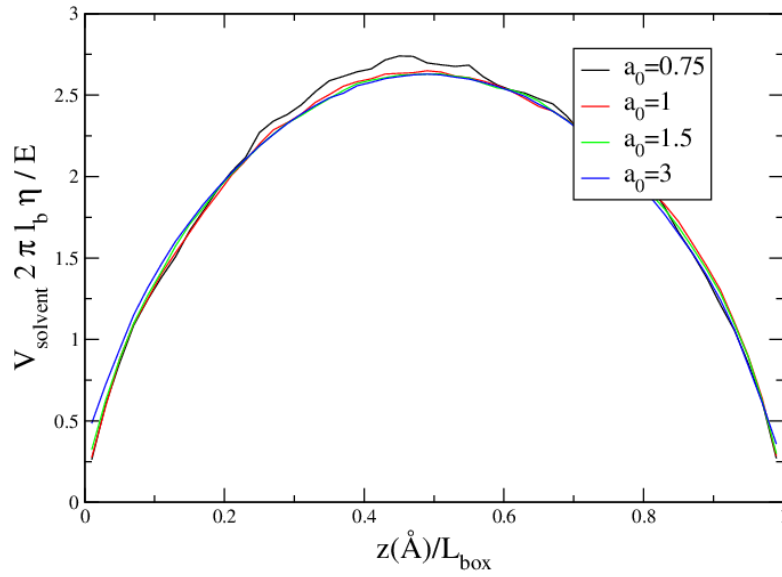
a_0 (Å)	$g(a_0/t_0^2)$
0.75	0.000018
1	0.000044
1.5	0.00015
3	0.0012

Table 3.2 – Corresponding values of g for different values of a_0 .

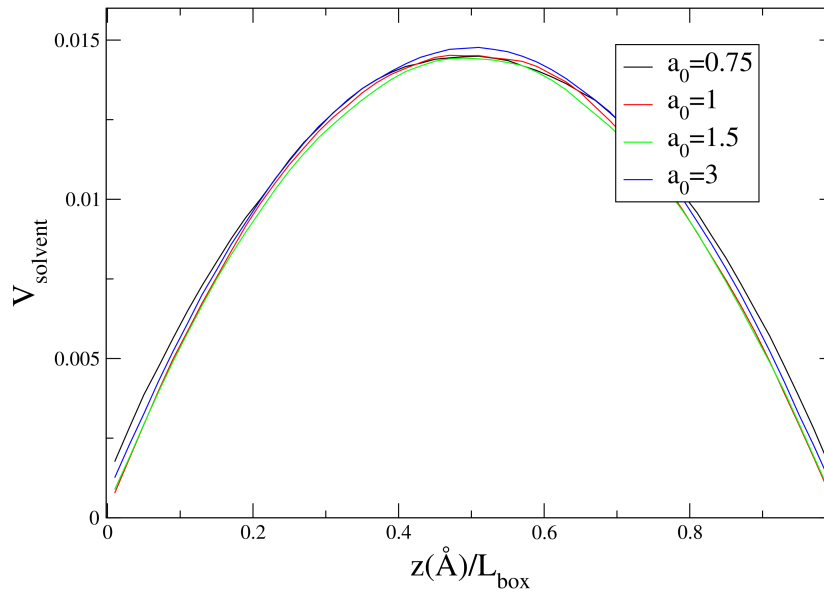
Thus, for each corresponding value of g (*i.e.* each a_0) a corresponding velocity profile is illustrated in Fig. 3.2 b).

In Fig. 3.2 (a) and (b), we can see that none of the profiles seem to be affected by the choice of a_0 . Indeed the curves obtained for different values of a_0 overlap each other. In fact, the small differences present are only due to poor statistics. Consequently, we can conclude that a preferential value of the size cell cannot be determined from such analysis. Therefore, another study has to be carried in order to get the correct value of a_0 . Indeed, another way to deduce it is considering how ionic diffusion coefficients depend on a_0 .

In Ref 104, Dahirel *et al.* analysed the diffusion coefficients of solutes as a function of the ratio between the size of the collision cell and the hard-sphere radius of solute a_0/a_{HS} for a given volume fraction. They found that for small values of a_0 , the diffusion coefficient does not depend on the cell size, whereas for a_0 larger than $1.5 a_{HS}$, the diffusion coefficient of the solute decreases dramatically. Since the maximum distance between two solutes in a



(a)



(b)

Figure 3.2 – In order to choose the correct value of a_0 (the simulation cell size), the electro-osmotic (a) and Poiseuille (b) flow profile were obtained as a function of the distance to the wall for different values of a_0 by using the MPCD code.

collision cell is equal to $\sqrt{3} a_0 \approx 1.73 a_0$, we must have $2 a_{HS} > 1.73 a_0$ or $a_0/a_{HS} < 1.16$ in order to ensure that two hard-sphere solutes cannot be in the same collision cell. Another difficulty concerns the effective hydrodynamic radius of the solute. In Ref. 104 the effective hydrodynamic radius (at infinite dilution of a solute in collisional coupling with the MPCD solvent) was computed using two different methods. The first method consists in using the Stokes law to deduce σ_{hyd} , using its self-diffusion coefficient at infinite dilution. Whereas, the second is to induce a solvent flow around the solute from non-equilibrium simulations, and to compare the simulated flow to the analytical result. For both cases, the study of the hydrodynamic radius as a function of the mass of the solute M was carried out. They found that the hydrodynamic radius is an increasing function of the mass, which can be fitted by an exponential function, $\sigma_{hyd} = 0.295(1 - \exp(-M/3.3))$. Indeed, when the solute is heavy enough, the solvent particles in its cell are basically stopped because of the collision step, so the hydrodynamic radius becomes independent from the solute mass at large mass, reaching a maximum value of $0.3 a_0$ (this is achieved since the value of $M = 10 m_f$). Finally, the particle size value (diameter of the solute) needs to be close enough to σ_{hyd} (in order to consider hydrodynamic contributions) and small enough so that the amount of solute in a cell of simulation remains 1. Thus the value selected was $\sigma_w = 1.5 a_0$ and $a_0 = 1.5 \text{ \AA}$ *i.e.* $\sigma_w = 2.25 \text{ \AA}$. However, the previous study does not help us to choose a correct value for the solute mass.

Therefore, to select the value of M , we can refer to the work of Ripoll *et al.* (see the discussion in 92), where the authors show the relative deviation of the simulated diffusion coefficient D_M with respect to the Brownian approximation D_0 as a function of M/m_f . We can see that the values corresponding to $M/m_f = 10$ and $M/m_f = 5$ are close. Furthermore, the former case is close to 75% enhancement of the hydrodynamic term over the Brownian one, which is optimum. That is the reason why, a value of $M = 10$ was selected, as $m_f = 1$ since the solvent particles are considered to be point-like particles.

3.2.3 System studied

Now that the correct parameters for the simulations were selected, we can turn to the physical phenomena we want to simulate. Specifically, we investigate how the surface charge density at the walls (σ_{wall}), the concentration of added salt (c_{add}) and the confinement (distance between the walls L_z) affect the dynamics of ions and solvent molecules. To do so the system presented in Fig 3.3 is simulated with our MPCD code with two parallel infinite walls. This is achieved using periodic boundary conditions along the x and y -axis and confining the electrolyte along the z direction. The distance between the two walls is given by $L_z = L_{hyd}$, whereas L_{el} denotes the space where the ion center can move. Each unit of charge $-e$ on the solid wall is divided among d sites, leading to a charge $-e/d$, located at a depth w . The sites are randomly placed, with the only constraint being that the charges cannot get closer than half the average distance $1/\sqrt{|\sigma_w|}$. The ions diameter are given by σ_w . Then, an external electric field, parallel to the walls ($eE = 0.2 a_0^{-2} t_0^{-1}$), is applied to the system in order to induce an electro-osmotic flow. Table 3.3 illustrates the different physical configuration that were simulated for each L_z value, *i.e.* each color of the table corresponds to a different confinement. Besides, L_z corresponds to the value of L_{hyd} in Fig 3.3.

In order to choose the rank of values that would take σ_{wall} , c_{add} and L_z , we have to

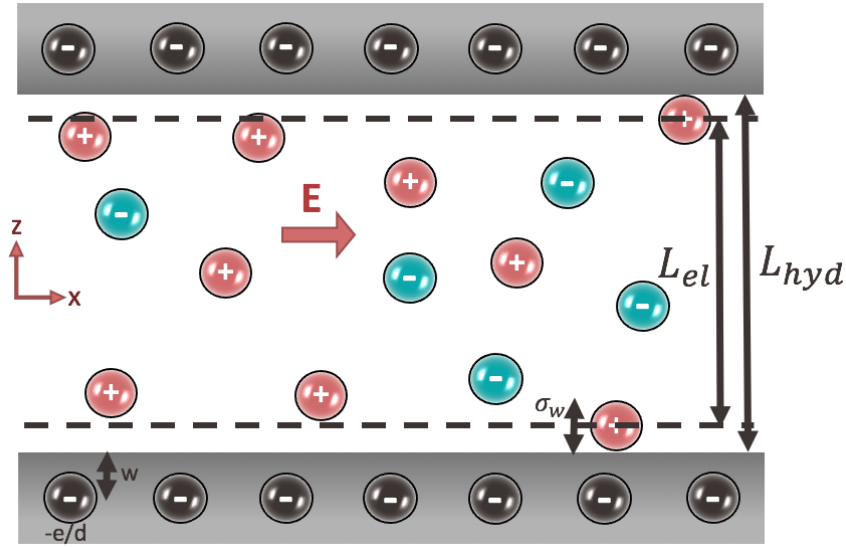


Figure 3.3 – System simulated with Multi-particle Collision Dynamics. Two parallel, infinite charged walls are separated by the ions in a solvent. An electric field E is applied along the surfaces. The solvent can explore the whole space between the walls, separated by a distance L_{hyd} , while an effective ion-wall diameter σ_w restricts the ion to a space of width $L_{el} = L_{hyd} - \sigma_w$. The average surface charge density σ_{wall} is distributed over discrete size of charge $-e/d$ located at a depth w within the solid wall.

consider the number of total ions (counterions + co-ions) that will be present in the system. Hence, the total amount should not be too large preventing the simulation to be too long. However, it should not be either too small or otherwise it would lead to poor statistics. That is the reason why the most concentrated system for $L_z = 4.5 \text{ nm}$, *i.e.* $\sigma_{wall} = -2 \text{ e/nm}^2$ and $c_{add} = 2 \text{ mol/L}$, has a total of 192 ions, from which 70 are co-ions and 122 are counterions. On the contrary, the least concentrated case, *i.e.* $\sigma_{wall} = -0.5 \text{ e/nm}^2$ and $c_{add} = 0 \text{ mol/L}$, has a total of 14 ions counterions. Furthermore, the values for σ_{wall} are in accordance with real systems, since the value of $\sigma_{wall} = -0.5 \text{ e/nm}^2$ can be found in clays, more specifically in Montmorillonite. Similarly, the values taken for L_z can be related to hydrated clays.

For each specific case, a bulk simulation (*i.e.* without confinement) and a simulation with neutral walls (*i.e.* not charged) were carried out in order to better account for the differences whenever confinement with charged walls is present.

Finally, in order to discretize the charge within the wall, the following procedure was carried out:

- The number of charges within the walls N is chosen. This selection depends on the σ_{wall} that we are interested in.
- N is divided by two, because it has to be distributed on both walls equally.
- A fix depth within the two wall is chosen in the z -direction (see Fig. 3.3) to distribute the charges. In our simulation the value of $w = 0.75 a_0$ was taken. Whereas in x and y -direction random positions are taken within the limits of the box size.

$L(nm)$	$\sigma_{wall}(e/nm^2)$	$c_{add}(mol/L)$
Lz=4.5	- 0.5	0
Ly=3.6	- 1	0.2
Lx=3.6	- 2	0.5
		1
		2
Lz=3	- 0.5	0
Ly=4.2	- 1	0.5
Lx=4.2		1
		1.5
Lz=1.5	- 0.5	0
Ly=4.8	- 1	0.5
Lx=4.8		1
		1.5

Table 3.3 – Simulation parameters used in the study. The concentration parameter $c_{add} = 0 \text{ mol/L}$ denotes an ionic solution with no added salt. The cell size is $a_0 = 0.15 \text{ nm}$.

3.3 Implementation of the MPCD code

3.3.1 Validation of the Ewald summation in a slab geometry

Special techniques are required to treat long-range electrostatic interactions in three-dimensions, when the system is finite in one dimension and infinite in the other two. The three-dimensional Ewald summation can thus be adopted for this purpose, but needs to be restricted to the reciprocal-space sum for vectors in the x and y direction.

Considering that the energy is given by the Coulomb energy:

$$U_{Coulomb} = \frac{1}{2} \sum_{i,j=1}^N \sum'_n \frac{q_i q_j}{|\mathbf{r}_{ij} + \mathbf{n}|} \quad (3.4)$$

where $\mathbf{n} = (L_x n_x, L_y n_y, 0)$ indicates that periodicity is only imposed in the x , y directions and the prime indicates that in cell $(0, 0, 0)$ the terms $i = j$ should be omitted. In Fourier space it reads:

$$U_{Coulomb} = \frac{1}{2} \sum_{i,j=1}^N q_i q_j \sum'_n \left[\frac{\text{erfc}(\alpha |\mathbf{r}_{ij} + \mathbf{n}|)}{|\mathbf{r}_{ij} + \mathbf{n}|} + \frac{\pi}{L^2} \sum_{\mathbf{h}>0} \cos(\mathbf{h} \cdot \mathbf{r}_{ij}) F(\mathbf{h}, z_{ij}, \alpha) - \mathfrak{g}(z_{ij}, \alpha) \right] - \frac{\alpha}{\sqrt{\pi}} \sum_{i=1}^M q_i^2 \quad (3.5)$$

where $\mathbf{h} \equiv (2\pi \mathbf{m}_x / L_x, 2\pi \mathbf{m}_y / L_y, 0)$ denotes a reciprocal lattice vector, z_{ij} is the distance between two particles in the z direction, and α is the screening parameter.

The function $F(\mathbf{h}, z, \alpha)$ is given by

$$F(\mathbf{h}, z, \alpha) = \frac{\exp(hz) \text{erfc}[\alpha z + h/(2\alpha)] + \exp(-hz) \text{erfc}[-\alpha z + h/(2\alpha)]}{2h} \quad (3.6)$$

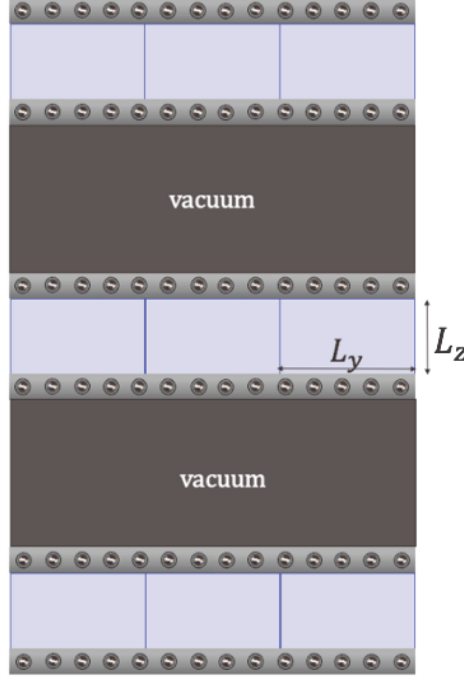


Figure 3.4 – Schematic representation of the system seen in Figure 5.3 when artificial periodic condition in the z direction is applied by adding a slab of vacuum that prevents long-range interactions.

which corrects the inhomogeneity in the non-periodic direction. The function $\mathfrak{g}(z, \alpha)$ reads

$$\mathfrak{g}(z, \alpha) = z \operatorname{erf}(\alpha z) + \exp[-(z\alpha)^2] / (\alpha\sqrt{\pi}) \quad (3.7)$$

However, from a computation point of view Eq. 3.5 is inconvenient. The double sum over the particles in the Fourier part of the eq. 3.5 cannot, in general, be expressed in terms of the square of a single sum. This makes the calculation much more expensive than the three-dimensional counterpart. Actually, an alternative to this exists, which is to use the three dimensional Ewald summation but placing a slab of vacuum between the periodic images (see Fig. 3.4)^[28]. We have used this method in our simulations.

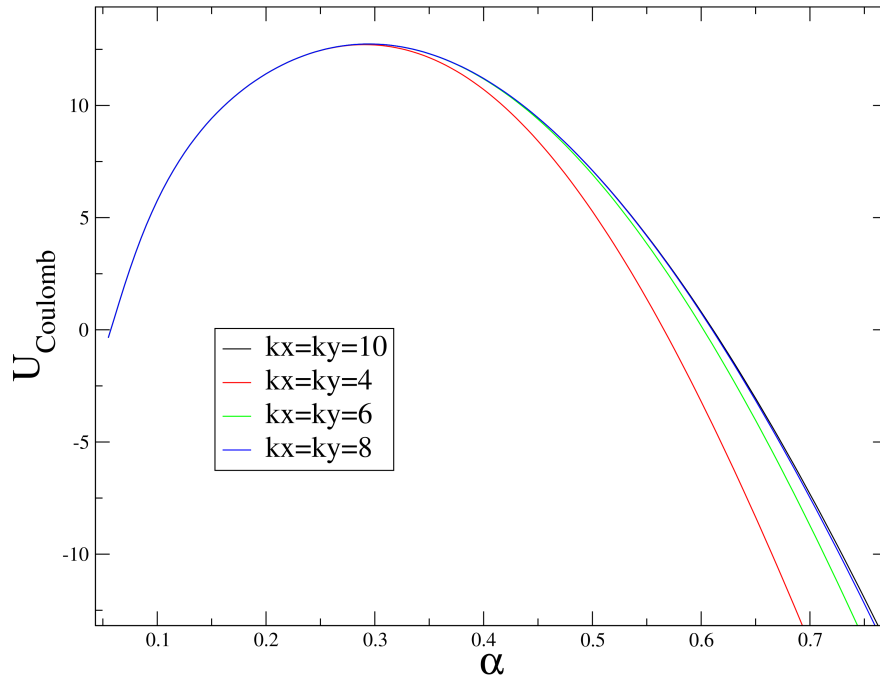
Then the equation reads:

$$\begin{aligned} \mathcal{U}_{Coulomb} = & \frac{1}{2V} \sum_{\mathbf{k} \neq 0} \frac{4\pi}{k^2} |\rho(\mathbf{k})|^2 \exp(-k^2/4\alpha) \\ & - (\alpha/\pi)^{1/2} \sum_{i=1}^N q_i^2 + \frac{1}{2} \sum_{i \neq j}^N \frac{q_i q_j \operatorname{erfc}(\sqrt{\alpha} r_{ij})}{r_{ij}} \end{aligned} \quad (3.8)$$

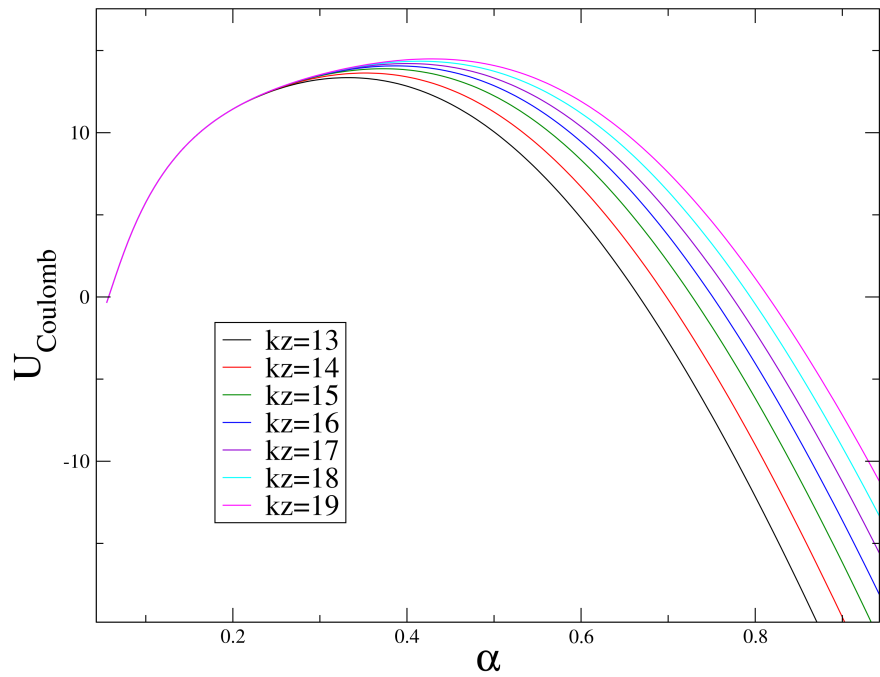
where we used the definition

$$\rho(\mathbf{k}) \equiv \sum_{i=1}^N q_i \exp(\mathbf{i}\mathbf{k} \cdot \mathbf{r}_i) \quad (3.9)$$

and where $\mathbf{k} = (2\pi/L)\mathbf{l}$ with $\mathbf{l} = (l_x, l_y, l_z)$ are the lattice vectors in Fourier space. The complementary error function is given by $\operatorname{erfc}(x) = 1 - \operatorname{erf}(x)$, where $\operatorname{erf}(x) = (2/\sqrt{\pi}) \int_0^x$



(a) $k_x=k_y=6$ fixed and varying k_z



(b) $k_z=11$ fixed and varying $k_x=k_y$

Figure 3.5 – In order to choose the correct value of the k -vectors, the Coulombic potential $U_{Coulomb}$ is obtained for different values of the k as a function of α . This is an example of the method carried out for a system with $\sigma_{wall} = -0.5 \text{ e/nm}^2$ and $c_{add} = 0.5 \text{ mol/L}$.

$\exp(-u^2)du$.

In order to choose correctly the parameters kx , ky and kz and the value of the parameter α we carried out a study to see how the Coulombic potential as a function of α is modified by varying the eigenvectors values of \mathbf{k} . More specifically, the $U_{Coulomb}$ was obtained by keeping fixed $kx = ky$, whereas the value of kz was varied and vice-versa. This analysis was made with the idea of being able to discern for which $kx = ky$ and kz values the Coulombic potential is not affected by the electrostatic forces due to the periodic images in the z -direction. To do so, we need to determine when the ion potential no longer changes when varying $kx = ky$ and kz . However, we have to notice that to compute the real part of the potential a parameter has to be defined, which is the cut off distance in real space r_{cut} . Indeed, the k vectors and α , depend on it. In this case this parameter was chosen to be half of the simulation box *i.e.* $r_{cut} = \frac{L_z}{2}$.

The procedure to choose α , kx , ky and kz as illustrated in Fig. 3.5 a) and b) for a system with $\sigma_{wall} = -0.5 e/nm^2$ and $c_{add} = 0.5 mol/L$. In Fig. 3.5 a) the Coulombic potential as a function of α when varying $kx = ky$ and keeping fixed kz is shown. We could observe that the ions potential curves keep on changing significantly as kz increases, except for $kz = 17, 18$ and 19 where the curves are almost identical. Similarly, Fig. 3.5 b) shows the Coulombic potential as a function of α by varying kz and keeping fixed $kx = ky$. Here, the electrostatic potential due to periodic images is no longer affected when the values of $kx = ky$ varies from 6 to 10, given the proximity of the curves. Therefore, for this particular case the values selected were $kz = 17$ and $kx = ky = 6$. Finally, to select the value of α , we look at the x -axis in both figures, which informs us that the value of α should be the one. In other words, it corresponds to the case where the different curves (which were obtained varying $kx = ky$ and kz) reach a plateau. In this particular case, the value of $\alpha = 0.3$ was chosen. This analysis was carried out for each system shown in Table 3.3.

3.4 Influence of the electrostatic confinement on the density profile of ions

We shall start the discussion by interpreting the result for the ions density profiles ($\rho_{\pm}(z)$) obtained from MPCD simulations, when no electric field is applied. It is important to mention that these are not new results in the sense that they were previously shown in others works. However, carrying out this analysis will enable us to understand how the ions are distributed in the slit pore, and help us explain how their contribution affects dynamical properties in the future analysis.

The study for each ion species (*i.e.* counterions or co-ions) is done separately considering their corresponding ion density profiles as a function of the distance to the wall (z) for different confinements (*i.e.* varying Lz). The units used in the figures are mol/L for $\rho_{\pm}(z)$ and nm for the distance z .

3.4.1 Counterions

We can observe as well that in the whole set of figures, most counterions are concentrated near the wall (green region). This can be explained as the walls bear a charge opposite to the counterions, thus exerting an electrostatic attraction which pulls the counterions closer to

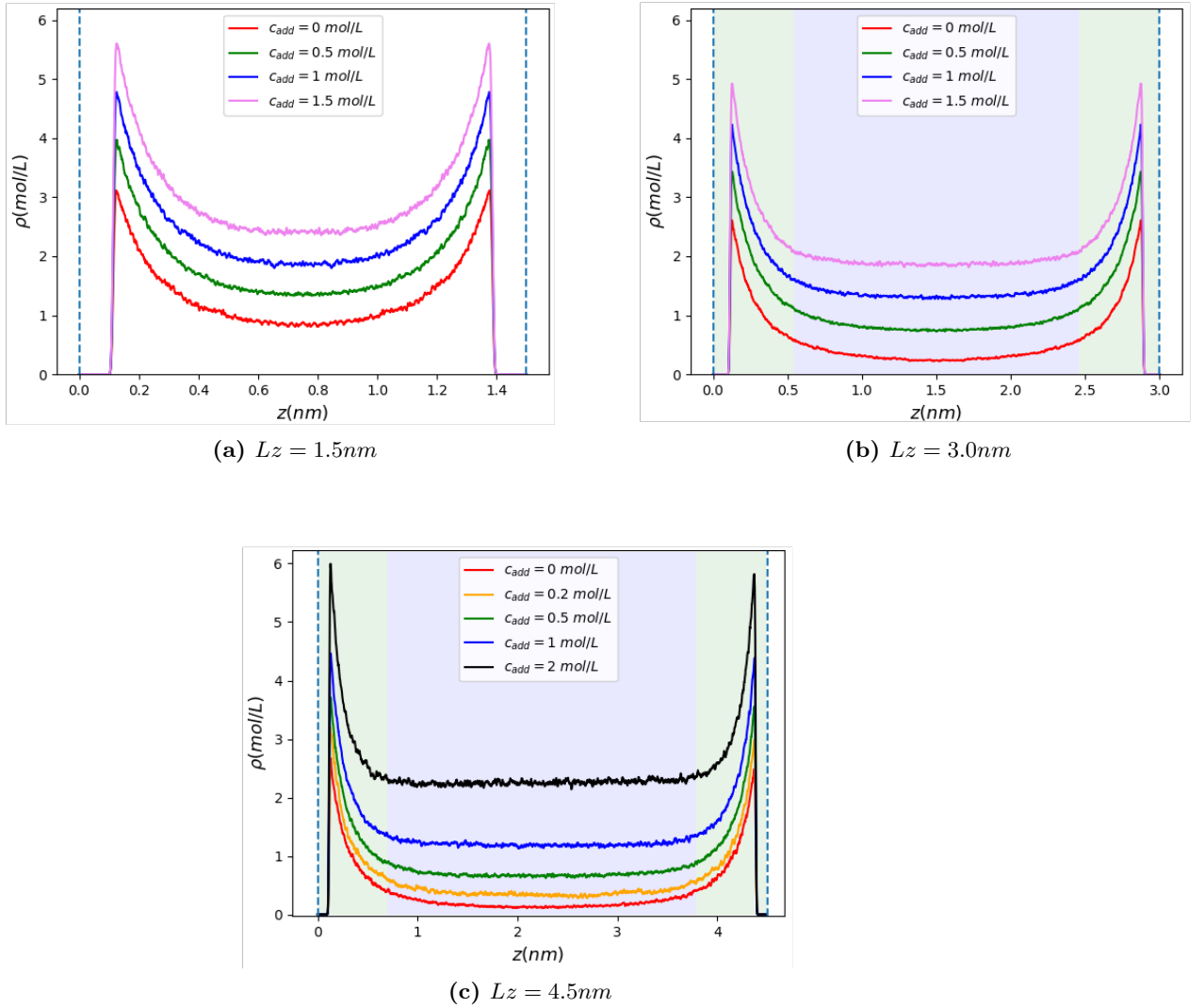


Figure 3.6 – Density profiles of counterions as function of the distance to the wall for $\sigma_{wall} = -0.5$ e/nm^{-2} . Vertical blue dashed lines represent the positions of the walls.

the walls. By doing so, a layer known as the Electric Double Layer is formed, which plays an important role on the dynamics of the system (see Chapter 1 for further discussion). Then, the concentration of counterions near the wall increases as the charge on the wall increases (see Fig. 3.6 (c) and Fig. 3.7 (c)). A natural scale that comes out at the level of ion-ion interactions is the so called Bjerrum length, which is defined as the distance at which the electrostatic interaction between two charged species becomes of the order of the thermal energy. It then reads as

$$l_B = z^2 e^2 / (4\pi\epsilon k_B T) \quad (3.10)$$

Considering bulk water at ambient temperature and valency $z = 1$, the Bjerrum length has a value of 0.71 nm. Another important length is the Debye length, which characterizes the electrostatic screening in the bulk electrolyte^[110]. It is given by

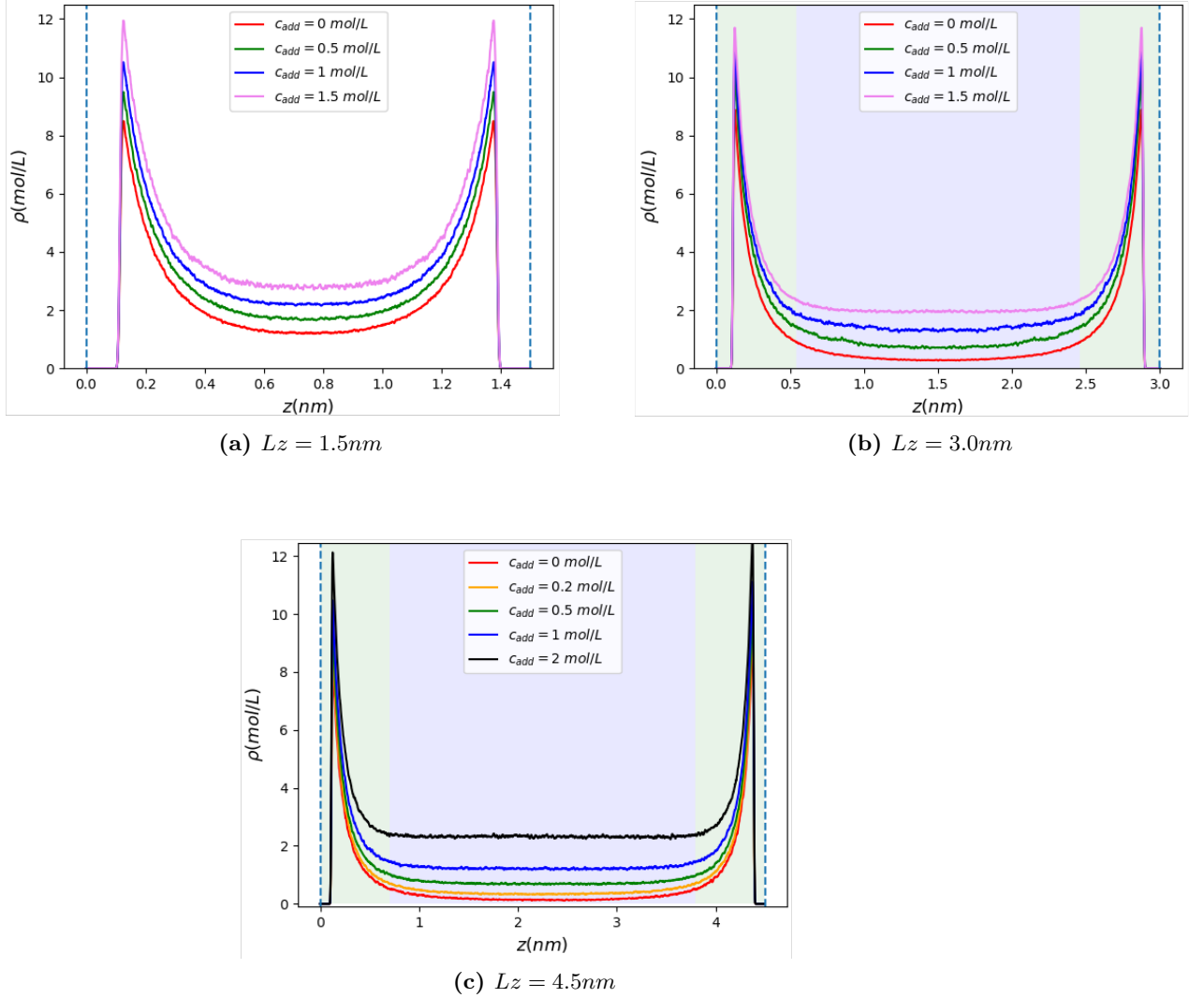


Figure 3.7 – Density profiles of counterions as a function of the distance to the wall for $\sigma_{wall} = -1 e/nm^{-2}$. Vertical blue dashed lines represent the position of the walls.

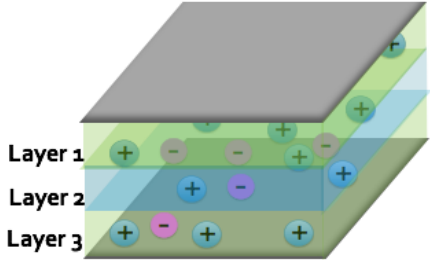
$$\lambda_D = (8\pi l_B \rho_s)^{-1/2} \quad (3.11)$$

where ρ_s denotes the salt concentration in the reservoir at equilibrium with the system which is not the same as the added salt concentration in our system (as discussed in Chapter 1). However, this formula is just applied considering low added salt values. The values of λ_D related to our systems are shown in Table 3.4. λ_D decreases as the concentration of added salt increases. λ_D is of the order of the EDL width, thus the screening created by the added salt is translated in a reduction on the EDL thickness. This fact is observed in the density profiles as they get closer and closer to the value of the salt concentration in the reservoir (flat part of ρ). Hence the density profile reaches the plateau value “faster” for the largest c_{add} than for the smallest added c_{add} . However, this effect is less clear for the smallest confinements due

concentration added salt (mol/L)	$\lambda_D(nm)$
0.2	0.55
0.5	0.37

Table 3.4 – Debye length compute for different added salt concentration. Following Eq. 3.11, where ρ_s the salt concentration in the reservoirs is taken from the plateau value of the ion density profile.

to the proximity of the order of magnitude between the confinement and the Debye length.



	Layer range (nm)
Layer 1	0 - 0.54
Layer 2	0.54 - 2.46
Layer 3	2.46 - 3.0
Layer 1	0 - 0.70
Layer 2	0.70 - 3.79
Layer 3	3.79 - 4.5

Table 3.5 – On the left side: Schematic representation of the layer division of the system, the blue part refers to layer 2 and green parts refer to layer 1 and layer 3. On the right side: A table showing the layers ranges defined in each system, where the blue part of the table corresponds to the lowest confinement, *i.e.* $Lz = 4.5nm$. The gray part is then the confinement $Lz = 3.0nm$.

The concentration of ions depends strongly on the region of the system where they lie. Thus, in order to make a better study of the dynamics part, a division of the system was done by defining three different layers for each confinement as shown in the figure of Table 3.5. The selection of the width layer is done taking into consideration the ions density profile at each confinement. Layer 2 is defined as the region where the density profile of ions reaches the plateau, whereas layer 1 and layer 3 encompass the remaining parts by each side until the wall is reached (dashed line). On the previous plots, these layers were represented following the same code of colours shown in the figure of Table 3.5. At $Lz = 1.5 nm$, no layer was determined. Finally, the range of each layer at different confinements is shown in Table 3.5, where the grey part is related to the confinement at $Lz = 3.0 nm$, whereas the blue part is for $Lz = 4.5 nm$.

3.4.2 Coions

The presentation of the co-ion density profiles follows the one made for counterions. Ergo, in Fig. 3.8 different confinements are shown ($Lz = 1.5 nm$, $3.0 nm$ and $4.5 nm$) in each plot, for the case of $\sigma_{wall} = -0.5 e/nm^{-2}$, whereas for Fig. 3.9 the value of σ_{wall} is $-1 e/nm^{-2}$.

Likewise, co-ions will follow the same division of the system by layers, *i.e.* we will take the same layers ranges as the ones that were defined by the ion density profile of counterions (see Table 3.5). The division of layers is shown on the co-ion density profiles by their respective colors (namely blue for layer 2 and green for layer 1 and layer 3).

The behaviour that co-ions present is opposite to counterions, since they have a tendency to move to the middle of the slit pore, away from the walls (diffusive part of the EDL), due to the electrostatic repulsion created by the charged wall. That is the reason why the

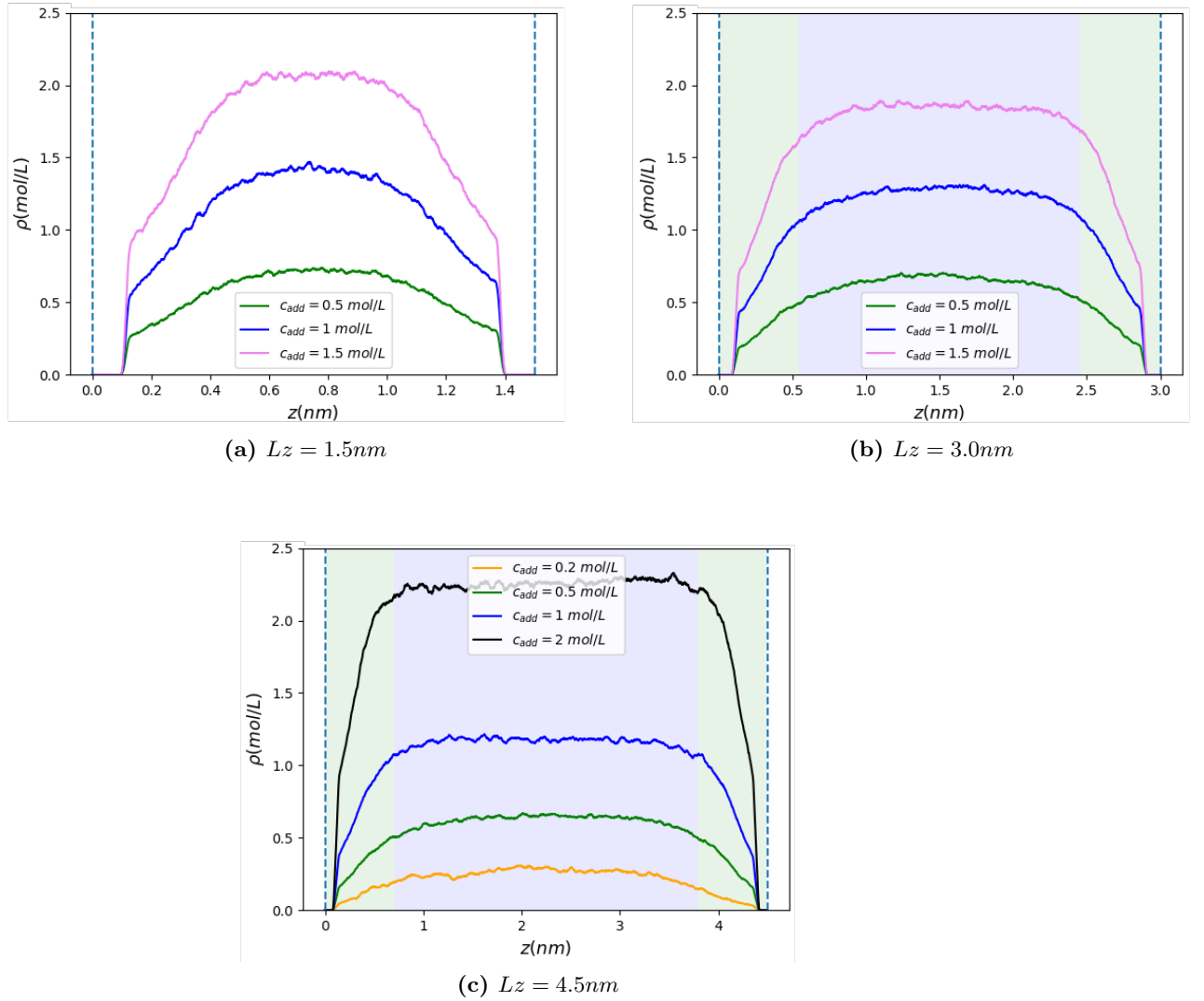


Figure 3.8 – Density profiles of co-ions as a function of the distance to the wall for $\sigma_{wall} = -0.5 e/nm^{-2}$. Vertical blue dashed lines represent the positions of the walls.

maximum value of the co-ion density profile are found in the middle of the slit pore, contrary to counterions where the maximum is close to the walls.

For confinements $L_z = 3.0\text{ nm}$ and $L_z = 4.5\text{ nm}$ there exists electroneutrality in the middle of the pore (bulk layer), meaning that the concentration of counterions and co-ions is found to be the same. And thus, creating an overlap of the curves corresponding to the counterions and co-ion density profile as shown in Fig. 3.11 and Fig. 3.12 in the middle of the pore. For the confinement $L_z = 1.5\text{ nm}$ electroneutrality is not reached contrary to the case previously shown when comparing the values at $L_z/2$ for $\rho_{\pm}(z)$ in Figure 3.6 (a) and Figure 3.7 (a). For example, if we consider the particular case of $c_{add} = 1.5\text{ mol/L}$ and $\sigma_{wall} = -0.5 e/nm^{-2}$, the value of the counterions density profile at $L_z/2 = 0.75\text{ nm}$ is 2.58 mol/L , whereas for the co-ion density profile is 2.1 mol/L . The values of the ionic

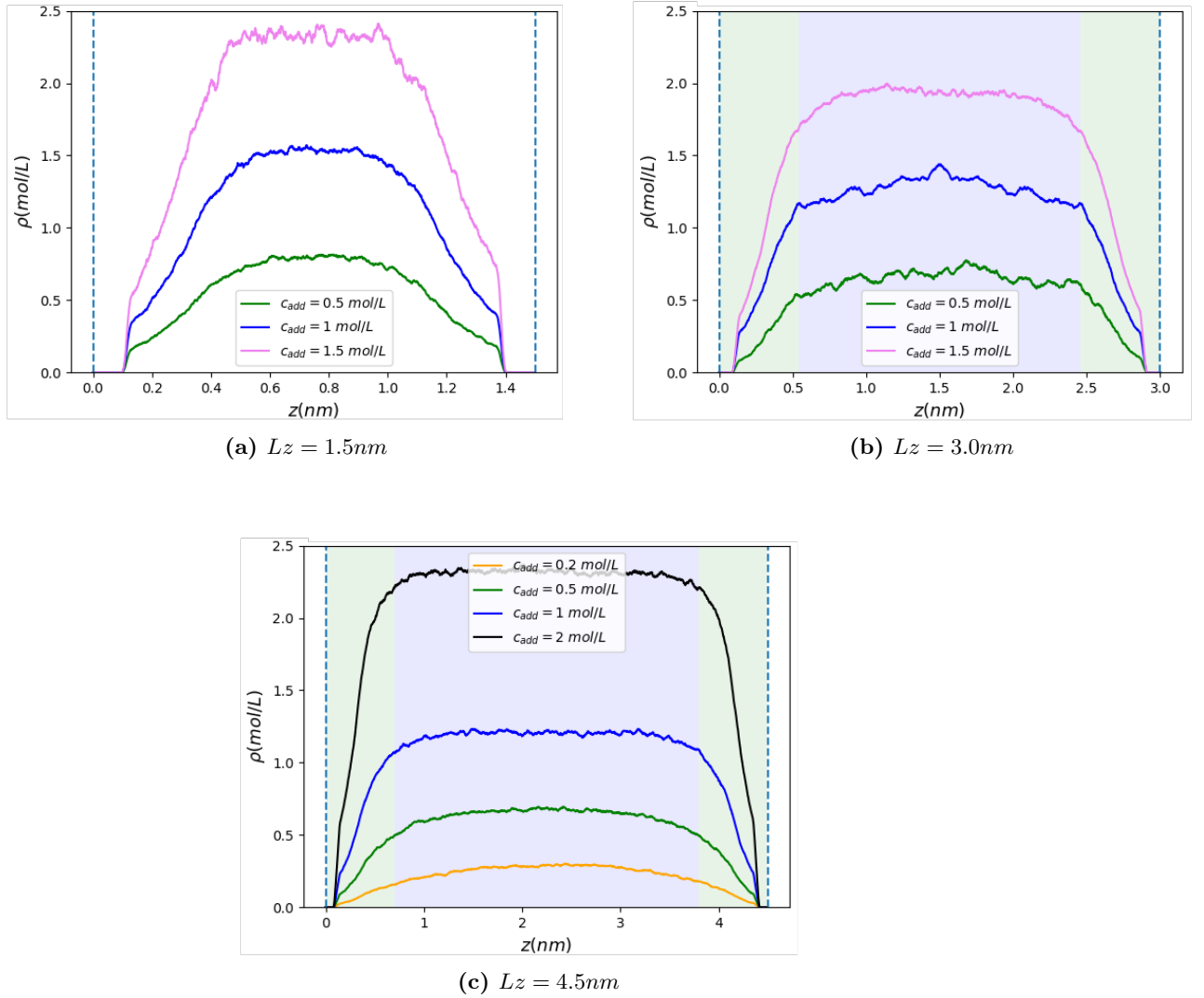


Figure 3.9 – Density profiles of co-ions as a function of the distance to the wall for $\sigma_{wall} = -1 e/nm^{-2}$. Vertical blue dashed lines represent the positions of the walls.

concentration in the middle of the pore are shown in Table 3.6 for the different systems studied for the lowest confinement, *i.e.*, $L_z = 4.5\text{ nm}$. Electroneutrality exists in the middle of the pore in this case. So that the concentration of co-ion and counterions is the same.

3.4.3 The ionic density profiles are those of PB

A comparison of the computed ionic density profiles in the direction perpendicular to the surface, with known semi-analytical results, was carried out. It is important to mention that this kind of comparison was previously done in other works^[111–114] for different simulation methods. Among them, the work done by Ceratti *et.al.*^[114] was obtained using the same method of simulation as the one in this work, *i.e.* MPCD in the case without added salt.

Value of the ion density profile in the middle (mol/L)				
σ_{wall} (e/nm^2)	$c_{add} = 0.2$ mol/L	$c_{add} = 0.5$ mol/L	$c_{add} = 1$ mol/L	$c_{add} = 2$ mol/L
-0.5	0.32	0.678	1.136	2.19
-1	0.32	0.67	1.23	2.29
-2	0.33	0.72	1.24	2.3

Table 3.6 – Values of the ion density profile in the middle of the slit pore where electroneutrality exists for the system with $L_z = 4.5$ nm.

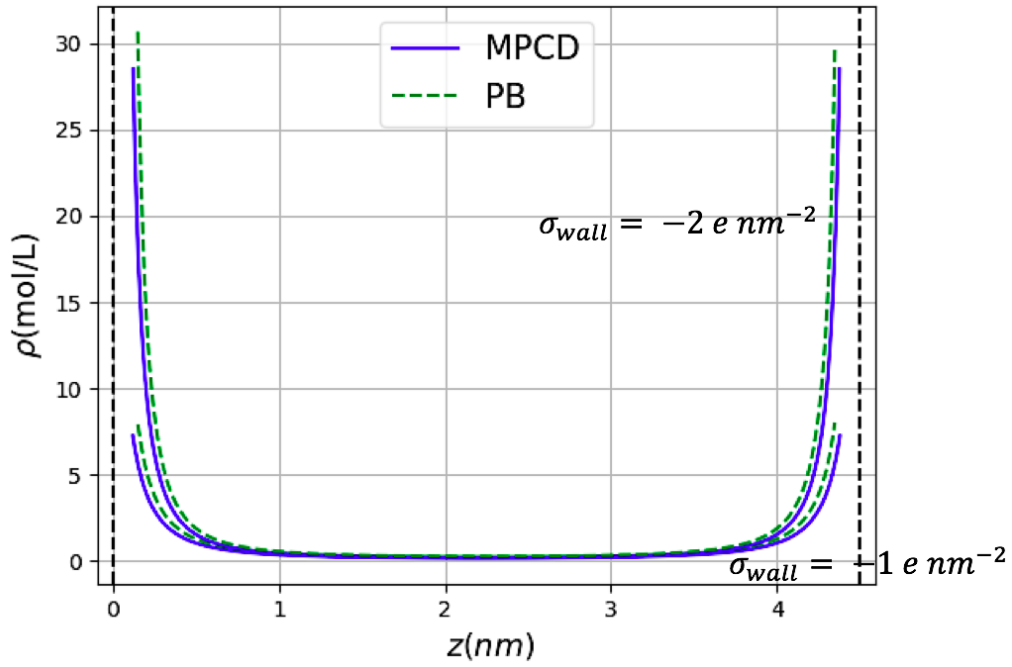
In this study a comparison between the counterions density profile from MPCD and the PB theory is presented. The authors discuss how the density profile is influenced:

1. By short-ranged repulsion vs no short range repulsion between counterions
2. By the discretization level d of the charge within the wall, *i.e.* the average surface charge is distributed over discrete size of charge $-e/d$ within the solid wall.
3. By the average charge on the wall

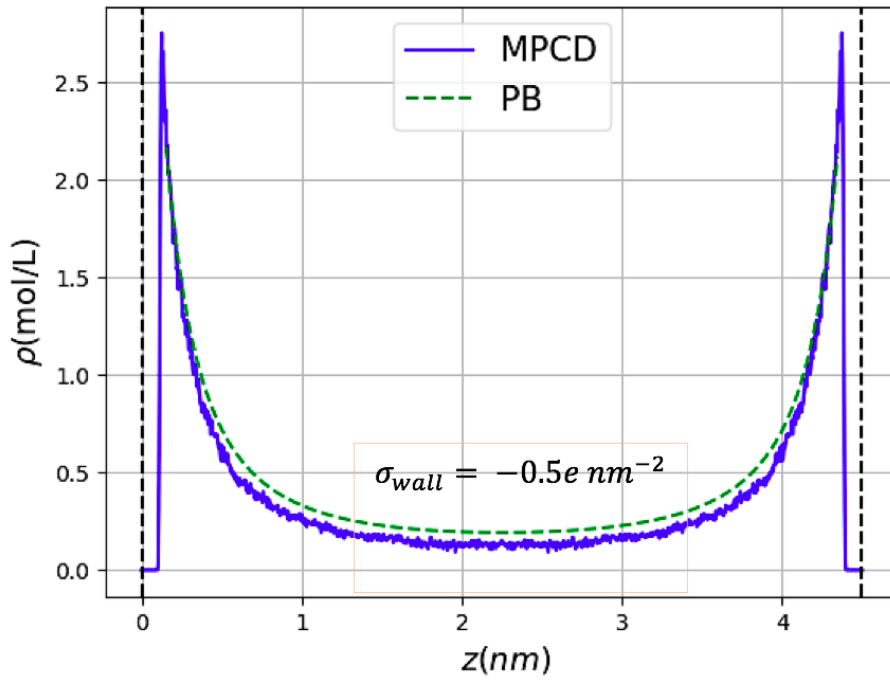
They found that adding a short-range WCA repulsion between ions does not affect the structure of the counterions density profile. In both cases (*i.e.* if WCA is considered or not) the comparison with the PB theory shows some differences at the wall. This was expected since the PB theory underestimates the ionic condensation at the surface. Indeed, in our study (added salt case), WCA interactions were taken into account, since they are important to assess the influence of excluded volume effects between ions. In order to carry out the discretization parameter analysis, different values of d were chosen. For the case of $d = 1$, *i.e.* when the charge is located in a certain specific position in the wall, the ion density profile (obtained through MPCD) overestimates the ionic condensation at the surface compared with the PB results. Moreover, as d increases, the overestimation is reduced.

The study concludes that interactions with the surface become smooth as d is increased, until the behaviour for a uniform continuous distribution is recovered. However, in real systems the charge on a surface is discretized. Thus for the added salt study presented further in this thesis, the value d was selected following a discretized distribution (their precise selection is discussed in section 3.2.3). Finally, when the average charge of the wall increases, the differences between the counterion density profiles predicted by the PB treatment and the ones obtained through simulation become significant. This is explained since ions in the PB theory are point-like particles contrary to MPCD simulation. Thus, the average distance between walls and counterions decreases as the charge surface increases, due to the increase of electrostatic correlations.

In order to complement the results obtained from Ceratti, the same study was carried out by us. In this, the analysed cases were $\sigma_{wall} = -0.5, -1$ and -2 e/nm^2 , that correspond to values not investigated in reference 114. Moreover, we only consider systems where WCA interactions between ions are taken into account, and where discretization level is $d = 1$. The results obtained are shown in Fig. 3.10. From this figure, we can conclude that small discrepancies appear between the PB and the MPCD ion density profiles (see Fig. 3.10). Moreover, these differences become larger as the concentration of the charge in the wall increase.

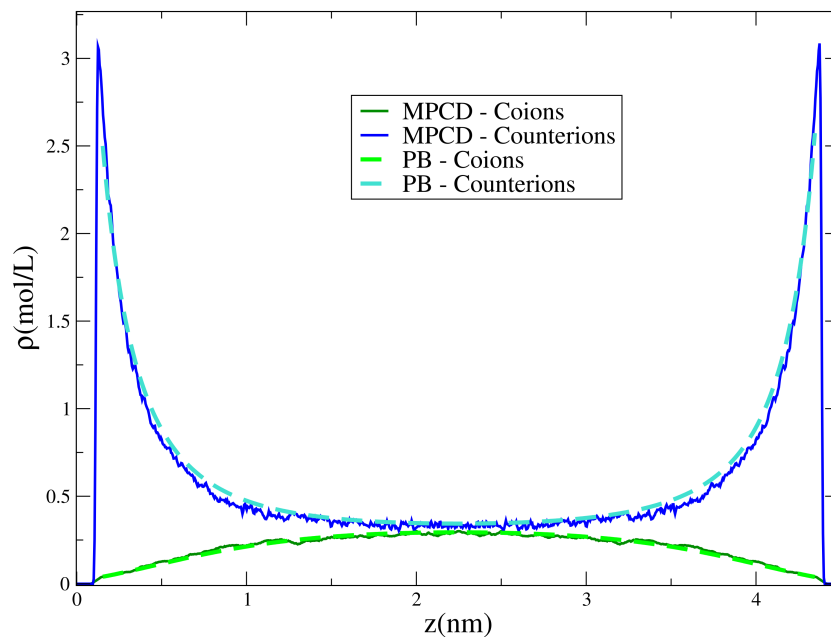


(a)

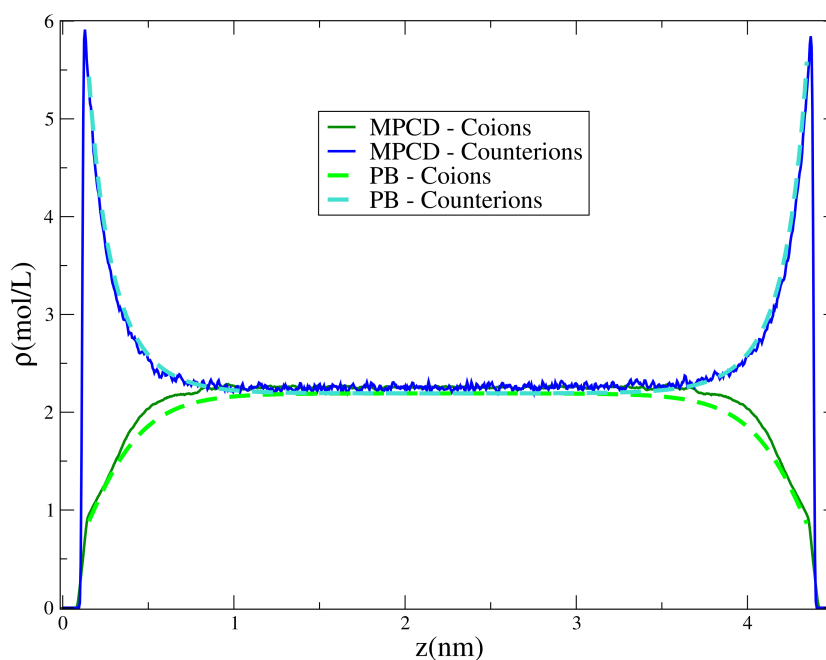


(b)

Figure 3.10 – Comparison between ion density profiles obtained through PB (green dashed line) and MPCD (blue line) as a function of the distance to the wall. The case shown here corresponds to $\sigma_{wall} = -0.5$ (Figure (b)), -1 and $-2 e/nm^{-2}$ (Figure (a)) and no added salt. Black dashed vertical lines indicate the positions of the walls. For PB calculations we took $L_z = L_{el}$ (see Fig. 3.3).

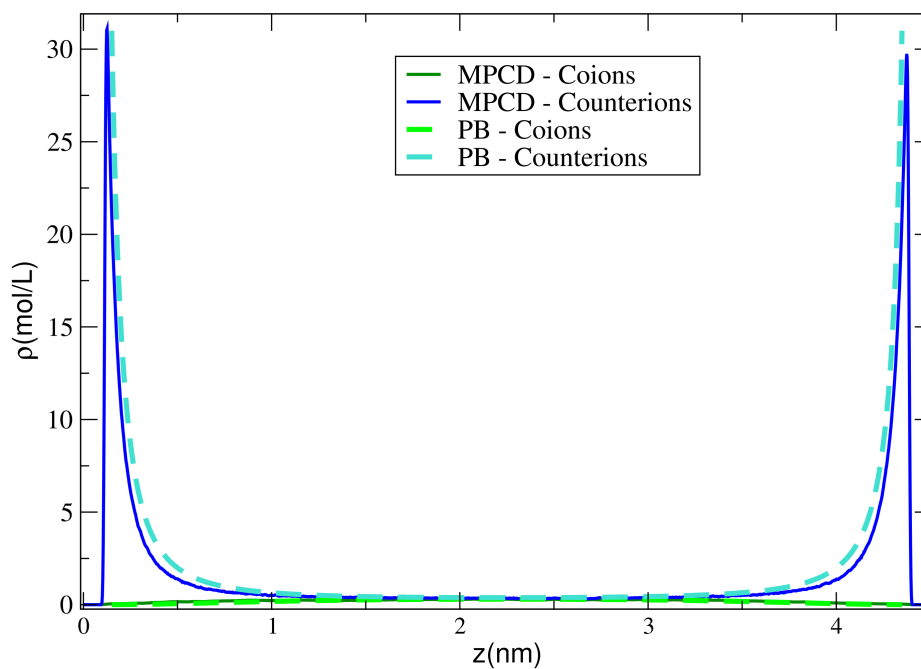


(a) concentration of added salt 0.2 mol/L

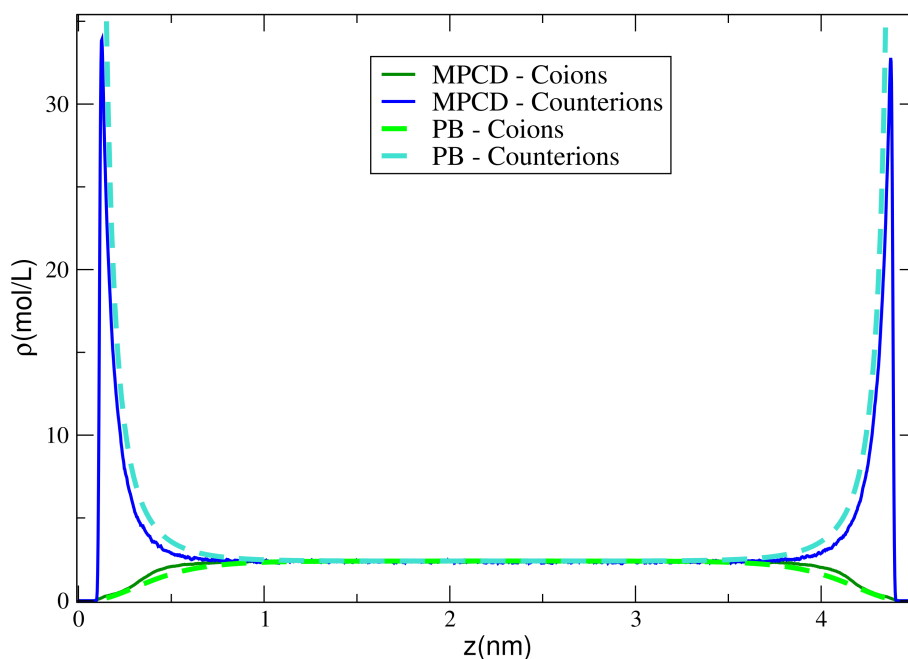


(b) concentration of added salt 2 mol/L

Figure 3.11 – Comparison between ion density profiles obtained through PB and MPCD as a function of the distance to the wall. Counterions density profiles correspond to blue lines (MPCD) and dashed lines (PB) and co-ions density profiles correspond to green lines (MPCD) and dashed lines (PB) for the case of $\sigma_{wall} = -0.5 e/nm^{-2}$. Black dashed vertical lines indicate the positions of the walls.



(a) concentration of added salt 0.2 mol/L



(b) concentration of added salt 2 mol/L

Figure 3.12 – Comparison between ion density profiles obtained through PB and MPCD as a function of the distance to the wall. Counterions density profiles correspond to blue lines (MPCD) and dashed lines (PB) and co-ions density profiles correspond to green lines (MPCD) and dashed lines (PB) for the case of $\sigma_{wall} = -2 e/nm^{-2}$. Black dashed vertical lines indicate the positions of the walls.

Secondly, we made a comparison of the ion density profile obtained through MPCD and Poisson Boltzman theory (when Donnan effect is taken into account) in the case with added salt. The value of $Lz = L_{el}$ (*i.e.* $L_{el} = L_{hyd} - \sigma_w$) was taken for Poisson Boltzman theory. As well as, $c_{reservoir} = c_{middle}$, where c_{middle} corresponds to the value of the ion density profile at the middle of the slit pore.

In Fig. 3.11 and Fig. 3.12, the counterions and co-ions density profiles are shown for the most extreme cases in terms of charge of the wall and of the added salt concentration. In other words, we consider the four possible combinations of $\sigma_{wall} = -0.5$ and $-2 e/nm^2$ and $c_{add} = 0.2$ and $2 mol/L$ for the largest separation L_z between the walls, as shown in Table 3.3. When the charge on the walls increases, the differences between the ion density profiles predicted by PB and the ones obtained through MPCD simulations become slightly apparent. A good agreement is found in the middle region of the channel (*i.e.* bulk region) for all the cases. However a small difference slowly appears as we get closer to the walls (dashed lines). This difference is normal as the MPCD method considers explicit ions with a finite size. Thus as σ_{wall} increases, the average distance between ions at the surface decreases.

In conclusion we can say that the ionic density profiles computed from MPCD simulations, that account for excluded volume between ions, are correctly described by the PB approximation except for the region very close to the wall.

3.5 Diffusion Coefficient of ions

The diffusion coefficient of ions in the direction parallel to the walls is computed using the method explained in Chapter 2. This method has the advantage that the diffusion coefficient can be obtained in defined layers of the system, allowing us to study the ions dynamics behaviour in more details.

In the two first subsections (bulk and neutral walls), the diffusion coefficient is computed over the whole space, *i.e.* in all the simulation box for bulk and for the space between the slit pore for neutral walls. Then, it is divided by $D^0 = 0.04174 a_0^2 t_0^{-1}$ which is the diffusion coefficient of an ion at infinite dilution (see Chapter 2 for further discussions on the numerical calculation of this parameter). Whereas in subsection 3.5.3, the case of the diffusion coefficient in a system under electrostatic confinement is analysed.

3.5.1 Diffusion in bulk solution

First, the diffusion coefficient of ions in bulk solution was computed using the MPCD code, and then compared to the experimental results found in Reference 115 (see Fig. 3.13) for the self-diffusion coefficients of Cl^- ion in a series of alkali metal chloride solutions. From this comparison, we can observe that in both cases the behaviour has the same tendency, *i.e.* the diffusion coefficient decreases as the concentration increases and reaches a plateau value with $\frac{D}{D^0} \approx 0.91$ in MPCD. This behaviour is expected and is attributed to the electrostatic interaction between ions. As the concentration of ions increases, ions tend to be closer and closer and thus to be more influenced by the ionic electrostatic interactions.

Nevertheless, different orders of magnitude of difference can be observed when comparing MPCD and experiments results, which is explained by the fact that no specific kind of particle and solvent was considered in our simulations, contrary to the experiment which was carried

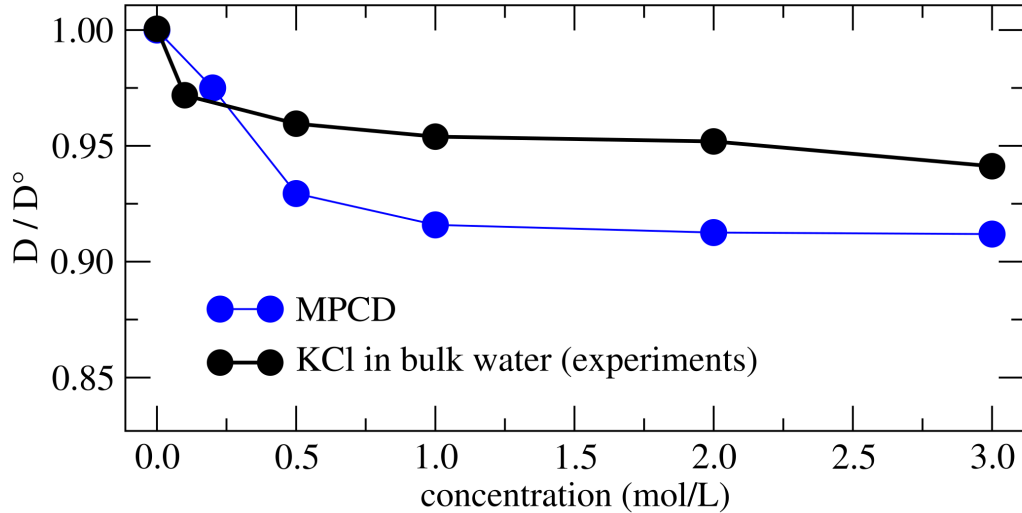


Figure 3.13 – Comparison of the ionic diffusion coefficient in bulk solutions between MPCD and experimental results. This as a function of the ion concentration and divided by the diffusion coefficient of an ion at infinite dilution. Experiments correspond to an aqueous solution of potassium chloride at 198 K.

out in a specific solution of potassium chloride. Thus, the lack of detail in our simulation method can lead to differences on the values of the diffusion coefficient when comparing them with any experimental result. From here we can say that the MPCD results obtained for the diffusion coefficient are qualitatively correct. This allows us to carry on the analysis of this transport coefficient for different cases, such as an ionic solution between neutral walls and charged walls.

3.5.2 Influence of a neutral confinement

A comparison of D/D^0 was done for the cases of a bulk solution and a solution confined between neutral walls in Fig. 3.14 (for different confinements). We observe that D/D^0 has larger values in the bulk than when confined by neutral walls. Indeed, for this last case, D/D^0 decreases as the concentration c increases, contrary to the bulk where we an almost constant value for $c > 1 \text{ mol/L}$ is found.

Furthermore, looking at the result carried out for neutral walls, we notice that D/D^0 presents a small confinement dependence. Indeed, the diffusion coefficient for the same system (*i.e.* same concentration) slightly decreases as the confinement increases (*i.e.* lower values of Lz), implying that D slightly depends on the confinement width. This can be explained by looking at the ion density profiles in section 3.4. For both ions we observe that as confinement increases (*i.e.* lower values of Lz), the bulk part of the ion density profile decreases. Therefore, less and less ions will have the bulk behaviour, and will thus start to be more affected by the walls presence. Indeed other works^[116] similar results were found.

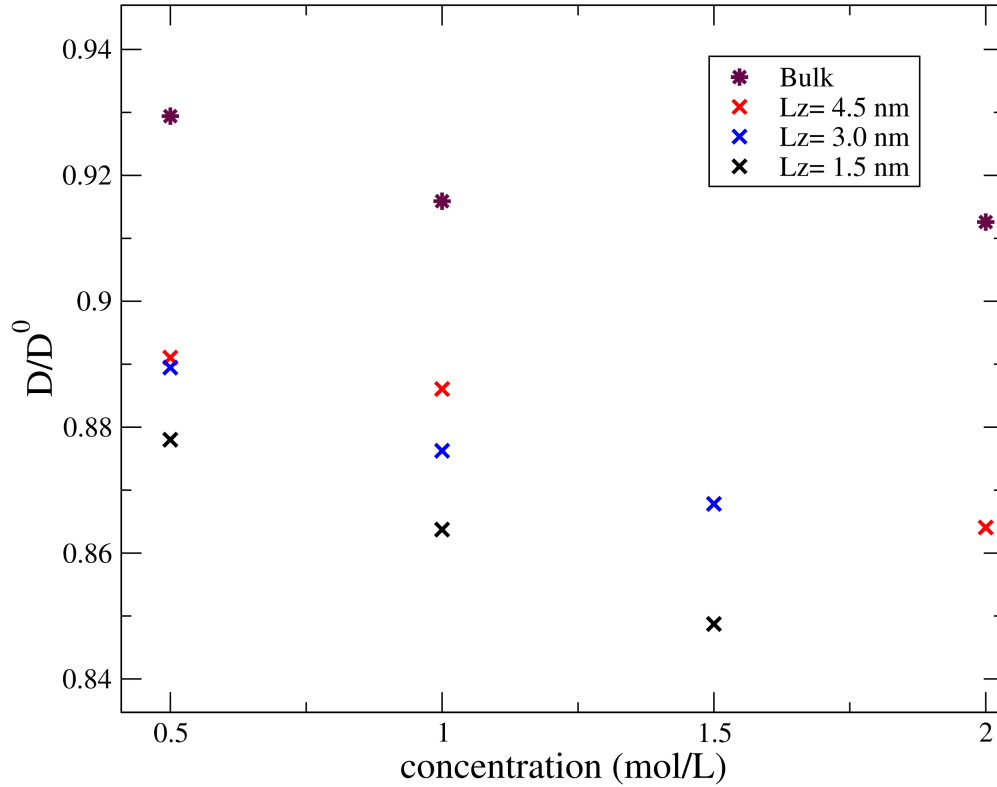


Figure 3.14 – Comparison of the diffusion coefficient parallel to the wall (in the whole space between the slit pore) between a bulk ionic solution and an ionic solution confined between neutral walls, as a function of the ion concentration. In the latter case, different confinements are considered, *i.e.* different distances between walls in the slit pore (values of the distances are designated by the different color crosses).

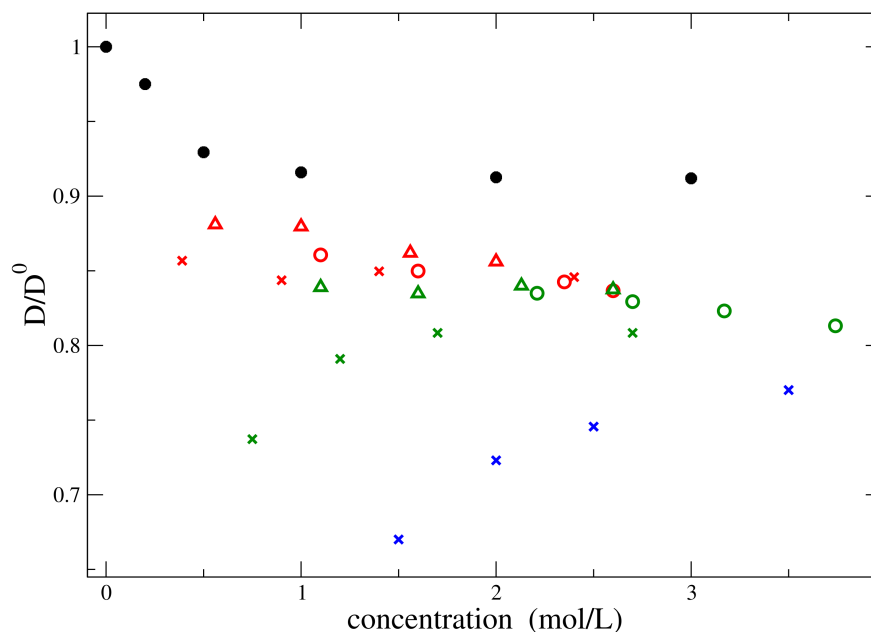
3.5.3 Influence of an electrostatic confinement

Here we consider the case where walls bear a surface charge density and co-ions and counterions do not have the same behaviour anymore.

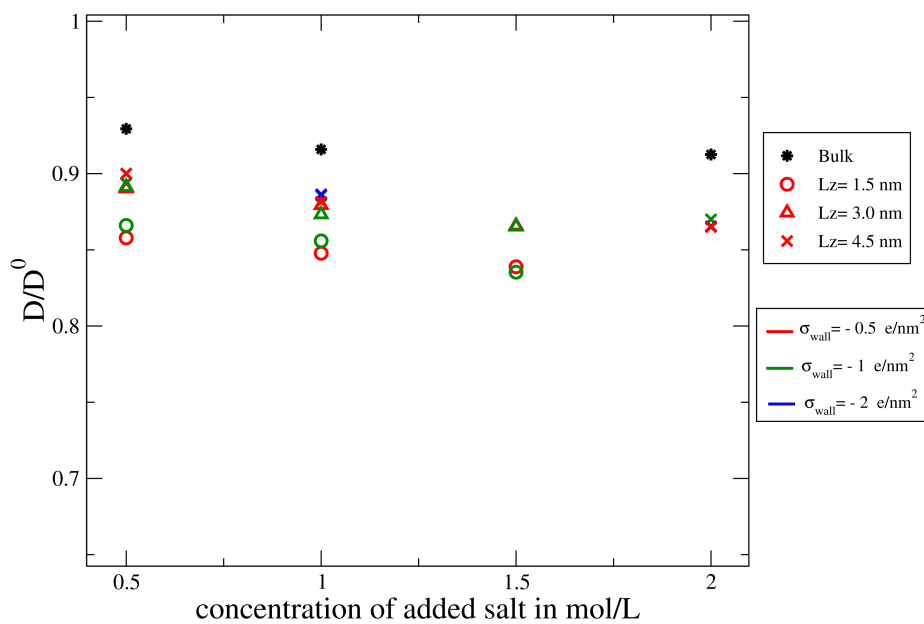
3.5.3.1 Diffusion coefficient averaged over all the simulation box

The diffusion coefficient for counterions as a function of the concentration is shown in Fig. 3.15 a) for different confinements. The concentration in this case corresponds to the concentration of the added salt plus the concentration of the neutralizing counterions (*i.e.* the number of ions to neutralize the charge on the wall). Whereas, for co-ions the concentration in Fig. 3.15 b) refers to the concentration of added salt. This difference was necessary in order to be able to compare the diffusion coefficient of each ion to the bulk case.

From the figures we can see that in both cases the diffusion coefficient in the bulk is larger than in the charged wall case. This result is expected since confinement slows down the movement of ions. Furthermore, it is evident that the behaviour between counterions and co-ions is completely different. On one hand, the diffusion coefficient of co-ions does not seem to be affected by the change of surface charge for any given confinement. Moreover, D/D^0 seems to slightly decrease as the concentration of added salt increases. On the other



(a) Self diffusion coefficient of counterions as a function of the concentration (concentration of added salt + concentration of neutralizing counterions). Bulk diffusion coefficient is shown as a point of reference (black dots).



(b) Self diffusion coefficient of co-ions as a function of the concentration (concentration of added salt). Bulk diffusion coefficient is shown as a point of reference (black dots).

Figure 3.15 – Self diffusion coefficient of ions with direction parallel to the walls in a slit pore of charged walls as a function of the concentration and of the charge of the walls (different colors) for different confinements (different symbols). Figure a) counterions and b) co-ions. In each case a comparison with the bulk case is carried out.

hand, the diffusion coefficient of counterions decreases as σ_{wall} increases for all confinements. Specifically, in the case of $\sigma_{wall} = -1 e/nm^2$ and $-2 e/nm^2$, D/D^0 increases as the concentration increases. In order to understand this behaviour, a study of the diffusion coefficient by layers was carried out.

3.5.3.2 Diffusion coefficient as a function of the distance to the walls

So far, the diffusion coefficient computed over the whole space between the slit pore was obtained for different cases (*i.e.* bulk, neutral and charged walls). However, as we are interested in the EDL behaviour, an analysis of the diffusion coefficient computed layer by layer was carried out. To do so, we follow the method described in Section 2.1.3. And, similarly to the previous results, D_i is divided by the value of the diffusion coefficient corresponding to an infinite dilution.

In the following figures we shall refer to "close to the surface" as the region corresponding to surface layer. Similarly, bulk layer will be denoted as "far from the surface". Specifically for the case "close to the surface", results obtained in layer 1 and layer 3 are averaged. This is possible considering that the density profiles of the ions are symmetric and thus this process will lead us to better statistics in our results.

Moreover, as the concentration of ions is known to influence the diffusion coefficient, an analysis related to this parameter was carried out. To do so, the ratio of the total number of ions (counterions+co-ions) in the layer close to the walls divided by the total number of ions far from the wall (*i.e.* $\frac{N_{layer1}}{N_{layer2}}$) is presented as a function of the concentration of added salt, for different values of the charge of the wall. In fact, this analysis illustrates the tendency that ions have to remain on the surface or in the bulk layer region.

- If $N_{layer1}/N_{layer2} = 1$, there is an equal quantity of ions in both layers.
- if $N_{layer1}/N_{layer2} > 1$, ions are more abundant in surface layer.
- if $N_{layer1}/N_{layer2} < 1$, ions dominate in bulk layer.

This study was carried out at each confinement.

1. Low confinement $Lz = 4.5 nm$

Considering the system with smallest confinement (*i.e.* $Lz = 4.5 nm$), the diffusion coefficient of ions is computed in the chosen layers as defined in Section 3.4.

Figure 3.16 shows the ratio of the total number of ions (counterions and co-ions) in the layer close to the walls divided by the total number of ions (counterions and co-ions) far from the wall, as a function of the concentration of added salt for different values of σ_{wall} .

For the no salt case, we can observe in Figure 3.16 that ions have a tendency to be more in the surface layer than in the bulk layer, as σ_{wall} increases. This is due to the electrostatic attraction that the charged walls exert on the counterions. However, as the concentration of added salt increases the ions have the tendency to be more in bulk than surface layer. This is explained by the screening caused by the added salt, which prevents the counterions from being attracted by the walls.

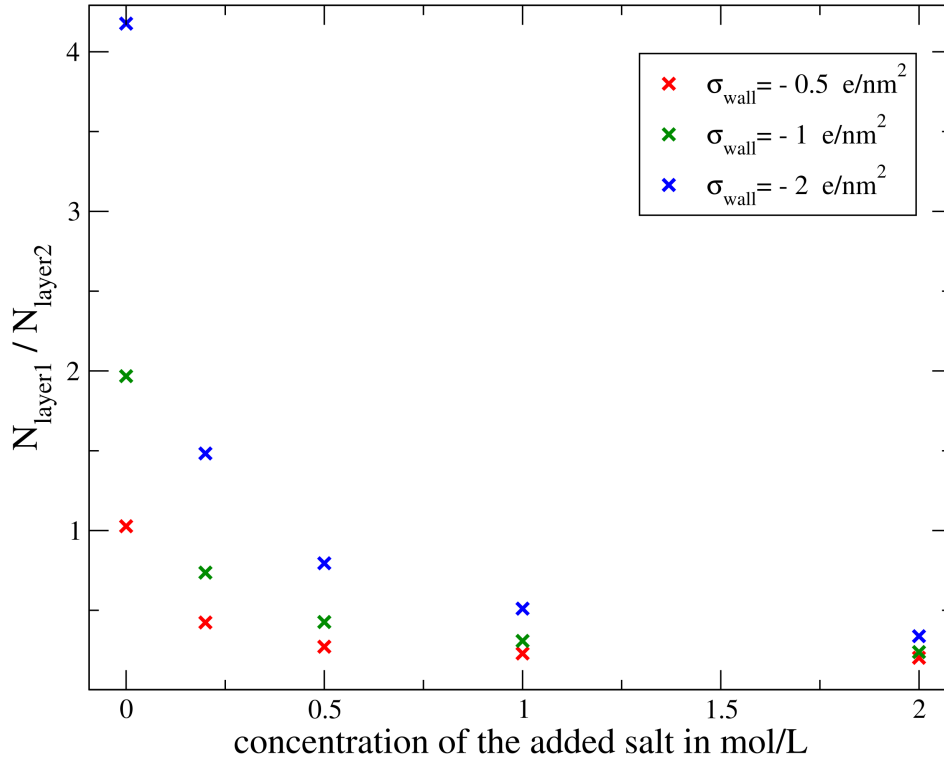
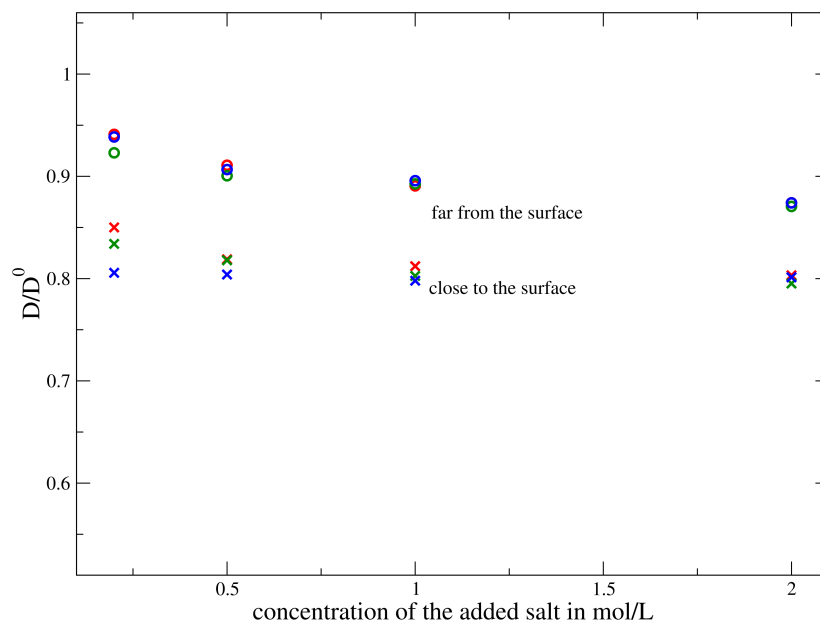


Figure 3.16 – N_{layer1}/N_{layer2} is presented as a function of the concentration of added salt varying the charge on the wall. Where the number of ions that is considered here is of both ions (counterions and co-ions). This analysis is made for the confinement $Lz = 4.5 \text{ nm}$.

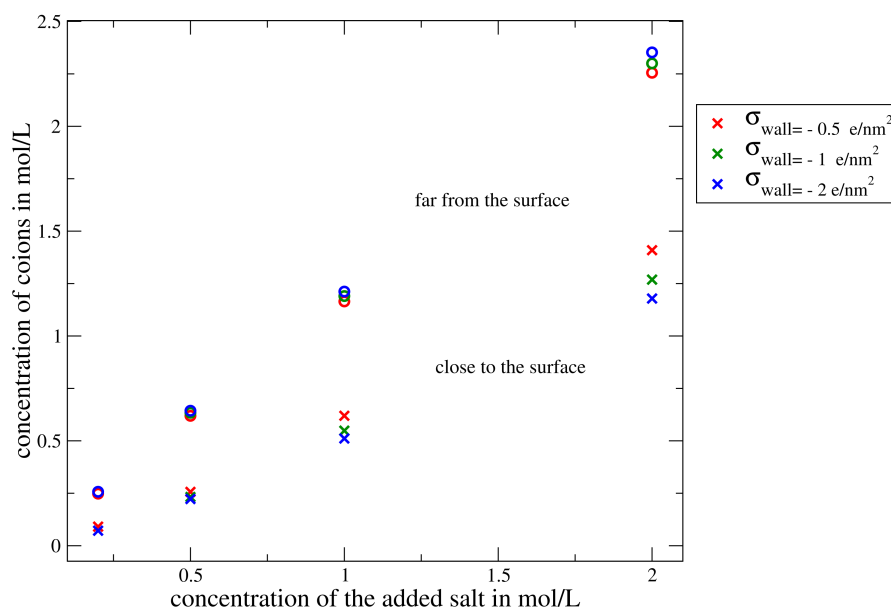
Two contributions that play an important role on the diffusion coefficient are the concentration and the electrostatic interactions (ion-ion and ion-wall). That is the reason why, varying these parameters (*i.e.* σ_{wall} and c_{add}) allows us to determine how much influence they have on the diffusion coefficient. In Figure 3.17 (a) the values for D/D^0 of co-ions are exposed for the cases near and far from the walls.

In this particular situation we see that D/D^0 is higher in the region far from the wall than close to the wall. Moreover, for both cases the diffusion coefficient slightly decreases as the concentration of added salt increases and seems to be less perturbed by the surface charge density. Then, we conclude that the concentration plays a larger contribution than the electrostatic interactions with the wall. This last deduction can be justified by looking at the Figure 3.17 (b), where a higher concentration of co-ions far from the wall than close to the surface is observed for each value of the charge of the wall.

Figure 3.18 (a) gives the results obtained for counterions ; two different phenomena were observed. The first corresponds to the case far from the surface. where the bulk behaviour is recovered: D/D^0 slightly decreases as c_{add} increases. The second, corresponds to the study in the region close to the surface, for a given charge on the wall, where the diffusion coefficient is almost constant and does not depend on the concentration. Furthermore, comparing figure 3.18 (a) and figure 3.17 (a) shows that counterions have a larger difference between the values for the diffusion coefficients close and far from the

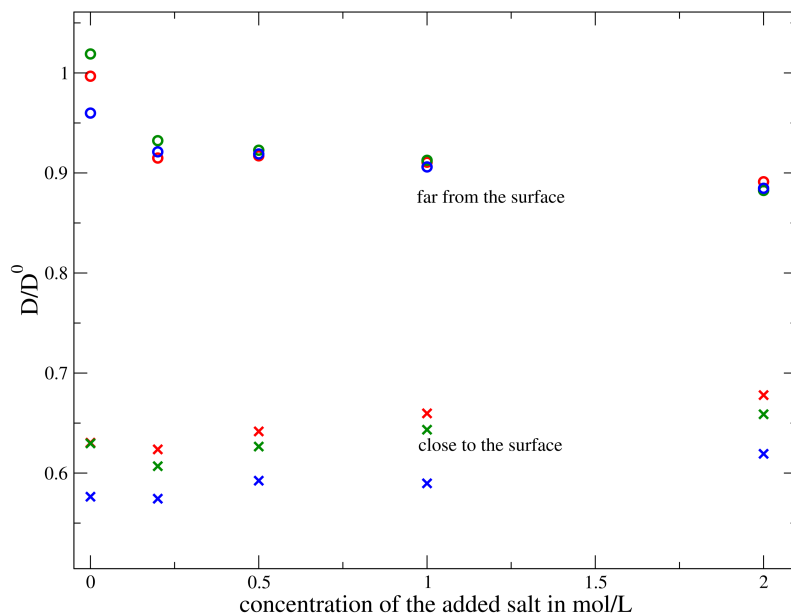


(a) Diffusion coefficient of co-ions computed by layers.

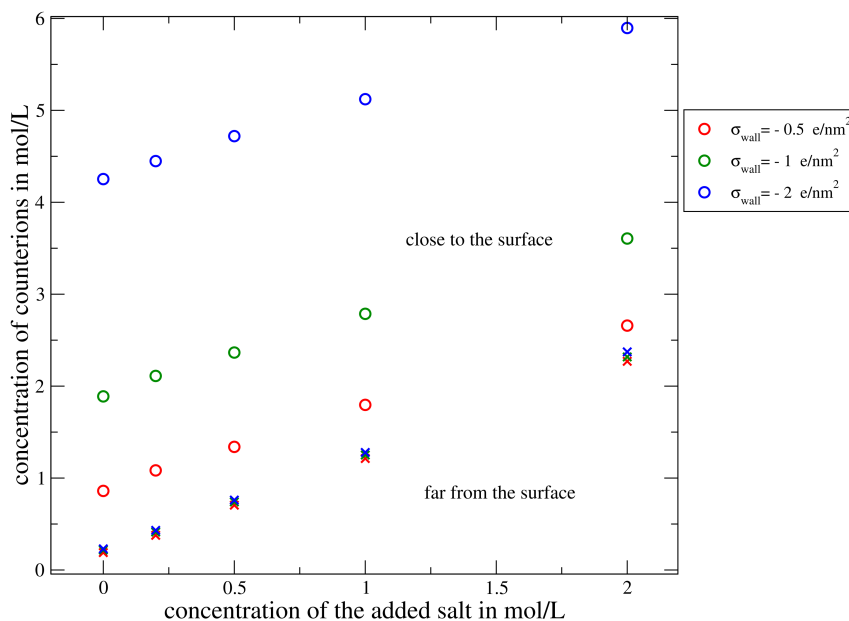


(b) Concentration of co-ions computed by layers.

Figure 3.17 – (a) Self diffusion coefficient of co-ions computed by layers in the direction parallel to the wall as a function of the concentration and of the charge of the walls for the low confinement *i.e.* $Lz = 4.5 \text{ nm}$. (b) Concentration of co-ions as a function of the concentration of added salt varying the charge on the wall computed by layer for the low confinement *i.e.* $Lz = 4.5 \text{ nm}$.



(a) Diffusion coefficient of counterions computed by layers.



(b) Concentration of counterions computed by layers.

Figure 3.18 – (a) Self diffusion coefficient of counterions computed by layers in the direction parallel to the wall as a function of the concentration and of the charge of the walls for the low confinement *i.e.* $Lz = 4.5 \text{ nm}$. (b) Concentration of counterions as a function of the concentration of added salt varying the charge on the wall computed by layer for the low confinement *i.e.* $Lz = 4.5 \text{ nm}$.

Diffusion coefficient of counterions $a_0 t_0^{-1}$						
$\sigma_{wall}(e/nm^2)$	-0.5		-1		-2	
$c_{add}(mol/L)$	D_{av}	D_{pore}	D_{av}	D_{pore}	D_{av}	D_{pore}
0	0.73	0.85	0.66	0.73	0.59	0.67
0.2	0.73	0.85	0.66	0.74	0.60	0.70
0.5	0.73	0.84	0.69	0.79	0.63	0.72
1	0.75	0.84	0.72	0.80	0.65	0.74
2	0.75	0.84	0.74	0.80	0.69	0.77

Table 3.7 – Comparison of the values of the counterions diffusion coefficient, where D_{pore} correspond to the results obtained at subsection 3.5.3.2 and as D_{av} to the results computed using eq. 3.12 for all the systems.

wall in comparison to the co-ions, which show how electrostatic interactions due to the charge wall play a strong effect on counterions in the region close to the surface.

A straightforward way to explain the variation of the average value of D/D^0 , is to account for the relative proportions of counterions in these layers. Taking a look into figure 3.18 (b), we can say that the effect of the increase of the surface charge is to increase the proportion of ions close to the surface, whereas the effect of the increase of added salt concentration is to increase the proportion of ions far from the surface.

Thus, by using the study of the diffusion coefficient by layers, it is possible now to explain the behaviour seen in Figure 3.15 (a), where D/D^0 for counterions is obtained for the whole space between the slit pore. We see how the increase of σ_{wall} leads to an increase of the proportion of counterions at surface layer. This can be deduced since the value of D/D^0 as the charge on the wall increase tends to the counterions diffusion coefficient average value at the region close to the surface (*i.e.* around 0.61). On the other hand, increasing the concentration of added salt leads to an increase of the proportion of counterions in bulk layer. To explain this behaviour, we have to look at the curves that correspond to the cases of $\sigma_{wall} = -1$ and $-2 e/nm^2$ in Figure 3.15 (a). As the concentration of added salt increases, the values of D/D^0 tend to the counterion average value of the diffusion coefficient at the region far from the surface (*i.e.* around 0.91). Finally a comparison of the values of the diffusion coefficient obtained over all the simulation box (see subsection 3.5.3.2) and the "average diffusion coefficient" computed through the results obtained for the diffusion coefficient of ions as a function of the distance to the wall was done. To do so, we computed

$$D_{av} = \eta_{L_{13}} D_{L_{13}} + \eta_{L_2} D_{L_2} \quad (3.12)$$

where $\eta_{L_{2/13}} = \langle N_{L_{2/13}} \rangle / \langle N_{L_{13}} \rangle + \langle N_{L_2} \rangle$, $D_{L_{2/13}}$ correspond to the diffusion coefficient far/close to the surface obtained in this section and $\langle N_{L_{2/13}} \rangle$ is the average number of ions that are present at the layer far/close to the surface at a given time. This procedure was carried out for each system, *i.e.* for each c_{add} and σ_{wall} at this confinement. In what follows we will refer as D_{pore} the results obtained at subsection 3.5.3.2 and as D_{av} the results computed using Eq. 3.12. Thus, as a result two tables with the comparison between the values obtained for the diffusion coefficient are shown

Diffusion coefficient of co-ions $a_0 t_0^{-1}$						
$\sigma_{wall}(e/nm^2)$	-0.5		-1		-2	
$c_{add}(mol/L)$	D_{av}	D_{pore}	D_{av}	D_{pore}	D_{av}	D_{pore}
0.2	0.91	0.90	0.90	0.92	0.90	0.92
0.5	0.88	0.90	0.88	0.89	0.88	0.89
1	0.86	0.88	0.86	0.88	0.86	0.88
2	0.84	0.86	0.84	0.84	0.84	0.86

Table 3.8 – Comparison of the values of the co-ions diffusion coefficient, where D_{pore} correspond to the results obtained at subsection 3.5.3.2 and as D_{av} to the results computed using eq. 3.12 for all the systems.

in Table 3.7 for counterions and in Table 3.8 for co-ions for each system. Comparing the values of the diffusion coefficient for the same system (*i.e.* the same c_{add} and σ_{wall}), we observed that the magnitude is not the same for counterions and neither for co-ions. However, their behaviour for both ions is the same (*i.e.* the tendency is the same when varying c_{add} and σ_{wall}). Thus, the differences of magnitude can be linked to the fact that the number of ions that is used in Eq. 3.12 is an approximate number, leading to errors when computing the final value.

2. High confinement $Lz = 3.0 \text{ nm}$

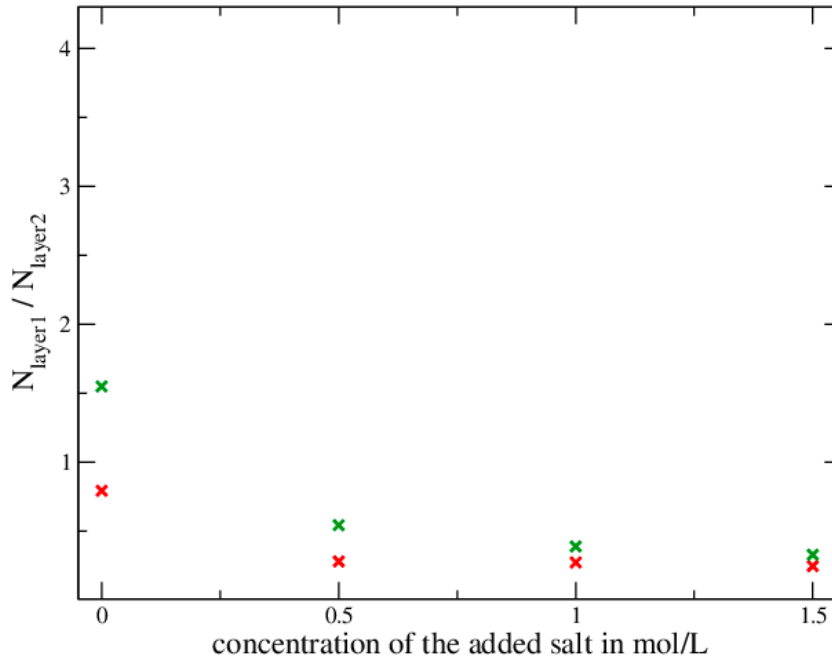
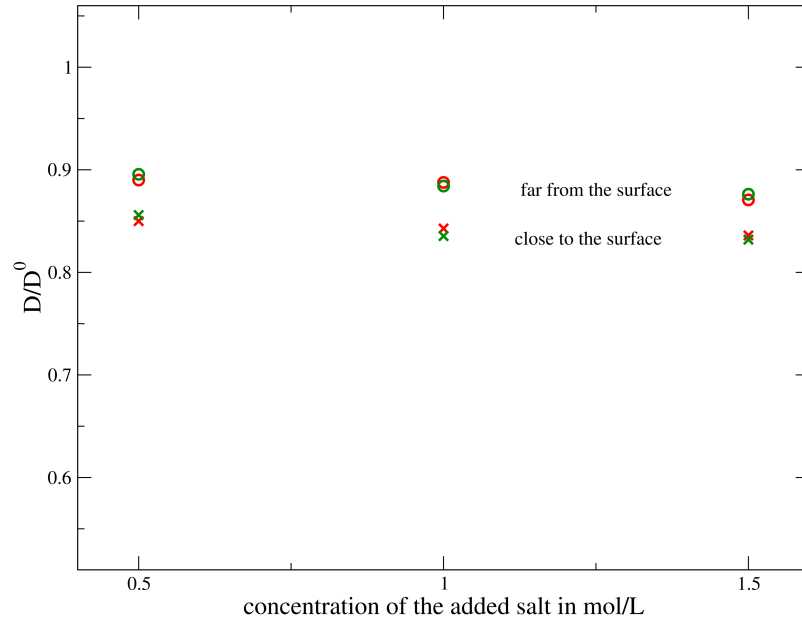
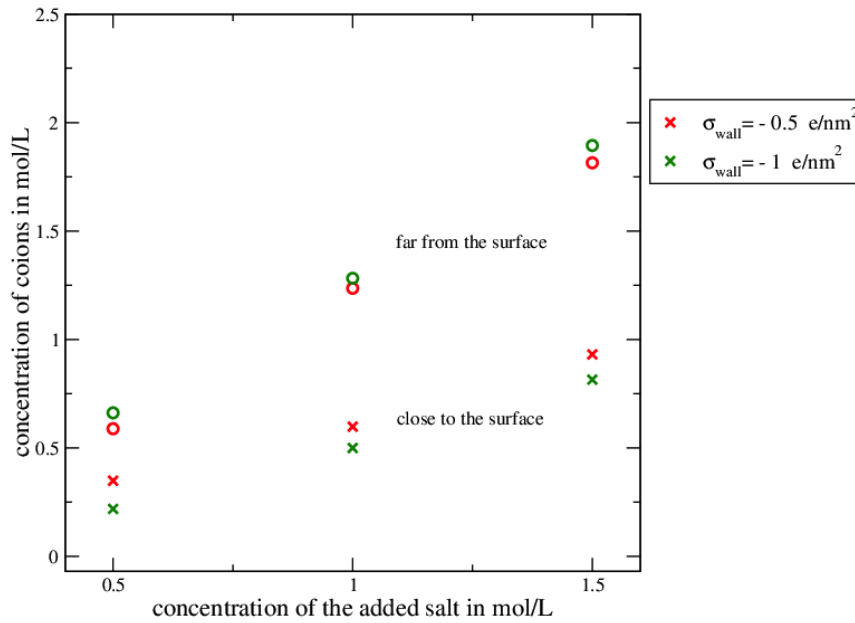


Figure 3.19 – N_{layer1}/N_{layer2} is presented as a function of the concentration of added salt varying the charge on the wall. The number of ions that is considered here is for both ions (counterions and co-ions). This analysis is made for the confinement $Lz = 3.0 \text{ nm}$.

In this section, the same analysis is carried out for the case of $Lz = 3.0 \text{ nm}$. Thus, the diffusion coefficients of ions are computed in the layers chosen in Section 3.4. Comparing

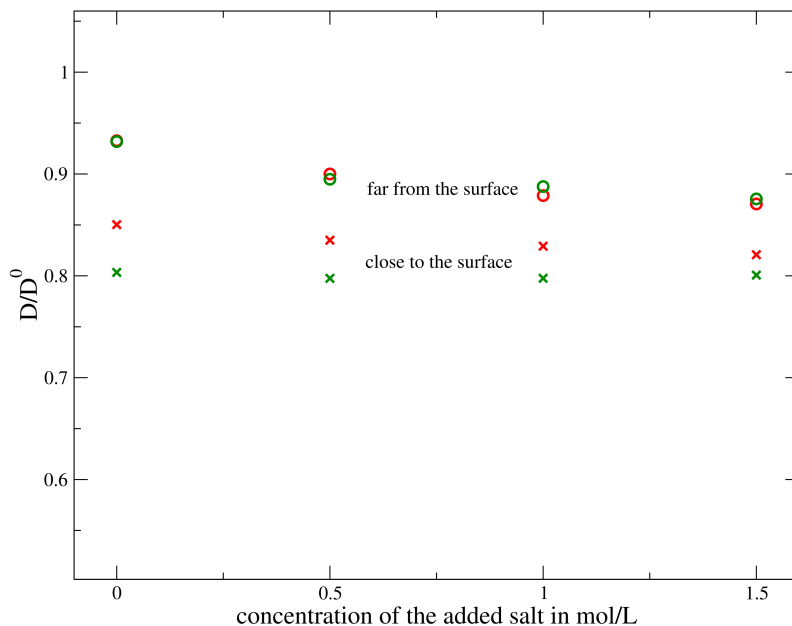


(a) Diffusion coefficient of co-ions computed by layers.

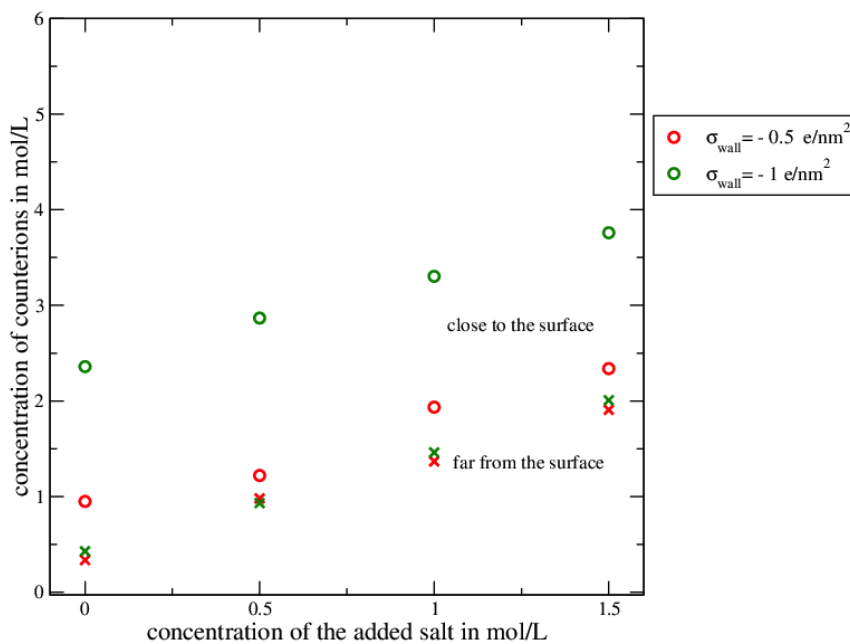


(b) Concentration of co-ions computed by layers.

Figure 3.20 – (a) Self diffusion coefficient of co-ions computed by layers in the direction parallel to the wall as a function of the concentration and of the charge of the walls for the low confinement *i.e.* $Lz = 3.0 \text{ nm}$. (b) Concentration of co-ions as a function of the concentration of added salt varying the charge on the wall computed by layer for the low confinement *i.e.* $Lz = 3.0 \text{ nm}$.



(a) Diffusion coefficient of counterions computed by layers.



(b) Concentration of counterions computed by layers.

Figure 3.21 – (a) Self diffusion coefficient of counterions computed by layers in the direction parallel to the wall as a function of the concentration and of the charge of the walls for the low confinement *i.e.* $Lz = 3.0 \text{ nm}$. (b) Concentration of counterions as a function of the concentration of added salt varying the charge on the wall computed by layer for the low confinement *i.e.* $Lz = 3.0 \text{ nm}$.

Fig. 3.16 and Fig. 3.19 it is notice that the values of N_{layer1}/N_{layer2} keeps an equal order of magnitude on both cases, except for the no added salt case.

In Fig. 3.20 (a) are presented the values of D/D^0 for co-ions as a function of the concentration of added salt, varying the density charge at the wall.

At the region close to the wall, a larger value of the diffusion coefficient is observed for $Lz = 3.0 \text{ nm}$ compared to $Lz = 4.5 \text{ nm}$ (see Fig. 3.20 (a) and Fig. 3.17 (a)). Whereas, the values for the diffusion coefficient computed far from the wall, present the same order of magnitude for both cases (*i.e.* $Lz = 4.5 \text{ nm}$ and $Lz = 3.0 \text{ nm}$). As a conclusion, it seems that confinement has an influence on the co-ion diffusion coefficient in the region close to the surface.

Similarly to the co-ion case, the counterion values of D/D^0 are illustrated in Fig. 3.21 (a) as a function of the concentration of added salt, varying the density charge at the wall. From the graph we can see that D/D^0 in the region far from the wall does not depend on Lz (see Fig. 3.18 (a) and Fig. 3.21 (a)), contrary to the region close from the surface where the diffusion coefficient of counterions depends on the confinement. Indeed, a value of D/D^0 larger is obtained at $Lz = 3.0 \text{ nm}$ than for $Lz = 4.5 \text{ nm}$.

Finally, the case of highest confinement (*i.e.* $Lz = 1.5 \text{ nm}$), was not discussed here since no layer was defined.

3.5.4 Summary of the main findings

From the previous analysis we can conclude that:

- Different contributions influence the diffusion coefficient of co-ions and counterions:
 - D/D^0 of co-ions is mostly influenced by the ionic concentration,
 - D/D^0 of counterions is due to an interplay between electrostatic and concentration contributions.
- Confinement has an influence on the dynamics of both ions in the region close to the wall. Indeed the diffusion coefficient for the same system (*i.e.* same c_{add} and σ_{wall}) increases as the confinement increases (*i.e.* as Lz decreases).

3.6 Velocity field of solvent and ions

3.6.1 Electro-osmosis flow

When an electric field is applied to the system described in Section 2.3.2, a motion of the solvent across the slit pore is induced. This effect is known as electro-osmotic flow and plays an important role in microfluidic devices (see Chapter 1). Thus, a study of this phenomenon was carried out using MPCD simulation by varying the charge density on the walls and the concentration of added salt, as illustrated in Table 3.3. It is important to mention that this is not a new result in the sense that others works have shown it previously. However it is presented here for further references (see Chapter 4).

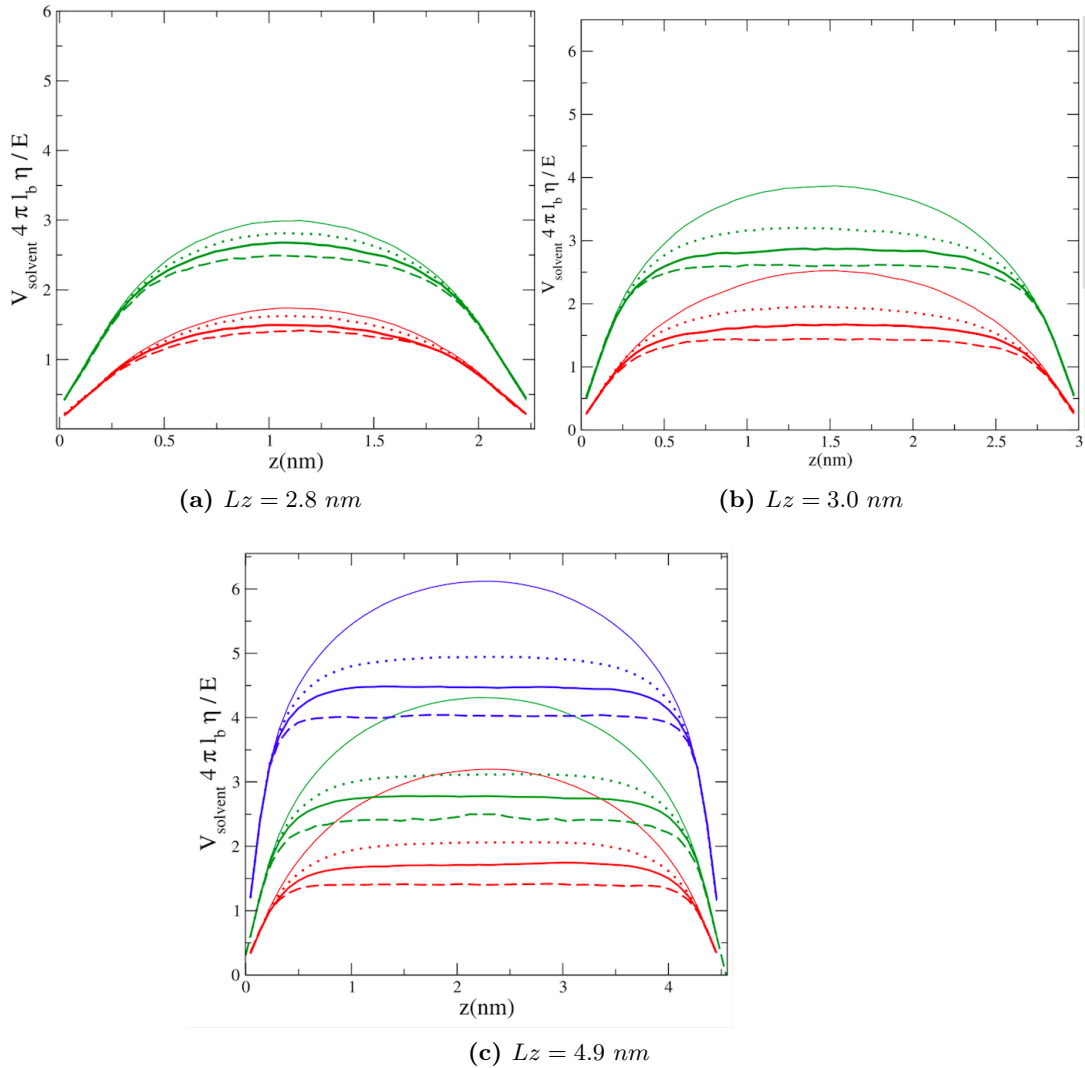


Figure 3.22 – Velocity profile of the solvent (electro-osmotic velocity) as a function of the distance to the wall, varying σ_{wall} and c_{add} . Each plot corresponds to a different confinement. The different values of the concentration of added salt are represented by the different line styles, *i.e.* continuous thin lines are $c_{\text{add}} = 0 \text{ mol/L}$, dotted lines correspond to $c_{\text{add}} = 0.5 \text{ mol/L}$, continuous thick lines belong to the case $c_{\text{add}} = 1 \text{ mol/L}$ and finally dashed lines refers to $c_{\text{add}} = 2 \text{ mol/L}$. Whereas, the different σ_{wall} are given by different colors, being red lines -0.5 e/nm^2 , green -1 e/nm^2 and blue -2 e/nm^2

An electro-osmotic profile was computed as a function of the distance to the wall for each confinement (see Fig. 3.22), where each curve was divided by $E/4\pi\eta l_b$.

Figure 3.22 shows that when c_{add} is fixed, the electro-osmotic velocity increases as the density of the charge wall increases. This is due to electrostatic interactions from the walls on the ions. As a consequence, the ion movement is translated in the solvent movement, which defines the electro-osmotic flow. If σ_{wall} is fixed, the velocity of the solvent increases as the concentration of added salt decreases. Furthermore, for high c_{add} , the parabolic profile is replaced by a "plug"-like profile which only varies along the double layer. As expected, a

higher salt concentration increases electrostatic screening and diminishes the velocity.

When we vary the distance between the walls, while keeping both σ_{wall} and c_{add} constant, we observe that the electro-osmotic velocity increases as the distance between the wall increases (see Fig 3.22 (a), (b) and (c)). Moreover, the effect of the wall charge density on the electro-osmotic profile seems to be less strong for higher confinements. Furthermore, the plug like shape observed on the profiles corresponding to $Lz = 3.0 \text{ nm}$ and $Lz = 4.5 \text{ nm}$ for higher added salt concentration, is no longer observed at the highest confinements (*i.e.* for $Lz = 1.5 \text{ nm}$). In the middle of the slit pore there exists a lack of electroneutrality, which leads to non flat velocity profile.

3.6.2 Electro-osmotic velocity obtained through MPCD compared with the velocity obtained through Smoluchovski theory

We can compare the velocity profile to theoretical predictions. More specifically, we compare our numerical results with:

- A full Poisson-Nernst-Planck theory based on a Poisson-Boltzmann distribution of the ions as discussed in Chapter 1
- The solvent velocity profile computed from the ionic concentration profiles as obtained numerically by our simulations. In other words, the velocity profile reads

$$v(z) = v(L_{hyd}/2) - \frac{eE}{\eta} \int_{L_{hyd}/2}^z \int_0^{z'} (\rho_+(z'') - \rho_-(z'')) dz'' dz' \quad (3.13)$$

where $v(L_{hyd}/2)$ is determined by the boundary conditions (see Chapter 1 for derivation).

If we plug the PB solution for the theoretical concentration profiles, we have a full PNP, otherwise, inserting the numerical solution for ρ_i yields the modified PNP theory.

Once again the case of no added salt was already studied in Ref. 114. The electro-osmotic flow was compared with PNP theory results. Ceratti *et. al.* discussed how the velocity flow of the solvent is influenced:

1. By short-ranged repulsions vs no short-range repulsions between counterions,
2. By the discretization level d of the charge within the wall, *i.e.* the average surface charge is distributed over discrete size of charge $-e/d$ within the solid wall,
3. By the average charge on the wall.

To do so, the values of the viscosity and L_{hyd} taken are $4.04 m_f a_0^{-1} t_0^{-1}$ and $L_{hyd} = 4.5 \text{ nm}$ respectively. On one hand, they found that when short-range repulsions are neglected (*i.e.* no WCA), the velocity profile obtained using MPCD is remarkably close to the one obtained using the simulated counterion density ρ_+ . Whereas, when comparing PNP with MPCD results, the difference increases as the charge on the wall increases, being around 4% of difference for the lowest charge on the wall case (*i.e.* -0.2 e/nm^2). Moreover, a partial slip at the fluid/solid boundary condition is found in MPCD simulations. However, the velocity at the wall is small compared to the maximum velocity.

On the other hand, when considering WCA interactions, differences appear. In fact, introducing repulsion among counterions leads to a significant reduction of the electro-osmotic flow when compared to the previous case (*i.e.* no WCA interactions). As PNP does not take into account these interactions, a comparison cannot be done since PNP theory cannot be taken as a benchmark. Nevertheless, the overall agreement is good for the systems studied meaning that MPCD predicts the same behaviour as the Stokes equation, showing that MPCD may be used to simulate electrokinetic effects and more generally to study fluid transport in the low Reynolds number limit.

Regarding the discretization level parameter d , a study was carried out considering that no WCA interactions are taken into account. The more localized the charge (*i.e.* the smaller d), the larger the decrease in the electro-osmotic flow. Indeed, the more pronounced effect of the d parameter is seen for smaller σ_{wall} , whereas as σ_{wall} increases, the velocity profiles obtained by MPCD and by using the simulated counterion density ρ_+ (*i.e.* Eq. 3.13) are in better agreement. For all cases, PNP theory does not agree with any case (MPCD and velocity profiles computed from the concentration profiles). This last result underlines the limitation of the PNP approach with continuous surface charge distribution for systems in which the charge is indeed localized.

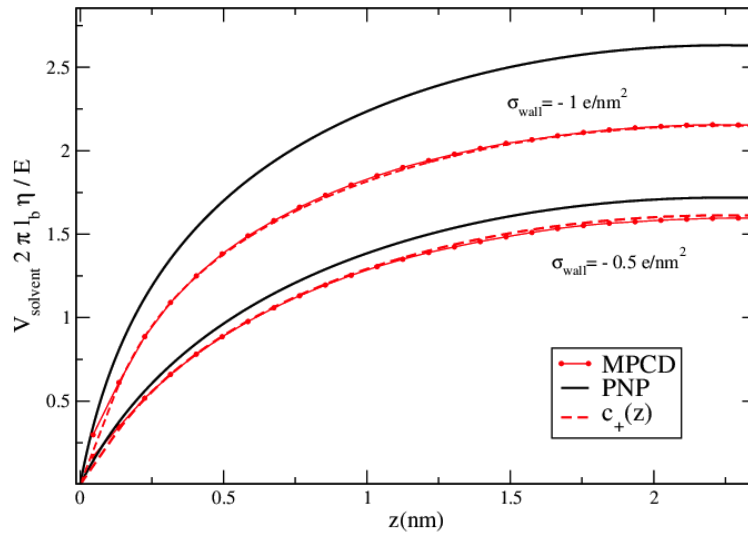


Figure 3.23 – Comparison of solvent velocity profiles as a function of the distance to the wall obtained from a) full PNP, b) MPCD and c) applying Eq. 3.13 to the density profiles obtained through MPCD. This was done for the low confinement *i.e.* when $Lz = 4.5 \text{ nm}$ when no added salt is considered.

Finally, as the charge on the wall increases, the difference between the velocity profile obtained through PNP theory and MPCD results increases; more specifically the difference between the maximum velocities $\approx 34\%$ for the most charged case *i.e.* $-4e/nm^2$.

In order to corroborate the results obtained from Ceratti, the same study was carried out by us. They analysed the cases with $\sigma_{wall} = -0.5$ and $-1 e/nm^2$, which correspond to two

	Slip length (Å)		
	$\sigma_{wall} = 0.5 \text{ e/nm}^{-2}$	$\sigma_{wall} = 1 \text{ e/nm}^{-2}$	$\sigma_{wall} = 2 \text{ e/nm}^{-2}$
$c_{add} = 0 \text{ mol/L}$	0.22	0.14	0.03
$c_{add} = 0.2 \text{ mol/L}$	0.23	0.03	0.06
$c_{add} = 0.5 \text{ mol/L}$	0.17	0.006	0.14
$c_{add} = 1 \text{ mol/L}$	0.18	0.07	0.03
$c_{add} = 2 \text{ mol/L}$	0.17	0.03	0.08

Table 3.9 – Values of the slip length for different systems at the larger confinement $Lz = 4.5 \text{ nm}$

values that are shown in reference 114. Moreover, we only consider systems where WCA interactions are taken into account, and where the discretization level is $d = 1$. The results obtained are shown in Fig. 3.23. We see that like in the work of Ceratti, PNP predictions overestimate the curves of the MPCD results and the modified PNP (*i.e.* $c_+(z)$ computed by using Eq. 3.13).

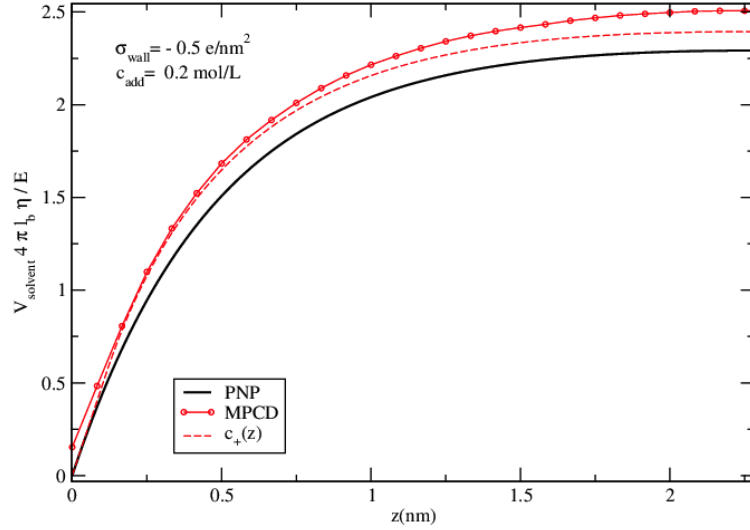
For instance, in reference 114, the discrepancy between these two plots exist and gets smaller as the charge on the wall increases. Whereas, in Fig. 3.23 both curves barely present any difference. A possible explanation is that this could be due to the fact that in Ceratti’s results the statistics obtained on the solvent velocity profile is still poor, leading to the appearance of these differences.

The case of added salt is shown in Fig. 3.24, for $\sigma_{wall} = 0.5$ and 2 e/nm^2 and $c_{add} = 0.2$ and 2 mol/L at the largest separation Lz between the walls., where each curve was multiplied by the value of $4\pi l_b \eta / E$, where η has the value computed in Section 3.2.1 (that corresponds to the prefactor of the theoretical velocity profile (see Chapter 1)). The curves show that partial slip velocity at the fluid-solid boundary occurs in MPCD simulations, which is not predicted by the PNP theory: the velocity of the solvent is not 0 at $z = 0$ in MPCD .

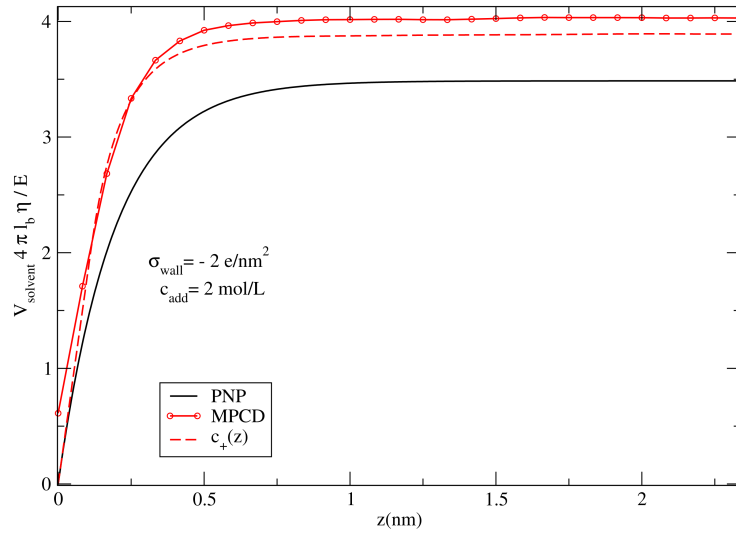
As commented in Section 2.2.4, the slip length is defined as the (hypothetical) distance into the surface at which the relative tangential velocity vanishes. Conventionally a positive slip length is associated with a positive slip velocity, while a (less common) negative length would indicate an apparent change in the sign of the velocity field near the solid. Table 3.9 presents the slip length values for different concentrations of added salt and surface charge densities at the walls, for the case of largest confinement (*i.e.* $Lz = 4.5 \text{ nm}$). These values were obtained directly from the plots, meaning that the distance at which the velocity profile is zero inside the wall ($z = 0$) is computed. To do so, a linear regression using the last points of the curve, close to the walls, was done.

As it appears in Table 3.9, as σ_{wall} increases, the slip length decreases. A possible explanation is that the ions close to the surface become more and more immobile as the surface charge density increases, due to electrostatic interactions.

Moreover, in the MPCD scheme, ions participate to the collision step, so they decrease the velocity of fluid particles. Therefore, the velocity at the wall tends to zero as σ_{wall} increases. Finally, looking again at Fig. 3.24, we notice that when the surface charge density increases, the differences between the full PNP results and the two other curves become more apparent.



(a) $c_{add} = 0.2 \text{ mol/L}$ $\sigma_{wall} = -0.5 \text{ e/nm}^2$



(b) $c_{add} = 2 \text{ mol/L}$ $\sigma_{wall} = -2 \text{ e/nm}^2$

Figure 3.24 – Comparison of solvent velocity profile as a function of the distance to the wall obtained from a) full PNP, b) MPCD and c) applying Eq. 3.13 to the density profiles obtained through MPCD. This was done for the low confinement *i.e.* when $Lz = 4.5nm$. The corresponding values for the concentration of added salt and the charge surface are shown in the sub-caption of each figure.

3.7 Poiseuille flow: study of the viscosity

In the previous section, we found that the velocity profiles present a not desired slip velocity at the fluid-solid boundary. Meaning that the stick boundary condition was not implemented perfectly in our method of simulation. However, it seems that as the concentrations of ions increase, the slip length decreases (see table 3.9). Therefore, in order to find an explanation a first assumption was made: The presence of ions increases the mass and thus the viscosity near to the wall compensating the non-perfect implementation of the stick boundary conditions.

A way to check if our hypothesis is true was achieved by comparing the Poiseuille flow obtained through an analytic solution and the MPCD simulation method. Both profiles were obtained without and with ions, for different force strengths. Indeed, the reason why the Poiseuille flow was chosen to carry out this study is because of the precise analytic solution that can be obtained. More specifically, in order to estimate if the Poiseuille flow changes when ions are or are not considered, the viscosity for both cases was obtained by fitting the analytic solution with the Poiseuille flows obtained with the MPCD code. To do so, the following equation was used with η being the fitting parameter:

$$V_x(z) = V_{max} \left(\frac{4z}{L_z} - \frac{4z^2}{L_z^2} \right) \quad (3.14)$$

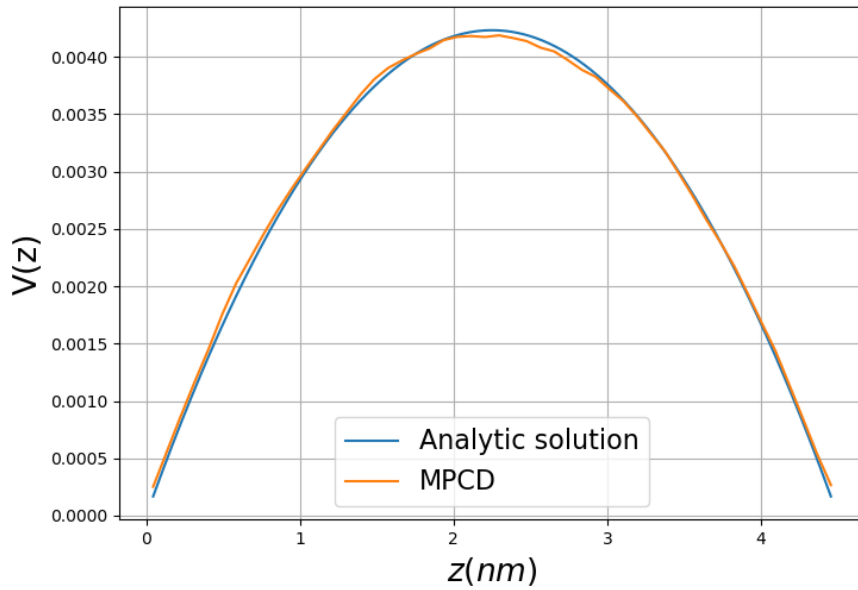
where $V_{max} = -\frac{L_z^2}{8\eta} \frac{\partial p}{\partial x}$ and in particular for MPCD $\frac{\partial p}{\partial x} = -\gamma g$. This equation corresponds to the theoretical prediction of the Poiseuille flow (with stick boundary conditions). The gravity force values that were chosen to realize this study are the following $g = 3 \times 10^{-5} a_0/t_0^2$, $1.5 \times 10^{-5} a_0/t_0^2$ and $7.5 \times 10^{-6} a_0/t_0^2$. However, here only the case for $g = 3 \times 10^{-5} a_0/t_0^2$ will be presented since this is the one that has the best statistics.

Before starting the analysis, it is important to have a reference value for η , to see how it is affected by the presence of ions. Indeed, in Section 3.2.1 the corresponding value of η was obtained according to the chosen simulation parameters used in the MPCD code. The value is $\eta = 3.96 a_0/t_0^2$.

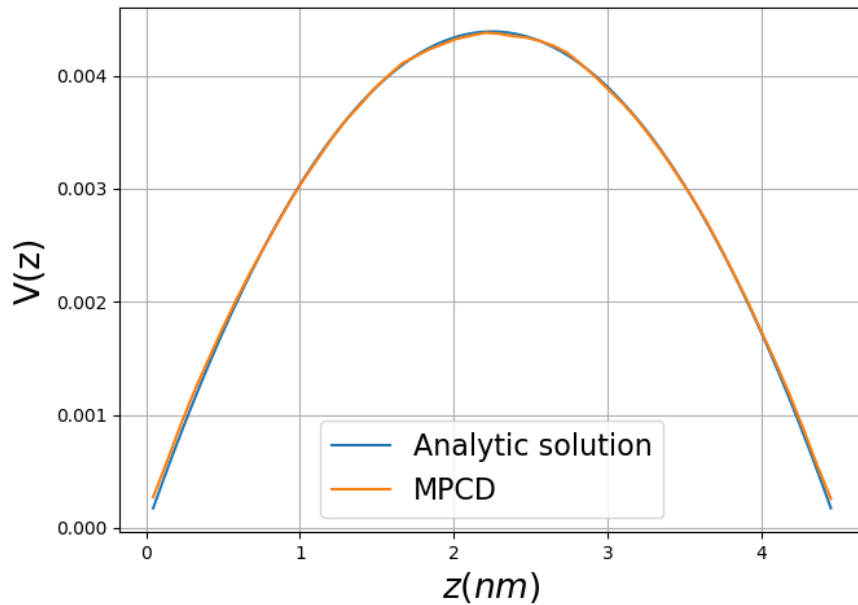
The results obtained by doing the fitting process are observed in Fig 3.25 (a) when there is a presence of ions and (b) when there is not, for the strength force $g = 3 \times 10^{-5} a_0/t_0^2$. For the case with ions, the value obtained for the viscosity is $\eta = 3.97 1/a_0 t_0$. Whereas for the case without ions, the value of the fitted viscosity is $\eta = 3.84 1/a_0 t_0$. Thus, the value of the fitted viscosity when ions are present is higher than when they are not. In fact, the same behaviour was observed for others strength forces. Moreover, when we compare the reference value for $\eta = 3.96 a_0$ with the results obtained, we realize that the viscosity fitted with ions is closer to the expected viscosity for all the strength forces. Therefore we can deduce that when there is a presence of ions in the system, the viscosity increases and is close to the expected viscosity.

However, from the previous study it is difficult to deduce wether is true or not that the presence of ions impacts the slip length. Then another analysis was carried out. The new study consists in keeping fixed the value of the viscosity, for a value as computed in Section 3.2.1, *i.e.*, $\eta = 3.96 a_0/t_0^2$. We could thus make a fitting of the curves where the fitting parameter is now a new parameter L_{znew} . More precisely, the Eq. 3.14 is modified and re-written as:

$$V_x(z) = \frac{L_{znew}^2 \gamma g}{8\eta} \left(\frac{4(z + (L_{znew} - L_z)/2)}{L_{znew}} - \frac{4(z + (L_{znew} - L_z)/2)^2}{L_{znew}^2} \right) \quad (3.15)$$

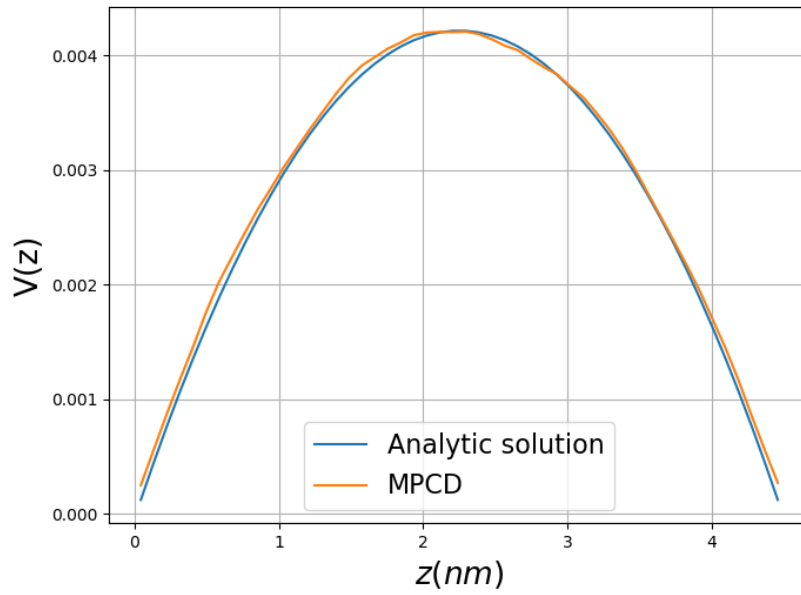


(a) with ions ($\eta = 3.97 \text{ } 1/a_0t_0$)

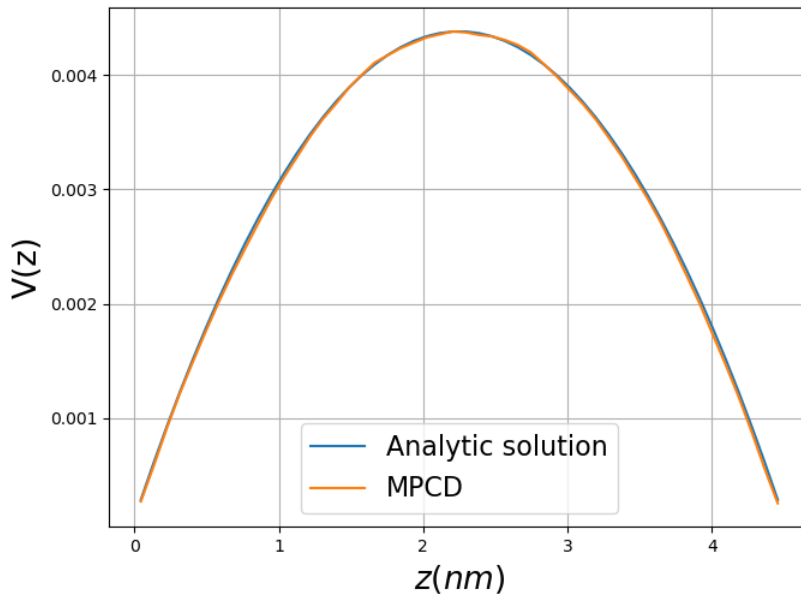


(b) without ions ($\eta = 3.84 \text{ } 1/a_0t_0$.)

Figure 3.25 – Poiseuille velocity profiles obtained from MPCD simulations compared to the analytic result of Eq. 3.14 with a value of η fitted so that the agreement with MPCD is the best. A comparison of the MPCD curves (orange lines) and the fitting curves (blue lines) is shown for the case where ions (a) and no ions (a) are taken into account by using $g = 3 \times 10^{-5} a_0/t_0^2$.



(a) with ions



(b) without ions

Figure 3.26 – Fitting of the Poiseuille profiles obtained through MPCD done by using Eq. 3.15 keeping the viscosity fixed at the expected value with L_z new as fitting parameters. Comparison of the MPCD curves (orange lines) and the fitting curves (blue lines) for the case where ions (a) and no ions (b) are taken into account by using $g=3 \times 10^{-5} a_0/t_0^2$.

where L_{znew} is the fitted parameter and L_z is the value that is known and used in our simulations, *i.e.* 4.5 nm. Figure 3.26 (a) shows the result in the case when the ions are present, and figure 3.26 (b) the case of pure fluid. From this analysis we found that when ions are present, the parameter obtained is $L_{znew} = 4.47$ nm, whereas for the other case we obtained $L_{znew} = 4.56$ nm. Therefore, the difference between the value used in our simulation (*i.e.* $L_z = 4.5$ nm) and the values obtained, seems to be larger for the case of no ions. In fact the same behaviour was observed for the other strength forces. Thus, we can say that the presence of ions makes a difference on the value of the slip length. As a conclusion, it occurs that the implementation of the stick boundary condition is not perfect. Hence, in the following sections, we propose to consider the slip length following the viscosity that was imposed in our simulations.

3.7.1 Velocity field of ions

To study the influence of hydrodynamics, electrostatics and excluded volume effects on the dynamics of ions, we compute the velocity of ions as a function of the distance to the wall in the reference frame of the solvent (*i.e.* $V_{ion} - V_{solvent}$). It is important to mention that these results are new, thus to the best of our knowledge, they are not present in other previous works of the literature. That is the reason why our simulation method (MPCD) has an advantage. Although MD simulations could also allow us to obtain the ion velocity profiles, MPCD is still more convenient since it provides us the results with a shorter simulation time. In what follows, the results were divided by the value of a characteristic velocity which is obtained by $V^0 = D^0 eE / k_B T$ and corresponds to the velocity that would have an ion at infinite dilution under the applied electric field E . This means that if the ionic velocity was obtained in an infinitely dilute solution, we would have $V/V^0 = 1$. In the following study, the color code is the same as in the previous plots, where the same color indicates the same σ_{wall} , whereas different line styles show the different c_{add} considered. The results were obtained for the different confinements (*i.e.* different L_z), following the parameters present in Table 3.3.

3.7.1.1 Low confinement

Starting with the largest value of L_z , the velocity of counterions and co-ions are shown in Fig 3.27 a) and b) respectively. First we observe important departures from the ideal behaviour as V_{ion} is smaller than 1 in any case. We recall that in the standard PNP description of this situation $V/V^0 = 1$. In both cases, $(V_{ion} - V_{solvent})/V^0$ decreases as the concentration of added salt increases *i.e.* $(V_{ion} - V_{solvent})/V^0$ has a larger value for $c_{add} = 0.5$ mol/L (dotted lines) than for $c_{add} = 2$ mol/L (dashed lines). This is expected since the concentration leads to a restriction on the space, and thus a reduction on the velocity. Moreover, the velocity of both ions seems to be unaffected by the change of the density charge at the wall, since for different values of added salt concentration the same curves are found for different σ_{wall} (different color of the curves). Indeed a clear pattern is shown, since for the different values of σ_{wall} but same concentration of added salt, curves superpose on each other. The fact that some curves match better than others is due to the statistics achieved. For $c_{add} = 0.5$ mol/L (dotted lines) less statistic was obtained because for this case a small number of ions is taken into consideration in the simulation box.

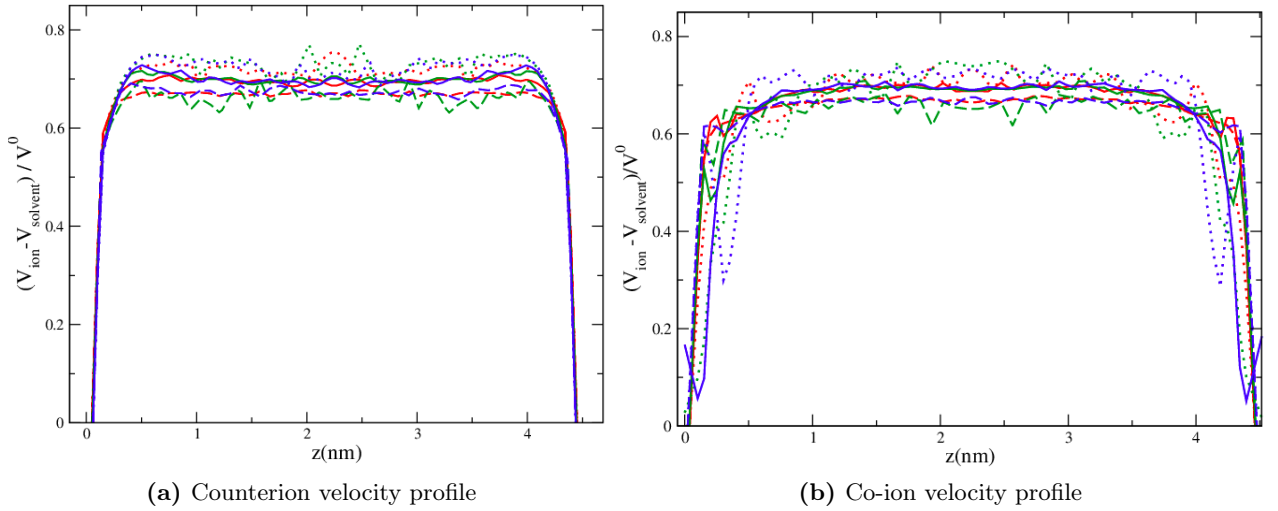


Figure 3.27 – Ion velocity profile as a function of the distance to the walls for several concentrations of added salt and surface charge on the walls. The different values of the concentration of added salt are represented by the different line styles, *i.e.* dotted lines correspond to $c_{\text{add}} = 0.5 \text{ mol/L}$, continuous thick lines belong to the case $c_{\text{add}} = 1 \text{ mol/L}$ and finally dashed lines refers to $c_{\text{add}} = 2 \text{ mol/L}$. Whereas, the different σ_{wall} are given by different colors, being red lines -0.5 e/nm^2 , green -1 e/nm^2 and blue -2 e/nm^2 . This case correspond to $Lz = 4.5 \text{ nm}$.

3.7.1.2 Medium confinement

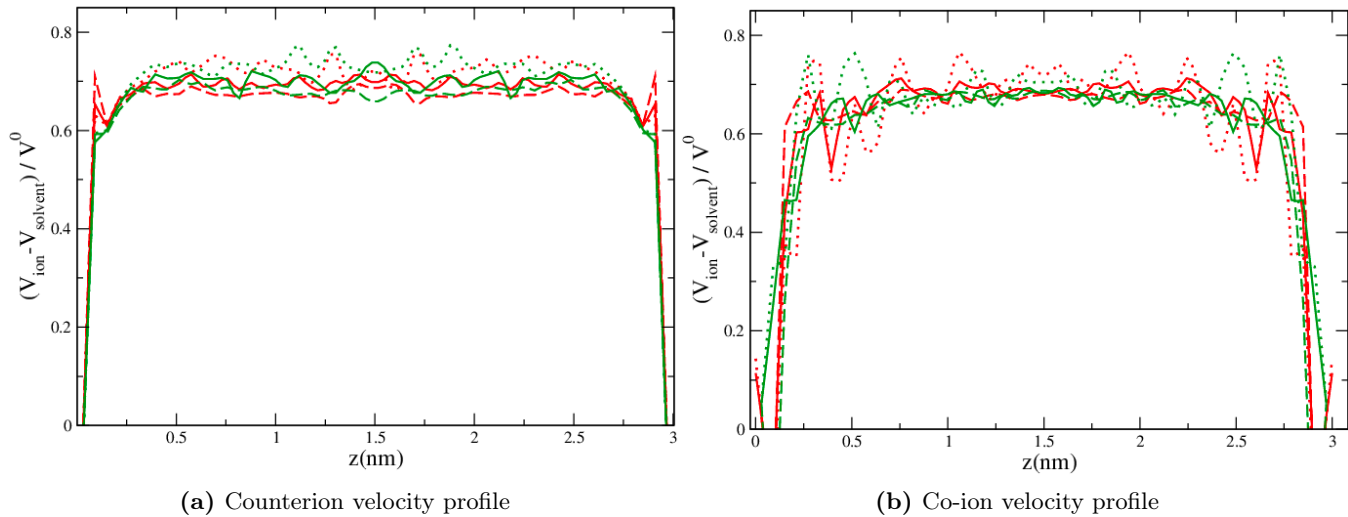


Figure 3.28 – Ion velocity profile as a function of the distance to the walls for several concentrations of added salt and surface charge on the walls. The different values of the concentration of added salt are represented by the different line styles, *i.e.* dotted lines correspond to $c_{\text{add}} = 0.5 \text{ mol/L}$, continuous thick lines belong to the case $c_{\text{add}} = 1 \text{ mol/L}$ and finally dashed lines refers to $c_{\text{add}} = 2 \text{ mol/L}$. Whereas, the different σ_{wall} are given by different colors, being red lines -0.5 e/nm^2 , green -1 e/nm^2 and blue -2 e/nm^2 . This case correspond to $Lz = 3.0 \text{ nm}$.

The same behaviour is observed for the counterions at the $Lz = 3.0 \text{ nm}$ case. Nonetheless,

in Fig 3.27 a) co-ions do not show any special pattern. This is due to the lack of statistics, since co-ions are less numerous than counterions.

Thus, longer simulation are required in order to achieve the same statistics. For counterions, the effect of the confinement is reflected on the region that corresponds to the middle of the slit pore, where slightly larger values are found when compared to the case of $Lz = 4.5 \text{ nm}$ for the same systems.

3.7.1.3 High confinement

Finally, the case of $Lz = 1.5 \text{ nm}$ is shown in Fig 3.29 a) and b) for counterions and co-ions respectively. In this particular confinement, the case for $c_{add} = 0.2 \text{ mol/L}$ (thin lines) was obtained for the different values of σ_{wall} . However, this was not possible for previous confinements since this case requires a large amount of statistics since the number of ions (counterions and co-ions) is small. For counterions we observe the same behaviour, *i.e.* $(V_{ion} - V_{solvent})/V^0$ decreases as the concentration of added salt increases. On the contrary, co-ions do not present the same influence. This can be explained from the fact that the number of co-ions in this system is lower than the number of counterions. Therefore, making it difficult to achieve good statistics for co-ions.

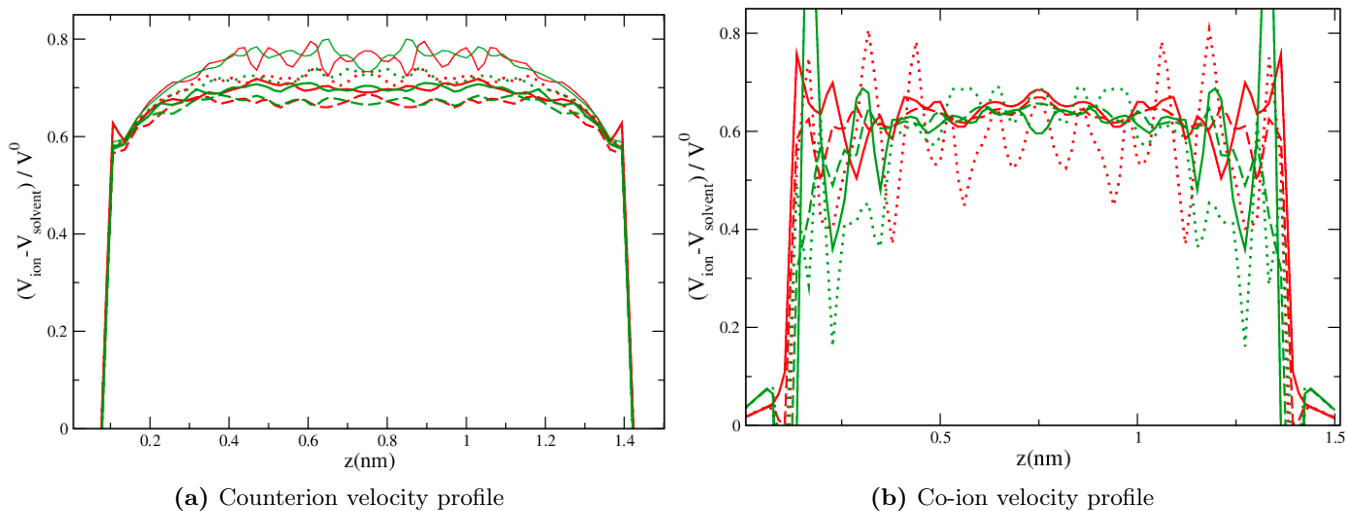


Figure 3.29 – Ion velocity profile as a function of the distance to the walls for several concentrations of added salt and surface charge on the walls. The different values of the concentration of added salt are represented by the different line styles, *i.e.* continuous thin lines are $c_{add} = 0.2 \text{ mol/L}$, dotted lines correspond to $c_{add} = 0.5 \text{ mol/L}$, continuous thick lines belong to the case $c_{add} = 1 \text{ mol/L}$ and finally dashed lines refers to $c_{add} = 2 \text{ mol/L}$. Whereas, the different σ_{wall} are given by different colors, being red lines -0.5 e/nm^2 , green -1 e/nm^2 and blue -2 e/nm^2 . This case correspond to $Lz = 1.5 \text{ nm}$

3.8 Electric conductivity

We now turn to the study of another transport coefficient, namely the electric conductivity, which will help us understand how concentration and hydrodynamic couplings contribute to the dynamics of the EDL.

We were able to get the electric conductivity from the ion velocity and density profiles obtained with the MPCD code. Specifically, we have computed the conductivity by applying the following equation,

$$\frac{\sigma(z)\vec{E}}{e} = \rho_+(z)\vec{V}_+ - \rho_-(z)\vec{V}_- \quad (3.16)$$

where $\rho_{+/-}(z)$ are the counterion and co-ion density profiles and $\vec{V}_{+/-}$ are the counterion and co-ion velocity profiles. For the ionic solution in the charged slit pore the electro-osmotic part was removed in order to obtain the electric conductivity in the reference frame of the solvent. To do so, the equation 3.16 is used with \vec{V}_{\pm} computed in the reference frame of the solvent *i.e.* $\vec{V}_{\pm}^s = \vec{V}_{\pm} - \vec{V}_{solvent}$. In what follows conductivity is divided by σ^0 , which denotes the ideal conductivity that is given by: $\sigma^0 = \frac{1}{k_B T} \sum_i c_i z_i^2 e^2 D_i^0$, where i denotes the specie of the particle (*i.e.* counterions and co-ions in our case), c_i is the concentration of the i specie and D_i^0 is the diffusion coefficient at infinite dilution.

3.8.1 Conductivity in bulk solution

First, the conductivity in the bulk is computed using the MPCD code, and compared to the experimental results found in Reference 117 for the conductivity of *KCl* solutions (see Fig. 3.30). As it is well known, the electrical conductivity of an ionic solution decreases strongly when the concentration increases because of hydrodynamic coupling, electrostatic interactions and excluded volume effects.

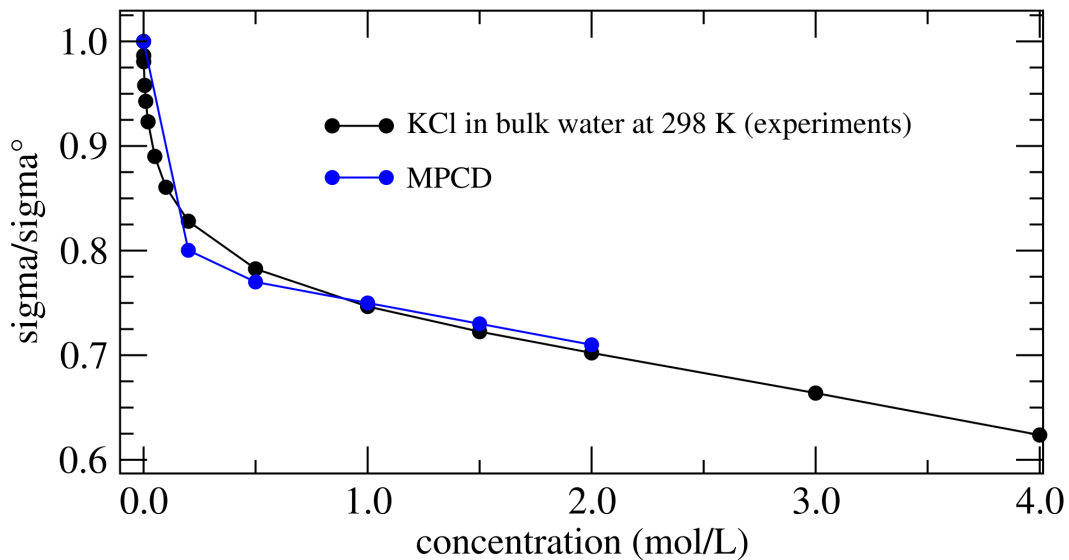


Figure 3.30 – Comparison of the conductivity in bulk solutions of a 1-1 electrolyte in water between MPCD and experimental results as a function of the ion concentration, and divided by the ideal conductivity σ^0).

Then, a good agreement is found when comparing experimental and MPCD results. However, a small difference in magnitude can be observed for the MPCD results, which is explained

by the fact that no specific kind of ion was considered in our simulations, contrary to the experiment which was carried out for potassium chloride in water at 298 K. Therefore, despite this lack of prior assumptions, we can say that the MPCD results obtained for the conductivity are qualitatively good

3.8.2 Influence of a neutral confinement

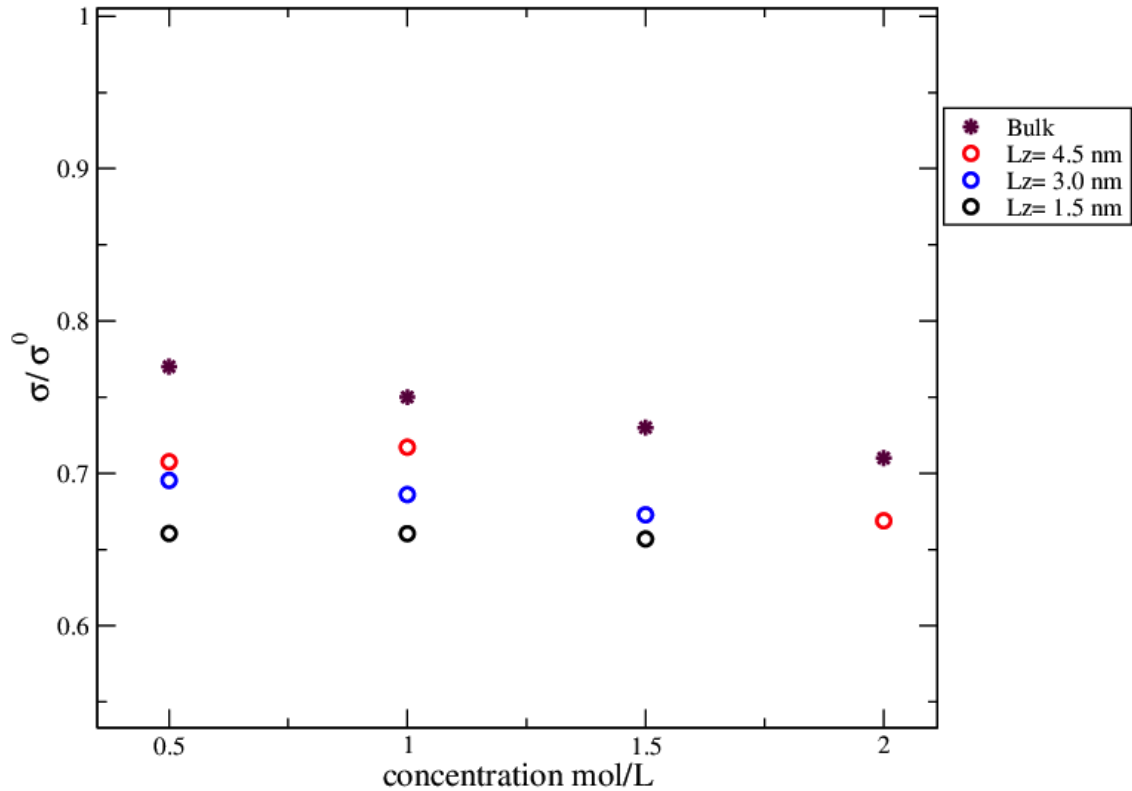


Figure 3.31 – Comparison of the conductivity (in the whole space between the slit pore) between a bulk solution and an ionic solution confined between neutral walls, as a function of the ion concentration. For the latter case, different confinements are taken into account, *i.e.* different distances between walls in the slit pore (values of the distance are designated by the different coloured circles).

A comparison of σ/σ^0 is done for the cases of a bulk solutions and for an ionic solution confined between neutral walls for different confinements, as presented in Fig. 3.31. For all the values conductivity is divided by σ^0 , which denotes the conductivity in the ideal case.

We observe that σ/σ^0 has larger values in the bulk than when confined by neutral walls. Although both present the same behaviour as a function of the ion concentration, *i.e.*, σ/σ^0 slightly decreases as the ion concentration increases. Furthermore, looking at the results carried out for neutral walls, we notice that σ/σ^0 present a small confinement dependence: The conductivity slightly decreases as the confinement increases (*i.e.* low value of L_z).

3.8.3 Influence of an electrostatic confinement

3.8.3.1 Conductivity by layers

In order to study the effect of an electrostatic confinement, the conductivity of an ionic solution confined between two charge walls is obtained for different configurations (see Table 3.3).

Since we are interested on how the ions dynamics behaviour changes along the slit pore, we decided to tackle our analysis by layers. To do so, the method previously selected was adopted with the difference being that now only the part of the ion density and velocity profiles which is defined in each layer is taken.

Indeed, conductivity is due to several contributions whose order of magnitude varies with increasing concentration. For example, without added salt the conductivity is only due to the contribution of counterions and to the electro-osmotic flow. In other words, the ionic atmosphere around counterions is not distorted by the opposite movement of the possible anions. However, in the case of added salt a new contribution appears, which is added to the previous ones. In what follows, we will remove the electro-osmotic contribution to the analysis of conductivity by layers and each value will be divided by σ^0 , which denotes the corresponding ideal conductivity. This means that we compute the electric conductivity, in the reference frame of the solvent.

- Low confinement

We first analyse the low confinement case (*i.e.* $Lz = 4.5 \text{ nm}$) and compute the conductivity in the layers chosen in Section 3.4.

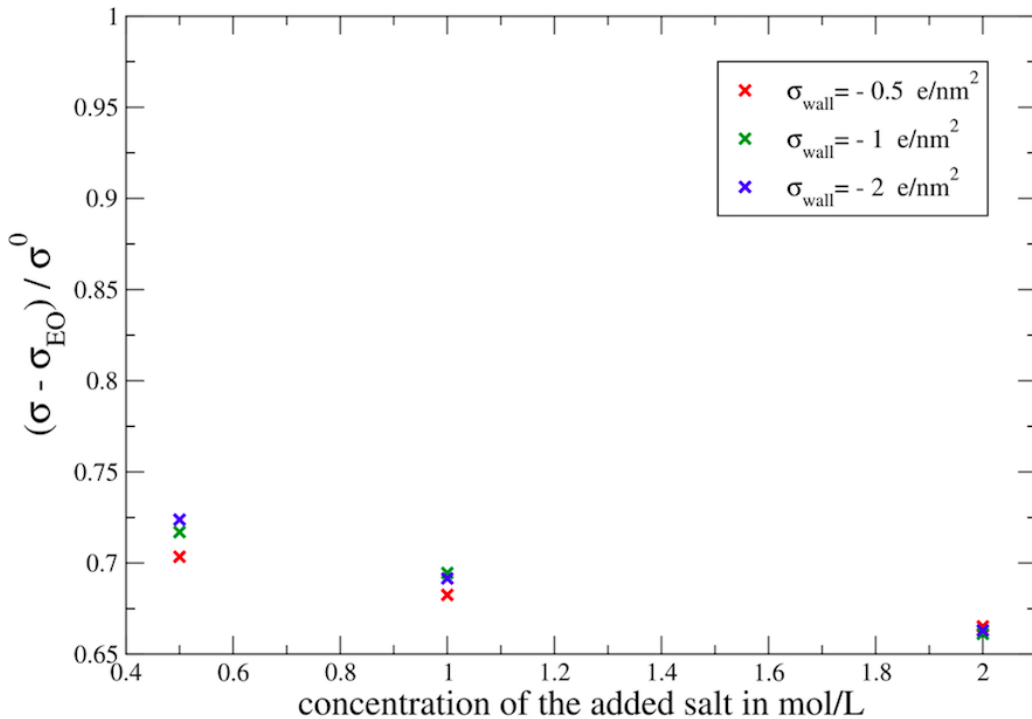


Figure 3.32 – Electric conductivity in the middle of the pore as a function of the concentration of added salt and varying the charge on the wall. The electro-osmotic contribution is removed for each case and the conductivity is divided by the ideal conductivity value. This is the case $Lz = 4.5 \text{ nm}$.

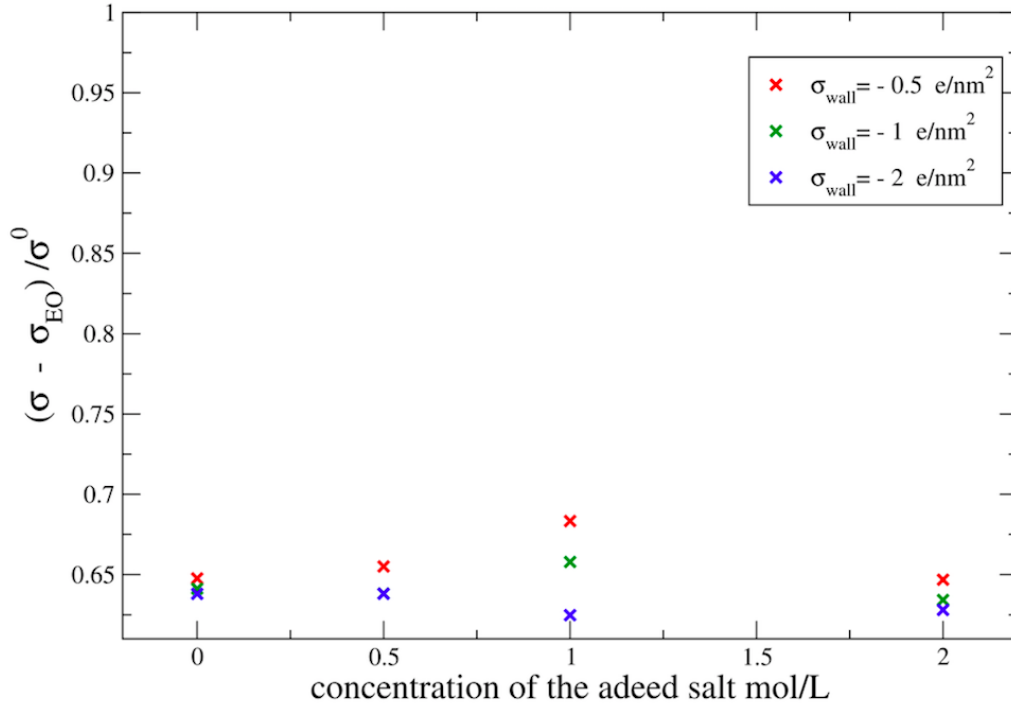


Figure 3.33 – Electric conductivity in the region close to the walls as a function of the concentration of added salt and varying the charge on the wall. The electro-osmotic contribution is removed for each case and the conductivity is divided by the ideal conductivity value. This is the case $Lz = 4.5 \text{ nm}$.

In Fig. 3.32, the values of σ/σ^0 are shown for the region in the middle of the pore as a function of the concentration of added salt and for different values of the charge on the wall. The plot shows how σ/σ^0 slightly decreases as the concentration of added salt increases. Whereas, σ/σ^0 seems to not be influenced by the charge on the wall.

On the other hand, in Fig. 3.33, the values of σ/σ^0 are shown for the region close to the wall as a function of the concentration of added salt and for different values of the charge on the wall. First, it is observed that the values of σ/σ^0 in the region referred as “close to the surface” are smaller than the ones at “far from the surface” (see Fig. 3.32 and Fig. 3.33). This illustrates how the ion conductivity is influenced by hydrodynamic interactions with the wall, by slow it down the movement of the ion particles. Second, contrary to the previous case, σ/σ^0 does not seem to be affected by c_{add} and neither by σ_{wall} . Thus, the differences observed among each configuration (for example the discrepancy between the different values of σ_{wall} at 1 mol/L) are just due to poor statistics on the ion density and velocity profiles.

Now, since we want to know how the confinement affects conductivity a larger confinement is considered, (*i.e.*) for smaller Lz .

- High confinement

Selecting now the system with $Lz = 3.0 \text{ nm}$, the ion conductivity is computed at the layers chosen in Section 3.4, where the same analysis as the one made for $Lz = 4.5 \text{ nm}$ is carried out.

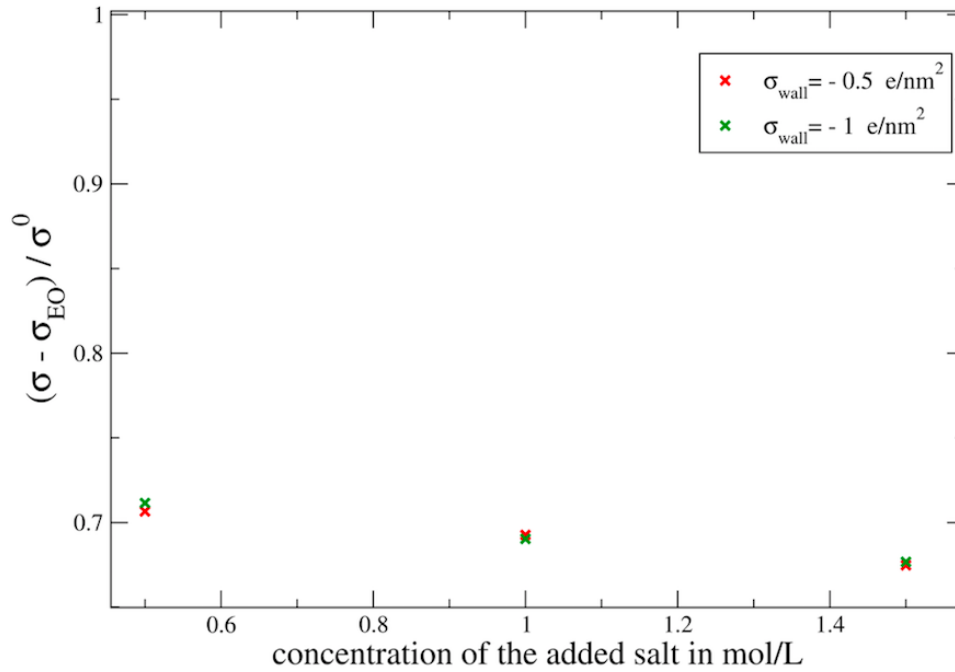


Figure 3.34 – Electric conductivity in the middle of the pore as a function of the concentration of added salt and varying the charge on the wall. The electro-osmotic contribution is removed for each case and the conductivity is divided by the ideal conductivity value. This is the case $Lz = 3.0 \text{ nm}$

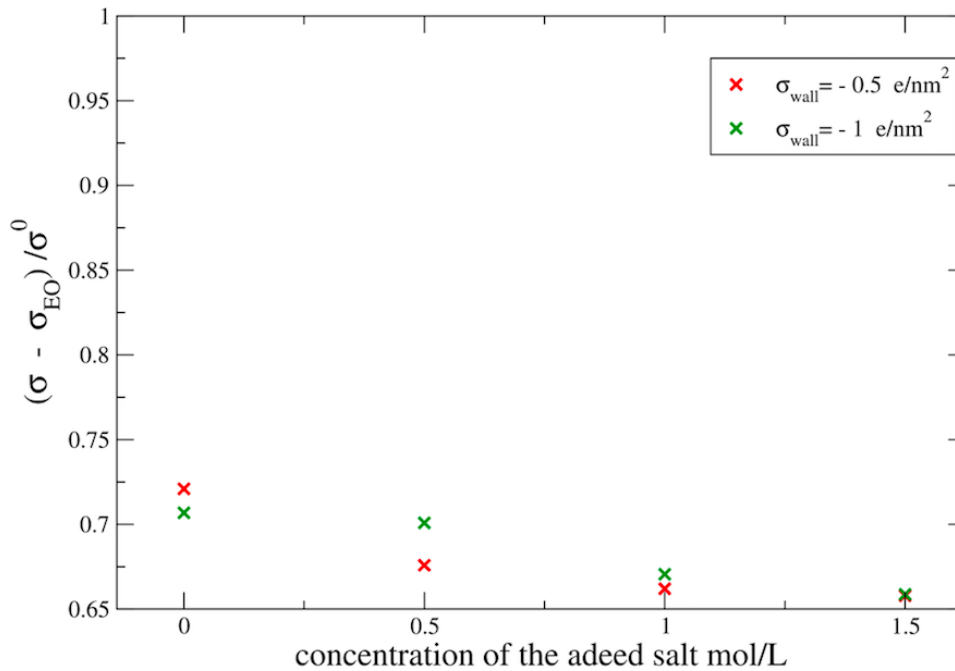


Figure 3.35 – Electric conductivity in surface layer as a function of the concentration of added salt and varying the charge on the wall. The electro-osmotic contribution is removed for each case and divided by the ideal conductivity value. This is the case $Lz = 3.0 \text{ nm}$

In Fig. 3.34, the values of σ/σ^0 are shown for the region in the middle of the pore as a function of the concentration of added salt and for different values of the charge on the wall. Indeed, the behaviour observed in this case resembles to the one illustrated for the $Lz = 4.5 \text{ nm}$ confinement.

On the other hand, Fig. 3.33 illustrates the values of σ/σ^0 for the region close to the wall as a function of the concentration of added salt and for different values of the charge on the wall. When, comparing the dependence of σ/σ^0 with the concentration of added salt in the two confinements we notice a difference. Contrary to the lowest confinement, σ/σ^0 slightly decreases as the concentration of added salt increases.

Finally, in order to see the effect of the confinement for the region close to the wall, a comparison of Fig. 3.34 and Fig. 3.35 is carried out. As a result, a larger value of σ/σ^0 is founded for the case of $Lz = 3.0 \text{ nm}$. Thus, confinement takes place into the ion conductivity.

3.8.4 Conclusion

As a conclusion we can say that:

- σ/σ^0 is larger for the region far to the wall than close to the wall
- Confinement contributes to conductivity, as Lz decreases σ/σ^0 increases at the region close to the walls.

3.9 Prediction of the ionic velocity profiles

3.9.1 Introduction

The objective of this part is to see if we can account for the behaviour of the conductivity, that is very different from the ideal behaviour, from a simple analytic prediction. To do so, first we need to obtain the ion densities and velocity profiles via theory. Indeed, the ion density profile can be recovered using Poisson-Boltzmann theory (see Chapter 1). As we have seen in the beginning of this chapter that our simulation results were close to PB results. However the problem comes from the ion velocity profiles, which cannot be get with known theories. In what follows we propose a simple way to predict the velocity profile of ions and thus the conductivity in the reference frame of the solvent. The velocity profile of ions is affected first by the hydrodynamic contribution due to the presence of the walls, second by the hydrodynamic coupling between ions and third by the electrostatic and excluded volume effects between ions (non-ideal effects).

3.9.2 Hydrodynamic calculation of the solute velocity between walls

When an ion in a solvent is subjected to an external field, its velocity relative to the solvent is limited by the efficiency of the back-flow, in other words the flow of the solvent around the ion. Moreover, when a wall exist, the back-flow is modified, as the hydrodynamic boundary conditions are not the same as in bulk solutions. In our case, the two walls diminish the back-flow of the solvent. Mathematically, when an ion moves close to a wall, the hydrodynamic effect can be taken into account by considering a non-confined solvent and a hydrodynamic image of the solute mirrored with respect to the wall but with an opposite velocity. Thus,

the effect of the wall is taken because the image neutralizes the solvent velocity created by the solute at the wall. However, when there are two parallel walls, the hydrodynamic problem is more complicated. This is because there are an infinite number of hydrodynamic images. To solve this problem, Saugey et al. derived an analytical expression for the ion mobility constrained in a slit pore, for low and high confinement. This was done by using a hydrodynamic approximation detailed in Ref 33. First, an analytical expression for the friction force is obtained by applying an iterative reflection method^[118]. Indeed, such approach can be applied in the case where the particle of radius a is small compared to the confinement size. As a result, the force acting on a particle moving along a single planar wall, at a distance from the wall l , in conditions with a slip length δ is:

$$\mathbf{F}_{1,wall} = \frac{6\pi\eta a}{1 - \frac{a}{z}C[\frac{l}{\delta}]} \mathbf{V} \quad (3.17)$$

where \mathbf{V} is the velocity vector and C the function which is defined by:

$$C[y] = \frac{9}{16} \frac{1}{1 + \frac{1}{y} + O[\frac{1}{y^2}]} \quad (3.18)$$

which considers that the distance to the wall is large compared to the slip length δ . Thus, in order to compute the friction coefficient for a particle confined between two planar walls, it was made a further assumption: Each wall is assumed to contribute independently to the shift in the friction force from its bulk value, *i.e.*:

$$\mathbf{F}_{2walls} = \mathbf{F}_{1wall}(z, \delta) + \mathbf{F}_{1wall}(H - z, \delta) - \mathbf{F}_{bulk} \quad (3.19)$$

where H is the distance between the two walls and here z denotes the distance to the bottom wall. Then, taking into account the previous result, the velocity as a function of the distance to the wall can be written as^[33]:

$$V_{HM}(z) = \frac{V^0}{\frac{1}{1 - \frac{a}{z}C[\frac{z}{\delta}]} + \frac{1}{1 - \frac{a}{H-z}C[\frac{H-z}{\delta}]} - 1} \quad (3.20)$$

We can use this expression to compute the velocity in the direction parallel to the wall in the case of the lowest confinement.

To do so, the largest value of the slip length for this confinement (see Section 3.6.2) was used. In parallel, the velocity for the same system but now neglecting the slip length is obtained and compared to the previous result. In Fig. 3.36, a comparison of these outcomes is shown. It can be deduced that for our system, the values of the slip length does not affect the prediction for the velocity. It means that we can neglect the slip in the equation 3.20. Thus, in the limit of nil slip length, *i.e.* taking $\delta = 0$, the ion relative velocity becomes:

$$V_{HM}(z) = \frac{V^0}{\frac{1}{1 - \frac{R_h}{-z+z_\xi} \frac{9}{16}} + \frac{1}{1 - \frac{R_h}{z+z_\xi} \frac{9}{16}} - 1} \quad (3.21)$$

with z being the position in the slot, z_ξ the position of nil velocity, and R_h the hydrodynamic radius, deduced from the Stokes-Einstein law:

$$R_h = \frac{k_B T}{D^0 6\pi\eta} \quad (3.22)$$

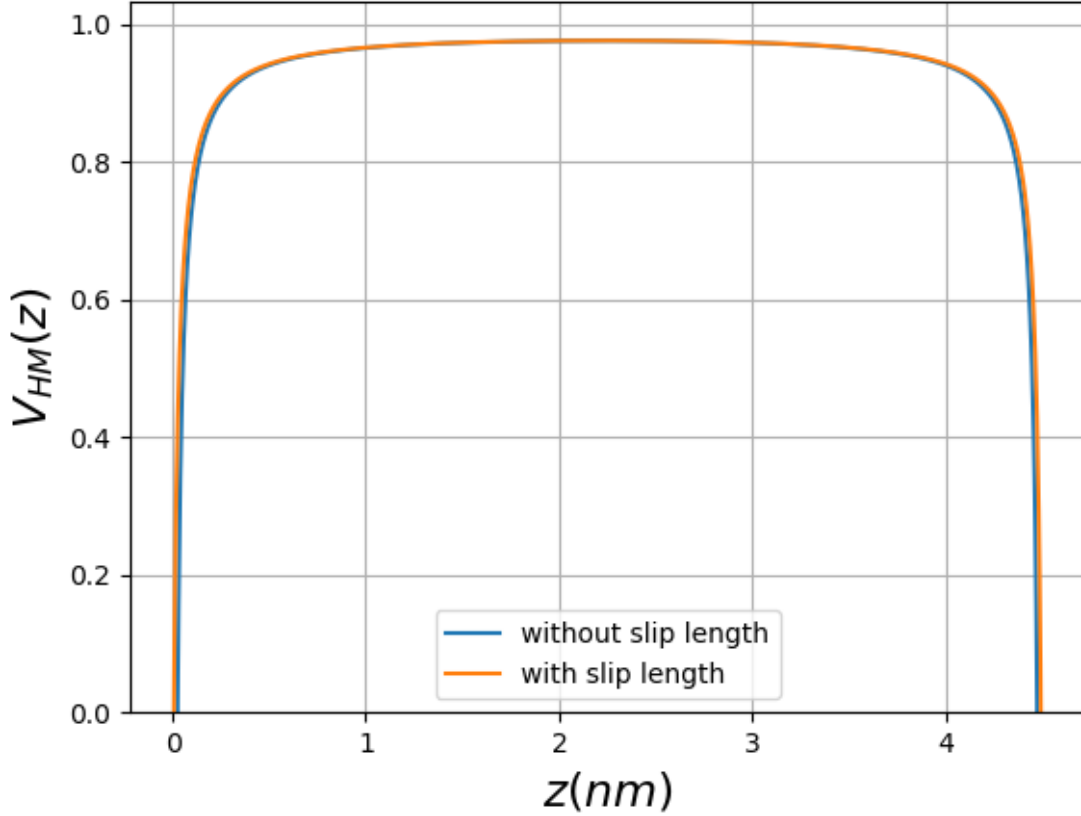


Figure 3.36 – Velocity parallel to the wall of a solute of radius $a = 2.25 \text{ \AA}$ in a slit pore of size $L_z = 4.5 \text{ nm}$ with $\delta = 0 \text{ \AA}$ (blue) and with $\delta = 0.23 \text{ \AA}$ (orange) computed by equation 3.20.

where D^0 is the diffusion coefficient at infinite dilution, and η the viscosity. It is important to note that in the limit where the distance to the surface is large compared to the hydrodynamic radius, this effect can be neglected: $V_{HM} = V^0$ and the classical Stokes-Einstein relation is recovered.

A comparison between the curve obtained using equation 3.21 and the velocity profile (for the cases $\sigma_{wall} = -0.5, -1$ and -2 e/nm^2 for a fix $c_{add} = 2 \text{ mol/L}$) obtained through MPCD code is done in Fig. 3.37. As a result we see that the prediction of the hydrodynamic calculations (see black line at Fig. 3.37) allows us to account for the global shape of the velocity profile but not for the quantitative value. Then, an overestimated value is found at the middle of the slit pore for the curve obtained through the hydrodynamic approach. Although the presence of the wall was taken into account by the hydrodynamic approach, still the hydrodynamic coupling between ions and the electrostatic interactions among them are not considered. Therefore, this is the reason why an overestimate value is observed in Fig. 3.37.

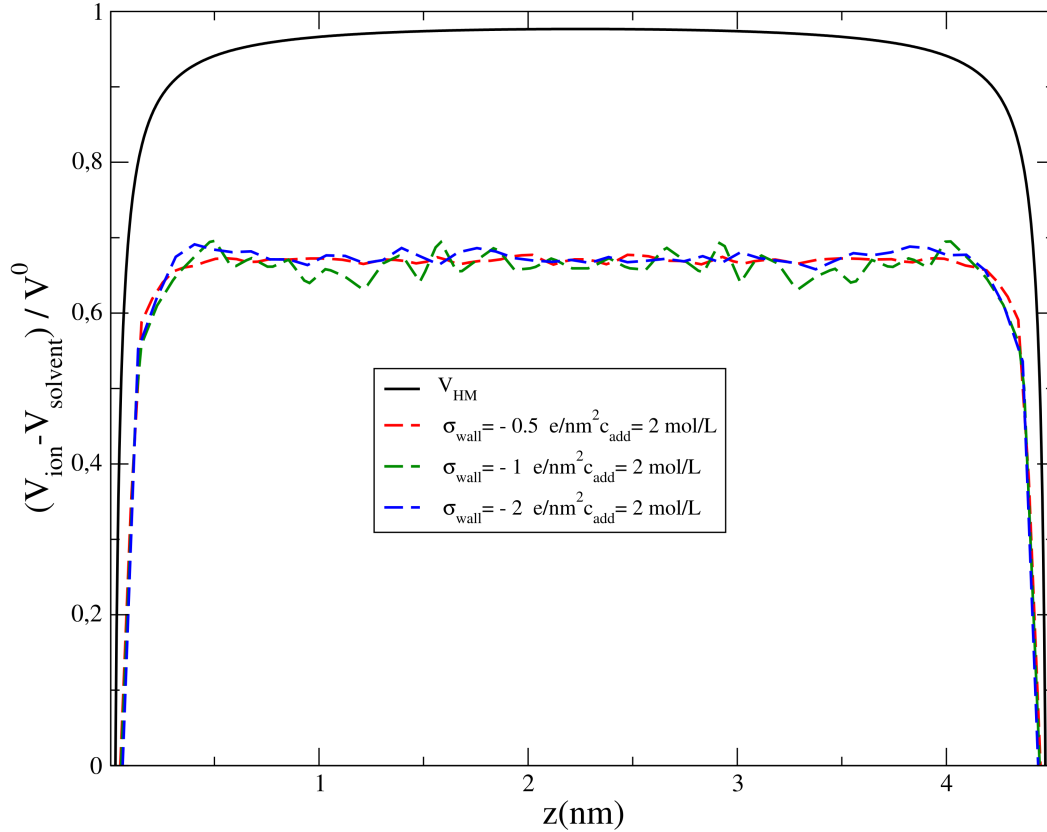


Figure 3.37 – Comparison of the mobility as a function to the distance to the wall predicted by equation 3.21 (black line), the ions velocity profiles for the systems $\sigma_{wall} = -0.5, -1$ and $-2 e/nm^2$ for a fixed $c_{add} = 2 mol/L$.

3.9.3 Accounting for non-ideal effects

It is well known that transport coefficients are strongly influenced by hydrodynamic and electrostatic interactions between ions. Actually, the values of two transport coefficients were obtained through the MPCD simulation for the corresponding bulk system. More specifically, we computed the values of the diffusion coefficient D/D^0 and conductivity σ/σ^0 for a bulk electrolyte solution at $2 mol/L$ by using the same methods presented in Chapter 2.

We propose here to multiply the velocity of the solute computed only with the hydrodynamic contribution from the wall by D/D^0 or σ/σ^0 . It is important to mention that in bulk $\sigma/\sigma^0 = \langle V_{bulk} \rangle / V^0$, so in what follows we will use this notation. Here we refer as $\langle V_{bulk} \rangle$ to the average ion velocity in bulk. In Figure 3.38 a comparison of these curves is shown. Blue curve correspond to the hydrodynamic contribution multiplied by D_{bulk}/D^0 , whereas orange curve is the hydrodynamic contribution multiplied by $\langle V_{bulk} \rangle / V^0$. From the comparison of these curves with the ion velocity profiles (dashed lines), we can conclude that multiplying by the bulk conductivity seems to account better for the non ideal contribution among ions. However, in order to corroborate if this is not only a particular coincidence, the same analysis was carried out for other systems and different confinements.

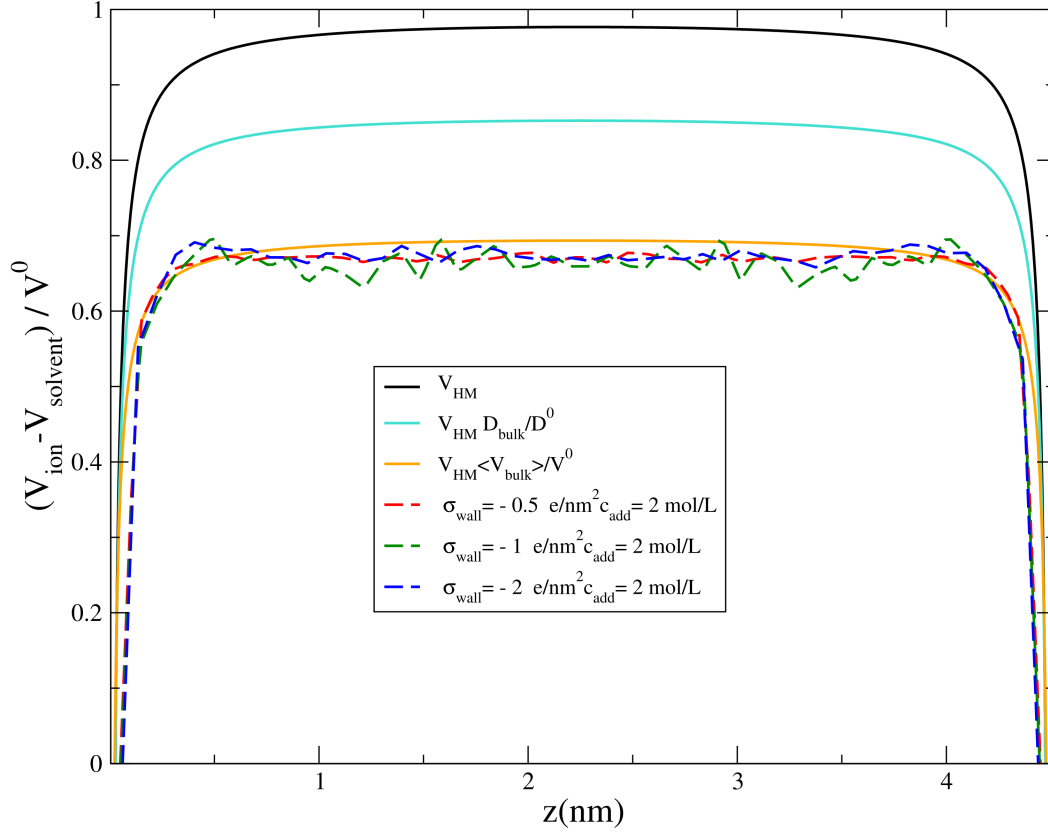


Figure 3.38 – Comparison of the mobility as a function to the distance to the wall predicted by equation 3.21 (black line), the ions velocity profiles for the systems $\sigma_{wall} = -0.5, -1$ and $-2 e/nm^2$ for a fixed $c_{add} = 2 mol/L$ (red and green dashed lines respectively) and the curve corresponding to μ_{HM} multiplied by $\langle V_{bulk} \rangle / V^0$ (orange line). Case of and $Lz = 4.5 nm$.

3.9.4 Application of the method

In the following results, a comparison of the corresponding curves obtained from the multiplication of eq 3.20 by the value of $\langle V_{bulk} \rangle / V^0$ is shown and compared to the counterion velocity profile obtained for the low confinement, *i.e.* the case of largest Lz . The values of the diffusion and conductivity for a bulk system were obtained when considering the following concentrations: $c = 0.5, 1, 1.5$ and $2 mol/L$ (see Table 3.10).

	$c = 0.5 mol/L$	$c = 1 mol/L$	$c = 1.5 mol/L$	$c = 2 mol/L$
$\langle V_{bulk} \rangle / V^0$	0.77	0.75	0.73	0.71
D_{bulk} / D^0	0.92	0.91	0.91	0.91

Table 3.10 – Values of the conductivity and diffusion in bulk, obtained for different ion concentrations by using MPCD simulation

From the figures, a good agreement of the counterions velocity profiles for all the cases of concentration of added salt is found when this is compared to the hydrodynamic approached multiplied by the value of V_{bulk} / V^0 .

To obtain the curve for μ_{HM} the value considered for z_ξ of equation 3.21 is not the value of the distance between the walls (*i.e.* L_{hyd} at Fig 3.3). Indeed the value L_{el} , this is the excluded volume of the ions is taken into account. For $c_{add} = 0.5 \text{ mol/L}$ and 1 mol/L (see Figure 3.39 and Figure 3.39), the curve of $\mu_{HM} \langle V_{bulk} \rangle / V^0$ does not match perfectly at the middle of the pore. This can be explained since for these cases the statistic for the ion profile of counterions is poor compared to the case of $c_{add} = 2 \text{ mol/L}$ (see Figure 3.38).

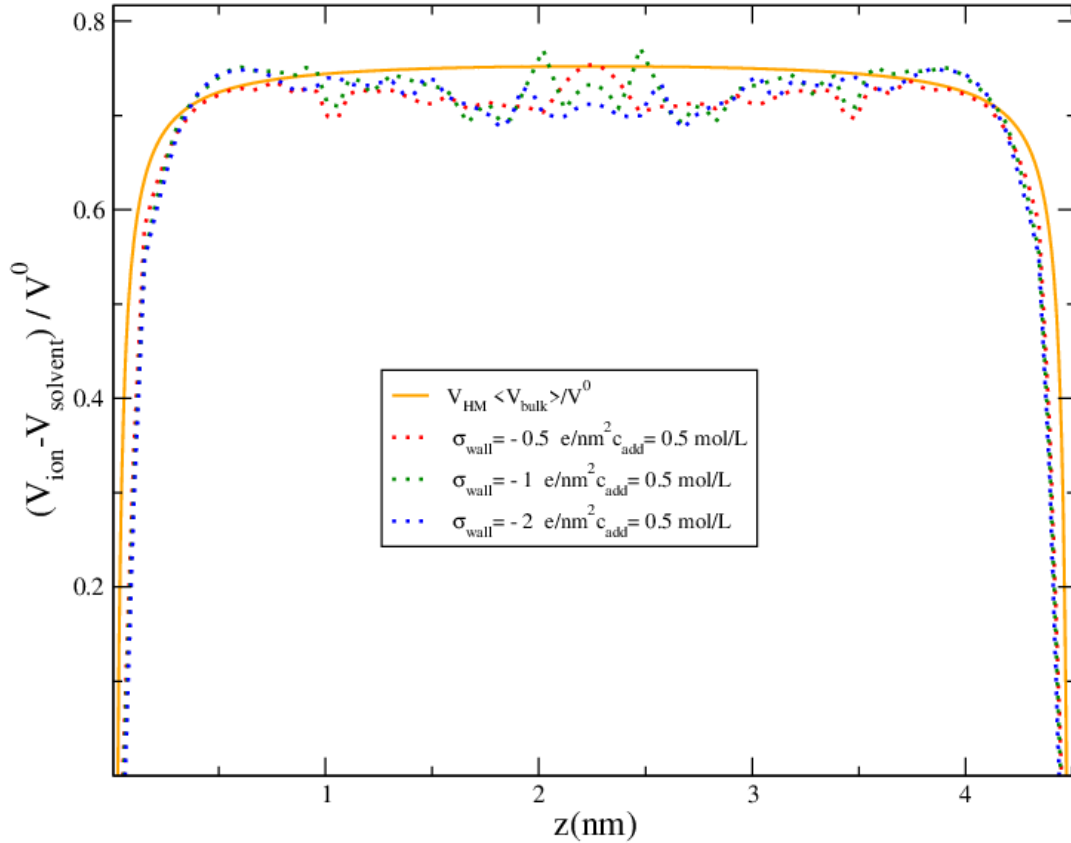


Figure 3.39 – Comparison between: a) Counterions velocity profile as function of the distance to the wall b) Hydrodynamic approach multiplied by the value of the velocity at bulk for the case of $c_{add} = 0.5 \text{ mol/L}$ and $Lz = 4.5 \text{ nm}$.

The rest of the results for the counterions and co-ions for the others systems in Table 3.3 are shown in section A.1 for each confinement.

3.9.5 Conclusion

As we have seen in this section, the velocity profiles of ions in a charged slit pore under an external electric field present strong deviations from the ideal behavior. We were able to account for these non ideal effects by using the following procedure. First, we have computed the velocity of ions as a function of the distance to the wall using the hydrodynamic approach proposed in Ref.^[119]. The only parameters needed to compute this contribution are: The hydrodynamic radius of the solute, the viscosity of the solution, and the distance between

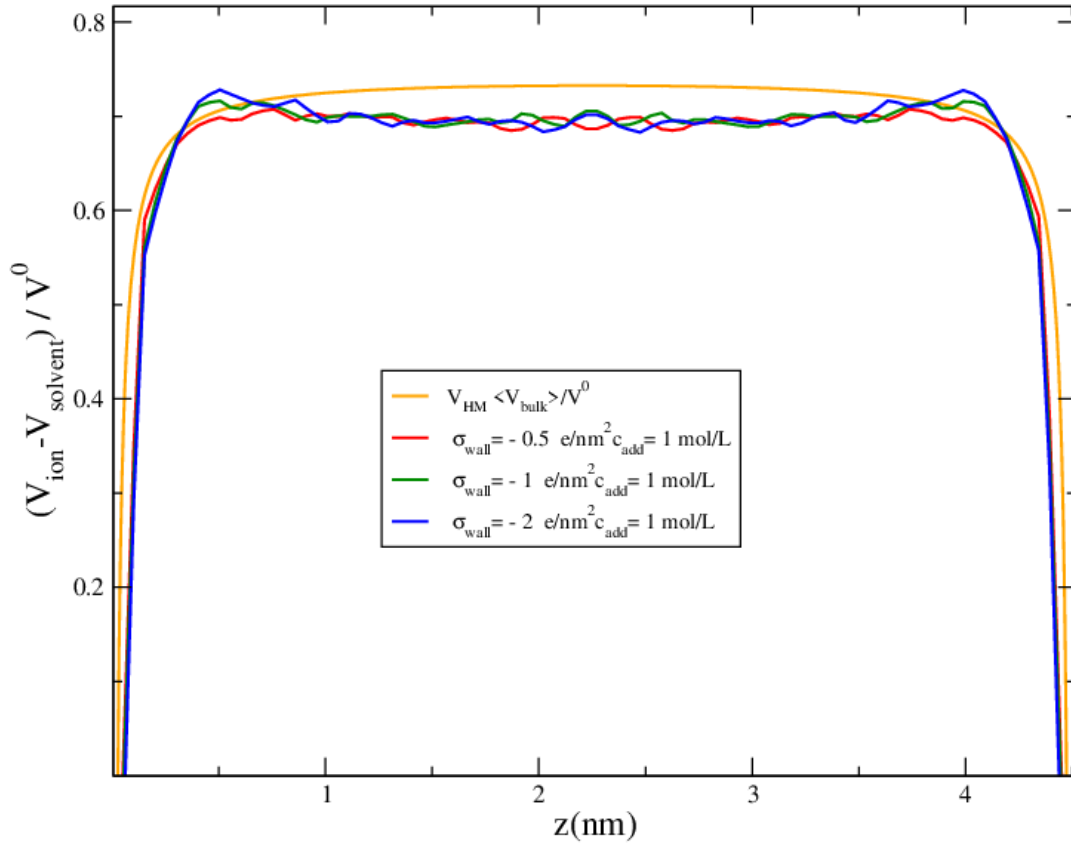


Figure 3.40 – Comparison between: a) Counterions velocity profile as function of the distance to the wall b) Hydrodynamic approach multiplied by the value of the velocity at bulk for the case of $c_{add} = 1 \text{ mol/L}$ and $Lz = 4.5 \text{ nm}$.

walls, assuming a stick boundary condition of the solvent on the wall. The hydrodynamic radius of the solute can be deduced from the self-diffusion coefficient at an infinite dilution through the Stokes law. Second, we have multiplied this hydrodynamic velocity profile by the electric conductivity σ of a bulk ionic solution at the concentration C divided by the ideal conductivity at the same concentration σ° . The concentration C is the ionic concentration in the middle of the slit pore, that in most cases corresponds to the added salt concentration. We have computed the ratio σ/σ° from MPCD simulations of the stationary velocity of ions in a bulk solution at the concentration C under the presence of an external electric field (denoted by $\langle V_{bulk} \rangle / V^0$). For all the systems investigated here, we have obtained an excellent agreement between the ionic velocity profiles computed from MPCD simulations of a charged slit pore and those predicted by combining the hydrodynamic approach with the bulk conductivity. Actually, analytic or semi-analytic calculations of the electric conductivity of bulk ionic solutions exist, that are known to provide reliable estimates of the conductivity up to the molar range^[4]. These results could thus be used to predict the ionic velocity profile in a charged slit pore. Finally, we can propose a whole semi-analytic procedure to predict the electric conductivity of an aqueous electrolyte solution in a charged slit pore. For a slit pore

with surfaces of charge σ_{wall} , distant by L_z , in the presence of an added salt at a concentration C with a the radius of ions and D° their self-diffusion coefficients at infinite dilution, knowing the viscosity η of the solution:

1. compute the ionic density profiles $\rho(z)$ from the Poisson-Boltzmann approximation, for a distance between walls equal to $L_{el} = L_z - 2a$ and a concentration of the ionic reservoir equal to C ;
2. compute the velocity profiles of ions from the hydrodynamic calculation proposed in Ref.^[119] (see Eq. 3.21), using the hydrodynamic radius of solutes deduced from the self-diffusion coefficient at infinite dilution;
3. multiply previous velocity profiles by the ratio σ/σ° , with σ the electric conductivity of a bulk ionic solution at the concentration C , obtained for example by analytical theory, and σ° its ideal value;
4. use Eq. 3.16 to compute the electric conductivity in the slit pore as a function of the distance to the wall, in the reference frame of the solvent.

Polymers in confinement

Contents

4.1	Brief introduction on polymers	104
4.1.1	What is a polymer?	104
4.1.2	Usual modelling of polymers	104
4.2	Structural properties of polymers	105
4.2.1	End-to-end distance and radius of gyration	105
4.2.2	Gyration tensor	107
4.3	Modelling of the system	108
4.3.1	Modelling of the polymer	108
4.3.1.1	Flexible polymer	108
4.3.1.2	Semi-flexible polymer	109
4.3.2	Modelling the interaction of the polymer with the walls	110
4.3.2.1	Purely repulsive wall	110
4.3.2.2	Attractive wall	112
4.4	Systems investigated in the present work	114
4.4.1	Systems under study	114
4.4.2	Simulation under flow	115
4.4.3	Case with repulsive walls	117
4.4.3.1	Results for $L_z \approx 4 R_g$	117
4.4.3.2	Results for $L_z \approx 8.15 R_g$	121
4.4.4	Influence of an attraction to the walls	127
4.4.4.1	Case of a flexible polymer	127
4.4.4.2	Influence of the stiffness of the polymer	133
4.4.5	Conclusion	137

A polymer is a macromolecule resulting from the association of small repeating units called monomers. Polymers are an intrinsic part of Nature. Indeed the best and perhaps most famous example is our DNA. Nevertheless despite its natural presence technological progress allowed the development of synthetic polymers. As a result both kinds of polymers play an essential role in everyday life. Their use range from biomedical or pharmaceutical science^[120,121] to nano-science and engineering^[122]. Specifically, in this thesis we are interested on the dynamics of polymers under flow which could have applications in separation processes. Specifically, in this thesis we are interested on the dynamics of polymers under flow, which could have applications in separation processes.

Contrary to the case of small ions, the typical size of polymers, as quantified for instance by its gyration radius, may not be small compared to the typical length scale at which the solvent velocity changes in a typical nanofluidic experiment. Moreover, polymers are soft molecules. As a consequence, the solvent shear may affect the folding of the polymer. It has been shown both experimentally and theoretically that the effect of a Poiseuille flow on the polymer conformations may cause an effective interaction with the wall, which disappears when the flow velocity vanishes in equilibrium situations. Therefore, the mass distribution of the polymer inside the channel depends on the intensity of the external force driving the flow. The non-equilibrium structure of the system is totally different from the equilibrium structure, while for confined electrolytes, the structure *e.g.* that predicted by Poisson-Boltzmann theory does not change in non-equilibrium situations.

During this Phd work, a secondment project have been designed in collaboration with Christos Likos and Lisa Weiss from Vienna University. While L. Weiss own PhD included the study of polymer separation under flow according to polymer topology, our work was devoted to investigate the influence of an electro-osmotic flow on the behaviour of linear polymers, since most of the existing literature considers polymer within a Poiseuille flow. Indeed, the shape of the electro-osmotic solvent flow differs from that of the Poiseuille flow, and is modified by adding salt. That is to say, the electro-osmotic profile becomes more flat at the region of the middle of the slit pore as the concentration of added salt increases (see Sec 3.6.1). In addition to the effect of the flow, we also investigate the influence of a screened Van der Waals attraction between the polymer and the walls.

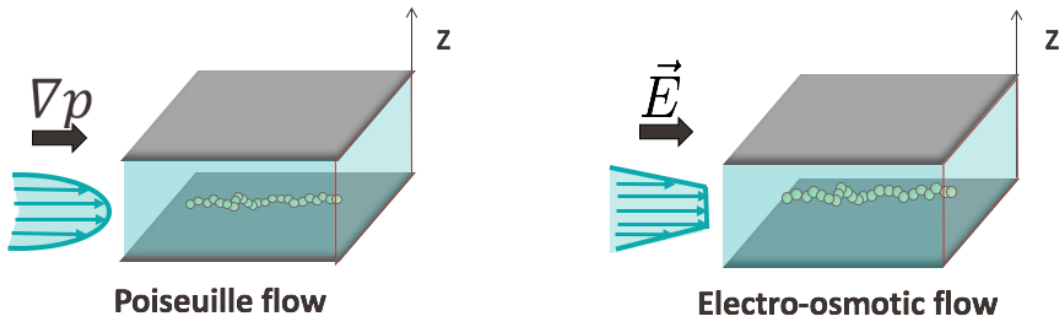


Figure 4.1 – Systems under study. On the left part: A Poiseuille flow is applied into a slit pore that contains a linear polymer. On the right part: An electro-osmotic flow is applied into a slit pore that contains a linear polymer.

4.1 Brief introduction on polymers

4.1.1 What is a polymer?

A polymer molecule is made of the same repeating units, called monomers, or of different but resembling units. There exist four architectures of a polymer molecule^[123]: a linear chain (a), a branched chain (b), a cross-linked polymer (c) and ring chain (d) (see Fig 4.2). A linear chain is the simplest architecture, and consists in a chain of monomers linked in a linear form, *i.e.* there are no ramifications. On the other hand, a branched chain has branches, long and short that are connected to a main linear chain. A cross-linked polymer forms a network encompassing the entire system. Finally a ring polymer, is a linear polymer where the first and last monomer are connected.

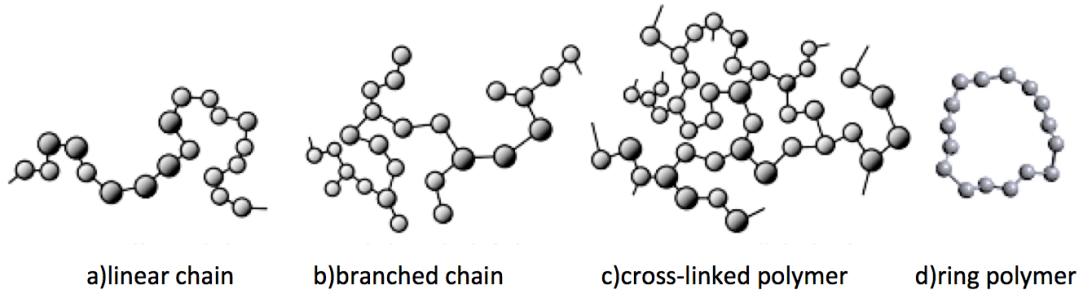


Figure 4.2 – Architecture of polymer chain: a linear chain (a), a branched chain (b), and a cross-linked polymer (c) , where a bead represents a monomer here.

Aside from the classification of polymers due to their architecture, another categorization is carried out considering the kind of monomers forming the polymer^[124]. Thus, when the polymer is formed by identical repeating units, a homo-polymer is obtained. For instance,

$$A + A + A + \dots = AAA\dots \quad (4.1)$$

On the other hand if the monomers are different we have then a copolymer, like

$$A + B + A + \dots = ABA\dots \quad (4.2)$$

In what follows, a linear chain formed by the same repeating units will be taken into account, *i.e.* we are interested in the case of linear homo-polymers.

4.1.2 Usual modelling of polymers

In order to study the properties of polymers several coarse-grained geometrical models are usually used in the literature. Among these, we have the bead-stick model (a), the bead-spring model (b), and the pearl-necklace model (c) (see Figure 4.3).

In the bead-stick model, the chain consists of beads and sticks that connect adjacent beads. Many variations are possible: (1) the bead diameter and the stick thickness can be any value, (2) we can restrict the angle between two adjacent sticks or let it free, or (3) we can restrict the torsional angle (dihedral angle) of a stick relative to the second next stick.

In the bead-spring model, the whole chain is represented by a series of beads connected by springs. The bead-spring model conveniently describes the motion of different parts of the chain. The segment of this model is a spring and a bead on its end.

In the pearl-necklace model, the beads (pearls) are always in contact with the two adjacent beads. This model is essentially a bead-stick model with the stick length equal to the bead diameter. As in the bead-stick model, we can restrict the bond angle and the dihedral angle.

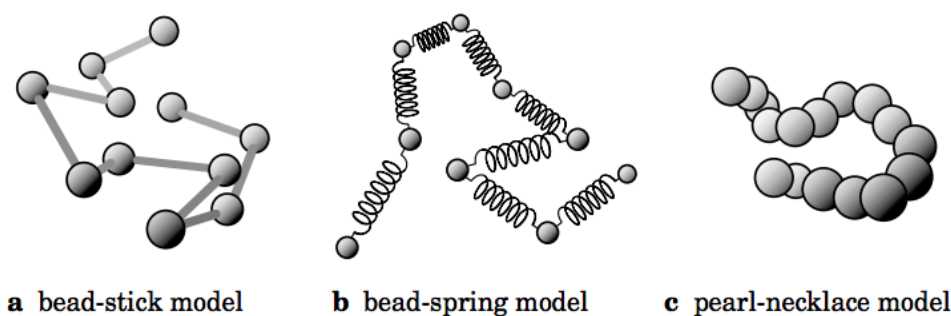


Figure 4.3 – Various models for a linear chain polymer in a continuous space: a bead-stick model (a), a bead-spring model (b), and a pearl-necklace model (c).

In what follows we will use a generic bead-spring model.

4.2 Structural properties of polymers

4.2.1 End-to-end distance and radius of gyration

The simplest measure of the length of a polymer chain is the contour length. This is the length of the stretched-out molecule, *i.e.* for a chain of N bonds of length b the contour length is Nb . However, this does not give a realistic measure of the size of the polymer chain.

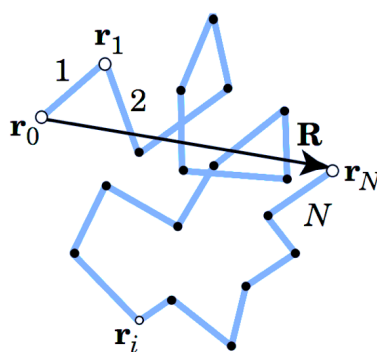


Figure 4.4 – End-to-end vector \mathbf{R} is defined by $\mathbf{R} = \mathbf{r}_N - \mathbf{r}_0$

Each chain adopts one of the plenty of possible conformations, *i.e.* there exist plenty of instantaneous shapes of a polymer chain in solution. Furthermore, the conformation is continuously changing due to thermal motion. For these two reasons, in order to assess the dimension or the size of a polymer molecule it is necessary to take a statistical average. Thus, we will use two useful average measures of the dimensions of polymer coils: the end-to-end

Chapter 4. Polymers in confinement

distance and the radius of gyration^[123]. Then for a linear chain that consists of N bonds of length b (see Fig. 4.4), it is convenient to define the end-to-end vector \mathbf{R} by

$$\mathbf{R} \equiv \mathbf{r}_N - \mathbf{r}_0 \quad (4.3)$$

where \mathbf{R} is different for each configuration of the chain. The positions of the joints are denoted by $\mathbf{r}_i (i = 0, 1, \dots, N)$. The two ends of the i th bond are at \mathbf{r}_{i-1} and \mathbf{r}_i . Although the chain ends are not necessarily faced outward and therefore \mathbf{R} does not always span the largest dimension of the chain, its average length is a good measure for the overall chain dimension. The root-mean-square end-to-end distance R_F (or simply end-to-end distance) of the chain is the root mean square of \mathbf{R} :

$$R_F^2 = \langle \mathbf{R}^2 \rangle \equiv \langle (\mathbf{r}_N - \mathbf{r}_0)^2 \rangle \quad (4.4)$$

We can regard the whole chain as roughly being contained in a sphere of diameter R_F . Another often used measure of the chain dimension is the root-mean-square radius of gyration R_g (or simply radius of gyration). Its square, R_g^2 , is the second moment around the center of mass of the chain. The latter is defined as the mean square of the distance between the beads and the center of mass (see Fig. 4.5) . Roughly, the chain occupies a space of a sphere of radius R_g . The center of mass \mathbf{r}_G of the chain is given as : $\mathbf{r}_G = \frac{1}{N+1} \sum_{i=0}^N \mathbf{r}_i$, where we assume that beads have the same mass and are connected by massless bonds. Then, R_g is given by:

$$R_g^2 = \left\langle \frac{1}{N+1} \sum_{i=0}^N (\mathbf{r}_i - \mathbf{r}_G)^2 \right\rangle = \frac{1}{N+1} \sum_{i=0}^N \langle (\mathbf{r}_i - \mathbf{r}_G)^2 \rangle \quad (4.5)$$

The following formula is useful:

$$R_g^2 = \frac{1}{2} \left\langle \frac{1}{(N+1)^2} \sum_{i,j=0}^N (\mathbf{r}_i - \mathbf{r}_j)^2 \right\rangle = \frac{1}{2(N+1)^2} \sum_{i,j=0}^N \langle (\mathbf{r}_i - \mathbf{r}_j)^2 \rangle \quad (4.6)$$

This formula indicates that we can use the mean square distance between two monomers to obtain R_g in place of first calculating \mathbf{r}_G and then the mean square distance between \mathbf{r}_G and each monomer. Because summation with respect to i and j is another averaging, we can say that R_g^2 is half of the average square distance between two monomers on the chain. We can prove the formula by using the following identity:

$$\sum_{i,j=0}^N (\mathbf{r}_i - \mathbf{r}_j)^2 = \sum_{i,j=0}^N [(\mathbf{r}_i - \mathbf{r}_G) - (\mathbf{r}_j - \mathbf{r}_G)]^2 \quad (4.7)$$

$$= \sum_{i,j=0}^N (\mathbf{r}_i - \mathbf{r}_G)^2 - 2 \sum_{i,j=0}^N (\mathbf{r}_i - \mathbf{r}_G) \cdot (\mathbf{r}_j - \mathbf{r}_G) + \sum_{i,j=0}^N (\mathbf{r}_j - \mathbf{r}_G)^2 \quad (4.8)$$

$$= 2(N+1) \sum_{i=0}^N (\mathbf{r}_i - \mathbf{r}_G)^2 - 2 \sum_{i=0}^N (\mathbf{r}_i - \mathbf{r}_G) \cdot \sum_{j=0}^N (\mathbf{r}_j - \mathbf{r}_G) \quad (4.9)$$

$$= 2(N+1) \sum_{i=0}^N (\mathbf{r}_i - \mathbf{r}_G)^2 \quad (4.10)$$

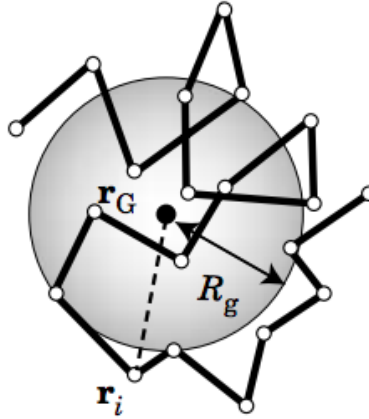


Figure 4.5 – Center of mass \mathbf{r}_G and the radius of gyration \mathbf{R}_g in the bead-stick model

This transformation does not assume any specific chain model. Equation 4.6 applies therefore to any chain conformation. Note that R_F is defined for linear chains only, but R_g can be defined for any chain architecture including non-linear chains such as branched chains. In this sense, R_g gives a more universal measure for the chain dimension.

4.2.2 Gyration tensor

In the previous section we defined two useful measurements of the dimension of polymers. However in order to capture the effect of elongation of the polymer another parameter is needed. So we can define the gyration tensor which captures the anisotropy, *i.e* the fact that the polymer chain can be elongated in one dimension more than in other dimensions. This is defined by:

$$S = \frac{1}{N} \begin{pmatrix} \sum_i (x_i - x_G)^2 & \sum_i (x_i - x_G)(y_i - y_G) & \sum_i (x_i - x_G)(z_i - z_G) \\ \sum_i (x_i - x_G)(y_i - y_G) & \sum_i (y_i - y_G)^2 & \sum_i (y_i - y_G)(z_i - z_G) \\ \sum_i (x_i - x_G)(z_i - z_G) & \sum_i (y_i - y_G)(z_i - z_G) & \sum_i (z_i - z_G)^2 \end{pmatrix} \quad (4.11)$$

Thus

$$S_{ij} = \begin{pmatrix} S_{xx} & S_{xy} & S_{xz} \\ S_{yx} & S_{yy} & S_{yz} \\ S_{zx} & S_{zy} & S_{zz} \end{pmatrix} \quad (4.12)$$

Since the gyration tensor is a symmetric 3x3 matrix, a Cartesian coordinate system can be found in which it is diagonal

$$S_{ij} = \begin{pmatrix} \lambda_x^2 & 0 & 0 \\ 0 & \lambda_y^2 & 0 \\ 0 & 0 & \lambda_z^2 \end{pmatrix} \quad (4.13)$$

Chapter 4. Polymers in confinement

where the axes are chosen such that the diagonal elements are ordered $\lambda_x^2 \leq \lambda_y^2 \leq \lambda_z^2$. These diagonal elements are called the principal moments of the gyration tensor.

Indeed, the principal moments can be combined to give several parameters. For example, the squared radius of gyration is the sum of the principal moments

$$R_g^2 = \lambda_x^2 + \lambda_y^2 + \lambda_z^2 \quad (4.14)$$

The asphericity b is defined by

$$b \stackrel{\text{def}}{=} \lambda_z^2 - \frac{1}{2}(\lambda_x^2 + \lambda_y^2) = \frac{3}{2}\lambda_z^2 - \frac{R_g^2}{2} \quad (4.15)$$

which is always non-negative and zero only when the three principal moments are equal, $\lambda_x = \lambda_y = \lambda_z$. This zero condition is met when the distribution of particles is spherically symmetric (hence the name asphericity) but also whenever the particle distribution is symmetric with respect to the three coordinate axes, *e.g.*, when the particles are distributed uniformly on a cube, tetrahedron or other Platonic solid.

Similarly, the acylindricity c is defined by

$$c \stackrel{\text{def}}{=} \lambda_y^2 - \lambda_x^2 \quad (4.16)$$

which is always non-negative and zero only when the two principal moments are equal, $\lambda_x = \lambda_y$. This zero condition is met when the distribution of particles is cylindrically symmetric (hence the name, acylindricity), but also whenever the particle distribution is symmetric with respect to the two coordinate axes, *e.g.*, when the particles are distributed uniformly on a regular prism.

4.3 Modelling of the system

4.3.1 Modelling of the polymer

4.3.1.1 Flexible polymer

An interaction potential was considered in order to simulate a polymer of M beads, which consists of two parts^[125]:

- A Weeks-Chandler-Andersen (WCA) potential U_{WCA} , which operates between all M beads in the system.

$$U_{WCA} = \sum_{i=1}^M \sum_{j=i+1}^M 4\epsilon_{MM} \left[\left(\frac{\sigma_{MM}}{r_{ij}} \right)^{12} - \left(\frac{\sigma_{MM}}{r_{ij}} \right)^6 + \frac{1}{4} \right] \Theta(2^{1/6}\sigma_{MM} - r_{ij}) \quad (4.17)$$

In Eq. 4.17 ϵ_{MM} denotes the monomer-monomer interaction strength in units of $k_B T$, σ_{MM} is the monomer diameter, r_{ij} is the distance between two monomers i and j , and Θ is the Heaviside function.

- A modified harmonic potential, U_{FENE} , which links the monomers into a polymer chain^[126].

$$U_{FENE} = \begin{cases} \text{if } r_{i,i+1} < R_0 & \sum_{i=1}^{M-1} \frac{k}{2} R_0^2 \ln \left(1 - \left(\frac{r_{i,i+1}}{R_0} \right)^2 \right) \\ \text{if } r_{i,i+1} > R_0 & \infty \end{cases} \quad (4.18)$$

with the standard Kremer-Grest parameters for the bond constant $k = 30 \epsilon_{MM}/\sigma_{MM}^2$ and the maximum bond extension $R_0 = 1.5\sigma_{MM}$ to prevent non-physical bond-crossing^[127]. This potential has the form of a simple harmonic potential for small $r_{i,i+1}$ but limits the spring extensibility to R_0 .

These simple potential models were used in the first part of our study and will give us clues as to the behaviour of generic polymers without the additional computer cost necessary to model a particular polymeric system with a more realistic potential.

4.3.1.2 Semi-flexible polymer

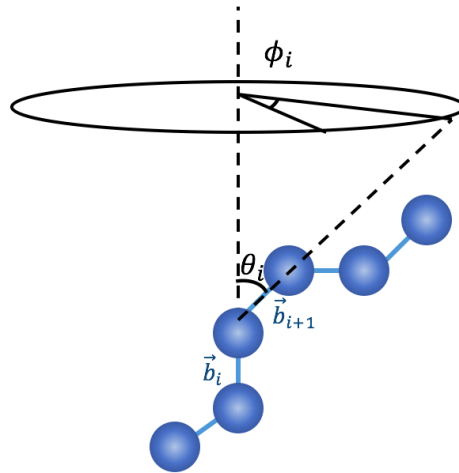


Figure 4.6 – Conformation of a chain with the arbitrary distribution of torsion angles ϕ_i and bending angles θ_i

A semiflexible chain with degree of polymerization N and with bond length b . Chain conformations are described by a set of bond angles θ_i and torsion angles ϕ_i (see Figure 1). The potential energy of a semiflexible chain in a given conformation with a set of torsion and bond angles ϕ_i, θ_i is given by

$$U_{\text{bend}} = k_B T \tilde{\epsilon}_{\text{bend}} \sum_{i=1}^{N-1} (1 - \cos(\theta_i)) \quad (4.19)$$

where $\tilde{\epsilon}_{\text{bend}}$ is a bending energy in terms of the thermal energy $k_B T$. Indeed, a bending potential Eq. 4.19 imposes restrictions on the accessible values of the bond angles θ_i but allows torsion angles to assume any value from the interval $-\pi < \phi_i < \pi$.

For a polymer chain the only correlation transmitted between two bond vectors \mathbf{b}_i and \mathbf{b}_{i+n} is the component of the bond vector \mathbf{b}_{i+1} along the vector \mathbf{b}_i , *i.e.* $b \langle \cos(\theta) \rangle$. Like there are free rotations of the torsion angle ψ_{i+1} , the component of the vector \mathbf{b}_{i+1} normal to the vector \mathbf{b}_i averages out to zero. Therefore, if we consider now the correlation of bond vector \mathbf{b}_i and \mathbf{b}_{i-1} , only projection of the bond vector \mathbf{b}_i onto \mathbf{b}_{i-1} survives due to free rotation of torsion angle ψ_i . This reduces correlations between vector \mathbf{b}_{i+1} and vector \mathbf{b}_{i-1} by the factor $\langle \cos(\theta) \rangle^2$. Thus, the correlations between bond vectors \mathbf{b}_i and \mathbf{b}_{i+n} are reduced by the factor $\langle \cos(\theta) \rangle^n$ due to independent rotation of n torsion angles between them:

$$\langle (\mathbf{b}_i \cdot \mathbf{b}_{i+n}) \rangle = b^2 \langle \cos(\theta(n)) \rangle = b^2 (\langle \cos(\theta) \rangle)^n \approx b^2 \left(\left\langle 1 - \frac{\theta^2}{2} \right\rangle \right)^n \approx b^2 \exp(-n \langle \theta^2 \rangle / 2) \quad (4.20)$$

where brackets $\langle \rangle$ denote the average over torsion angles ψ_i and bond angles θ_i . Thus, In the derivation of Eq. 4.19 it is assumed that the typical values of the bond angle θ are small such that $\cos(\theta)$ can be approximated by its power series, $\cos(\theta) \approx 1 - \frac{\theta^2}{2}$. This assumption is true for large values of the bending energy ϵ_{bend} . In this approximation the correlations between bond vectors \mathbf{b}_i and \mathbf{b}_{i+n} decay exponentially with the number of bonds n between them.

Thus since

$$\langle (\mathbf{b}_i \cdot \mathbf{b}_{i+n}) \rangle = b^2 \left(\left\langle 1 - \frac{\theta^2}{2} \right\rangle \right)^n \quad (4.21)$$

When $\theta \ll 1$, the correlation between \mathbf{b}_i and \mathbf{b}_{i+n} at two points separated by $l = bn$ along the contour is

$$\langle (\mathbf{b}_i \cdot \mathbf{b}_{i+n}) \rangle = b^2 \left(\left\langle 1 - \frac{\theta^2}{2} \right\rangle \right)^n = b^2 \left(\left\langle 1 - \frac{\theta^2}{2} \right\rangle \right)^{l/b} \quad (4.22)$$

Then if we consider the units vector of \mathbf{b}_i and \mathbf{b}_{i+n} , *i.e.* \mathbf{u}_i and \mathbf{u}_{i+n}

$$\langle (\mathbf{u}_i \cdot \mathbf{u}_{i+n}) \rangle = \left(\left\langle 1 - \frac{b}{l_p} \right\rangle \right)^{l/b} \approx \exp -l/l_p \quad (4.23)$$

where $l_p = \frac{2b}{\langle \theta^2 \rangle}$ is defined as the persistence length, which is the characteristic distance over which the bond vector-bond vector correlation decays. And we used the limit where $(1 + bx)^{1/b} \approx \exp x$.

The persistence length is a basic mechanical property quantifying the stiffness of a polymer. Informally, for pieces of the polymer that are shorter than the persistence length, the molecule behaves rather like a flexible elastic rod/beam (beam theory), while for pieces of the polymer that are much longer than the persistence length, the properties can only be described statistically, like a three-dimensional random walk. Formally, the persistence length, l_p , is defined as the length over which correlations in the direction of the tangent are lost.

4.3.2 Modelling the interaction of the polymer with the walls

4.3.2.1 Purely repulsive wall

Since the polymer will be confined between two infinite parallel walls in the z -direction, the interaction between the polymer and the walls has to be defined. Indeed this interaction will

Chapter 4. Polymers in confinement

influence the physical behaviour of our polymer. In the first case, we assume that the polymer experiences a purely repulsive wall potential^[128]. Thus, the potential will be obtained by the integration under an infinite plane of a Lennard-Jones potential, *i.e.*,

$$U_{\text{LJ}} = 4\epsilon \left[\left(\frac{\sigma}{r} \right)^{12} - \left(\frac{\sigma}{r} \right)^6 \right] \quad (4.24)$$

Here ϵ is the interaction strength, σ the particle diameter and $r = \sqrt{x^2 + y^2 + z^2}$ the distance between two particles. The first term is repulsive and mimics the repulsion of two atoms due to overlapping electron clouds. The second part is attractive and represents induced dipole interactions. The potential of an infinite wall in \mathbf{e}_x and \mathbf{e}_z direction and normal vector in \mathbf{e}_z is derived by:

$$U_{\text{W}}(z') = 4\epsilon\rho \int_{z'}^{-\infty} \int_{-\infty}^{\infty} \int_{-\infty}^{\infty} dx dy dz \left[\left(\frac{\sigma}{r} \right)^{12} - \left(\frac{\sigma}{r} \right)^6 \right] \quad (4.25)$$

By assuming a packing fraction of $P = 1$ of wall particles with radius $\sigma/2$, one can calculate a density of LJ particles of $\rho = \frac{P}{4/3\pi\sigma^3} = \frac{6}{\pi\sigma^3}$. The problem is point-symmetric with respect to the normal vector, thus it is useful to transform the coordinates to cylindrical coordinates ρ , ϕ and z :

$$\rho^2 = x^2 + y^2 \quad (4.26)$$

$$z = z \quad (4.27)$$

$$dx dy dz = \rho d\rho d\phi dz \quad (4.28)$$

Using cylindrical coordinates we obtain:

$$U_{\text{W}}(z') = \frac{24\epsilon}{\pi\sigma^3} \int_{z'}^{-\infty} dz \int_0^{2\pi} d\phi \int_0^{\infty} d\rho \rho \left[\left(\frac{\sigma^2}{\rho^2 + z^2} \right)^6 - \left(\frac{\sigma^2}{\rho^2 + z^2} \right)^3 \right] \quad (4.29)$$

$$= 48\epsilon \int_{z'}^{-\infty} dz \left[\frac{-\sigma^9}{10} (\rho^2 + z^2)^{-5} - \frac{-\sigma^3}{4} (\rho^2 + z^2)^{-2} \right]_0^{\infty} \quad (4.30)$$

$$= 48\epsilon \int_{z'}^{-\infty} dz \frac{\sigma^9}{10} z^{-10} - \frac{\sigma^9}{4} z^{-4} \quad (4.31)$$

$$= 48\epsilon \left[\frac{-1}{9 \cdot 10} \left(\frac{\sigma}{z} \right)^9 - \frac{-1}{3 \cdot 4} \left(\frac{\sigma}{z} \right)^3 \right]_{z'}^{-\infty} \quad (4.32)$$

$$= 4\epsilon \left[\frac{2}{15} \left(\frac{\sigma}{z'} \right)^9 - \left(\frac{\sigma}{z'} \right)^3 \right] \quad (4.33)$$

Eq. 4.33 can be subsequently shifted and truncated to achieve a purely repulsive wall potential without any discontinuity in its derivative. This is the wall potential which is currently implemented.

4.3.2.2 Attractive wall

When considering the case where there is added salt on the electro-osmotic flow, induced dipole interactions will be screened. We will approximate this screening by a Yukawa term $\exp(-\kappa r)$ acting only on the $-\frac{\sigma^6}{r^6}$ term in Eq 4.24. κ is the inverse Debye screening length and has a unit of length^{-1} . Integration of the first term in Eq 4.24 will not be influenced by the screening term as it approximates the core-core repulsion. Therefore, we assume a localization of induced dipole at the wall-fluid boundary ($z = 0$) eliminating the integration over z . For simplicity, we will subsequently omit all constant factors, which are $4\epsilon\sigma^6$.

$$U_Y(z) = \int_{-\infty}^{\infty} \int_{-\infty}^{\infty} dx dy \frac{\exp(-\kappa r)}{r^6} \quad (4.34)$$

$$= -2\pi \int_0^{\infty} d\rho \rho \frac{\exp\left(-\kappa(\rho^2 + z^2)^{1/2}\right)}{(\rho^2 + z^2)^3} \quad (4.35)$$

Subsequently, we will substitute:

$$\omega^2 = \rho^2 + z^2 \quad (4.36)$$

$$\rho = \sqrt{\omega^2 - z^2} \quad (4.37)$$

$$\frac{d\rho}{d\omega} = \frac{2\omega}{2\sqrt{\omega^2 - z^2}} \quad (4.38)$$

$$\rho d\rho = \omega d\omega \quad (4.39)$$

and change the integration boundaries accordingly:

$$U_Y(z) = -2\pi \int_z^{\infty} d\omega \frac{\exp(-\kappa\omega)}{\omega^5} \quad (4.40)$$

According to^[129], this integral can be expressed as:

$$U_Y(z) = -2\pi \left[-\frac{\exp(-\kappa\omega)}{4\omega^4} + \frac{\kappa \exp(-\kappa\omega)}{12\omega^3} - \frac{\kappa^2 \exp(-\kappa\omega)}{24\omega^2} + \frac{\kappa^3 \exp(-\kappa\omega)}{24\omega} + \frac{\kappa^4}{24} Ei(-\kappa\omega) \right]_z^{\infty} \quad (4.41)$$

Here, Ei is the exponential integral, defined as:

$$Ei(-\kappa\omega) = - \int_{-(-\kappa\omega)}^{\infty} \frac{\exp(-t)}{t} dt = -E_1(\kappa\omega) \quad (4.42)$$

E_1 is another description of the integral with $Ei(-x) = -E_1(x)$. To solve this integral, we can write the exponential function in a series expansion and integrate subsequently each term individually.

$$Ei(-\kappa\omega) = - \int_{\kappa\omega}^{\infty} dt \frac{1}{t} \left(\sum_{n=0}^{\infty} \frac{(-1)^n t^n}{n!} \right) \quad (4.43)$$

$$= - \int_{\kappa\omega}^{\infty} dt \frac{1}{t} + \sum_{n=1}^{\infty} \frac{(-1)^n t^{n-1}}{n!} \quad (4.44)$$

$$= - \left[\ln(t) + \sum_{n=0}^{\infty} \frac{(-1)^n t^n}{nn!} \right]_{\kappa\omega}^{\infty} \quad (4.45)$$

$$= \ln(\kappa\omega) + \gamma + \sum_{n=0}^{\infty} \frac{(-1)^n (\kappa\omega)^n}{nn!} \quad (4.46)$$

In Eq. 4.46, γ is the Euler constant $\gamma = 0.5772156$. This expression has to be evaluated with sufficient accuracy for $\kappa\omega < 1$. Numerical recipes can be found in^[130]. In the case of $\kappa\omega \geq 1$, one can express the integral as continued fraction. For large values of $\kappa\omega$, one can approximate $-E_1(\kappa\omega)$ by:

$$Ei(-\kappa\omega) = - \exp(-\kappa\omega) \frac{1}{\kappa\omega + \frac{1}{\kappa\omega + \frac{1}{\kappa\omega + \frac{2}{1+\dots}}}}} \quad (4.47)$$

$$\approx - \frac{\exp(-\kappa\omega)}{\kappa\omega} \quad (4.48)$$

using its representation as a continuous fraction [3]. Thus at large distances, the last two terms in Eq. 4.41 cancel and the potential is dominated by $\exp(-\kappa\omega)/\omega 2$. The constant factor we omitted while performing the integration is $4\epsilon\sigma^6$. Furthermore, we must take into account the two dimensional number density of wall particles $\rho_{2D} = 4/(\pi\sigma^2)$. Thus the prefactor reads as $\epsilon\sigma^4/\pi$, combined with 2π from the integration, we obtain $2\epsilon\sigma^4$. Combining these results lead to:

$$U_Y = -2\epsilon\sigma^4 \begin{cases} \exp(-\kappa z) \left[\frac{1}{4z^4} - \frac{\kappa}{12z^3} + \frac{\kappa^2}{24z^2} \right] & \text{for } \kappa z > 1 \\ \exp(-\kappa z) \left[\frac{1}{4z^4} - \frac{\kappa}{12z^3} + \frac{\kappa^2}{24z^2} - \frac{\kappa^4}{24} \left(\ln(\kappa z) + \gamma + \sum_{n=0}^{\infty} \frac{(-1)^n (\kappa z)^n}{nn!} \right) \right] & \text{for } \kappa z < 1 \end{cases} \quad (4.49)$$

A short cross-check of the units reveals that all terms in the square brackets have a dimension of length⁻⁴ annihilating the dimensions of the prefactor σ^4 . This potential has to be combined with the repulsive part of Eq. 4.33. It might be more reasonable to integrate the repulsive part of a LJ potential in only two dimensions (x and y here), as the screened attractive potential is integrated only over x and y. Furthermore, one should think about whether this potential will be implemented by using the approximate form of $\kappa z > 1$ or with a case distinction. In any case, we need a cut-off radius for the potential. To avoid any discontinuities in the forces, *i.e.* in the derivative of the potential, a smothering function should be employed^[131]:

$$U(z) = \begin{cases} U_Y(z) \cdot 1 & (z \leq a) \\ U_Y(z) \cdot \frac{(b^2 - z^2)^2 (b^2 + 2z^2 - 3a^2)}{(b-a)^3} & (a < z \leq b) \\ U_Y(z) \cdot 0 & (b < z) \end{cases} \quad (4.50)$$

4.4 Systems investigated in the present work

4.4.1 Systems under study

The Poiseuille and the electro-osmotic flow were induced into a slit pore when:

- Repulsive walls are considered for a
 - flexible linear polymer consisting of 40 beads
 - stiff linear polymer consisting of 40 beads with a persistence length of $l_p = 10 a_0^2 t_0^{-2} m_F$.
- Attractive walls are considered for a
 - flexible linear polymer consisting of 40 beads
 - stiff linear polymer consisting of 40 beads with a persistence length of $l_p = 10 a_0^2 t_0^{-2} m_F$

In order to carry out the simulations, the MPCD method was chosen (see Chapter 2). Then, for the sake of convenience, the cell length a_0 , the mass of the solvent particles m_S and the thermal energy $k_B T$ were set to 1 defining the unit of time $t_0 = a_0 \sqrt{\frac{m_s}{k_B T}}$. Finally, the parameters selected for the fluid, monomer and slit pore were the following:

- For the fluid: To restore the solvent mediated bead-bead and bead-wall hydrodynamic interactions, we employ the Multi-Particle Collision Dynamic (MPCD) fluid model (see Chapter 2). The viscosity of the MPCD-fluid is determined by the rotation angle $\alpha = 130^\circ$, the collision time step $t_c = 0.1 t_0$ and the average solvent number density $\nu = 5 a_0^{-3}$ leading to a dynamic viscosity of $\eta = 3.96 m_s / a_0 t_0$. The employed parameters ensure a liquid like MPCD-fluid with a Schmidt number $Sc = 12.4$. The temperature of solvent particles and monomers was controlled by employing a cell-level Maxwellian thermostat^[132]. This thermostat ensures constant temperature and particle densities over the complete channel cross-section in addition to the correct Maxwell-Boltzmann distribution for the relative solvent particle velocities^[132].
- For the monomers that build the polymer: Since hydrodynamics is preserved down to a cell level, the monomer size was set to the size of a collision cell, $\sigma_{MM} = \sigma_W = a_0$. The mass of a polymer bead m_M was set to the average solvent mass of a cell ($m_M = \rho m_S a_0^3 = 5 m_S$) representing a buoyant bead.
- For the slit pore: The length of the slit pore were the following: $L_x = 60 a_0$, $L_y = 45 a_0$ and $L_z = 17 a_0$ and $L_x = 60 a_0$, $L_y = 45 a_0$ and $L_z = 34 a_0$, where the confinement is applied only in z -direction and periodic boundary conditions in x and y -directions. Indeed, for the slit pore with $L_z = 17 a_0$, only the study of a flexible polymer in a slit pore with repulsive walls was carried out. On the other hand for $L_z = 34 a_0$ all the cases were studied.

Finally, the polymer is formed by 40 monomers, this because this amount is large enough to allow the polymer to feel the shear flow, but small enough to be the simulation time accessible.

4.4.2 Simulation under flow

In order to carry out the study, the Poiseuille and the electro-osmotic (EO) flow were induced into a slit pore that contains a linear polymer. To do so, for Poiseuille flow, a body force given by $f_x = \rho g$ (with acceleration g) is applied to all solvent particles, as described in Section 3.2.1. Whereas to induce the electro-osmotic flow, we designed an implicit approach to model an electro-osmotic flow equivalent to the one explicitly simulated in Chapter 3, but without any ion in the system. To do so, we have applied a force on solvent particles that allow us to recover the electro-osmotic flow:

$$f_x(z) = \frac{n_+(z) - n_-(z)}{\gamma} \frac{E_x}{z_i e} dV \quad (4.51)$$

Here, z denotes the direction of confinement and x the flow direction. γ is the average number of MPCD particles per box. The counter and co-ion density concentration is given by n_+ and n_- respectively for a surface charge density σ_{wall} . We have taken the density profiles of ions computed in Chapter 3 to derive this force. E is an electric field with component E_x in x direction and zero in y and z . $z_i e$ is the charge q_i , with z_i being the valency and e the elementary charge. Therefore, to obtain the force acting on a volume dV , the body force is multiplied by the corresponding volume.

Thus, in order to accomplish this analysis, we need to obtain a Poiseuille and an EOF profile that are comparable. Therefore, a condition has to be chosen, namely that both profiles must have the same global shear flow. To do so, Poiseuille and electro-osmosis flow should have the same V_{max} . Because the average of the shear gradient (in absolute value) is $2 V_{max}/L$ (in all cases where the maximum value is found to be at $L/2$, and for stick boundary condition).

Thus, in order to decide the electric field strength that will be applied for the electro-osmotic flow, two simulation tests were launched. In both of them, the electric fields applied were $E = 10 a_0 t_0^{-2}$ and $E = 100 a_0 t_0^{-2}$, for the cases with $c_{add} = 0 \text{ mol/L}$ and $c_{add} = 2 \text{ mol/L}$ for $\sigma_{wall} = -0.5 \text{ e/nm}^2$. Thus, for these eight simulations we computed V_{max} . As a result we obtained that for both concentration of added salt, the value of V_{max} for $E = 10 a_0 t_0^{-2}$ *i.e.* $(V_{max})_{(E=10)}$ is the same as $(V_{max})_{(E=100)}/10$ *i.e.* the value of V_{max} for $E = 100 a_0 t_0^{-2}$ divided by 10. Indeed, the reason why the maximum velocity for $E = 100 a_0 t_0^{-2}$ is divided by 10 is because it is the ratio of $E = 100/E = 10$. Therefore, this means that with two specified values for the electric field strength we have checked that the maximum velocity is linearly proportional to E . Then, the ratio of maximum velocities for the electro-osmotic profile $(V_{max})_{EOF,E2}/(V_{max})_{EOF,E1} = E_1/E_2$ must be equal to the ratio of the values of E employed (that is the linear proportionality). Since we are in the linear regime, everything (mean velocity, maximum velocity, mean shear gradient) is proportional to the external force.

So, in order to choose the values that will be used for the electric field strength, we first consider the strength forces applied for the study of the induced Poiseuille flow. Indeed, the lowest and strongest forces used in Ref. 133 were taken as a point of reference to compute the electric field strength for the electro-osmotic case. Then, the values of the electric field for the electro-osmotic flow can be computed following the procedure explained previously. To do so, the value of $\langle V_{max} \rangle_{EOF,E=10}$ and $E = 10 a_0 t_0^{-2}$ was taken as $\langle V_{max} \rangle_{EOF,E1}$ and $E1$, thus for $\langle V_{max} \rangle_{EOF,E2}$ we plugged in the value of $\langle V_{max} \rangle_{Poiseuille,g2}$ for $g2$, leaving $E2$ as unknown. The same procedure was carried out for each case.

Chapter 4. Polymers in confinement

Using the system for $\sigma_{wall} = -0.5 e/nm^2$ and $c_{add} = 0 mol/L$, the values that were taken for the electric field strength to create the flow were: $39.93 a_0/t_0^2$ and $160.62 a_0/t_0^2$ for the smallest and largest forces respectively. Whereas for $c_{add} = 2 mol/L$, the values that were taken for the the electric field strength to create the flow were: $76.24 a_0/t_0^2$ and $306.66 a_0/t_0^2$ for the smallest and largest forces respectively. Then, the flow profile for each system (Poiseuille and electro-osmotic flow) used in this study are shown in Figure 4.7.

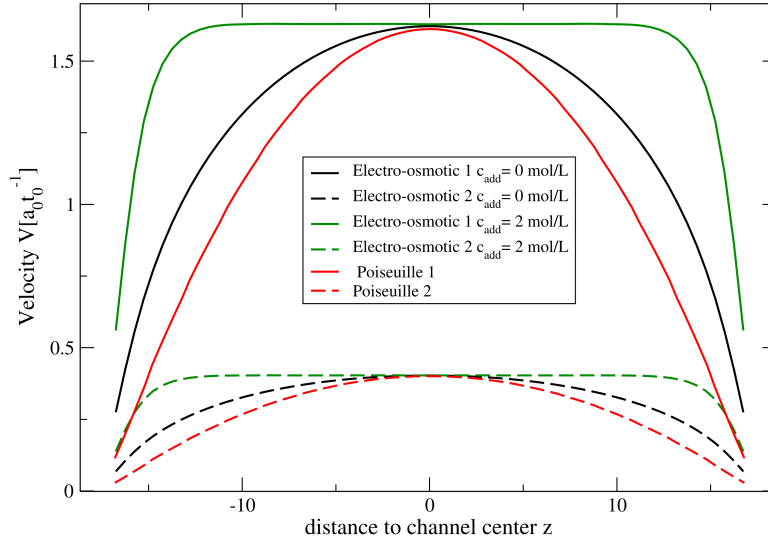


Figure 4.7 – Comparison of the profiles applied on the study: red curves correspond to the Poiseuille flow, whereas black and green curves correspond to the electro-osmotic flow for no salt and salt respectively. All the curves are taking considering the same v_{max} .

In what follows we have thus six different cases with flow. We will refer to those cases as:

- Poiseuille 1: Poiseuille flow with the highest force represented in Figure 4.7 as a red plain line.
- Poiseuille 2: Poiseuille flow with the lowest force represented in Figure 4.7 as a red dashed line.
- Electro-osmotic 1, $c_{add} = 0M$: electro-osmotic flow with a maximum velocity corresponding to that of Poiseuille 1, obtained when an electric field is applied in the direction \parallel to the surface of a charged slit pore with $\sigma_{wall} = -0.5 e/nm^2$ and $c_{add} = 0 mol/L$.
- Electro-osmotic 1, $c_{add} = 2M$: same as the previous one, but with $c_{add} = 2 mol/L$.
- Electro-osmotic 2, $c_{add} = 0M$: electro-osmotic flow with a maximum velocity corresponding to that of Poiseuille 2, obtained when an electric field is applied in the direction \parallel to the surface of a charged slit pore with $\sigma_{wall} = -0.5 e/nm^2$ and $c_{add} = 0 mol/L$.
- Electro-osmotic 2, $c_{add} = 2M$: same as the previous one, but with $c_{add} = 2 mol/L$.

In what follows we will compare in every case the results under flow to those obtained at equilibrium, *i.e.* without any flow.

4.4.3 Case with repulsive walls

4.4.3.1 Results for $L_z \approx 4 R_g$

The main idea of this analysis, was to investigate which is the influence of an electro-osmotic flow on the linear polymer behaviour. To do so, for each one of the cases under study (see section 4.4.1) the monomer probability distribution, as a function of the distance to the center of the channel, was obtained. This quantity tells us the tendency of the monomers (*i.e.* the building units of the polymer) to be located in certain regions, rather than others, in the slit pore. First, the linear flexible polymer (made of 40 beads) in a slit pore with repulsive walls is studied for the case of $L_z = 17 a_0 \approx 4 R_g$. To start the analysis, the system at equilibrium (*i.e.* when no flow is induced) is obtained, thus allowing us to compare it with non-equilibrium results.

- Structure of the polymer at equilibrium (without flow)

The monomer probability distribution as a function of the distance to the center channel, when no force is applied, is shown in Figure 4.8. From it, we can deduce that the tendency of the monomer to be at the center of the channel is higher than to be close to the wall. As the polymer gets closer to the wall, it starts to feel the interaction with the repulsive wall, which does not allow it to remain close.

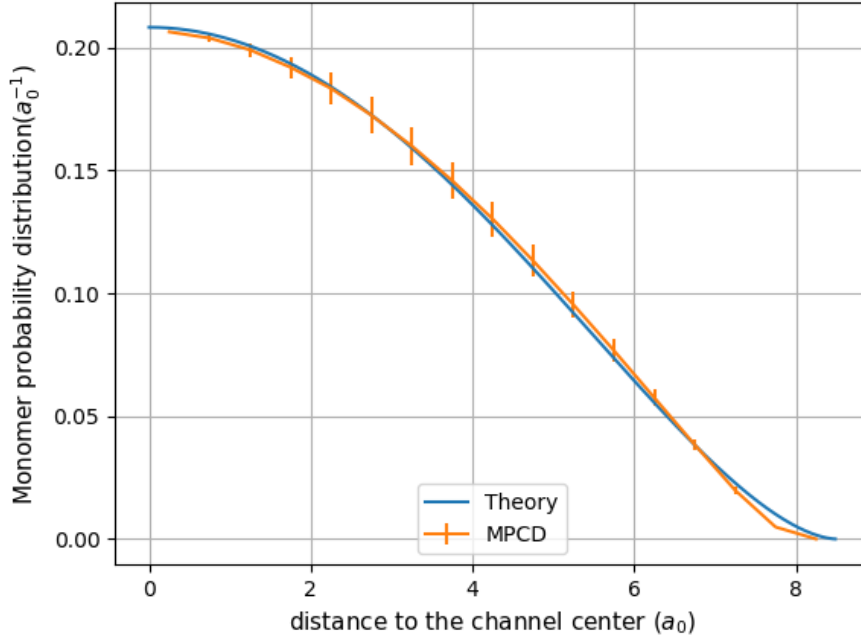


Figure 4.8 – Comparison of the monomer probability distribution obtained by the MPCD simulation and the theory (Eq. 4.53) as a function of the distance to the center channel when no flow is induced for the $L_z = 17 a_0 \approx 4 R_g$ case.

Indeed this case is well understood theoretically^[134]. The distribution of the end monomer position across the slit was studied extensively by Hsu and Grassberger^[135].

Let us denote scaling variable as the ratio $\zeta = z/L_z$, where z is the distance to the wall and L_z the distance between the walls. Considering a simple scaling formula that takes into account the mirror symmetry, with respect to the median plane, the expression for the distribution of the end monomer position has the following form:

$$\rho_{\text{end}}(\xi) = \frac{\Gamma(2 + 1/\nu)}{[\Gamma(1 + 1/2\nu)]^2} (1/4 - \xi^2)^{1/2\nu} \quad (4.52)$$

where ν is the Flory index. Moreover the distribution is properly normalized to unity. Furthermore Hsu and Grassberger made a hypothesis, stating that the same relation holds also for self-avoiding chains (*i.e.* our case)^[135]. They could then find a good agreement with other works^[135]. Therefore, with this ansatz, the monomer density profile can be written as:

$$\rho(\xi) = \frac{\Gamma(2 + 2/\nu)}{[\Gamma(1 + 1/\nu)]^2} (1/4 - \xi^2)^{1/\nu} \quad (4.53)$$

Thus, Eq. 4.53 was obtained for this system and compared to the MPCD simulation results in Figure 4.8. In the graph, we see that both curves match, meaning that our simulations are in agreement with the theory.

- Structure of the polymer

The monomer probability distribution is first obtained for a linear flexible polymer when an electro-osmotic flow is induced into the slit pore, for different electric field strengths. Indeed since the electro-osmotic flow presents different shapes as c_{add} varies, two different concentrations of added salt were considered, *i.e.* $c_{\text{add}} = 0 \text{ mol/L}$ and $c_{\text{add}} = 2 \text{ mol/L}$. For each case two strength forces were applied, *i.e.* a small and a high force. The choice of their respective values is explained in Section 4.4.2.

Figure 4.9 shows a comparison of the different monomer distributions for the two electro-osmosis flows when no added salt is considered and Figure 4.10 when a concentration of 2 mol/L is added. In both cases, the monomer probability distribution is compared with the equilibrium case, *i.e.* when no flow is induced. We observe a clear difference in the polymer behaviour when comparing the case with (*i.e.* 2 mol/L) and without added salt (*i.e.* 0 mol/L). For $c_{\text{add}} = 0 \text{ mol/L}$, the tendency of the polymer to be at the center of the channel increases, as the applied electric field strength increases. On the contrary, for $c_{\text{add}} = 2 \text{ mol/L}$, the tendency of the polymer to be at the center channel decreases as the applied electric field strength increases (electro-osmosis 1 corresponds to a maximum velocity of the solvent higher than electro-osmosis 2). This can be deduced thanks to the value of the monomer probability at the center channel, which is slightly low for the green than for the pink curve. However, the curves of the monomer probability distribution for both forces are quite close to the equilibrium curve. Thus, the influence of the electro-osmotic flow for the concentrated case of added salt, is small compared to the case without added salt.

A way to explain this phenomenon is to consider two aspects: the first is the shape of the electro-osmotic profile, for $c_{\text{add}} = 2 \text{ mol/L}$, which presents a homogeneous flat region

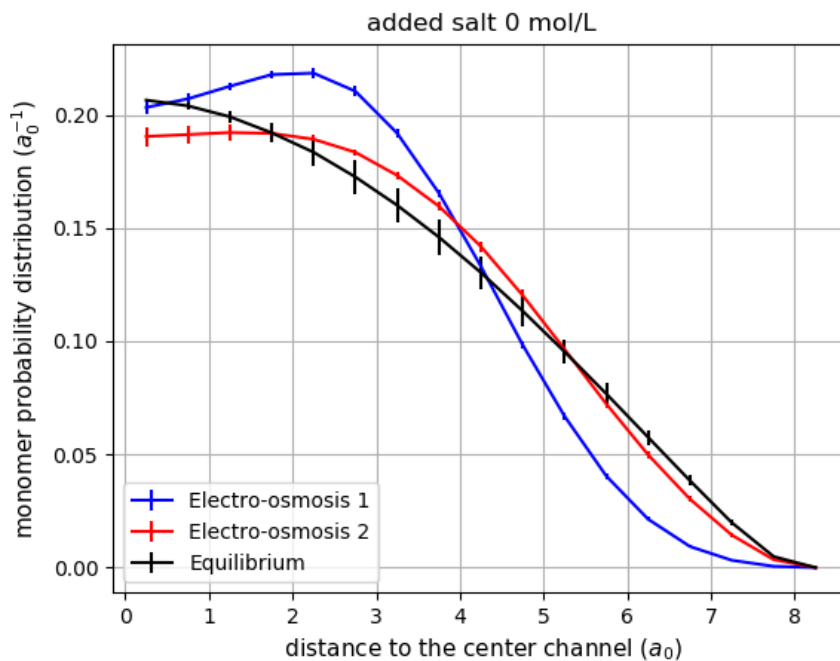


Figure 4.9 – Monomer probability distribution as a function of the distance to the center channel when applying an electro-osmotic flow for the no added salt case for the case $L_z = 17 a_0 \approx 4 R_g$.

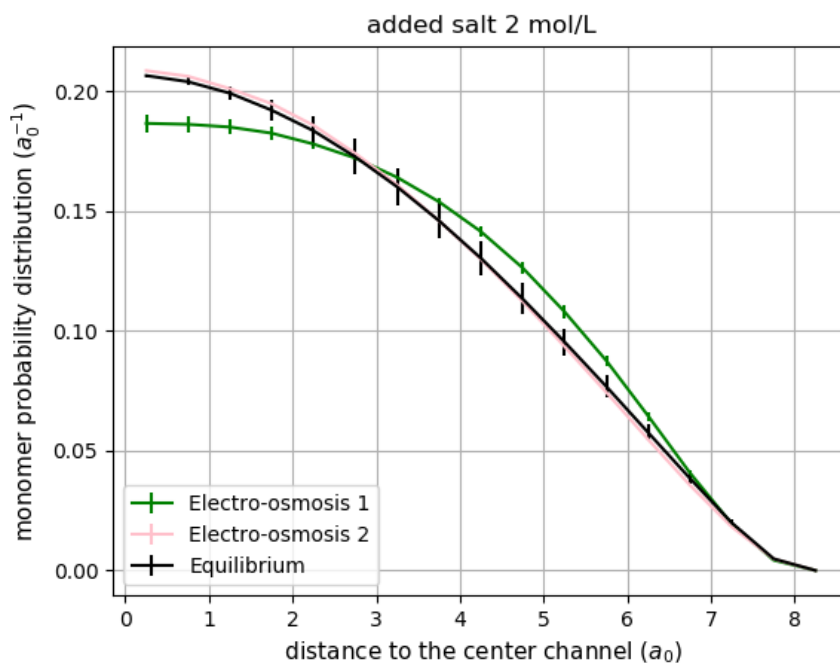


Figure 4.10 – Monomer probability distribution as a function of the distance to the center channel when applying an electro-osmotic flow for the case with 2 mol/L of added salt for the case $L_z = 17 a_0 \approx 4 R_g$.

in the middle of the slit pore, giving it a plug-like shape. The second is the polymer behaviour at equilibrium. In other words, the linear polymer has the tendency to be in the center of the channel, when no force is applied (see Figure 4.8). We can say that the reason why the polymer does not feel affected by the induced electro-osmotic flow, when varying the flow strength, is because it does not feel the steepest part of the flow profile (*i.e.* the highest slope part), which is located close to the walls, since it remains mostly at the center of the channel. Therefore, this is as if the polymer only experiences an induced constant force in the slit pore.

A comparison of the electro-osmotic and the Poiseuille flow was carried out in Figure 4.12 for small forces and in Figure 4.11 for high forces. In both plots, the curves that present a similar behaviour are Poiseuille and electro-osmotic flow with no added salt. This is expected because the shape of both profiles is similar (see Figure 4.7). For high forces, the induced electro-osmotic flow, for the no added salt case, is the one presenting a higher probability to be at the center of the channel. On the contrary, for the same flow, but for a high concentrated salt case, the linear polymer tends to be closer to the walls when compared to the other cases. For low forces, the difference between plots is less pronounced. The electro-osmotic flow for a concentration of added salt induces a higher probability for monomer to be at the center of the channel (see the pink curve in Figure 4.12).

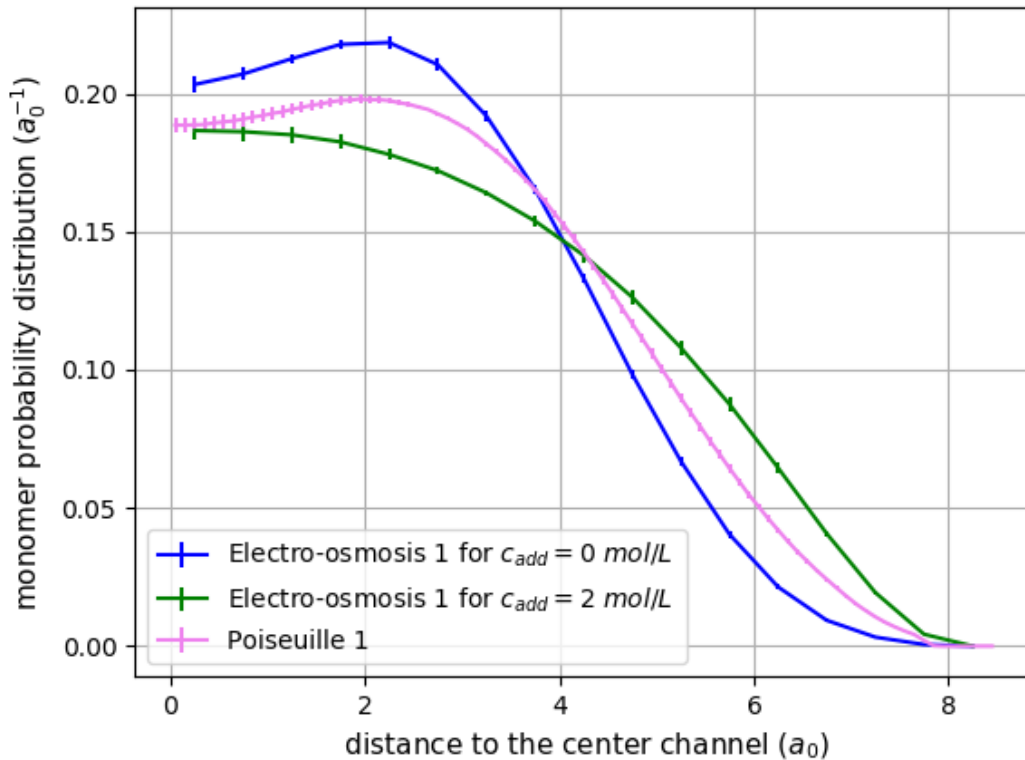


Figure 4.11 – Comparison of the monomer probability distribution for an induced Poiseuille and electro-osmotic flows for both concentrations of added salt as a function of the distance to the center channel when high forces are taken into account. Case of $L_z = 17 a_0 \approx 4 R_g$.

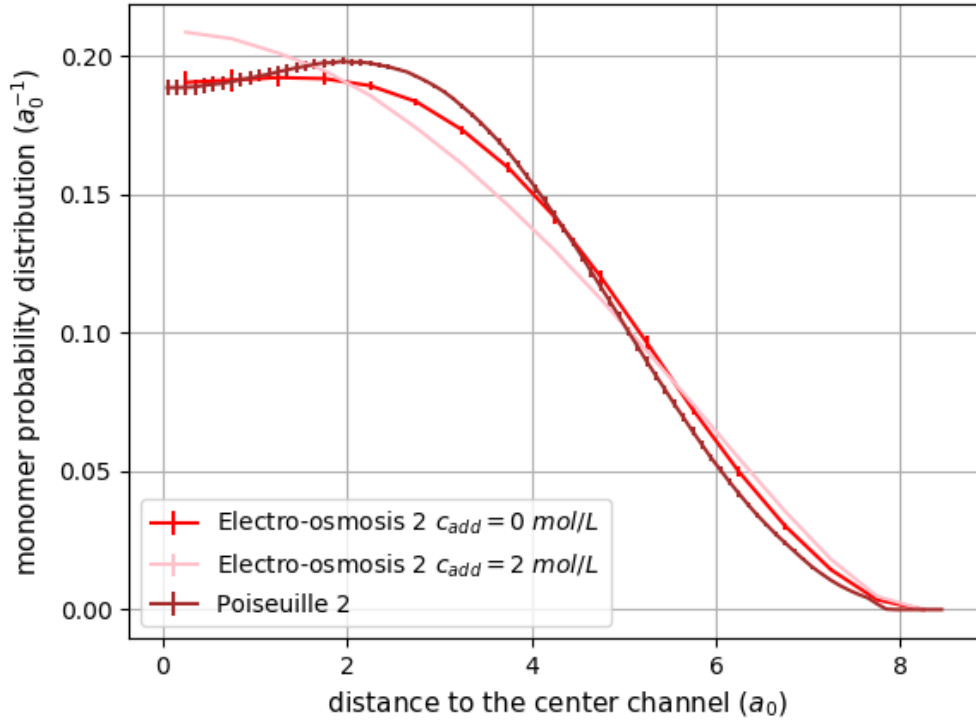


Figure 4.12 – Comparison of the monomer probability distribution for an induced Poiseuille and electro-osmotic flows for both concentrations of added salt as a function of the distance to the center channel when small forces are taken into account. Case of $L_z = 17 a_0 \approx 4 R_g$

4.4.3.2 Results for $L_z \approx 8.15 R_g$

Given the previous results, we want to know if we can make the polymer feel the presence of the steepest part of the electro-osmotic flow, when $c_{add} = 2 \text{ mol/L}$. To do so, we consider two options. The first consists in changing the number of monomers, to have a smaller polymer that can get closer to the walls. The second is to change the grid size of the simulation box, by making the distance between the walls larger. Therefore, we choose the second option and we propose $L_z = 34 a_0$. Thus, the previous analysis done is now carried out for a linear flexible polymer (made of 40 beads), in a slit pore with repulsive walls, for the case of $L_z = 34 a_0 \approx 8.15 R_g$. To start the analysis, the system at equilibrium (*i.e.* when no flow is applied) is obtained, thus allowing us to compare it with non-equilibrium results.

- Structure of the polymer at equilibrium (without flow)

The monomer probability distribution as a function of the distance to the center of the channel is shown in Figure 4.13, when no induced flow is taken into consideration. From it, we observe that the monomers maintain their tendency to stay at the centre of the channel, instead of being close to the walls, as in the previous case ($L_z = 17 a_0$). The asphericity (divided by $R_g^2 = 17.3 a_0^2$) as a function of the distance to the center of the channel is illustrated in Figure 4.14 for the same case. In order to compute the asphericity, equation 4.15 introduced in section 4.2.2 is used. Therefore, we see that the asphericity is always non zero for the equilibrium curve, independently of the distance from the walls.

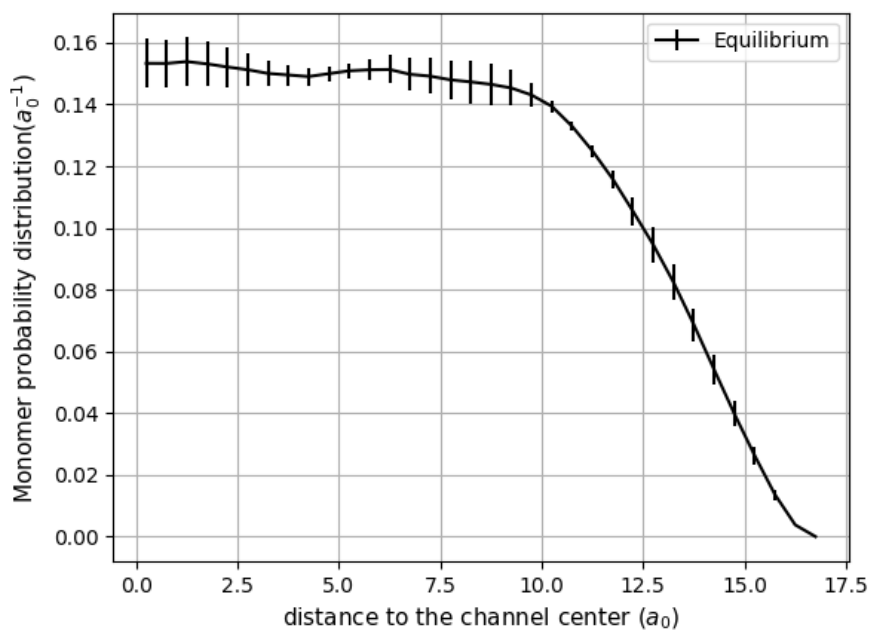


Figure 4.13 – Monomer probability distribution as a function of the distance to the center channel when no induced flow is consider for the case of $L_z = 34 a_0 \approx 8.15 R_g$.

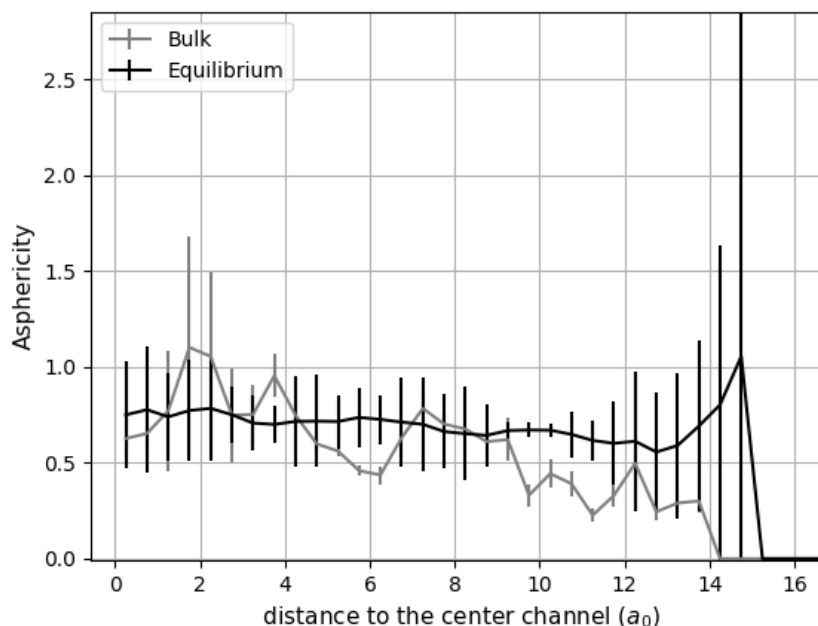


Figure 4.14 – Asphericity divided by R_g^2 as a function of the distance to the center channel when no induced flow is consider for the case of $L_z = 34 a_0 \approx 8.15 R_g$

This means that a no spherical distribution of the polymer is obtained along the slit pore. Moreover, its values remain almost constant along the slit pore, except for the region close to the wall, where the asphericity values increases. Nonetheless, the error bars at these values are large compared to the rest. Since monomers have less tendency to move towards the walls, the error is large due to a lack of information in that region. Moreover, when comparing the no induced flow and bulk case (see black and grey curve respectively), the value of the asphericity seems to be larger for the former case. This means that the presence of a wall influences slightly the distribution of the monomers (conforming the polymer) making them a little more aspherical than in the bulk.

- Structure of the polymer

The same study carried out for the case of $L_z = 17 a_0$ is now performed for $L_z = 34 a_0$. Then, new values for the electric field strength were obtained for the two concentrations of added salt by following the method described at section 4.4.2. For $c_{add} = 0 \text{ mol/L}$, the values of $83.38 a_0 t_0^{-2}$ and $20.73 a_0 t_0^{-2}$ are taken. Whereas, for $c_{add} = 2 \text{ mol/L}$, we used $168.95 a_0 t_0^{-2}$ and $42.0 a_0 t_0^{-2}$. In what follows we will refer to as "electro-osmosis 1" and "electro-osmosis 2" the electro-osmosis flow profiles obtained when considering high and small forces respectively, corresponding to Poiseuille 1 and Poiseuille 2 for each value of c_{add} .

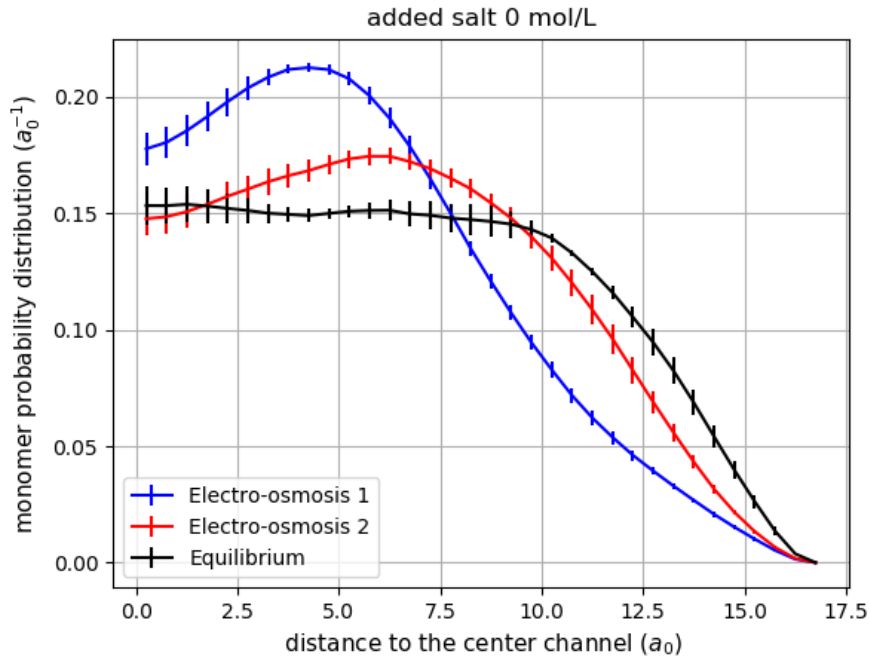


Figure 4.15 – Monomer probability distribution as a function of the distance to the center channel when applying an electro-osmotic flow for the no added salt case when $L_z = 34 a_0 \approx 8.15 R_g$.

Figure 4.15 and Figure 4.16 are obtained in order to see how the induced electro-osmotic flow affects the linear polymer behaviour, when different electric field strength are considered. For the case of no added salt (see Figure 4.15), the tendency of the polymer to be at the center of the channel increases as the applied electric field strength increases.

Whereas, the opposite is observed when $c_{add} = 2 \text{ mol/L}$ (see Figure 4.16) is taken into account. Indeed the same tendency was observed for the $L_z = 17 a_0$ case. However, still for $L_z = 34 a_0$, the effect of the induced electro-osmotic flow for $c_{add} = 2 \text{ mol/L}$ is not large. This is observed comparing pink and green curve which are close to the equilibrium case (black curve).

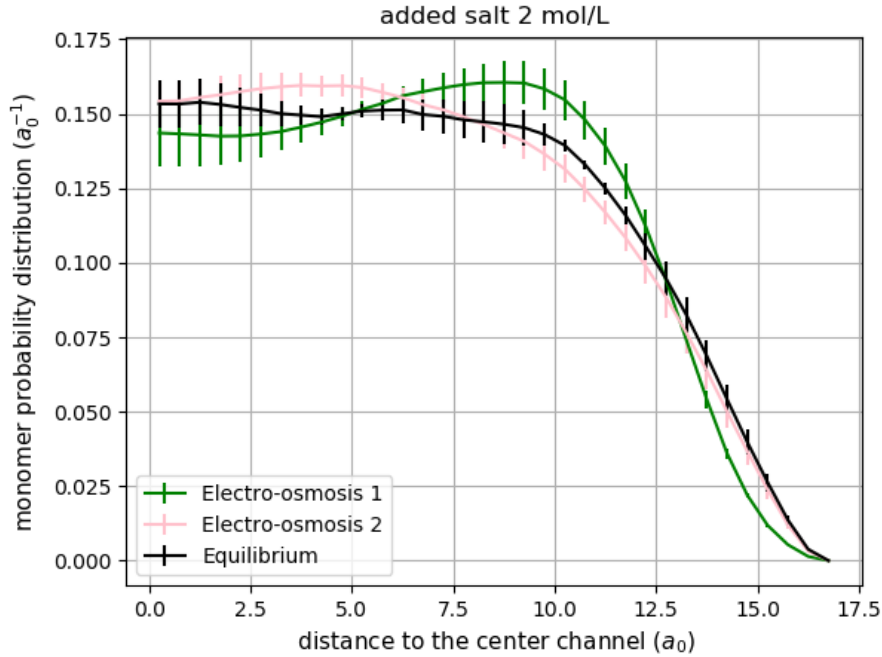


Figure 4.16 – Monomer probability distribution as a function of the distance to the center channel when applying an electro-osmotic flow for the added salt case (2 mol/L) when $L_z = 34 a_0 \approx 8.15 R_g$.

Then, in order to achieve a larger effect under an electro-osmotic flow for the added salt case, two new modifications were implemented. The first consists in considering an attractive wall as described in subsection 4.3.2.2. With this modification we hope to allow monomers to explore more the region closer to the wall, and thus as a consequence, be more influenced by the steepest part of the electro-osmotic flow. The second, is to take a stiff polymer. Therefore the monomers will have less degrees of freedom, *i.e.* the polymer will not be able to fold (see subsection 4.3.1.2). Therefore, a study varying this new parameters is carried out in the following section.

The comparison between the induced Poiseuille and electro-osmotic flows is shown in figure 4.17 only when considering high forces. We observed that when comparing Poiseuille flow and electro-osmotic flow for no added salt, the tendency of the monomers to be at the center of the channel is larger for the former than for the latter. Thus although both curves have the same maximum velocity and thus the same shear flow, the small difference in the shape impacts the polymer behaviour (see figure 4.7). Moreover, the largest contrast is seen when comparing the curve that corresponds to the induced electro-osmotic flow for added salt with the other ones.

Finally, the asphericity for an induced electro-osmotic flow (divided by R_g^2) as a function

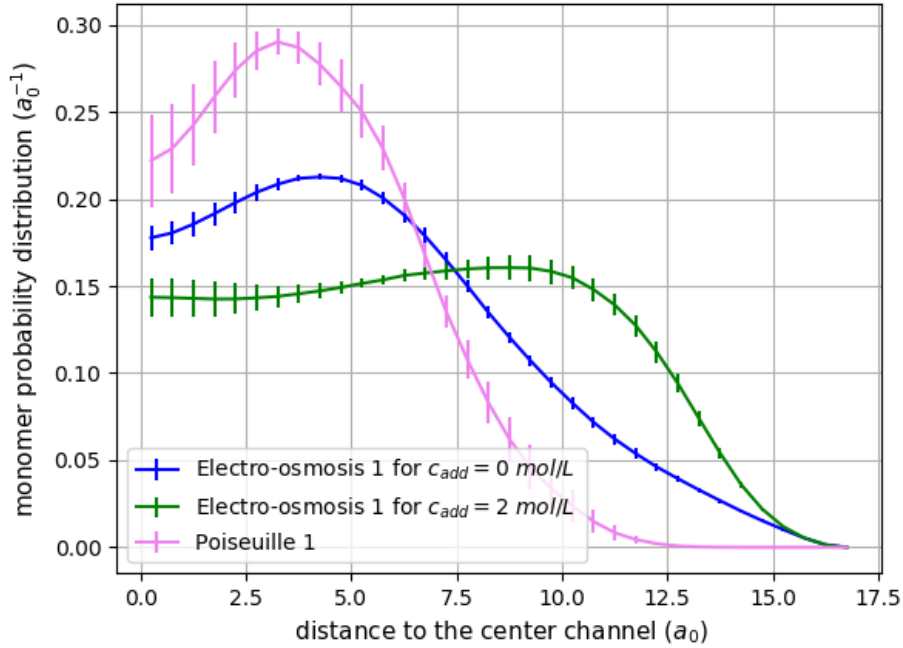


Figure 4.17 – Comparison of the monomer probability distribution as a function of the distance to the center of the channel for the induced Poiseuille and electro-osmotic flow (for $c_{add} = 0$ and 2 mol/L cases), when considering only high forces. Case of $L_z = 34 a_0 \approx 8.15 R_g$.

of the distance to the center of the channel is presented at Figure 4.18 (a) for the case of $c_{add} = 0 \text{ mol/L}$ and (b) for 2 mol/L . In both graphs the case of bulk, equilibrium and induced Poiseuille flow only for high forces is also shown in order to be able to analyse the difference between different cases.

First, for $c_{add} = 2 \text{ mol/L}$:

- For the region close to the wall (from 8 to $15 a_0$): as the strength of the electric field increases, asphericity decreases.
- For the region at the center of the channel (from 0 to $8 a_0$): as the strength of the electric field increases, asphericity remains constant. Indeed this value is the same as at equilibrium (see black curve).

Second, for $c_{add} = 0 \text{ mol/L}$:

- For the region close to the wall (from 10 to $15 a_0$): as the strength of the electric field increases, asphericity increases.
- For the region at the center of the channel (from 0 to $10 a_0$): as the strength of the electric field increases, asphericity decreases.

For both cases, the asphericity is under a Poiseuille flow is larger than the asphericity under an electro-osmotic flow at any distance to the center of the channel (where the monomers probability distribution for Poiseuille flow is defined *i.e.* where it is different from zero).

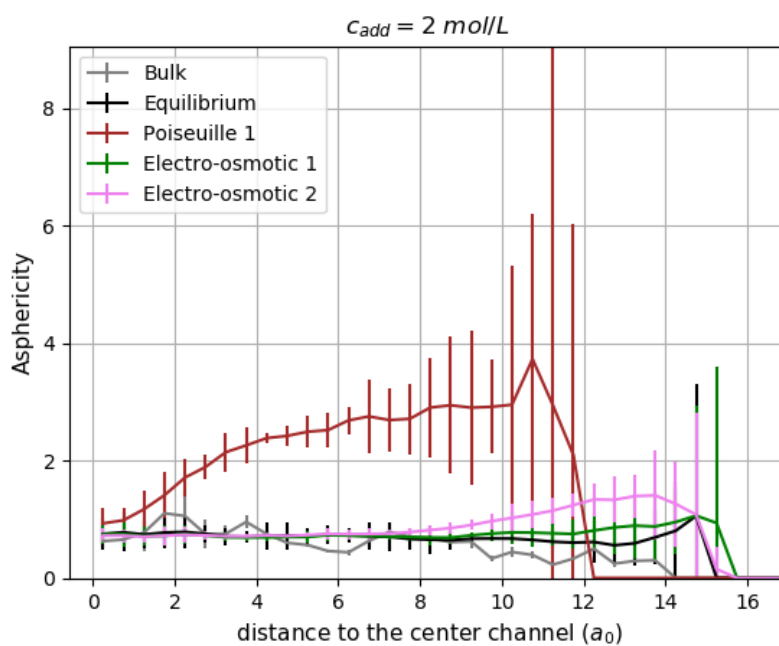
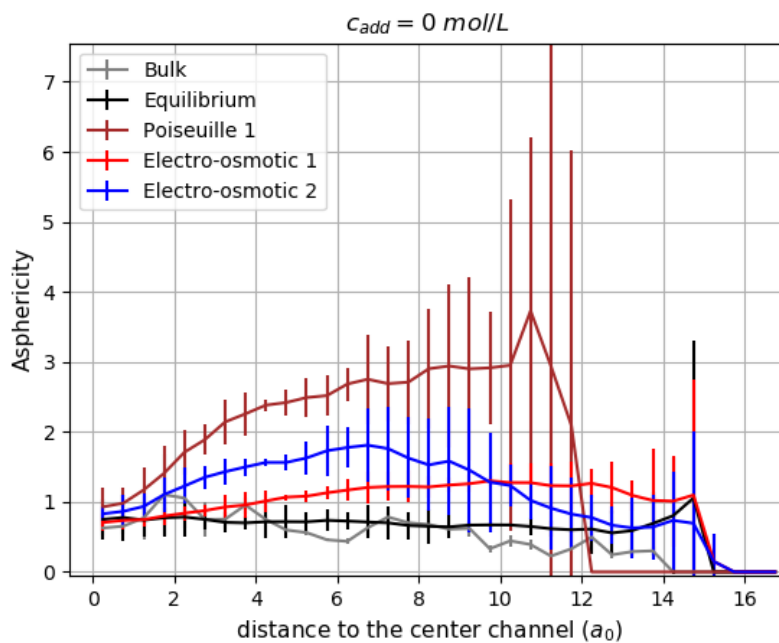


Figure 4.18 – Asphericity for an induced electro-osmotic flow (divided by R_g^2) as a function of the distance to the wall is shown for the case of $c_{add} = 2 \text{ mol/L}$ in (a) and for $c_{add} = 0 \text{ mol/L}$ in (b). In both graphs the case of bulk, equilibrium and induced Poiseuille flow only for high forces is also shown. Case of $L_z = 34 a_0 \approx 8.15 R_g$.

4.4.4 Influence of an attraction to the walls

4.4.4.1 Case of a flexible polymer

To include an attractive wall, the potential discussed at section 4.3.2.2 was implemented in the code. To do so, the parameters used were the following: $\sigma_w = a_0$, $\epsilon = k_B T$ for both cases (*i.e.* when $c_{add} = 0$ and 2 mol/L), whereas the value of the Debye length κ depends on the system. For $c_{add} = 0 \text{ mol/L}$, $\kappa = 0.23 \text{ 1/a}_0$ and for $c_{add} = 2 \text{ mol/L}$, $\kappa = 0.47 \text{ 1/a}_0$. Therefore, the previous cases were thus analysed, beginning with the linear flexible polymer case for $L_z = 34 a_0 \approx 8.15 R_g$.

- Structure of the polymer at equilibrium

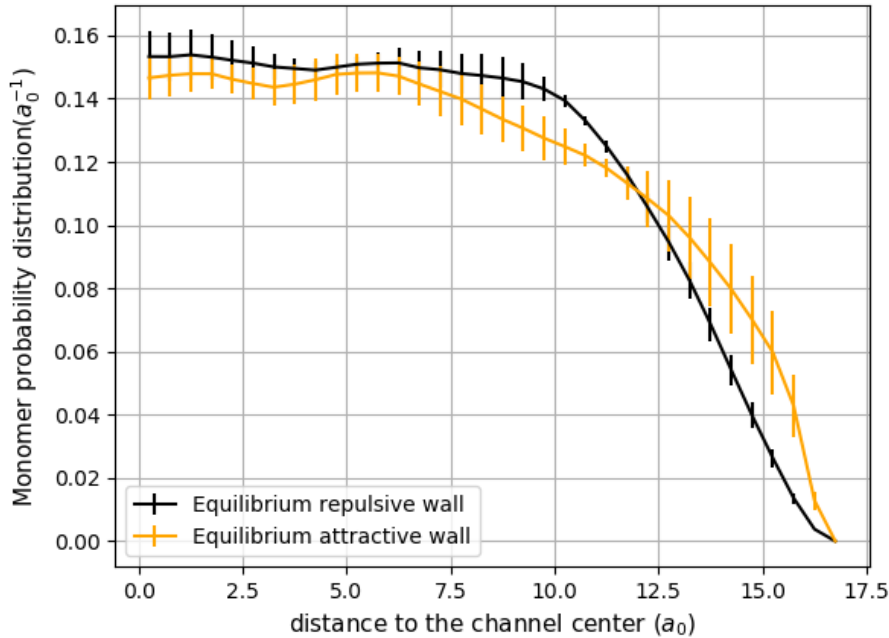


Figure 4.19 – Comparison of the monomer probability distribution at equilibrium considering an attractive and a repulsive wall, as a function of the distance to the center of the channel for the case of $L_z = 34 a_0 \approx 8.15 R_g$.

The monomer probability distribution as a function of the distance to the center of the channel, at equilibrium, is shown for the case of an attractive (orange curve) and a repulsive wall (black curve) in Figure 4.19. The tendency of the monomer to be close to the wall slightly increases when implementing a monomer-wall attraction. This is seen comparing orange and black curve from the region that comprehend $12.5 a_0$ to $16.5 a_0$. Nonetheless, the attractive wall does not have an impact on the asphericity. This is observed in Figure 4.20 where the asphericity (divided by R_g^2) as a function of the distance to the center of the channel, is shown for the case of an attractive (blue curve) and a repulsive wall (black curve). Indeed, both curves have the same behaviour and equal order of magnitude.

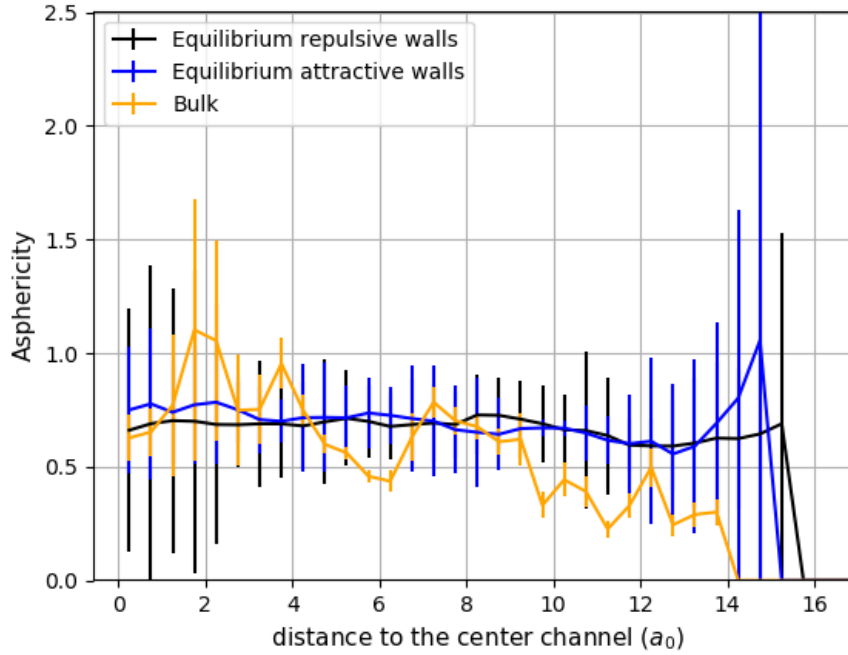


Figure 4.20 – Asphericity (divided by R_g^2) as a function of the distance to the center of the channel, at equilibrium, is shown for the case of an attractive (blue curve) a repulsive wall (black curve), for the case of $L_z = 34 a_0 \approx 8.15 R_g$, and for the bulk situation.

- Structure of the polymer

The study when inducing a Poiseuille and electro-osmotic flow is carried out now when attractive walls are considered for the $L_z = 34 a_0 \approx 8.15 R_g$ case. To do so, only the high strength forces for $c_{add} = 0 \text{ mol/L}$ and $c_{add} = 2 \text{ mol/L}$ considered in section 4.4.3.2 are taken. First the case of no added salt is treated.

- Case of no salt:

In Figure 4.21 is shown a comparison of the monomer probability distribution for the cases of repulsive and attractive walls, when considering an induced electro-osmotic flow (no added salt case), as a function of the distance to the center of the channel. The equilibrium curves (*i.e.* without flow) for both cases, are also plotted in order to have a point of reference.

From Figure 4.21, we see that the effect of the attractive wall is to decrease the tendency of the monomers to be close to the walls, which is contrary to what we were expecting. Moreover, the tendency of monomer to be at the center channel decreases as well. The value of the green curve at $0 a_0$ is low than the value of the red curve for the same abscissa. Nonetheless, the maximum value of the monomer probability distribution for the case of an attractive wall is larger than the case of a repulsive wall. Indeed both maximum are out of phase, *i.e.* their location according to the distance to the center of the channel is not the same.

In order to be able to explain this phenomenon, the asphericity (divided by R_g^2) as a function of the distance to the center channel was obtained for the same systems and shown in Figure 4.22. The case of bulk and equilibrium when considering repulsive and attractive walls were also plotted. This with the idea of having a point of reference.

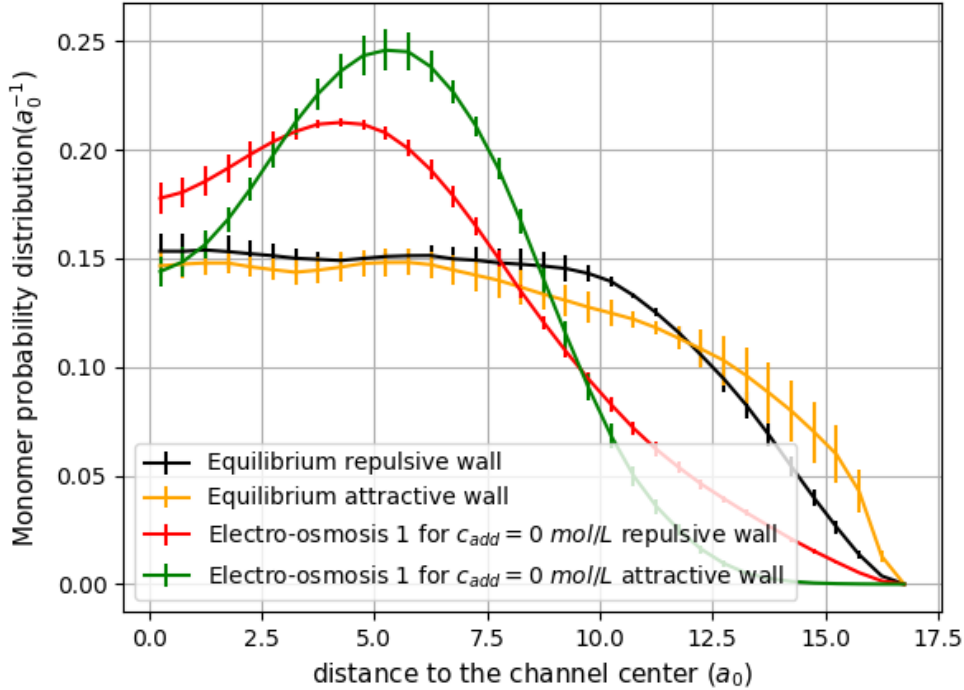


Figure 4.21 – Monomer probability distribution for the cases of a repulsive and an attractive wall, when considering an induced electro-osmotic flow (no added salt case), as a function of the distance to the center of the channel. The equilibrium curves (*i.e.* without flow) for both cases, are also plotted in order to have a point of reference. Case of $L_z = 34 a_0 \approx 8.15 R_g$.

From Figure 4.22, we observe that as expected, the asphericity close to the wall increases when there is a flow. Furthermore, comparing asphericity for attractive (red curve) and repulsive walls (green curve), we see that both curves present a similar behaviour when looking at the center channel region (from 0 to $7.5 a_0$). Asphericity increases as the distance to the center channel increases. However, as soon as the polymers start to get closer and closer to the walls (from 7.5 to $15 a_0$), a bigger effect due to the attractive walls is observed. Asphericity has a larger value when attractive walls are taken into account. Therefore, it is as if there was a coupling between the effect of the attraction on asphericity and the effect of the flow on asphericity.

This means that, the fact that asphericity increases close to the walls, leads the polymer to move away from it. As a consequence the presence of the shear flow due to the induced electro-osmotic flow affects the polymer, moving it closer to the

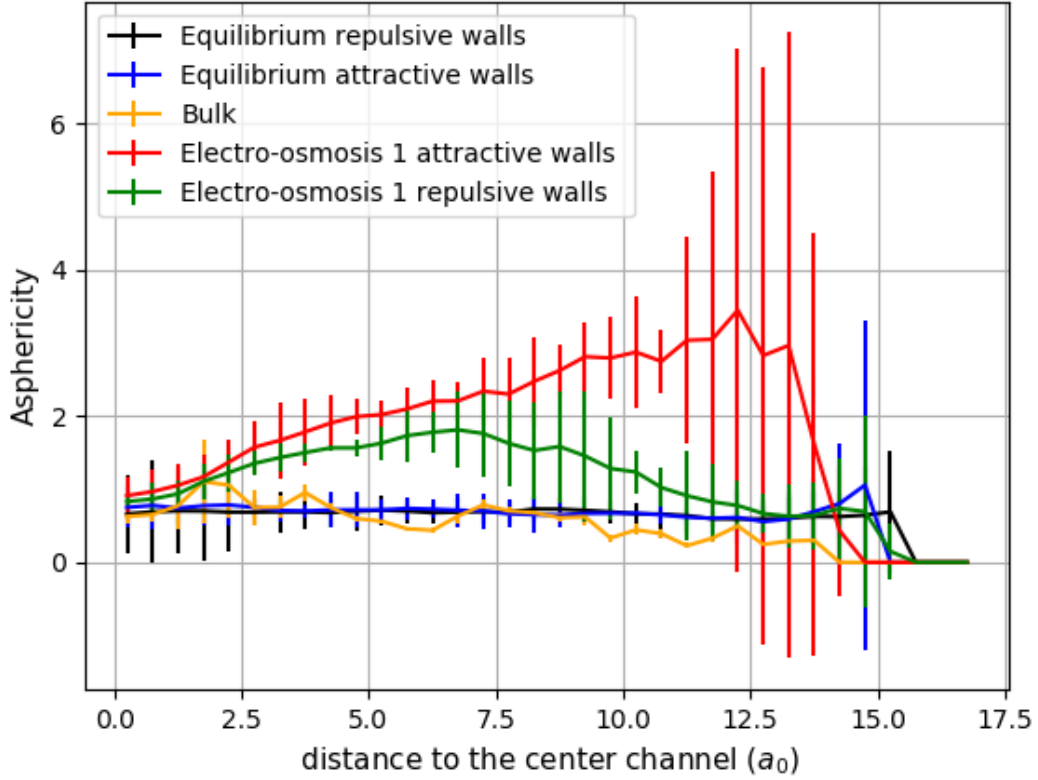


Figure 4.22 – Asphericity (divided by R_g^2) as a function of the distance to the center of the channel, when applying an electro-osmotic flow for attractive and repulsive walls, considering the $L_z = 34 a_0 \approx 8.15 R_g$ case. Here only the case of $c_{add} = 0 \text{ mol/L}$ for the electro-osmotic flow is taken into account. Bulk and equilibrium for attractive and repulsive walls are shown as references.

center of the channel.

Finally, in Figure 4.23 it is shown a comparison for the monomer probability distribution as a function of the distance to the center of the channel, between the case of a repulsive and an attractive wall for a Poiseuille flow. The equilibrium curves (*i.e.* without flow) for both cases, are also plotted.

From Figure 4.23 we observe that contrary to the case of an induced electro-osmotic flow, the tendency of the monomers to be in the region close to the wall does not decrease drastically in the presence of a Poiseuille flow for attractive walls (compare pink and blue curves). In the region at the center of the channel, the monomer probability is low when considering an attractive wall. This behaviour was as well observed for the electro-osmotic flow. Therefore, the only effect that the monomers-walls attraction has on this flow, it is to slightly move the maximum of the monomer probability distribution in the direction close to center of the channel. However, this effect is not large enough (around $1 a_0$).

In order to see if the concentration of added salt for an induced electro-osmotic

flow gives a different behaviour, the case of $c_{add} = 2 \text{ mol}/L$ is now treated.

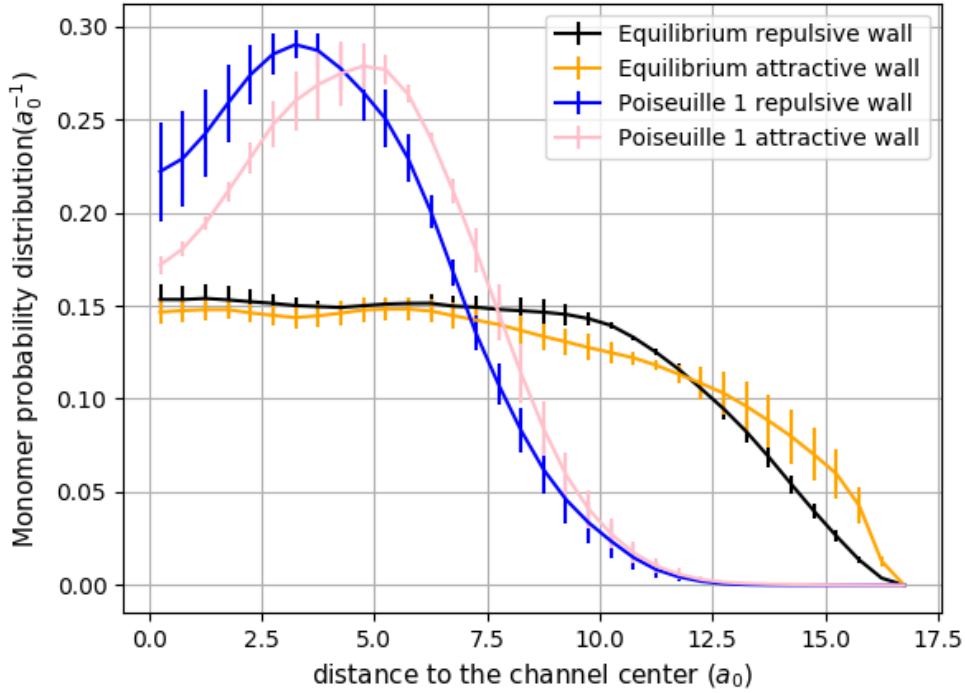


Figure 4.23 – Monomer probability distribution for the cases of repulsive wall and attractive wall, when considering an induced Poiseuille flow, as a function of the distance to the center of the channel. The equilibrium curves (*i.e.* without flow) for both cases, are also plotted in order to have a point of reference. Case of $L_z = 34 a_0 \approx 8.15 R_g$.

– Case of added salt:

The same study as the one carried out for the case of no added salt is now performed for an induced electro-osmotic flow when $c_{add} = 2 \text{ mol}/L$.

First, in Figure 4.24 a comparison of the monomer probability distribution under an induced electro-osmotic flow as a function of the distance to the center channel is shown, for the cases when a repulsive or an attractive wall are considered. Moreover, the equilibrium curves, are plotted.

From Figure 4.24 we observe the same effect as in the no added salt case, *i.e.* the effect of the attractive wall is to decrease the tendency of the monomer to be close to the wall. This is noticed by comparing green and red curve from 12.5 to 17 a_0 . Nonetheless this effect is small compared to the case of no added salt.

Second, the asphericity (divided by R_g^2) as a function of the distance to the center of the channel, is obtained for the same systems and shown in Figure 4.25. Then, by looking at the asphericity, we see that the same behaviour is found.

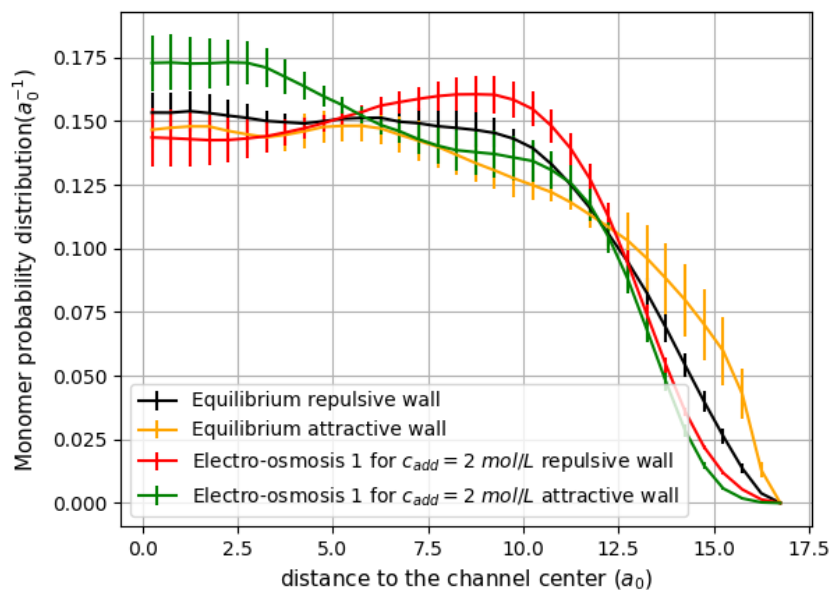


Figure 4.24 – Comparison of the monomer probability distribution under an induced electro-osmotic flow as a function of the distance to the center channel, for the cases when a repulsive and an attractive wall are considered. Case of $L_z = 34 a_0 \approx 8.15 R_g$.

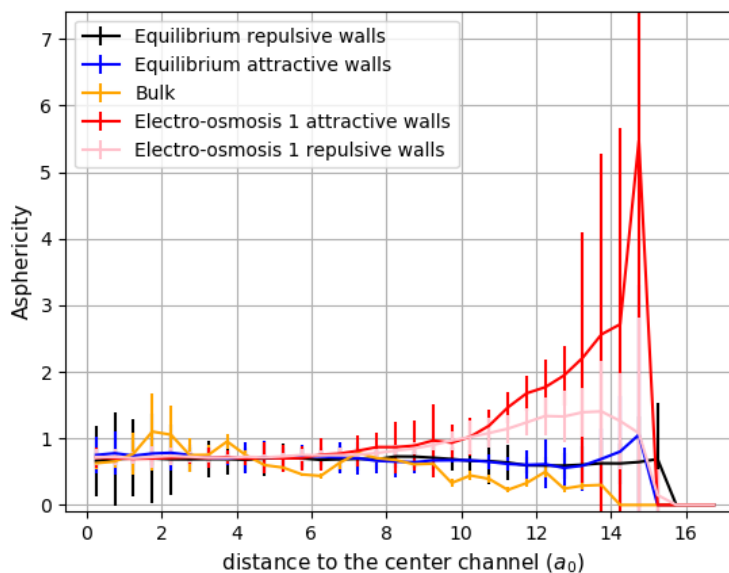


Figure 4.25 – Asphericity (divided by R_g^2) as a function of the distance to the center channel, when applying an electro-osmotic flow for attractive and repulsive walls, considering the $L_z = 34 a_0 \approx 8.15 R_g$ case. Here only the case of $c_{add} = 2 \text{ mol/L}$ for the electro-osmotic flow is taken into account. Bulk, and equilibrium for attractive and repulsive walls are also show.

4.4.4.2 Influence of the stiffness of the polymer

Now it is studied the influence of the stiffness of the polymer on its structure. To do so the potential described at section 4.3.1.2 is implemented in the code with a persistence length of $l_p = 10 a_0^2 t_0^{-2} m_F$. Thus the same analysis as in the previous section is carried out, starting by the case with no induced flow.

- Structure of the polymer at equilibrium

The monomer probability distribution as a function of the distance to the center of the channel without flow is shown in Figure 4.26 and Figure 4.27. To be more precise, in Figure 4.26, a comparison between the flexible and stiff polymers is shown, for the case where the walls are repulsive. Whereas, in Figure 4.27, the same comparison is illustrated, but now considering attractive walls.

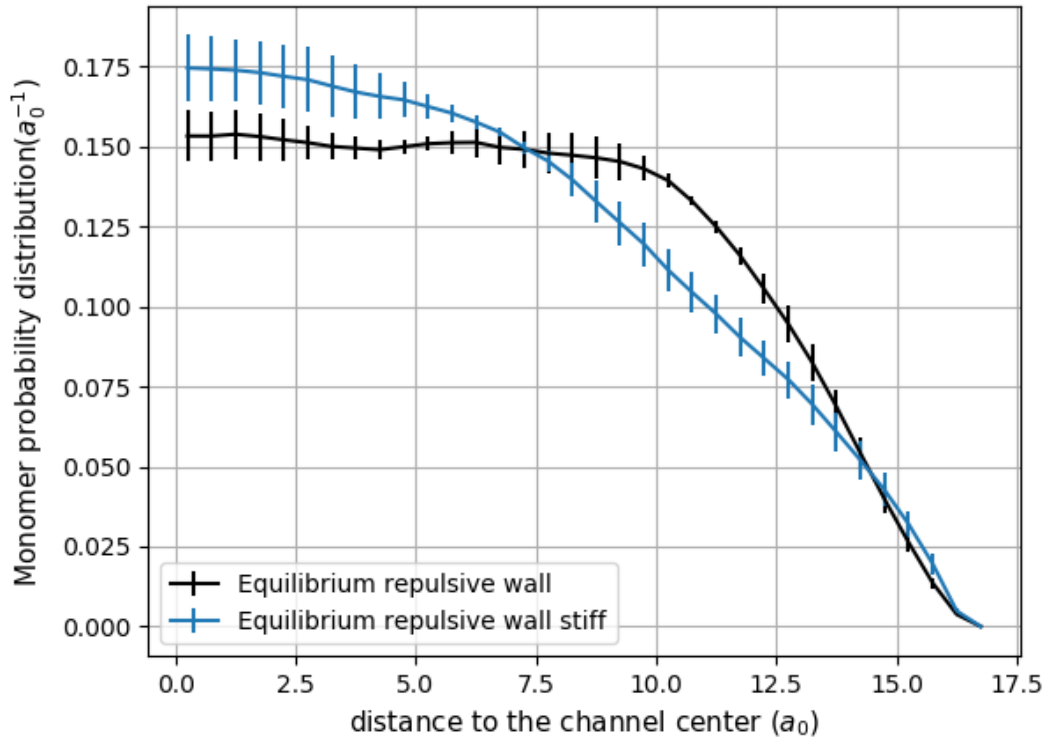


Figure 4.26 – Comparison between the monomer probability distribution of a flexible and stiff polymer, as a function of the distance to the center of the channel without flow for the case $L_z = 34 a_0 \approx 8.15 R_g$. In this case we considered the case with repulsive walls.

As a result we found that the effect that the stiffness has on the polymer behaviour, when considering repulsive walls (see blue and black curves in Figure 4.26), is that the tendency of the monomers to be at the center channel increases. On the contrary, when looking at the case of attractive walls (see orange and blue curves in Figure 4.27), the tendency of the monomers to be closer to the walls increases drastically.

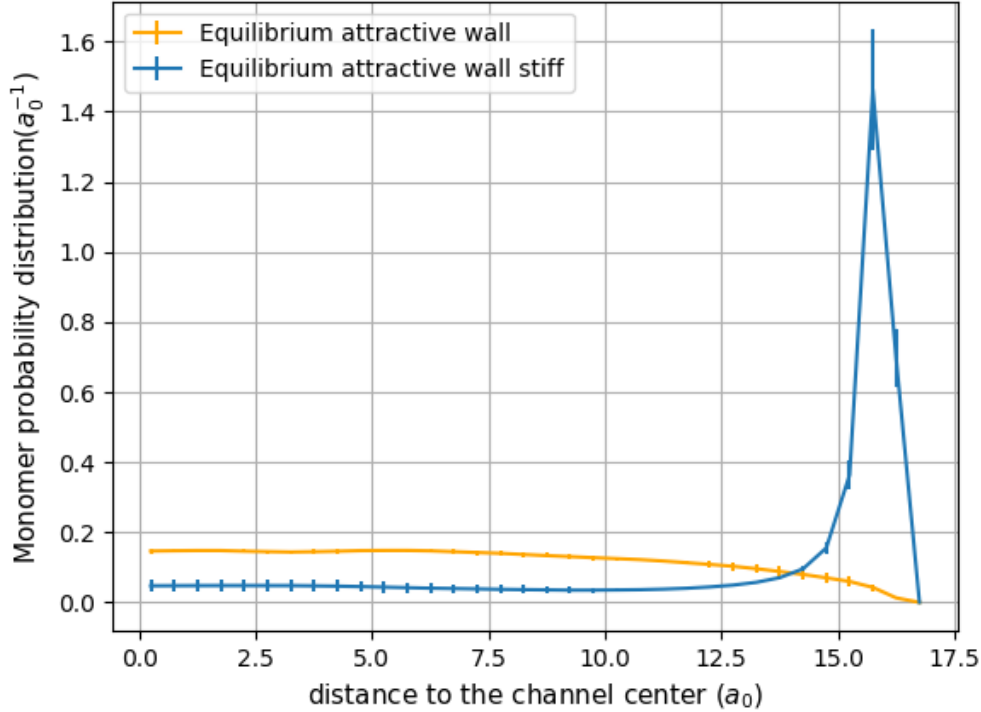


Figure 4.27 – Comparison between the monomer probability distributions of a flexible and of a stiff polymer, as a function of the distance to the center of the channel for the $L_z = 34 a_0 \approx 8.15 R_g$ case. In this case we considered the case with attractive walls.

- Structure of the polymer

The study when inducing a Poiseuille and electro-osmotic flow is carried out now when a stiff polymer is considered for the $L_z = 34 a_0 \approx 8.15 R_g$ case. To do so, only the high strength forces for $c_{add} = 0 \text{ mol/L}$ and $c_{add} = 2 \text{ mol/L}$ considered in section 4.4.3.2 are taken. First the case of no added salt is treated.

- Case of no added salt:

In Figure 4.28 are shown the monomer probability distributions under an electro-osmotic flow, as a function of the distance to the center of the channel, for the cases of a flexible and stiff polymer, when considering repulsive or attractive walls. First, when comparing the influence of the stiffness when repulsive walls are considered (see red and orange curves in Figure 4.28), we observe a decrease of the monomer probability to be close to the walls. Then, it seems that the repulsive walls for a stiff polymer acts in a more pronounced way than for flexible polymers. Second, comparing the influence of the stiffness when attractive walls are considered (see green and blue curves in Figure 4.28), the contrary happens. But again the effect of the wall is enhanced for a stiff polymer.

Indeed, the same behaviour is founded when a Poiseuille flow is considered (see Figure 4.29 and Figure 4.30). For this study the asphericity was not obtained

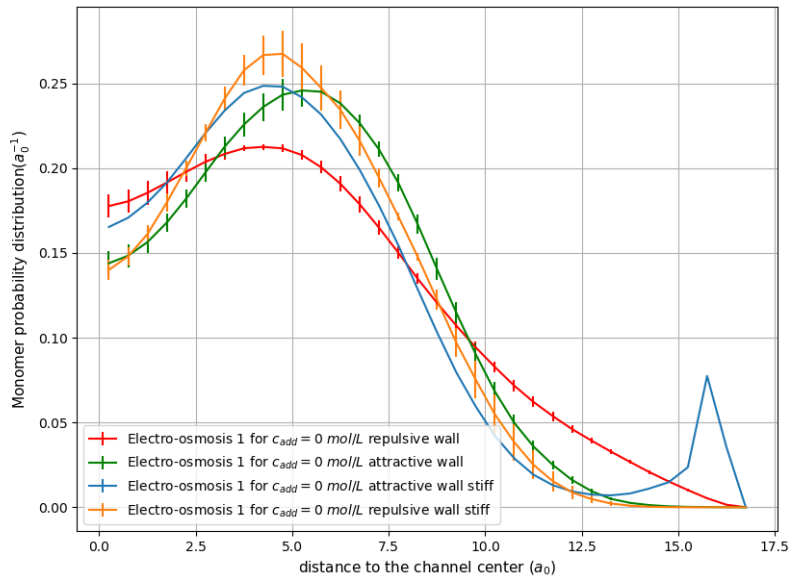


Figure 4.28 – Comparison between the monomer probability distribution, for a linear flexible and stiff polymer, as a function of the distance to the center channel when inducing an electro-osmotic flow (no added salt) for the $L_z = 34 a_0 \approx 8.15 R_g$ case. In this case we considered the case with repulsive and attractive walls.

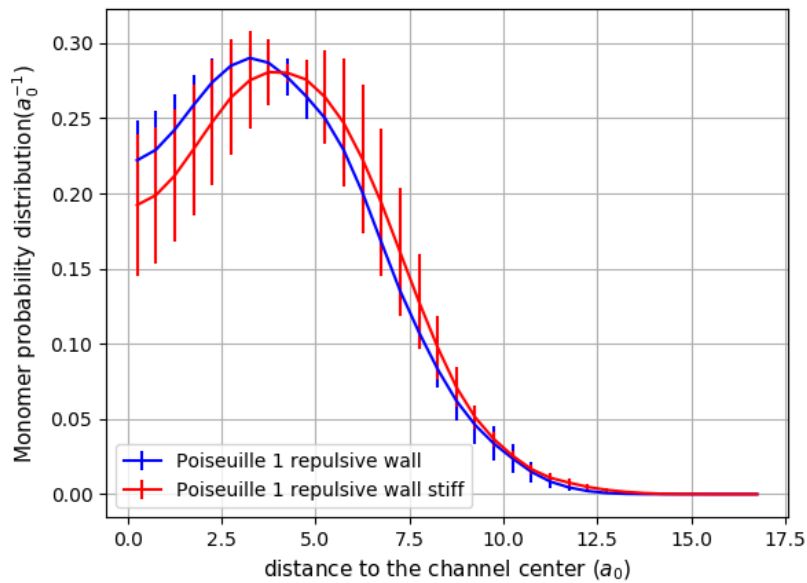


Figure 4.29 – Comparison between the monomer probability distribution, for a flexible and stiff polymer, as a function of the distance to the center of the channel under an induced Poiseuille flow for the case $L_z = 34 a_0 \approx 8.15 R_g$. In this case we considered the case with repulsive walls.

because the stiffness of the polymer does not allow it to fold and thus the R_g is affected.

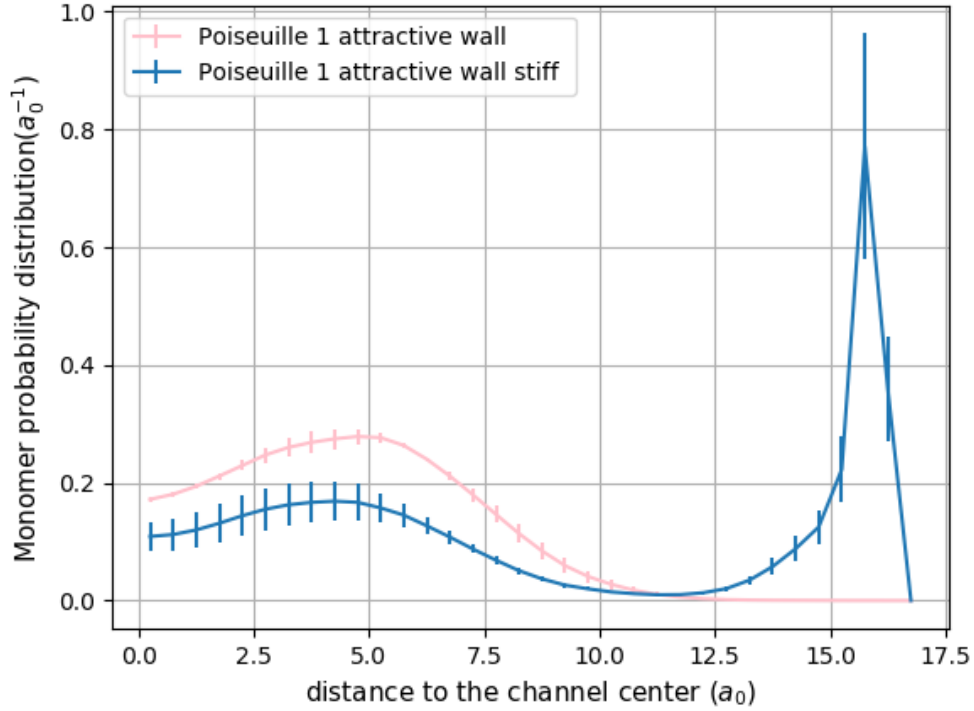


Figure 4.30 – Comparison between the monomer probability distribution, for a flexible and stiff polymer, as a function of the distance to the center of the channel under an induced Poiseuille flow for the case $L_z = 34 a_0 \approx 8.15 R_g$. In this case we considered the case with attractive walls.

– Case of added salt:

In Figure 4.31, are shown the monomer probability distributions as a function of the distance to the center channel for the cases of a repulsive or an attractive wall of a flexible and stiff polymer when inducing an electro-osmotic flow (added salt case). We observe the same behaviour as in $c_{add} = 0 \text{ mol/L}$ when comparing the influence of the stiffness when attractive walls are considered (see orange and green curves). However, for $c_{add} = 2 \text{ mol/L}$ in the region close to the wall, the increase of the monomer probability is not as big as for $c_{add} = 0 \text{ mol/L}$. But the decrease of the monomer probability in the region of the center of the channel is larger in this case.

On the other hand when looking at blue and red curve, we notice that the effect of the stiffness when repulsive wall is considered, does not seem to have a big impact since both curves are close to each other.

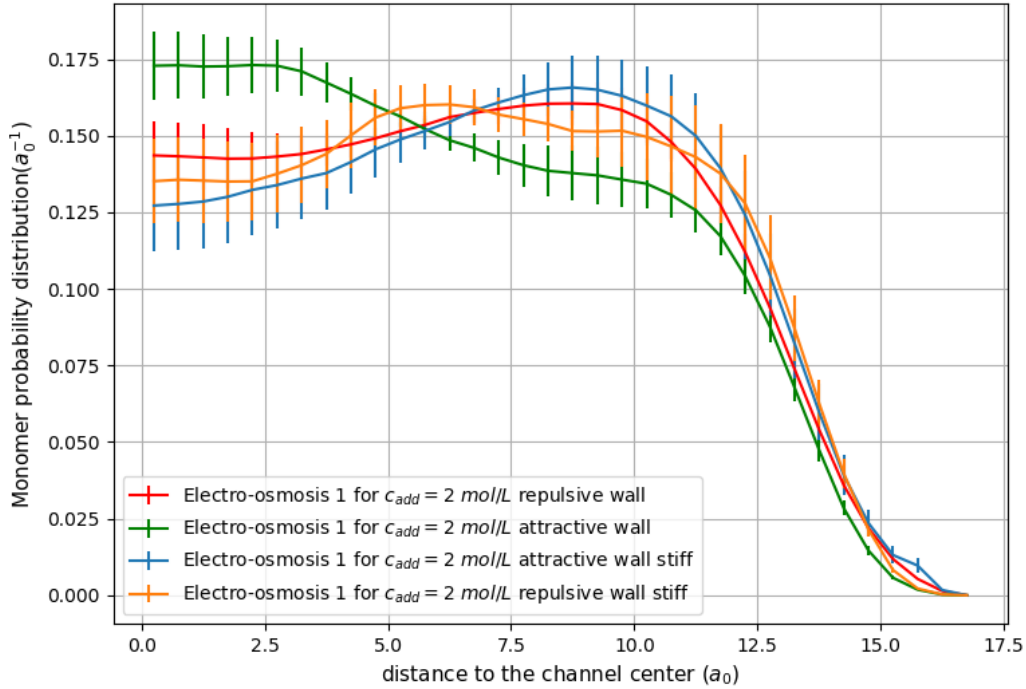


Figure 4.31 – Monomer probability distribution as a function of the distance to the center of the channel under an induced electro-osmotic flow for the case $L_z = 34 a_0 \approx 8.15 R_g$. A comparison between the case of repulsive and attractive walls for a flexible and stiff polymer is carried out.

4.4.5 Conclusion

The main idea of this analysis was to see which is the influence of an electro-osmotic flow on the structure of a polymer in a slit pore compared to the influence of a Poiseuille flow. To do so, several situations were investigated. First, as the shape of electro-osmotic flow depends on the concentration of added salt, two qualitatively distinct flow profiles were chosen ($c_{add} = 0 M$ and $c_{add} = 2 M$). Therefore we were interested to see how the difference between the shapes of the electro-osmotic flows influence the polymer behaviour.

First, when considering an induced electro-osmotic flow between walls exerting a repulsion on the polymer, two distances between the walls were studied that correspond to different confinement $L_z \approx 4 R_g$ and $L_z \approx 8 R_g$. The results were compared to those obtained in the same pore, but under a Poiseuille flow. As a result, for the induced electro-osmotic flow with added salt (*i.e.* $c_{add} = 2 M$), we found that the effect of increasing the electric field strength does not have a large influence on the polymer behaviour. This was observed since for both L_z studies, the curves for the high and small electric fields, were close to the equilibrium case. On the other hand, the structure under an electro-osmotic flow, in no added salt case, has a similar behaviour as the one seen under a Poiseuille flow.

Second, when considering an induced electro-osmotic flow between walls exerting an attraction on the polymer, the flexible and stiff polymer were studied for $L_z = 34 a_0 \approx 8 R_g$ only. For the flexible chain an interesting and not expected phenomenon was found under

Chapter 4. Polymers in confinement

an induced electro-osmotic flow. There seems to be a coupling between the effect of the attraction to the wall and the effect of the flow on the asphericity. Indeed, this behaviour was not seen under the induced Poiseuille flow. Finally, when considering a stiff polymer, this effect is not found. Therefore, a more extensive study, when considering attractive walls, for a linear flexible polymer, under induced electro-osmotic flow, should be carried out. Moreover, an analysis when increasing or decreasing the attraction force to the walls ought to be investigated, in order to see how the unexpected behaviour changes.

General conclusions

IN THIS THESIS we have used a mesoscopic simulation method, the Multiparticle Collision Dynamics (MPCD) to investigate the structural and dynamic behaviors of solutions confined in a slit pore under a flow. In MPCD the solvent is coarse-grained into a very simple granular solvent, whose dynamics is that of the Navier-Stokes equations. Two kinds of confined fluids were studied: ionic solutions and dilute suspensions of a linear polymer. One important difference between these two situations is that the solvent shear affects the structure of the polymer that is a soft molecule, whereas the structural organisation of ions in a double layer between the charged surfaces of a slit pore is unaffected by a flow.

The first part of our work (Chapter 3) was thus devoted to the dynamic properties of ions in charged slit pores, at equilibrium and under an external electric field. The presence of an electric field induce an electro-osmotic flow of the solvent, due to the inhomogeneous structure of charges within the pore. Such electrokinetic phenomenon is usually described by the Poisson-Nernst-Planck equation. In this framework, ions are assumed to be point-like particles, and excluded volume effects between ions, as well as hydrodynamic couplings between moving ions are not taken in account. As a consequence, the ionic mobility is ideal, *i.e.* it is equivalent to the one obtained in the case of a bulk solution at infinite dilution. It is well known from a long time for bulk electrolyte solutions that non ideal effects influence the transport properties of ions at finite concentration. One aim of the present work was to quantify these non ideal effects in charged slit pores.

At equilibrium, *i.e.* without any flow in the slit pore, we have computed the self-diffusion coefficients of ions. We have shown that the self-diffusion coefficient of co-ions, that have a charge of same sign as the surfaces of the pore, is mostly influenced by the ionic concentration and almost not by the surface charge. For counterions, an interplay between the electrostatic attraction with the wall and ionic concentration contributions influence de diffusion. Moreover, confinement has an influence on the ion diffusion coefficients, since for both ions D/D^0 decreases as the size of the pore decreases, hence the confinement increases.

We have then focused on the electric conductivity of the ionic solution, that was computed from non-equilibrium simulations, under an applied electric field, from the ionic velocity profiles in the direction perpendicular to the surfaces of the slit pore. Experimental determinations of dynamic properties of colloids are often interpreted by using the concept of surface conductivity, that reflects the excess of conductivity due to the presence of a charged interface. We have shown that the velocities of ions as a function of their distance to the walls exhibit strong departures from the ideal behaviour. These effects are due to the electrostatic and hydrodynamic coupling between ions and with the walls. For both ions, the velocity in the reference frame of the solvent decreases as the concentration of added salt increases, and does not depend on the charge of the wall. Moreover, we were able to predict these quantities by existing theories, *i.e.* using calculations that are be much faster to run than numerical simulations. To do so, we used the hydrodynamic approach proposed in Ref.^[119] and the conductivity of a bulk ionic solution at the concentration corresponding to the added salt concentration. For all the systems investigated, we have obtained an excellent agreement between the ionic velocity profiles computed from MPCD simulations in a charged slit pore

General conclusions

and those predicted by combining the hydrodynamic approach with the bulk conductivity. As the electric conductivity of the system can be computed from these velocity profiles, we thus propose a simple approach to compute the conductivity of the system as a function of the distance to the charged surface. This may be helpful to quantify the surface conductivity in a given system.

One limitation of our approach lies in the ionic concentration range that we have investigated, that is rather concentrated. Indeed, the non-ideal effect that we observed are almost independent on the concentration in this range. One interesting perspective of this work would be to study the case of dilute ionic solutions. To do so, we would need to simulate the behaviour of larger systems, in order to have a number of ions in the simulation sufficient to obtain a good statistics. Also, we have neglected the molecular details of the solvent and of the charged surfaces. Other studied focus on these aspects and our work appears to be complementary to these other works.

The second part of our work focuses on the structure of linear polymer under flow. The effect of a Poiseuille flow in a slit pore on polymer conformations is well documented in the literature. For example, it may cause an effective interaction with the wall, which disappears when the flow velocity vanishes in equilibrium situations. We have obtained in the first part of our work the electro-osmotic flow in a charged slit pore under an applied electric field, in various conditions. The shape of the electro-osmotic flow varies with the added salt concentration. Without added salt, it is close to a Poiseuille flow, but in the presence of added salt it becomes flat, so that the shear rate is less homogeneous and mainly located close to the walls of the slit pore. We have thus studied how the electro-osmotic flow affects the conformation of a polymer compared to a Poiseuille flow, in several situations. To do so, we have applied in the slit pore some of the electro-osmotic flows computed in Chapter 3, but without the explicit presence of ions. Two confinement distances were investigated ($L_z \simeq 4R_g$ and $L_z \simeq 8R_g$). We have also varied the stiffness of the chain, to compare the case of a flexible polymer to that of polymer with a persistence length of about ten times the size of monomer, for a chain of 40 monomers. Finally, the interaction with the wall was varied from purely repulsive to attractive.

The monomer probability distribution under an electro-osmotic flow is actually close to that obtained under a Poiseuille flow for the highest confinement investigated here. For the smallest confinement ($L_z \simeq 8R_g$), we have observed a behavior under an electro-osmotic flow that differs from the case of an applied Poiseuille flow, especially for the flat electro-osmotic flow obtained in the presence of an added salt: the monomer probability distribution is closer to that obtained at equilibrium than under a Poiseuille flow. In the presence of an attractive force between the polymer and the wall, the asphericity of the polymer is increased compared to the case where the interaction is repulsive. Actually, the fact that asphericity increases close to the walls, leads the polymer to move away from it. For a stiff polymer attracted to the wall, the probability to be in the vicinity of the wall increases significantly compared to what is observed in the same conditions but with a Poiseuille flow.

As a conclusion we could say that the MPCD simulation method is an efficient tool that accounts for the electrostatic effects and the coupling with hydrodynamics. It allowed us to account for the non ideal effects which cannot be captured in usual theories as PNP. This method should be complemented by descriptions at smaller scales which would account for

General conclusions

the molecular details of the solvent and of the surface.

Appendix

A.1 Results found in section 3.9

A.1.0.1 Low confinement

Starting from the ion velocity profiles for $Lz = 4.5 \text{ nm}$, the velocity ion profiles of counterions compared to the hydrodynamic approach multiplied by the value of the velocity at bulk (*i.e.* $\langle V_{bulk} \rangle / V^0$) are shown in Fig A.1, Fig A.2 and Fig A.3 , whereas the case of co-ion are illustrated in Fig A.4, Fig A.5 and Fig A.6. In both cases, each plot correspond to different added salt concentrations, starting from the low case (*i.e.* $c_{add} = 0.5 \text{ mol/L}$), and ending by the high concentration.

- Counterions

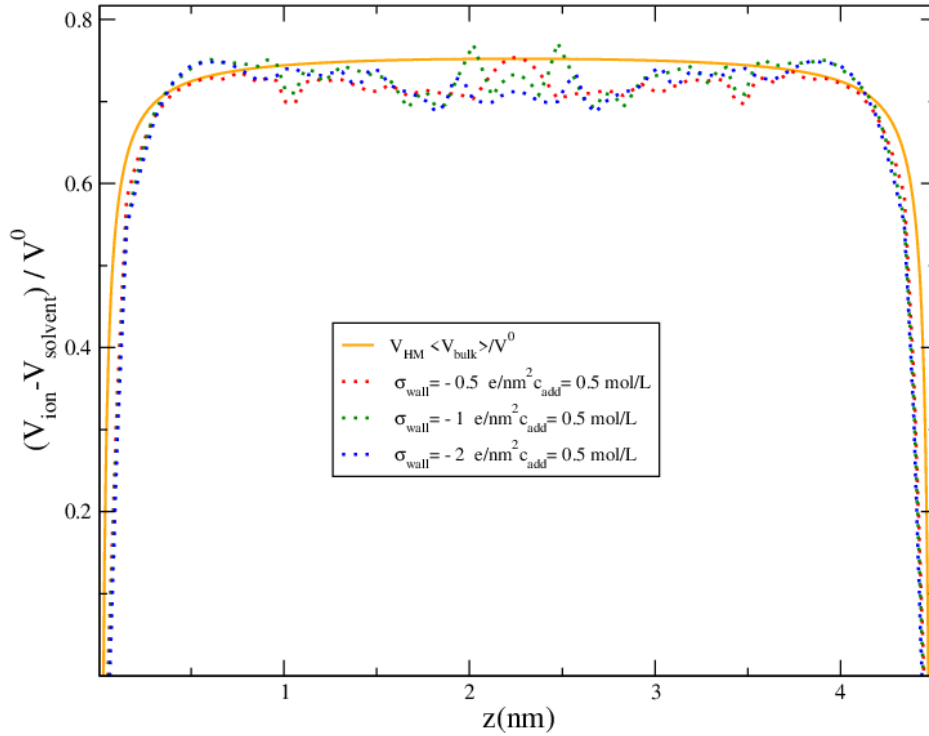


Figure A.1 – Comparison between: a) Counterions velocity profiles as function of the distance to the wall b) Hydrodynamic approach multiplied by the value of the velocity at bulk for the case of $c_{add} = 0.5 \text{ mol/L}$ and $Lz = 4.5 \text{ nm}$.

For counterions we can see that from the figures, a good agreement of the counterions velocity profiles for all the cases of concentration of added salt is found when this is compared to the hydrodynamic approached multiplied by the value of $\langle V_{bulk} \rangle / V^0$.

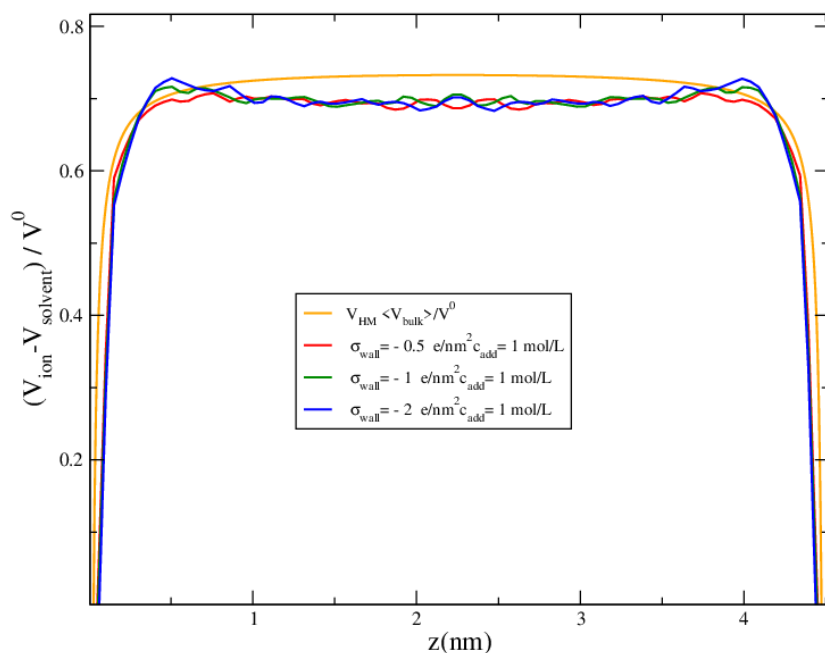


Figure A.2 – Comparison between: a) Counterions velocity profiles as function of the distance to the wall b) Hydrodynamic approach multiplied by the value of the velocity at bulk for the case of $c_{\text{add}} = 1 \text{ mol/L}$ and $Lz = 4.5 \text{ nm}$.

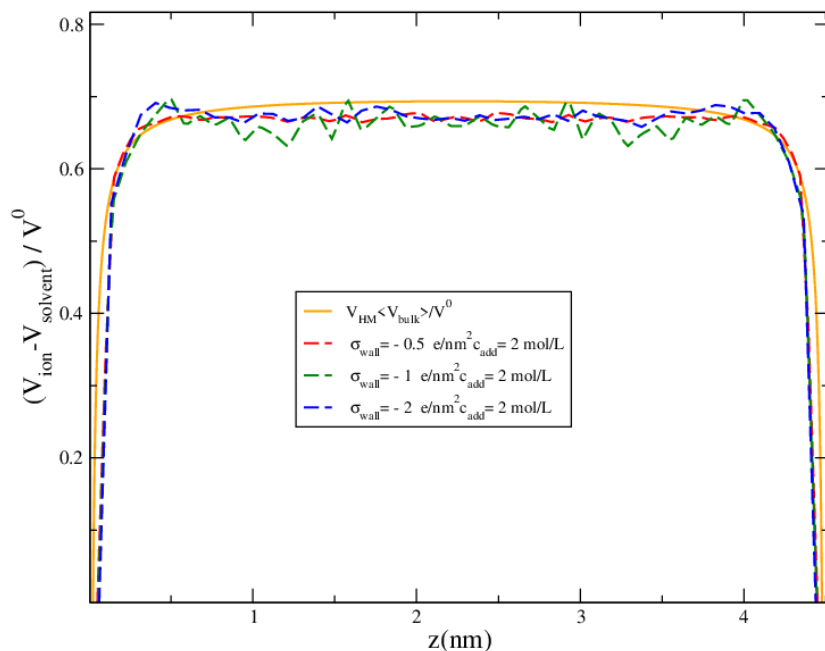


Figure A.3 – Comparison between: a) Counterions velocity profiles as function of the distance to the wall b) Hydrodynamic approach multiplied by the value of the velocity at bulk for the case of $c_{\text{add}} = 2 \text{ mol/L}$ and $Lz = 4.5 \text{ nm}$.

Appendix A.

To obtain the curve for μ_{HM} the value considered for z_ξ of equation 3.21 is not the value of the distance between the walls (*i.e.* L_{hyd} at Fig 3.3). Indeed the value L_{el} , this is the excluded volume of the ions is taken into account. For $c_{add} = 0.5 \text{ mol/L}$ and 1 mol/L , the curve of $\mu_{HM} < V_{bulk} > / V^0$ does not match perfectly at the middle of the pore. This can be explained since for these cases the statistic for the ion profile of counterions is poor compared to the case of $c_{add} = 2 \text{ mol/L}$.

- Co-ions

The same analysis is now made for the case of co-ions. We can conclude that as in the case of counterions, a good agreement is found when comparing $\mu_{HM} < V_{bulk} > / V^0$ with the co-ion velocity profiles. However, the match is less precise due to the poorest statistic of co-ions in comparison with counterions.

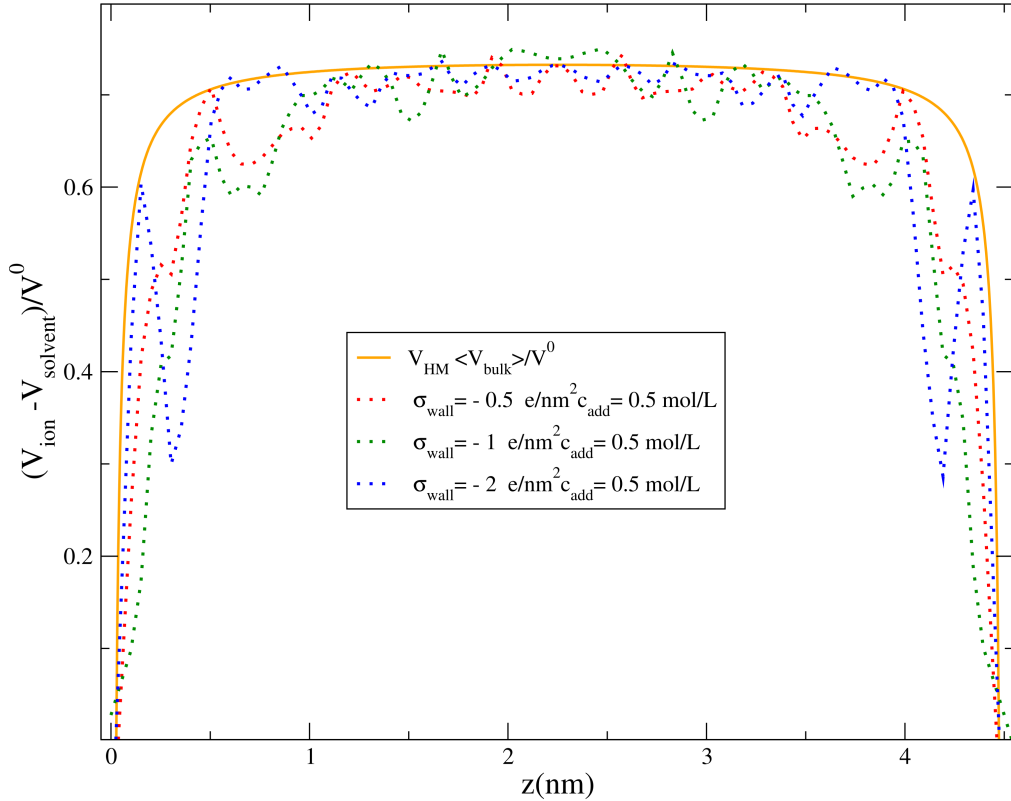


Figure A.4 – Comparison between: a) Co-ions velocity profiles as function of the distance to the wall b) Hydrodynamic approach multiplied by the value of the velocity at bulk for the case of $c_{add} = 0.5 \text{ mol/L}$ and $Lz = 4.5 \text{ nm}$.

A.1.0.2 Medium confinement

Considering the ion velocity profiles for $Lz = 3.0 \text{ nm}$ the same study is carried out. The velocity profiles of counterions compared to the hydrodynamic approach multiplied by the value of the velocity at bulk (*i.e.* $< V_{bulk} > / V^0$) are shown in Fig A.7, Fig A.8 and Fig A.9, whereas the case of co-ion are illustrated in Fig A.10, Fig A.11 and Fig A.12. In both

Appendix A.

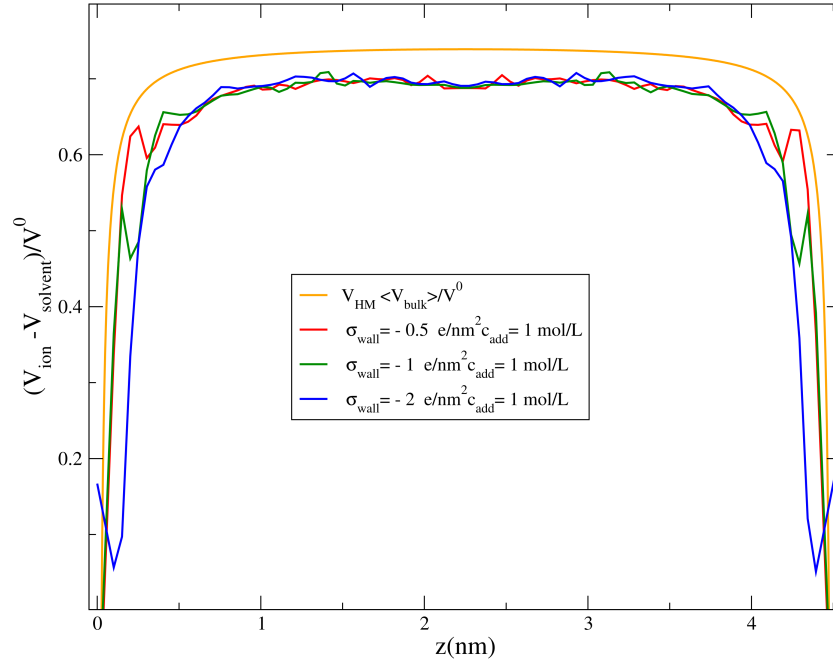


Figure A.5 – Comparison between: a) Co-ions velocity profiles as function of the distance to the wall b) Hydrodynamic approach multiplied by the value of the velocity at bulk for the case of $c_{\text{add}} = 1 \text{ mol/L}$ and $L_z = 4.5 \text{ nm}$.

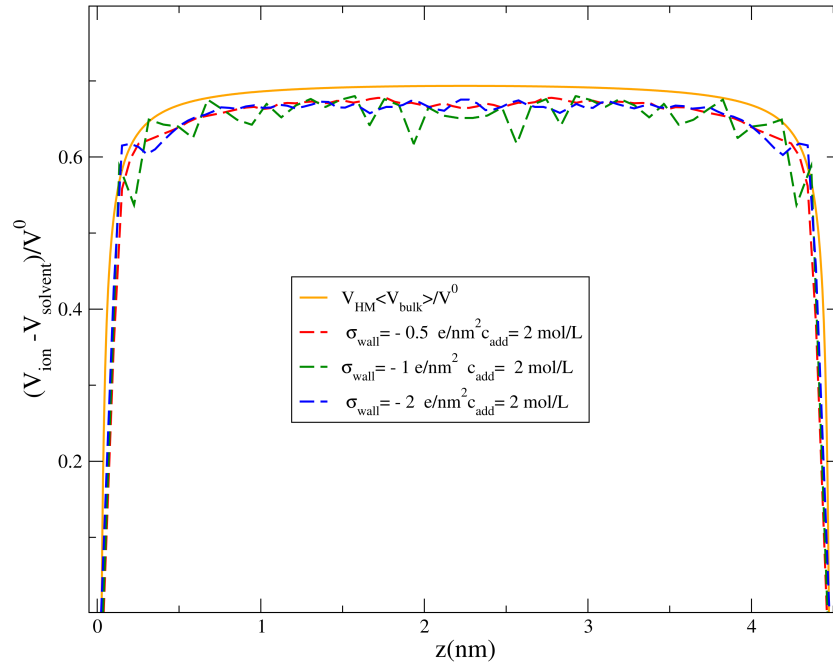


Figure A.6 – Comparison between: a) Co-ions velocity profiles as function of the distance to the wall b) Hydrodynamic approach multiplied by the value of the velocity at bulk for the case of $c_{\text{add}} = 2 \text{ mol/L}$ and $L_z = 4.5 \text{ nm}$.

Appendix A.

cases, each plot correspond to different added salt concentrations, starting from the lowest case, and ending by the higher concentration.

For this confinement, when comparing $\mu_{HM} \langle V_{bulk} \rangle / V^0$ and the counterion velocity profiles for all the cases, is found a good agreement, even a better match for the values at the middle of the pore is observed compared to the $Lz = 4.5nm$ case. This can be explained since a better statistic was obtained. It is important to note that the profiles given by $\mu_{HM} \langle V_{bulk} \rangle / V^0$ takes into account the excluded volume of the ions, because both profile match perfectly at the region close to the wall.

- Counterions

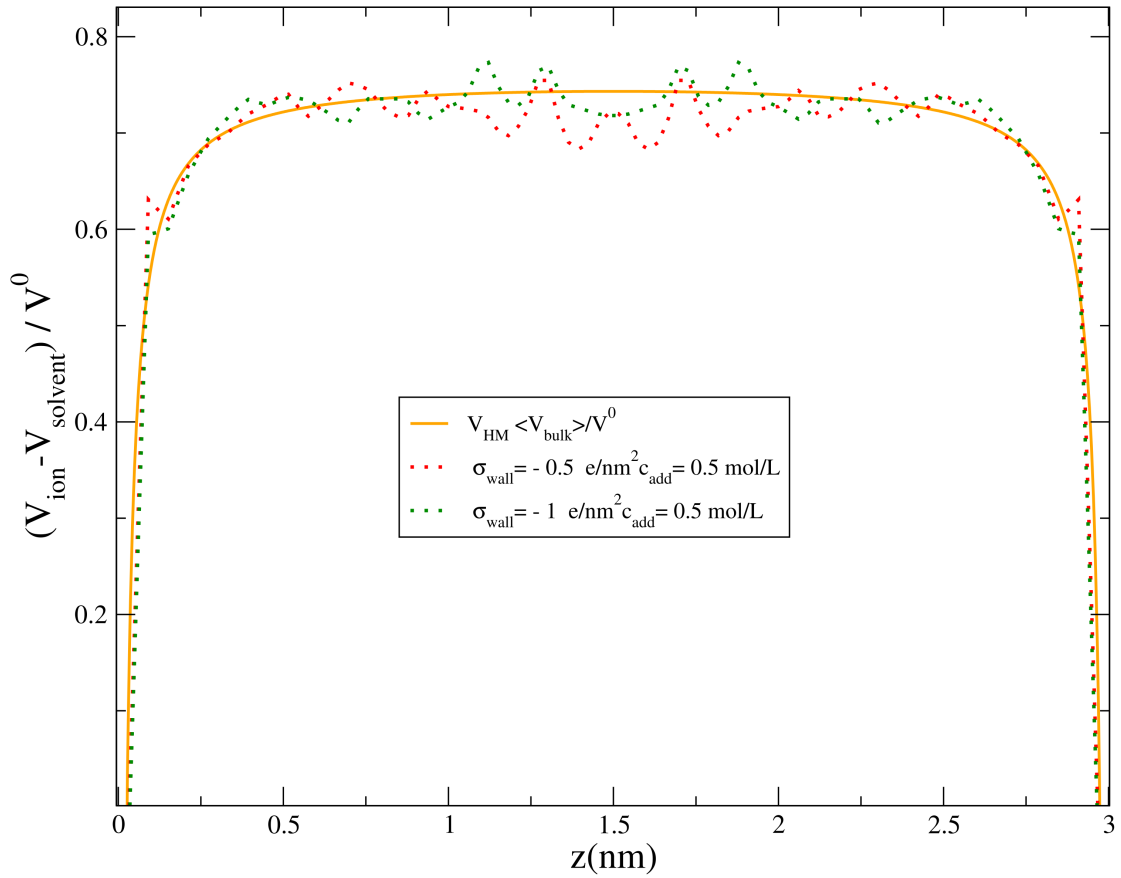


Figure A.7 – Comparison between: a) Counterions velocity profiles as function of the distance to the wall b) Hydrodynamic approach multiplied by the value of the velocity at bulk for the case of $c_{add} = 0.5 \text{ mol/L}$ and $Lz = 4.5 \text{ nm}$.

- Co-ions

For co-ions, the best agreement is found when considering $\mu_{HM} \langle V_{bulk} \rangle / V^0$ for all the cases, however the poor statistic does not allow us to determined with certainty if this match is good enough.

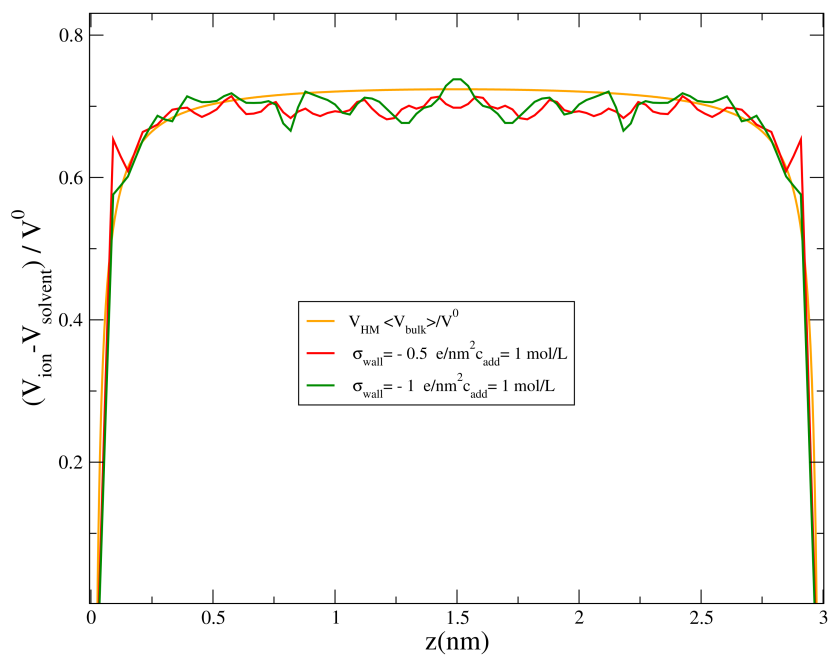


Figure A.8 – Comparison between: a) Counterions velocity profiles as function of the distance to the wall b) Hydrodynamic approach multiplied by the value of the velocity at bulk for the case of $c_{add} = 1 \text{ mol/L}$ and $Lz = 4.5 \text{ nm}$.

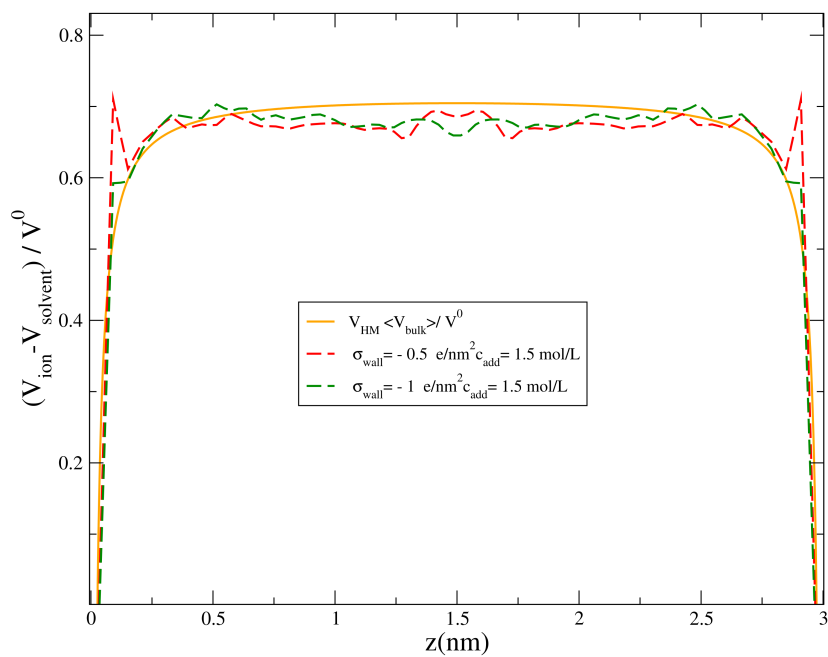


Figure A.9 – Comparison between: a) Counterions velocity profiles as function of the distance to the wall b) Hydrodynamic approach multiplied by the value of the velocity at bulk for the case of $c_{add} = 2 \text{ mol/L}$ and $Lz = 4.5 \text{ nm}$.

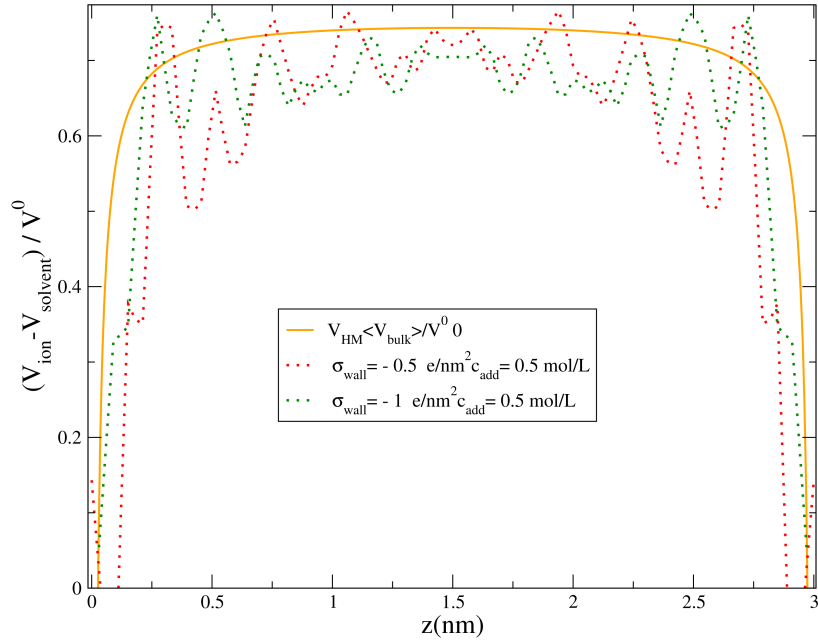


Figure A.10 – Comparison between: a) Co-ions velocity profiles as function of the distance to the wall b) Hydrodynamic approach multiplied by the value of the velocity at bulk for the case of $c_{add} = 0.5 \text{ mol/L}$ and $Lz = 4.5 \text{ nm}$.

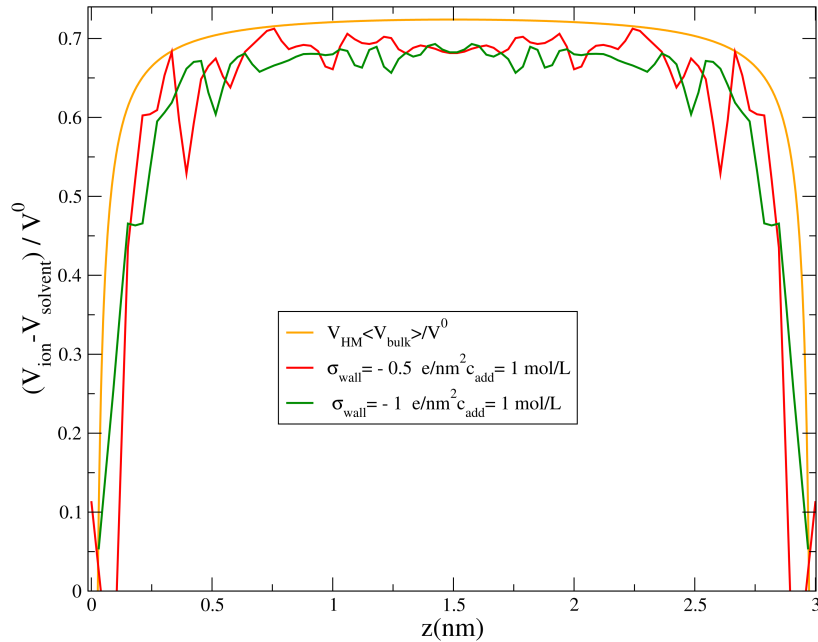


Figure A.11 – Comparison between: a) Co-ions velocity profiles as function of the distance to the wall b) Hydrodynamic approach multiplied by the value of the velocity at bulk for the case of $c_{add} = 1 \text{ mol/L}$ and $Lz = 4.5 \text{ nm}$.

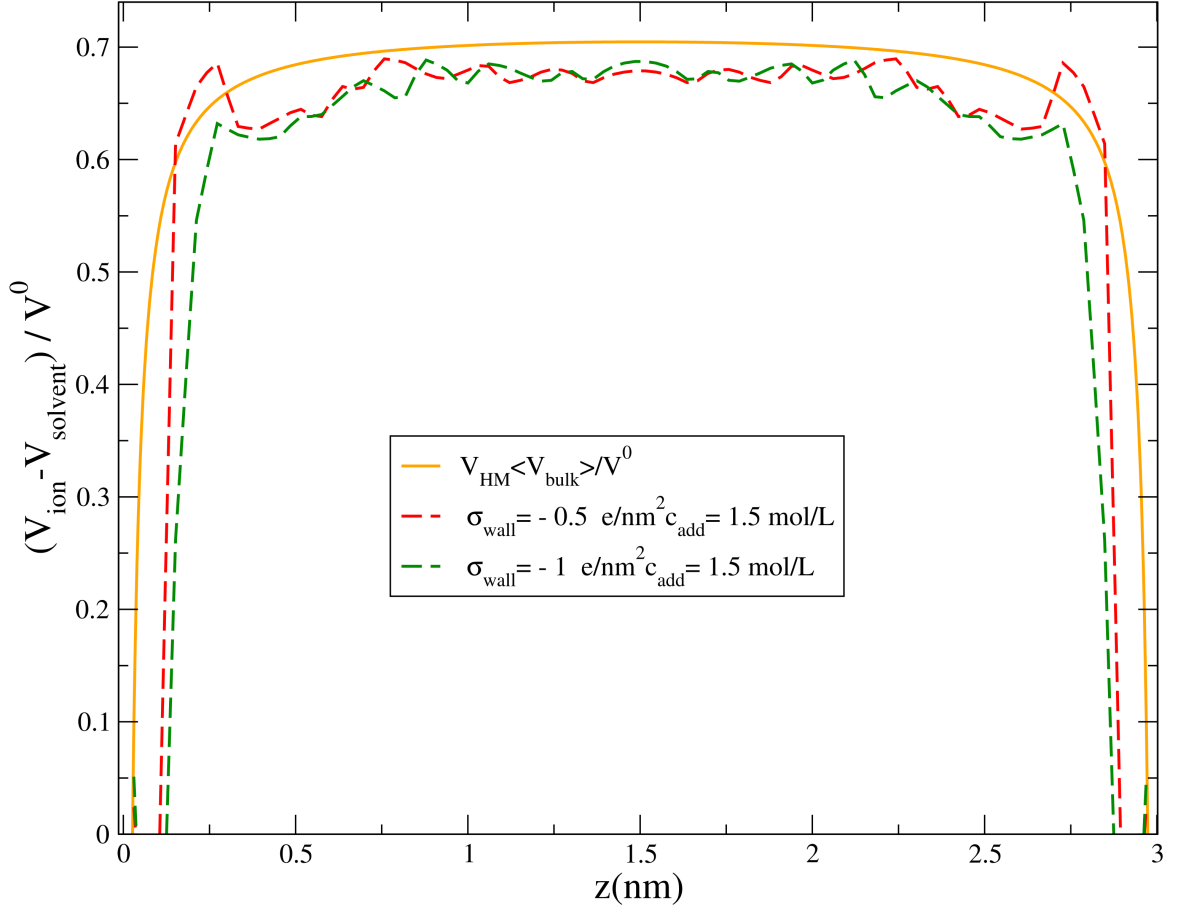


Figure A.12 – Comparison between: a) Co-ions velocity profiles as function of the distance to the wall b) Hydrodynamic approach multiplied by the value of the velocity at bulk for the case of $c_{add} = 2 \text{ mol/L}$ and $Lz = 4.5 \text{ nm}$.

A.1.0.3 High confinement

Finally, the same study for the ion velocity profiles for $Lz = 1.5 \text{ nm}$ is done. The velocity profiles of counterions compared to the hydrodynamic approach multiplied by the value of the velocity at bulk (*i.e.* $\langle V_{bulk} \rangle / V^0$) are shown in Fig A.13, Fig A.14 and Fig A.15. Each plot corresponds to different added salt concentration, starting from the lowest case, and ending by the higher concentration. In this case, co-ions are not shown due to the poor statistics which does not allow us to see the effect of the concentration of added salt as in the other cases.

At this case, a good agreement is found, being better at the region of the middle of the pore, compare to near the walls.

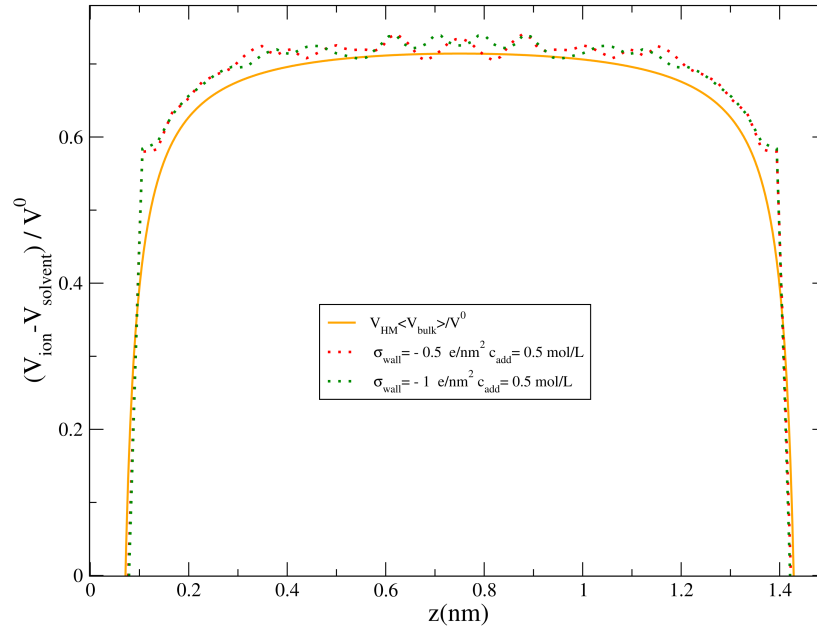


Figure A.13 – Comparison between: a) Counterions velocity profiles as function of the distance to the wall b) Hydrodynamic approach multiplied by the value of the velocity at bulk for the case of $c_{\text{add}} = 0.5 \text{ mol/L}$ and $Lz = 1.5 \text{ nm}$.

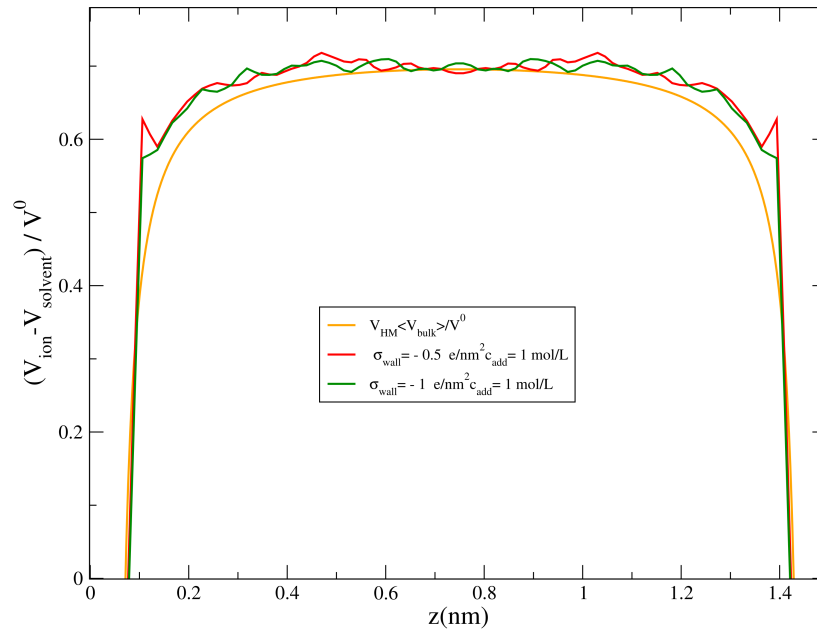


Figure A.14 – Comparison between: a) Counterions velocity profiles as function of the distance to the wall b) Hydrodynamic approach multiplied by the value of the velocity at bulk for the case of $c_{\text{add}} = 1 \text{ mol/L}$ and $Lz = 1.5 \text{ nm}$.

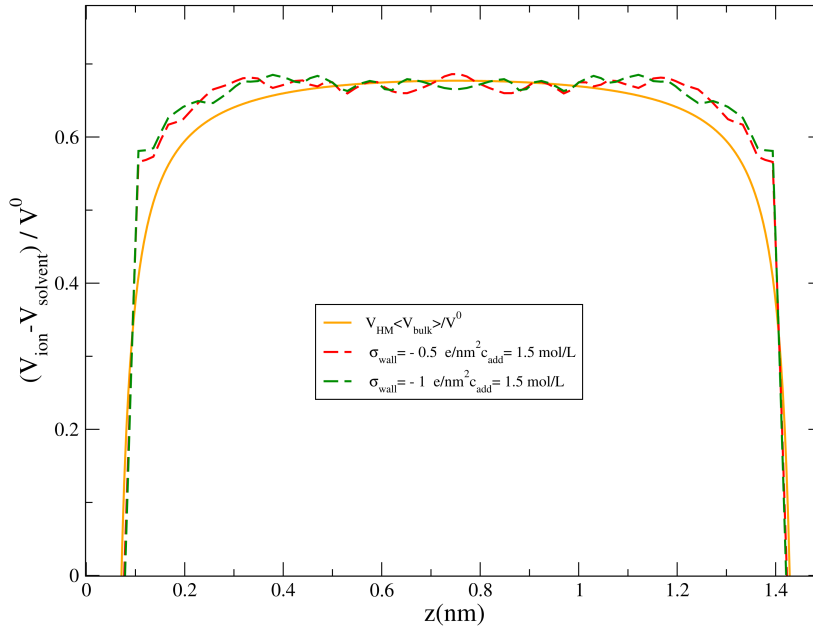


Figure A.15 – Comparison between: a) Counterions velocity profiles as function of the distance to the wall b) Hydrodynamic approach multiplied by the value of the velocity at bulk for the case of $c_{add} = 1.5 \text{ mol/L}$ and $Lz = 1.5 \text{ nm}$.

A.2 Main findings of the previous work of L. Weiss *et.al.*

We do here a summary of the previous work of L. Weiss *et.al.* (see Ref^[133]). Since under Poiseuille flow polymers experience a broad range of shear rates, they tested the possibility to separate them by exploiting their distinct sensitivity to shear. More explicitly, they first investigated the transport and migration behavior of linear and ring polymers for varying flow strengths and rigidities in a bare slit channel with purely smooth, repulsive walls. To do so, they tested two channel widths corresponding to 4 and 8 times the radius of gyration Rg of a linear flexible chain ($Rg = 4.17 \pm 0.03a_0$ for a chain of 40 monomers) and varied the flow strength.

Migration of linear polymers had already been studied in other works^[136–139]. An agreement with previous works was founded. Linear polymers moves away from the channel walls with increasing flow strength due to the anisotropic diffusivity caused by the deformation of the chain. When comparing linear with ring polymer they found that the depletion in the channel center is more pronounced for linear chains compared to ring polymers. However, in such bare channels they observed only minor differences ($< 5\%$) in the relative transport velocities between chains and rings of the same molecular weight, making an efficient separation of the two species difficult (see Figure A.16).

On the other hand, increasing the bending rigidity leads to the enhance most of the depletion for both topologies. Nonetheless when comparing the relative velocity of the rings with the chains polymers as a function of the flow strength f for varying rigidity, the differences are not sufficiently large to yield a proper separation of the two species (see Figure A.17).

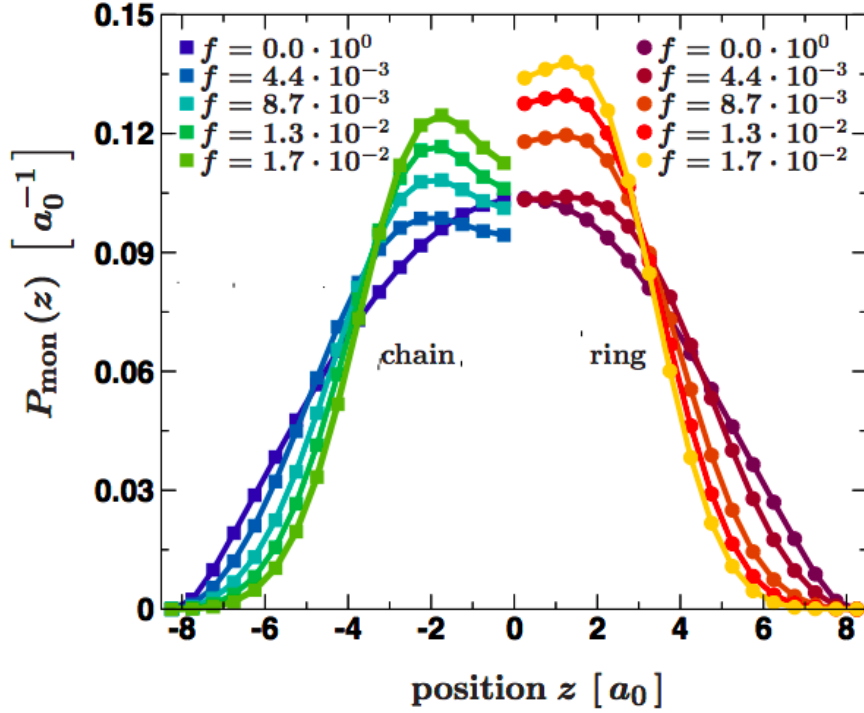


Figure A.16 – Monomer probability distribution $P_{mon}(z)$ for fully flexible chains as a function of the applied flow strengths. Taking into account the channel symmetry with its center at $z = 0$, only half the profile of each topology is depicted; ring polymers are in red/yellow, linear ones in green/blue. Forces f are in units of $m_S a_0 t_0^2$ ^[133].

Thus, as an alternative they proposed to add attractive spots at the channel walls in addition to a short-ranged purely repulsive wall potential in order to obtain the desired topological filtering. Since the interaction potential is short ranged, the polymers can only be adsorbed once they diffuse close enough to the walls. As a result the ratio of the ring polymer velocity v_R to the linear polymer velocity v_L shows an impressive increase of up to an order of magnitude (see Figure A.18). Linear chains are firmly adsorbed onto the spots reducing their transport velocity to zero. For rings polymers, the attractive spots promote tank treading as the dominant pattern of motion. This tank treading motion, which is not available for linear polymers, results in a higher average transport velocity of circular polymers. This mechanism holds true for polymers of varying stiffness, and the major advantage of the presented strategy is that it allows for a truly continuous separation. As a result they demonstrated an efficient and continuous mechanism for separating polymers depending on their stiffness and topology.

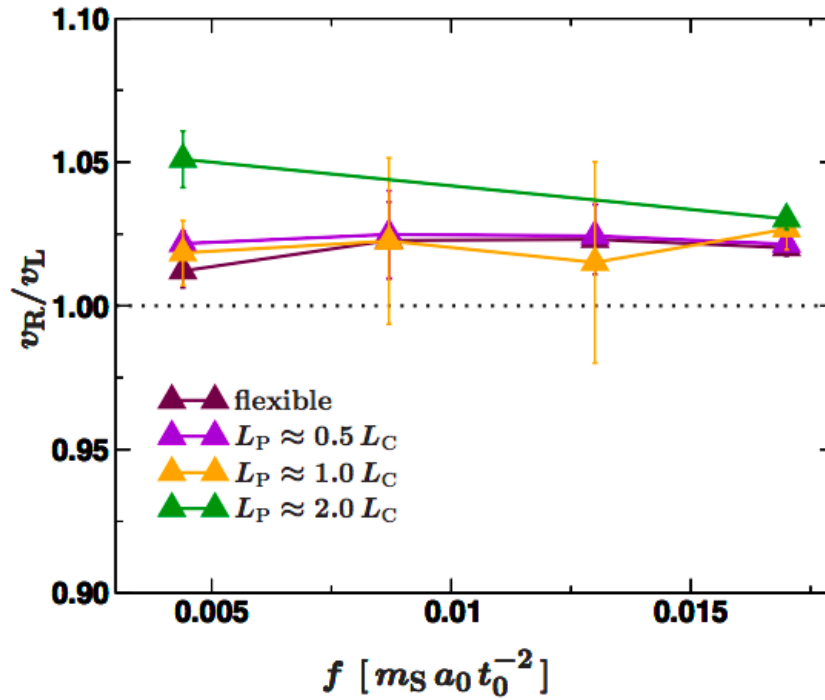


Figure A.17 – Ratio of ring polymer velocity v_R to linear polymer velocity v_L depicted as a function of the flow strength f for varying rigidity^[133].

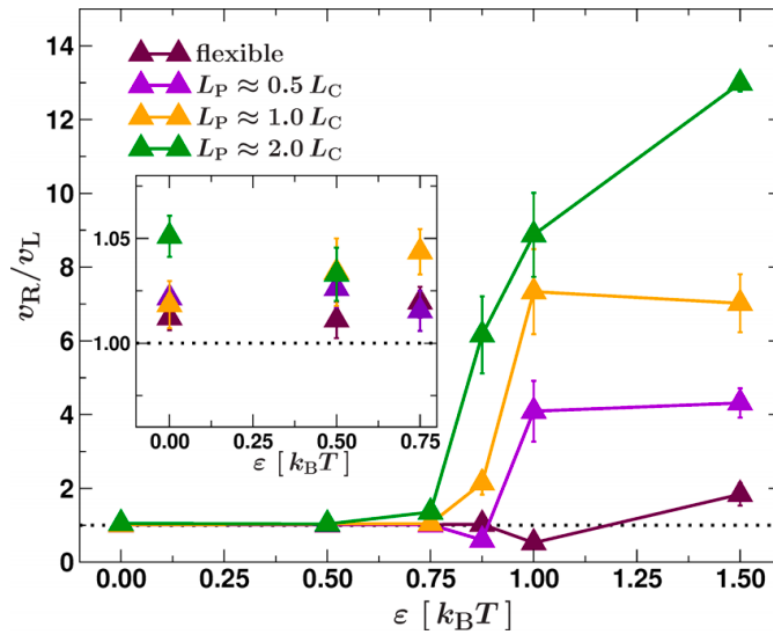


Figure A.18 – Relative increase of the transport velocity of ring polymers v_R to linear ones v_L is plotted as a function of the attraction to the spots strength ϵ . Polymers of various persistence lengths L_P are shown. Error bars are either indicated or smaller than the symbols. $\epsilon = 0k_B T$ corresponds to an undecorated channel wall. The inset depicts the enlargement for weak attraction strengths^[133].

Bibliography

- [1] Wall, S. The history of electrokinetic phenomena. *Current Opinion in Colloid & Interface Science*, 15(3):119–124, **2010**. URL <https://linkinghub.elsevier.com/retrieve/pii/S1359029409001162>. *Cited on pages 2 & 17*
- [2] Masliyeh, J. H. & Bhattacharjee, S. *Electrokinetic and Colloid Transport Phenomena*. John Wiley & Sons, **2006**. Google-Books-ID: GV95Ycfc8QEC. *Cited on page 2*
- [3] Duf r che, J., Bernard, O., Durand-Vidal, S. & Turq, P. Analytical theories of transport in concentrated electrolyte solutions from the msa. *The Journal of Physical Chemistry B*, 109(20):9873/9884, **2005**. URL <https://pubs.acs.org/doi/10.1021/jp050387y>. *Cited on page 3*
- [4] Turq, P., Blum, L., Bernard, O. & Kunz, W. Conductance in associated electrolytes using the mean spherical approximation. *The Journal of Physical Chemistry*, 99(2):822–827, **1995**. URL <https://pubs.acs.org/doi/abs/10.1021/j100002a053>. *Cited on pages 3 & 100*
- [5] Roger, G. M., Durand-Vidal, S., Bernard, O. & Turq, P. Electrical conductivity of mixed electrolytes: Modeling within the mean spherical approximation. *The Journal of Physical Chemistry B*, 113(25):8670–8674, **2009**. URL <https://pubs.acs.org/doi/10.1021/jp901916r>. *Cited on page 3*
- [6] Jardat, M., Cartailier, T. & Turq, P. Counterion and polyion dynamics in highly asymmetrical electrolyte solutions. *The Journal of Chemical Physics*, 115(2):1066–1072, **2001**. URL <http://aip.scitation.org/doi/10.1063/1.1376425>. *Cited on page 3*
- [7] Botan, A., Rotenberg, B., Marry, V., Turq, P. & Noetinger, B. Carbon dioxide in montmorillonite clay hydrates: Thermodynamics, structure, and transport from molecular simulation. *The Journal of Physical Chemistry C*, 114(35):14962–14969, **2010**. URL <https://pubs.acs.org/doi/10.1021/jp1043305>. *Cited on page 3*
- [8] Marinova, K. G., Alargova, R. G., Denkov, N. D., Velev, O. D., Petsev, D. N., Ivanov, I. B. & Borwankar, R. P. Charging of oil-water interfaces due to spontaneous adsorption of hydroxyl ions. *Langmuir*, 12(8):2045–2051, **1996**. URL <https://doi.org/10.1021/la950928i>. *Cited on page 5*
- [9] Lyklema, J. *Fundamentals of Interface and Colloid Science: Fundamentals*. Elsevier Science, **1991**. Google-Books-ID: FkyMvgAACAAJ. *Cited on page 5*
- [10] Delgado, A. V., Gonz lez-Caballero, F., Hunter, R. J., Koopal, L. K. & Lyklema, J. Measurement and interpretation of electrokinetic phenomena (iupac technical report). *Pure and Applied Chemistry*, 77(10):1753–1805, **2005**. URL <http://www.degruyter.com/view/j/pac.2005.77.issue-10/pac200577101753/pac200577101753.xml>. *Cited on pages iii, 6, 7, 8, & 20*
- [11] Ohshima, H. & Furusawa, K. *Electrical Phenomena at Interfaces, Second Edition: Fundamentals Measurements, and Applications*. CRC Press, **1998**. Google-Books-ID: lCgwchqTJkoC. *Cited on page 6*
- [12] Lyklema, J., Rovillard, S. & De Coninck, J. Electrokinetics: The properties of the stagnant layer unraveled. *Langmuir*, 14(20):5659–5663, **1998**. URL <https://pubs.acs.org/doi/10.1021/la980399t>. *Cited on page 6*

Bibliography

- [13] Lorimer, J. Phenomenological coefficients and frames of reference for transport processes in liquids and membranes. *Journal of Membrane Science*, 14(3):275–302, **1983**. URL <http://linkinghub.elsevier.com/retrieve/pii/0376738883800064>. *Cited on page 6*
- [14] Lyklema, J. & Minor, M. On surface conduction and its role in electrokinetics. *Colloids and Surfaces A: Physicochemical and Engineering Aspects*, 140(1):33–41, **1998**. URL <http://www.sciencedirect.com/science/article/pii/S0927775797002665>. *Cited on pages iii, 8, 19, & 20*
- [15] Dubois, M., Zemb, T., Belloni, L., Delville, A., Levitz, P. & Setton, R. Osmotic pressure and salt exclusion in electrostatically swollen lamellar phases. *The Journal of Chemical Physics*, 96(3):2278–2286, **1992**. URL <http://aip.scitation.org/doi/10.1063/1.462078>. *Cited on page 12*
- [16] Bikerman, J. J. Ionentheorie der elektrosmose, der strömungsströme und der oberflächenleitfähigkeit. *Zeitschrift für Physikalische Chemie*, 163A(1), **1933**. URL <http://www.degruyter.com/view/j/zpch.1933.163.issue-1/zpch-1933-16333/zpch-1933-16333.xml>. *Cited on page 21*
- [17] Corry, B., Kuyucak, S. & Chung, S.-H. Tests of continuum theories as models of ion channels. ii. poisson-nernst-planck theory versus brownian dynamics. *Biophysical Journal*, 78(5):2364–2381, **2000**. URL <http://www.sciencedirect.com/science/article/pii/S0006349500767816>. *Cited on page 21*
- [18] Cárdenas, A. E., Coalson, R. D. & Kurnikova, M. G. Three-dimensional poisson-nernst-planck theory studies: Influence of membrane electrostatics on gramicidin a channel conductance. *Biophysical Journal*, 79(1):80–93, **2000**. URL <http://www.sciencedirect.com/science/article/pii/S0006349500762758>. *Cited on page 21*
- [19] Gillespie, D., Nonner, W. & Eisenberg, R. S. Coupling poisson nernst planck and density functional theory to calculate ion flux. *Journal of Physics: Condensed Matter*, 14(46):12129–12145, **2002**. URL <http://stacks.iop.org/0953-8984/14/i=46/a=317?key=crossref.ba92c5696eb235f1fe610679ba75a5dd>. *Cited on page 21*
- [20] Lu, B., Holst, M. J., Andrew McCammon, J. & Zhou, Y. C. Poisson-nernst-planck equations for simulating biomolecular diffusion-reaction processes i: Finite element solutions. *Journal of Computational Physics*, 229(19):6979–6994, **2010**. URL <http://www.sciencedirect.com/science/article/pii/S0021999110002962>. *Cited on page 21*
- [21] Zhou, S.-A. & Uesaka, M. Modeling of transport phenomena of ions and polarizable molecules: A generalized poisson-nernst-planck theory. *International Journal of Engineering Science*, 44(13):938–948, **2006**. URL <http://www.sciencedirect.com/science/article/pii/S0020722506000929>. *Cited on page 21*
- [22] R. Saidur, K. L. & Mohammad, H. A review on applications and challenges of nanofluids. *Renewable and Sustainable Energy Reviews*, 15(3):1646–1668, **2011**. URL <http://www.sciencedirect.com/science/article/pii/S1364032110004041>. *Cited on page 22*
- [23] Q. Pu, H. T., J. Yun & Liu, S. Ion-enrichment and ion-depletion effect of nanochannel structures. *Nano Letters*, 4(6):1099–1103, **2004**. URL <https://doi.org/10.1021/nl0494811>. *Cited on page 22*
- [24] Karnik, R., Duan, C., Castelino, K., Daiguji, K. & Majumdar, A. Rectification of ionic current in a nanofluidic diode. *Nano Letters*, 7(3):547–551, **2007**. URL <https://doi.org/10.1021/nl062806o>. *Cited on page 22*

Bibliography

- [25] Z. Siwy, Z. & Fulinski, A. Fabrication of a synthetic nanopore ion pump. Physical Review Letters, 89(19):198103, **2002**. URL <https://link.aps.org/doi/10.1103/PhysRevLett.89.198103>. Cited on page 22
- [26] Bocquet, L. & Charlaix, E. Nanofluidics, from bulk to interfaces. Chemical Society Reviews, 39(3):1073–1095, **2010**. URL <https://pubs.rsc.org/en/content/articlelanding/2010/cs/b909366b>. Cited on page 22
- [27] Ishido, T. & Mizutani, H. Experimental and theoretical basis of electrokinetic phenomena in rock-water systems and its applications to geophysics. Journal of Geophysical Research: Solid Earth, 86(B3):1763–1775, **1981**. URL <https://agupubs.onlinelibrary.wiley.com/doi/abs/10.1029/JB086iB03p01763>. Cited on page 22
- [28] Frenkel, D. & Smit, B. Understanding Molecular Simulation: From Algorithms to Applications. Elsevier, **2001**. Google-Books-ID: 5qTzldS9ROIC. Cited on pages 23 & 53
- [29] Allen, M. P. & Tildesley, D. J. Computer Simulation of Liquids. Oxford University Press, **2017**. Google-Books-ID: WFExDwAAQBAJ. Cited on page 23
- [30] Satoh, A. Introduction to Practice of Molecular Simulation: Molecular Dynamics, Monte Carlo, Brownian Dynamics, Lattice Boltzmann and Dissipative Particle Dynamics. Elsevier, **2010**. Google-Books-ID: 8l8ktuA65dEC. Cited on page 23
- [31] Marry, V., Dufreche, J. F., Jardat, M., Meriguet, G., Turq, P. & Grun, F. Dynamics and transport in charged porous media. Colloids and Surfaces A: Physicochemical and Engineering Aspects, 222(1):147–153, **2003**. URL <http://www.sciencedirect.com/science/article/pii/S0927775703002516>. Cited on page 24
- [32] Yoshida, H., Mizuno, H., Kinjo, T., Washizu, H. & Barrat, J.-L. Molecular dynamics simulation of electrokinetic flow of an aqueous electrolyte solution in nanochannels. The Journal of Chemical Physics, 140(21):214701, **2014**. URL <https://aip.scitation.org/doi/abs/10.1063/1.4879547>. Cited on page 24
- [33] Siboulet, B., Hocine, S., Hartkamp, R. & Dufrêche, J.-F. Scrutinizing electro-osmosis and surface conductivity with molecular dynamics. The Journal of Physical Chemistry C, 121(12):6756–6769, **2017**. URL <http://pubs.acs.org/doi/10.1021/acs.jpcc.7b00309>. Cited on pages 24 & 95
- [34] Marry, V., Dufrêche, J.-F., Jardat, M. & Turq, P. Equilibrium and electrokinetic phenomena in charged porous media from microscopic and mesoscopic models: electro-osmosis in montmorillonite. Molecular Physics, 101(20):3111–3119, **2003**. URL <http://www.tandfonline.com/doi/abs/10.1080/00268970310001626432>. Cited on page 24
- [35] Felderhof, B. U. Hydrodynamic interaction between two spheres. Physica A: Statistical Mechanics and its Applications, 89(2):373–384, **1977**. URL <http://www.sciencedirect.com/science/article/pii/037843717790111X>. Cited on page 24
- [36] Bernard, O., Kunz, W., Turq, P. & Blum, L. Conductance in electrolyte solutions using the mean spherical approximation. The Journal of Physical Chemistry, 96(9):3833–3840, **1992**. URL <https://doi.org/10.1021/j100188a049>. Cited on page 25
- [37] Fuoss, R. M. & Onsager, L. Conductance of unassociated electrolytes. The Journal of Physical Chemistry, 61(5):668–682, **1957**. URL <https://doi.org/10.1021/j150551a038>. Cited on page 25

Bibliography

- [38] Ahlrichs, P., Everaers, R. & Dünweg, B. Screening of hydrodynamic interactions in semidilute polymer solutions: A computer simulation study. *Physical Review E*, 64(4):040501, **2001**. URL <https://link.aps.org/doi/10.1103/PhysRevE.64.040501>. *Cited on page 25*
- [39] Zimm, B. H. Dynamics of polymer molecules in dilute solution: Viscoelasticity, flow birefringence and dielectric loss. *The Journal of Chemical Physics*, 24(2):269–278, **1956**. URL <https://aip.scitation.org/doi/10.1063/1.1742462>. *Cited on page 25*
- [40] Rotne, J. & Prager, S. Variational treatment of hydrodynamic interaction in polymers. *The Journal of Chemical Physics*, 50(11):4831–4837, **1969**. URL <https://aip.scitation.org/doi/10.1063/1.1670977>. *Cited on page 25*
- [41] Frisch, U., Hasslacher, B. & Pomeau, Y. Lattice-gas automata for the navier-stokes equation. *Physical Review Letters*, 56(14):1505–1508, **1986**. URL <https://link.aps.org/doi/10.1103/PhysRevLett.56.1505>. *Cited on page 25*
- [42] McNamara, G. R. & Zanetti, G. Use of the boltzmann equation to simulate lattice-gas automata. *Physical Review Letters*, 61(20):2332–2335, **1988**. URL <https://link.aps.org/doi/10.1103/PhysRevLett.61.2332>. *Cited on page 25*
- [43] Gingold, R. A. & Monaghan, J. J. Smoothed particle hydrodynamics: theory and application to non-spherical stars. *Monthly Notices of the Royal Astronomical Society*, 181(3):375–389, **1977**. URL <https://academic.oup.com/mnras/article/181/3/375/988212>. *Cited on page 25*
- [44] Kum, O., Hoover, W. G. & Posch, H. A. Viscous conducting flows with smooth-particle applied mechanics. *Physical Review E*, 52(5):4899–4908, **1995**. URL <https://link.aps.org/doi/10.1103/PhysRevE.52.4899>. *Cited on page 25*
- [45] Hoogerbrugge, P. J. & Koelman, J. M. V. A. Simulating microscopic hydrodynamic phenomena with dissipative particle dynamics. *Europhysics Letters (EPL)*, 19(3):155–160, **1992**. URL <http://stacks.iop.org/0295-5075/19/i=3/a=001?key=crossref.197c567e055a029b59860f932faf76d1>. *Cited on pages 25 & 26*
- [46] Ermak, D. L. A computer simulation of charged particles in solution. i. technique and equilibrium properties. *The Journal of Chemical Physics*, 62(10):4189–4196, **1975**. URL <https://aip.scitation.org/doi/abs/10.1063/1.430300>. *Cited on page 25*
- [47] Tanaka, H. & Araki, T. Simulation method of colloidal suspensions with hydrodynamic interactions: Fluid particle dynamics. *Physical Review Letters*, 85(6):1338–1341, **2000**. URL <https://link.aps.org/doi/10.1103/PhysRevLett.85.1338>. *Cited on page 25*
- [48] Brookshaw, L. Smooth particle hydrodynamics in cylindrical coordinates. *ANZIAM Journal*, 44:114, **2003**. URL <http://journal.austms.org.au/ojs/index.php/ANZIAMJ/article/view/675>. *Cited on page 25*
- [49] Ermak, D. L. & McCammon, J. A. Brownian dynamics with hydrodynamic interactions. *The Journal of Chemical Physics*, 69(4):1352–1360, **1978**. URL <https://aip.scitation.org/doi/abs/10.1063/1.436761>. *Cited on page 25*
- [50] Panwar, A. S. & Kumar, S. Brownian dynamics simulations of polymer stretching and transport in a complex electroosmotic flow. *The Journal of Chemical Physics*, 118(2):925–936, **2002**. URL <https://aip.scitation.org/doi/abs/10.1063/1.1523912>. *Cited on page 25*
- [51] Joly, L., Ybert, C., Trizac, E. & Bocquet, L. Hydrodynamics within the electric double layer on slipping surfaces. *Physical Review Letters*, 93(25):257805, **2004**. URL <https://link.aps.org/doi/10.1103/PhysRevLett.93.257805>. *Cited on page 25*

Bibliography

- [52] Jardat, M., Bernard, O., Turq, P. & Kneller, G. R. Transport coefficients of electrolyte solutions from smart brownian dynamics simulations. The Journal of Chemical Physics, 110(16):7993–7999, **1999**. URL <https://aip.scitation.org/doi/10.1063/1.478703>. *Cited on page 25*
- [53] Singh, S. P., Huang, C.-C., Westphal, E., Gompper, G. & Winkler, R. G. Hydrodynamic correlations and diffusion coefficient of star polymers in solution. The Journal of Chemical Physics, 141(8):084901, **2014**. URL <http://aip.scitation.org/doi/10.1063/1.4893766>. *Cited on pages 25 & 27*
- [54] Stoltz, C., de Pablo, J. J. & Graham, M. D. Simulation of nonlinear shear rheology of dilute salt-free polyelectrolyte solutions. The Journal of Chemical Physics, 126(12):124906, **2007**. URL <https://aip.scitation.org/doi/10.1063/1.2712182>. *Cited on page 25*
- [55] Cerbelaud, M., Videcoq, A., Abélard, P., Pagnoux, C., Rossignol, F. & Ferrando, R. Heteroaggregation between $al_2 o_3$ submicrometer particles and sio_2 nanoparticles: Experiment and simulation. Langmuir, 24(7):3001–3008, **2008**. URL <https://pubs.acs.org/doi/10.1021/1a702104u>. *Cited on page 25*
- [56] Cerbelaud, M., Videcoq, A., Abélard, P., Pagnoux, C., Rossignol, F. & Ferrando, R. Self-assembly of oppositely charged particles in dilute ceramic suspensions: predictive role of simulations. Soft Matter, 6(2):370–382, **2010**. URL <http://xlink.rsc.org/?DOI=B908671D>. *Cited on page 25*
- [57] Roberts, G. O. & Rosenthal, J. S. Optimal scaling of discrete approximations to langevin diffusions. Journal of the Royal Statistical Society: Series B (Statistical Methodology), 60(1):255–268, **1998**. URL <https://rss.onlinelibrary.wiley.com/doi/abs/10.1111/1467-9868.00123>. *Cited on page 25*
- [58] Beenakker, C. W. J., van Saarloos, W. & Mazur, P. Many-sphere hydrodynamic interactions: Iii. the influence of a plane wall. Physica A: Statistical Mechanics and its Applications, 127(3):451–472, **1984**. URL <http://www.sciencedirect.com/science/article/pii/0378437184900360>. *Cited on page 25*
- [59] Rex, M. & Löwen, H. Influence of hydrodynamic interactions on lane formation in oppositely charged driven colloids. The European Physical Journal E, 26(1):143–150, **2008**. URL <https://doi.org/10.1140/epje/i2007-10274-4>. *Cited on page 25*
- [60] Cichocki, B., Jones, R. B., Kutteh, R. & Wajnryb, E. Friction and mobility for colloidal spheres in stokes flow near a boundary: The multipole method and applications. The Journal of Chemical Physics, 112(5):2548–2561, **2000**. URL <https://aip.scitation.org/doi/abs/10.1063/1.480894>. *Cited on page 25*
- [61] Dünweg, B. & Ladd, A. J. C. Lattice boltzmann simulations of soft matter systems. Dans: Advanced Computer Simulation Approaches for Soft Matter Sciences III, édité par Holm, C. & Kremer, K., Advances in Polymer Science, pages 89–166. Springer Berlin Heidelberg, Berlin, Heidelberg, **2009**. URL https://doi.org/10.1007/978-3-540-87706-6_2. *Cited on pages 25, 26, 31, & 32*
- [62] Ladd, A. J. C., Colvin, M. E. & Frenkel, D. Application of lattice-gas cellular automata to the brownian motion of solids in suspension. Physical Review Letters, 60(11):975–978, **1988**. URL <https://link.aps.org/doi/10.1103/PhysRevLett.60.975>. *Cited on page 26*
- [63] Koelman, J. M. V. A. Cellular-automaton-based simulation of 2d polymer dynamics. Physical Review Letters, 64(16):1915–1918, **1990**. URL <https://link.aps.org/doi/10.1103/PhysRevLett.64.1915>. *Cited on page 26*

Bibliography

- [64] Padding, J. T. & Louis, A. A. Hydrodynamic and brownian fluctuations in sedimenting suspensions. Physical Review Letters, 93(22), **2004**. URL <https://link.aps.org/doi/10.1103/PhysRevLett.93.220601>. Cited on pages *iii*, *26*, *27*, *31*, & *38*
- [65] Moeendarbary, E., Ng, T. Y. & Zangeneh, M. Dissipative particle dynamics in soft matter and polymeric applications. International Journal of Applied Mechanics, 02(01):161–190, **2010**. URL <http://www.worldscientific.com/doi/abs/10.1142/S1758825110000469>. Cited on page *26*
- [66] Español, P. Dissipative particle dynamics for a harmonic chain: A first-principles derivation. Physical Review E, 53(2):1572–1578, **1996**. URL <https://link.aps.org/doi/10.1103/PhysRevE.53.1572>. Cited on page *26*
- [67] Marsh, C. A., Backx, G. & Ernst, M. H. Static and dynamic properties of dissipative particle dynamics. Physical Review E, 56(2):1676–1691, **1997**. URL <https://link.aps.org/doi/10.1103/PhysRevE.56.1676>. Cited on pages *26* & *27*
- [68] Koelman, J. M. V. A. & Hoogerbrugge, P. J. Dynamic simulations of hard-sphere suspensions under steady shear. Europhysics Letters (EPL), 21(3):363–368, **1993**. URL <http://stacks.iop.org/0295-5075/21/i=3/a=018?key=crossref.df54a773858864fbda3b148e7c79c125>. Cited on page *27*
- [69] Groot, R. D. & Warren, P. B. Dissipative particle dynamics: Bridging the gap between atomistic and mesoscopic simulation. The Journal of Chemical Physics, 107(11):4423–4435, **1997**. URL <http://aip.scitation.org/doi/10.1063/1.474784>. Cited on page *27*
- [70] Malevanets, A. & Kapral, R. Mesoscopic model for solvent dynamics. The Journal of Chemical Physics, 110(17):8605–8613, **1999**. URL <https://aip.scitation.org/doi/abs/10.1063/1.478857>. Cited on pages *27*, *29*, *30*, & *32*
- [71] Xing, X. Poisson-boltzmann theory for two parallel uniformly charged plates. Physical Review E, 83(4):041410, **2011**. URL <https://link.aps.org/doi/10.1103/PhysRevE.83.041410>. Cited on page *27*
- [72] Kikuchi, N., Pooley, C. M., Ryder, J. F. & Yeomans, J. M. Transport coefficients of a mesoscopic fluid dynamics model. The Journal of Chemical Physics, 119(12):6388–6395, **2003**. URL <http://aip.scitation.org/doi/10.1063/1.1603721>. Cited on pages *27*, *30*, & *31*
- [73] Tomilov, A., Videcoq, A., Chartier, T., Ala-Nissilv , T. & Vattulainen, I. Tracer diffusion in colloidal suspensions under dilute and crowded conditions with hydrodynamic interactions. The Journal of Chemical Physics, 137(1):014503, **2012**. URL <http://aip.scitation.org/doi/10.1063/1.4731661>. Cited on page *27*
- [74] Tomilov, A., Videcoq, A., Cerbelaud, M., Piechowiak, M. A., Chartier, T., Ala-Nissila, T., Bochicchio, D. & Ferrando, R. Aggregation in colloidal suspensions: Evaluation of the role of hydrodynamic interactions by means of numerical simulations. The Journal of Physical Chemistry B, 117(46):14509–14517, **2013**. URL <https://pubs.acs.org/doi/10.1021/jp407247y>. Cited on page *27*
- [75] Hecht, M., Harting, J., Bier, M., Reinshagen, J. & Herrmann, H. J. Shear viscosity of claylike colloids in computer simulations and experiments. Physical Review E, 74(2), **2006**. URL <https://link.aps.org/doi/10.1103/PhysRevE.74.021403>. Cited on page *27*
- [76] Hecht, M., Harting, J., Ihle, T. & Herrmann, H. J. Simulation of claylike colloids. Physical Review E, 72(1):011408, **2005**. URL <https://link.aps.org/doi/10.1103/PhysRevE.72.011408>. Cited on pages *27* & *39*

Bibliography

- [77] Frank, S. & Winkler, R. G. Polyelectrolyte electrophoresis: Field effects and hydrodynamic interactions. *EPL (Europhysics Letters)*, 83(3):38004, **2008**. URL <http://stacks.iop.org/0295-5075/83/i=3/a=38004>. Cited on pages 27 & 38
- [78] Nikoubashman, A., N. Likos, C. & Kahl, G. Computer simulations of colloidal particles under flow in microfluidic channels. *Soft Matter*, 9(9):2603–2613, **2013**. URL <https://pubs.rsc.org/en/content/articlelanding/2013/sm/c2sm26727f>. Cited on page 27
- [79] Jiang, L., Watari, N. & Larson, R. G. How accurate are stochastic rotation dynamics simulations of polymer dynamics? *Journal of Rheology*, 57(4):1177–1194, **2013**. URL <https://sor.scitation.org/doi/abs/10.1122/1.4807857>. Cited on pages 27 & 38
- [80] Frank, S. & Winkler, R. G. Mesoscale hydrodynamic simulation of short polyelectrolytes in electric fields. *The Journal of Chemical Physics*, 131(23):234905, **2009**. URL <https://aip.scitation.org/doi/10.1063/1.3274681>. Cited on pages 27 & 38
- [81] Ihle, T. & Kroll, D. M. Stochastic rotation dynamics. i. formalism, galilean invariance, and green-kubo relations. *Physical Review E*, 67(6), **2003**. URL <https://link.aps.org/doi/10.1103/PhysRevE.67.066705>. Cited on pages 29, 30, & 31
- [82] Ihle, T. & Kroll, D. M. Stochastic rotation dynamics. ii. transport coefficients, numerics, and long-time tails. *Physical Review E*, 67(6), **2003**. URL <https://link.aps.org/doi/10.1103/PhysRevE.67.066706>. Cited on pages 29, 30, & 31
- [83] Ihle, T., Tüzel, E. & Kroll, D. M. Resummed green-kubo relations for a fluctuating fluid-particle model. *Physical Review E*, 70(3):035701, **2004**. URL <https://link.aps.org/doi/10.1103/PhysRevE.70.035701>. Cited on page 30
- [84] Ihle, T., Tüzel, E. & Kroll, D. M. Equilibrium calculation of transport coefficients for a fluid-particle model. *Physical Review E*, 72(4):046707, **2005**. URL <https://link.aps.org/doi/10.1103/PhysRevE.72.046707>. Cited on page 30
- [85] Granick, S., Zhu, Y. & Lee, H. Slippery questions about complex fluids flowing past solids. *Nature Materials*, 2:221, **2003**. URL <https://doi.org/10.1038/nmat854>. Cited on pages 31 & 32
- [86] Whitmer, J. K. & Luijten, E. Fluid-solid boundary conditions for multiparticle collision dynamics. *Journal of Physics: Condensed Matter*, 22(10):104106, **2010**. URL <http://stacks.iop.org/0953-8984/22/i=10/a=104106?key=crossref.0ea1f56b7578d02049a6429b3a5101cb>. Cited on page 32
- [87] Inoue, Y., Chen, Y. & Ohashi, H. Development of a simulation model for solid objects suspended in a fluctuating fluid. *Journal of Statistical Physics*, 107(1):85–100, **2002**. URL <https://doi.org/10.1023/A:1014550318814>. Cited on page 32
- [88] Padding, J. T., Wysocki, A., Löwen, H. & Louis, A. A. Stick boundary conditions and rotational velocity auto-correlation functions for colloidal particles in a coarse-grained representation of the solvent. *Journal of Physics: Condensed Matter*, 17(45):S3393, **2005**. URL <http://stacks.iop.org/0953-8984/17/i=45/a=027>. Cited on page 32
- [89] Lamura, A., Gompper, G., Ihle, T. & Kroll, D. M. Multi-particle collision dynamics: Flow around a circular and a square cylinder. *Europhysics Letters (EPL)*, 56(3):319–325, **2001**. URL <http://stacks.iop.org/0295-5075/56/i=3/a=319?key=crossref.29a6db78cdc6b006b4a25b199c236195>. Cited on page 33

Bibliography

- [90] Götze, I. O., Noguchi, H. & Gompper, G. Relevance of angular momentum conservation in mesoscale hydrodynamics simulations. *Physical Review E*, 76(4), **2007**. URL <https://link.aps.org/doi/10.1103/PhysRevE.76.046705>. *Cited on page 33*
- [91] Lamura, A. & Gompper, G. Numerical study of the flow around a cylinder using multi-particle collision dynamics. *The European Physical Journal E*, 9(1):477–485, **2002**. URL <https://doi.org/10.1140/epje/i2002-10107-0>. *Cited on page 34*
- [92] Ripoll, M., Mussawisade, K., Winkler, R. & Gompper, G. Dynamic regimes of fluids simulated by multiparticlecollision dynamics. *Physical Review E*, 72(1), **2005**. URL <https://link.aps.org/doi/10.1103/PhysRevE.72.016701>. *Cited on pages 35, 38, 40, 46, 47, & 50*
- [93] Gonnet, P. A simple algorithm to accelerate the computation of non-bonded interactions in cell-based molecular dynamics simulations. *Journal of Computational Chemistry*, 28(2):570–573, **2007**. URL <https://onlinelibrary.wiley.com/doi/abs/10.1002/jcc.20563>. *Cited on page 36*
- [94] N Heinz, T. & H Hünenberger, P. A fast pairlist-construction algorithm for molecular simulations under periodic boundary conditions. *Journal of computational chemistry*, 25:1474–86, **2004**. *Cited on page 36*
- [95] Malevanets, A. & Kapral, R. Solute molecular dynamics in a mesoscale solvent. *The Journal of Chemical Physics*, 112(16):7260–7269, **2000**. URL <http://aip.scitation.org/doi/10.1063/1.481289>. *Cited on page 37*
- [96] Padding, J. T. & Louis, A. A. Hydrodynamic interactions and brownian forces in colloidal suspensions: Coarse-graining over time and length scales. *Physical Review E*, 74(3), **2006**. URL <https://link.aps.org/doi/10.1103/PhysRevE.74.031402>. *Cited on pages 37 & 38*
- [97] Malevanets, A. & Yeomans, J. M. Dynamics of short polymer chains in solution. *Europhysics Letters (EPL)*, 52(2):231–237, **2000**. URL <http://arxiv.org/abs/cond-mat/0007123>. ArXiv: cond-mat/0007123. *Cited on pages 37 & 38*
- [98] Götze, I. O. & Gompper, G. Dynamic self-assembly and directed flow of rotating colloids in microchannels. *Physical Review E*, 84(3), **2011**. URL <https://link.aps.org/doi/10.1103/PhysRevE.84.031404>. *Cited on page 38*
- [99] Holm, C. & Kremer, K. *Advanced Computer Simulation Approaches for Soft Matter Sciences III*, vol. 173. **2009**. *Cited on page 38*
- [100] Mussawisade, K., Ripoll, M., Winkler, R. G. & Gompper, G. Dynamics of polymers in a particle-based mesoscopic solvent. *The Journal of Chemical Physics*, 123(14):144905, **2005**. URL <http://aip.scitation.org/doi/10.1063/1.2041527>. *Cited on page 38*
- [101] Poblete, S., Wysocki, A., Gompper, G. & Winkler, R. G. Hydrodynamics of discrete-particle models of spherical colloids: A multiparticle collision dynamics simulation study. *Physical Review E*, 90(3), **2014**. URL <https://link.aps.org/doi/10.1103/PhysRevE.90.033314>. *Cited on page 38*
- [102] Batôt, G., Dahirel, V., Mériguet, G., Louis, A. A. & Jardat, M. Dynamics of solutes with hydrodynamic interactions: Comparison between brownian dynamics and stochastic rotation dynamics simulations. *Physical Review E*, 88(4), **2013**. URL <https://link.aps.org/doi/10.1103/PhysRevE.88.043304>. *Cited on pages 39 & 47*

Bibliography

- [103] Lettinga, M. P., Dhont, J. K. G., Zhang, Z., Messlinger, S. & Gompper, G. Hydrodynamic interactions in rod suspensions with orientational ordering. *Soft Matter*, 6(18):4556, **2010**. URL <http://xlink.rsc.org/?DOI=c0sm00081g>. *Cited on page 39*
- [104] Dahirel, V., Zhao, X., Couet, B., Batôt, G. & Jardat, M. Hydrodynamic interactions between solutes in multiparticle collision dynamics. *Physical Review E*, 98(5), **2018**. URL <https://link.aps.org/doi/10.1103/PhysRevE.98.053301>. *Cited on pages 39, 48, & 50*
- [105] Liu, P., Harder, E. & Berne, B. J. On the calculation of diffusion coefficients in confined fluids and interfaces with an application to the liquid-vapor interface of water. *The Journal of Physical Chemistry B*, 108(21):6595–6602, **2004**. URL <https://pubs.acs.org/doi/10.1021/jp0375057>. *Cited on page 40*
- [106] Botan, A., Rotenberg, B., Marry, V., Turq, P. & Noetinger, B. Hydrodynamics in clay nanopores. *The Journal of Physical Chemistry C*, 115(32):16109–16115, **2011**. URL <https://pubs.acs.org/doi/10.1021/jp204772c>. *Cited on page 40*
- [107] Yeh, I.-C. & Hummer, G. System-size dependence of diffusion coefficients and viscosities from molecular dynamics simulations with periodic boundary conditions. *The Journal of Physical Chemistry B*, 108(40):15873–15879, **2004**. URL <https://pubs.acs.org/doi/10.1021/jp0477147>. *Cited on page 41*
- [108] Botan, A., Marry, V. & Rotenberg, B. Diffusion in bulk liquids: finite-size effects in anisotropic systems. *Molecular Physics*, 113(17-18):2674–2679, **2015**. URL <http://www.tandfonline.com/doi/full/10.1080/00268976.2015.1021730>. *Cited on page 41*
- [109] Zhao, X. *Simulation mésoscopique pour le transport d'électrolytes asymétriques en taille et en charge*. Thèse de doctorat, **2016**. *Cited on page 41*
- [110] Lipowsky, R. & Sackmann, E. *Structure and Dynamics of Membranes: I. From Cells to Vesicles / II. Generic and Specific Interactions*. Elsevier, **1995**. Google-Books-ID: V1H9oVpNC7wC. *Cited on page 56*
- [111] Hartkamp, R., Siboulet, B., Dufrêche, J.-F. & Coasne, B. Ion-specific adsorption and electroosmosis in charged amorphous porous silica. *Physical Chemistry Chemical Physics*, 17(38):24683–24695, **2015**. URL <http://xlink.rsc.org/?DOI=C5CP03818A>. *Cited on page 60*
- [112] Qiao, R. & Aluru, N. R. Ion concentrations and velocity profiles in nanochannel electroosmotic flows. *The Journal of Chemical Physics*, 118(10):4692–4701, **2003**. URL <http://aip.scitation.org/doi/10.1063/1.1543140>. *Cited on page 60*
- [113] Svensson, B., Joansson, B. & Woodward, C. E. Monte carlo simulations of an electric double layer. *The Journal of Physical Chemistry*, 94(5):2105–2113, **1990**. URL <https://pubs.acs.org/doi/abs/10.1021/j100368a068>. *Cited on page 60*
- [114] Ceratti, D. R., Obliger, A., Jardat, M., Rotenberg, B. & Dahirel, V. Stochastic rotation dynamics simulation of electro-osmosis. *Molecular Physics*, 113(17-18):2476–2486, **2015**. URL <http://www.tandfonline.com/doi/full/10.1080/00268976.2015.1037370>. *Cited on pages 60, 61, 79, & 81*
- [115] Mills, R. The self-diffusion of chloride ion in aqueous alkali chloride solutions at 25°. *The Journal of Physical Chemistry*, 61(12):1631–1634, **1957**. URL <http://pubs.acs.org/doi/abs/10.1021/j150558a015>. *Cited on page 65*

Bibliography

- [116] Ju, S.-P., Chang, J.-G., Lin, J.-S. & Lin, Y.-S. The effects of confinement on the behavior of water molecules between parallel plates of (001) planes. The Journal of Chemical Physics, 122(15):154707, **2005**. URL <http://aip.scitation.org/doi/10.1063/1.1878552>. *Cited on page 66*
- [117] Chambers, J. F., Stokes, J. M. & Stokes, R. H. Conductances of concentrated aqueous sodium and potassium chloride solutions at 25°. The Journal of Physical Chemistry, 60(7):985–986, **1956**. URL <http://pubs.acs.org/doi/abs/10.1021/j150541a040>. *Cited on page 89*
- [118] Happel, J. & Brenner, H. Low Reynolds number hydrodynamics: with special applications to particulate media. Springer Science & Business Media, **2012**. *Cited on page 95*
- [119] Saugey, A., Joly, L., Ybert, C., Barrat, J. L. & Bocquet, L. Diffusion in pores and its dependence on boundary conditions. Journal of Physics: Condensed Matter, 17(49):S4075–S4090, **2005**. URL <http://stacks.iop.org/0953-8984/17/i=49/a=005?key=crossref.ea67d6812d5b416bdf92aa242bb7c08>. *Cited on pages 99, 101, & 139*
- [120] Galipoğlu, M., Erdal, M. S. & Güngör, S. Biopolymerbased transdermal films of donepezil as an alternative delivery approach in alzheimer’s disease treatment. AAPS PharmSciTech, 16(2):284–292, **2014**. URL <https://www.ncbi.nlm.nih.gov/pmc/articles/PMC4370960/>. *Cited on page 103*
- [121] Iqbal, J., Sarti, F., Perera, G. & Bernkop-Schnürch, A. Development and in vivo evaluation of an oral drug delivery system for paclitaxel. Biomaterials, 32(1):170 – 175, **2011**. URL <http://www.sciencedirect.com/science/article/pii/S0142961210011919>. *Cited on page 103*
- [122] Li, H. & Huck, W. T. S. Polymers in nanotechnology. Current Opinion in Solid State and Materials Science, 6(1):3 – 8, **2002**. URL <http://www.sciencedirect.com/science/article/pii/S1359028602000086>. *Cited on page 103*
- [123] Teraoka, I. Polymer solutions: An introduction to physical properties. Dans: Polymer solutions, pages i–xv. **2002**. *Cited on pages 104 & 106*
- [124] Buschow, K. H. J. Encyclopedia of Materials: Science and Technology. Elsevier, **2001**. *Cited on page 104*
- [125] Bishop, M., Kalos, M. H. & Frisch, H. L. Molecular dynamics of polymeric systems. The Journal of Chemical Physics, 70(3):1299–1304, **1979**. URL <http://aip.scitation.org/doi/10.1063/1.437567>. *Cited on page 108*
- [126] Armstrong, R. C. Kinetic theory and rheology of dilute solutions of flexible macromolecules. i. steady state behavior. The Journal of Chemical Physics, 60(3):724–728, **1974**. URL <http://aip.scitation.org/doi/10.1063/1.1681141>. *Cited on page 109*
- [127] Kremer, K. & Grest, G. S. Dynamics of entangled linear polymer melts: A molecular-dynamics simulation. The Journal of Chemical Physics, 92(8):5057–5086, **1990**. URL <http://aip.scitation.org/doi/10.1063/1.458541>. *Cited on page 109*
- [128] Lenz, D. A., Blaak, R. & Likos, C. N. Adsorption characteristics of amphiphilic dendrimers. Soft Matter, 5(15):2905, **2009**. URL <http://xlink.rsc.org/?DOI=b904163j>. *Cited on page 111*
- [129] Gradshteyn, I. S. & Ryzhik, I. M. Table of Integrals, Series, and Products. Academic Press, **2014**. Google-Books-ID: F7jiBQAAQBAJ. *Cited on page 112*
- [130] Press, W. H. Numerical Recipes in Fortran 90, vol. 2. 2002 édition. URL <http://www.nehudlit.ru/books/detail5672.html>. *Cited on page 113*

Bibliography

- [131] Narros, A., Moreno, A. J. & Likos, C. N. Effects of knots on ring polymers in solvents of varying quality. *Macromolecules*, 46(9):3654–3668, **2013**. URL <https://www.ncbi.nlm.nih.gov/pmc/articles/PMC3667624/>. *Cited on page 113*
- [132] Huang, C. C., Chatterji, A., Sutmann, G., Gompper, G. & Winkler, R. G. Cell-level canonical sampling by velocity scaling for multiparticle collision dynamics simulations. *Journal of Computational Physics*, 229(1):168–177, **2010**. URL <http://www.sciencedirect.com/science/article/pii/S0021999109005166>. *Cited on page 114*
- [133] Weiss, L. B., Nikoubashman, A. & Likos, C. N. Topology-sensitive microfluidic filter for polymers of varying stiffness. *ACS Macro Letters*, 6(12):1426–1431, **2017**. URL <http://pubs.acs.org/doi/10.1021/acsmacrolett.7b00768>. *Cited on pages xi, 115, 152, 153, & 154*
- [134] Dimitrov, D. I., Milchev, A., Binder, K., Klushin, L. I. & Skvortsov, A. M. Universal properties of a single polymer chain in slit: Scaling versus molecular dynamics simulations. *The Journal of Chemical Physics*, 128(23):234902, **2008**. URL <http://aip.scitation.org/doi/10.1063/1.2936124>. *Cited on page 117*
- [135] Hsu, H.-P. & Grassberger, P. Polymers confined between two parallel plane walls. *The Journal of Chemical Physics*, 120(4):2034–2041, **2004**. URL <http://aip.scitation.org/doi/10.1063/1.1636454>. *Cited on pages 117 & 118*
- [136] Jendrejack, R. M., Schwartz, D. C., de Pablo, J. J. & Graham, M. D. Shear-induced migration in flowing polymer solutions: Simulation of long-chain dna in microchannels. *The Journal of Chemical Physics*, 120(5):2513–2529, **2004**. URL <http://aip.scitation.org/doi/10.1063/1.1637331>. *Cited on page 152*
- [137] Reddig, S. & Stark, H. Cross-streamline migration of a semiflexible polymer in a pressure driven flow. *The Journal of Chemical Physics*, 135(16):165101, **2011**. URL <https://aip.scitation.org/doi/full/10.1063/1.3656070>. *Cited on page 152*
- [138] Ma, H. & Graham, M. D. Theory of shear-induced migration in dilute polymer solutions near solid boundaries. *Physics of Fluids*, 17(8):083103, **2005**. URL <http://aip.scitation.org/doi/10.1063/1.2011367>. *Cited on page 152*
- [139] Steinhauser, D., Köster, S. & Pfohl, T. Mobility gradient induces cross-streamline migration of semiflexible polymers. *ACS Macro Letters*, 1(5):541–545, **2012**. URL <https://pubs.acs.org/doi/10.1021/mz3000539>. *Cited on page 152*